Master of Science Thesis

Towards high-fidelity aero-servo-elasticity analysis

Yannick Bunk

Faculty of Aerospace Engineering · Delft University of Technology

Acknowledgement

I had the pleasure to work on the development of a code for high-fidelity large-eddy simulations coupled with structural models as part of my master thesis at the TU Delft. Starting the development from scratch gave me an immense learning opportunity as I was in contact with all components of the code through technical discussions with my team, code reviews and feature testing.
I herewith would like to state my gratitude to everyone that has supported me during my master thesis project. First and foremost I would like to thank my two supervisors Prof. dr. Stefan Hickel and Dr. Vito Pasquariello who supported me throughout this project from the selection of the thesis topic, through the development of the solver and during the review of my final work. Further, I would like to thank my whole team, who got us from simulations of the Taylor Green vortex to simulations of complex moving geometries coupled with structural models and adaptive mesh refinement in the short period of one and a half years. I would like to express my gratitude to Dr. Christoph Brehm and his team for supporting us on the immersed boundary method and giving us insight into coupling wall modeling approaches to immersed boundary methods.
Last but not least I would like to thank my parents for all the support they have given me during the exhausting Corona period and for always providing me a warm home during the lengthy home office periods.

Summary

The development of a high-fidelity fluid-structure interaction tool for the simulation of aircraft flight dynamics in the subsonic flow regime is presented. The tool combines a high-fidelity large-eddy simulation code with an immersed boundary method, a multi-body solver and a loose coupling scheme between fluid and solid. The development of the code is motivated by the need to accurately and efficiently simulate aircraft flight dynamics at off-design conditions, such as in separated flow states. The accurate simulations are necessary for the continuous optimization of current aircraft designs and the development of novel aircraft concepts.

The developments presented in this thesis focus on three fields of the fluid-structure interaction problem. The modeling of solid geometries in the fluid solver through an immersed boundary method, the coupling of the fluid and solid domain through a loose coupling scheme, and the development of a multi-body solver for the simulation of aircrafts and their components.

An extensive literature review is presented on these three fields of the fluid-structure interaction problem. The literature review is conducted to select appropriate methods for the final solver. Based on this review, a ghost-cell approach is selected for the immersed boundary method of the solver. A loosely coupled serial staggered procedure is selected to couple the fluid and solid domains in the solver. The floating frame of reference approach is selected for the derivation of the multi-body solver and a Newmark time integration method is selected for the integration of the equations of motion.

The mathematical formulation of the selected methods is presented. Novel approaches are derived for the immersed boundary method and multi-body solver. A hybrid-cell treatment is derived to reduce spurious numerical oscillations in flow fields with moving geometries. Further, the integration of wall-modeling approaches into the ghost-cell immersed boundary method is presented. A controller approach based on the time integration scheme of the multi-body solver is derived. The controller allows user-prescribed dynamic positions and orientations of constraints and bodies.

The developed fluid-structure interaction solver has been rigorously verified and validated for multiple test cases. Simulations of an oscillating cylinder and moving airfoil are presented for the verification of the hybrid-cell treatment. Results with hybrid-cell treatment enabled and disabled demonstrate the effectiveness of the developed approach

in the suppression of spurious oscillations in the flow field. Simulations of a single and double pendulum are presented to verify the implementation of the multi-body equations of motion and constraints. The validation of the developed solver is performed with reference numerical and experimental results. Results of the laminar flow around an inline-oscillating cylinder are in excellent agreement with available numerical and experimental reference results. Simulations of the dynamic stall problem of helicopter blade sections are presented. The results show that the solver accurately predicts the flow features of the dynamic stall problem. Discrepancies between the present code and the available numerical and experimental results are attributed to an insufficient modeling and resolution of the near-wall flow field. Last but not least, flutter of a two degree of freedom NACA0012 airfoil is simulated. The developed solver accurately predicts the presence of stable, limit cycle and flutter regions. Discrepancies were found in the response frequencies between the results of the present code and available numerical and experimental results. The discrepancies are caused by insufficient resolution of the near-wall flow field.
The verification and validation simulations proof the effectiveness of the derived methods and the correct implementation. The validation results further show that the solver accurately and efficiently predicts the flow field of complex flows and fluid-structure interaction problems.

Contents

List of Figures

List of Tables

Chapter 1

Introduction

The global Corona pandemic has caused a significant decrease in global air travel. At the same time however, it has not stopped the development of new aircraft concepts for short and long haul flights and it has not stopped the emerging urban air mobility sector. Both targeted towards providing more environmental friendly and more economically beneficial solutions for transportation via a continuous improvement of existing aircrafts and by establishing new modes of transportation via novel aircraft concepts.
The development of these aircrafts is enabled through electrification, advances in materials and advances in aircraft integration. Besides these fields, advances in the computational methods play an equally important role in the development of future aircrafts. As they enable the design of more efficient aircraft components by providing more accurate and detailed analysis and by providing predictions for coupled phenomena such as aero-elasticity and aero-servo-elasticity.
While the development of such tools is not new, the literature review in the present thesis shows that existing tools are either of varying fidelity, targeted towards different applications and are often designed for high modularity and flexibility rather than for optimal performance. The need for a high-fidelity scale-resolving fluid dynamic solver coupled with a multi-body solver which is targeted specifically to the aero-servo-elasticity analysis of aircraft was derived from this conclusion. For that reason, the development of the coupling between the computational fluid dynamic solver and the multi-body solver extended to the modeling of the geomtries in the flow field and solution of the multi-body equations form the topic of this thesis project.
The aforementioned need and current state of computational tools is extensively studied in the literature review part. A discussion is held on the currently available computational tools and it is presented how the coupling of high-fidelity scale-resolving computational fluid dynamics solvers with multi-body solvers and flight dynamics tools aids the design of future aircrafts. Subsequently, the envisioned high-fidelity aero-servo-elasticity tool is broken down in its individual components. The breakdown indicates three subjects: (1) The modeling of the fluid domain, which focuses on the numerical modeling of the solid/elastic boundaries of the aircraft components. (2) The modeling of the solid domain, either as rigid body or elastic body, the solution of the constraint rigid and elastic

body system and reduced order modeling techniques for improved efficiency. (3) Coupling schemes for the fluid and solid domains, which include the coupling of the spatial solution in either domain and the time integration of the coupled system.
Following the literature study, the development of the components of the computational tool is presented. The development of the tool concentrates on sub-parts of the presented three fields. A hybrid ghost-cell immersed boundary method is developed for the simulation of moving geometries in the flow field. The developed immersed boundary method enables the simulation of low and high Reynolds number wall-bounded flow with a wall-modeling approach.
On the structural side, the development of a multi-body solver for rigid bodies is presented. The developed solver enables the simulation of aircrafts, split into individual components, such as fuselage, wings and control surfaces. Spring and damper constraints are implemented to investigate aero-elastic phenomena such as flutter. A control strategy on acceleration level is developed to enable the user to control the position of geometries and constraints via user-prescribed paths. A loose coupling approach is implemented to couple the fluid solver with the multi-body solver. The development of the full elastic multi-body solver and implementation of reduced order models is beyond the scope of this thesis.
The developed tools and methods are validated with data from experimental and numerical simulations. The validation of the tool includes low and high Reynolds number flow problems around geometries with user-prescribed paths for the validation of the hybrid ghost-cell immersed boundary method. Simulations of high Reynolds number flow around static geometries are performed for the validation of the wall-modeling approach, and simulations of a sprung mounted airfoil are performed to validate the multi-body solver and coupling of the multi-body solver with the fluid dynamic solver.
The results of the literature study are presented in chapter 2. The development of the immersed boundary method is described in chapter 3. The chapter explains the implementation of no-slip wall boundary conditions and wall-modeled boundary conditions. A hybrid-cell treatment is introduced in order to reduce spurious oscillations in simulations of moving geometries. Chapter 4 shows the derivation of the multi-body equations of motion. The chapter covers further the derivation of the geometrical, spring and damper constraints, the time integration and solution procedure for the multi-body system, and the control strategy of the rigid bodies and constraints. The verification tests of the immersed boundary method and multi-body solver are conducted separately. The results of the immersed boundary verification tests are presented in chapter 5 and the results of the multi-body solver verification tests are presented in chapter 6. The validation of the developed tool is started with a low Reynolds number flow case in form of an in-line oscillating cylinder, in chapter 7. The validation of the solver is extended to high Reynolds number flow with simulations of flow around a NACA0012 airfoil at static angles of attack and with simulations of a dynamic stall problem with the identical NACA0012 airfoil. The results of the static and dynamic simulations are presented in chapter 8. The validation of the developed solver is finished with a study on flutter of a sprung mounted NACA0012 airfoil. The case is selected for the validation of the multi-body solver and the implemented loose coupling scheme. The results of the validation case are presented in chapter 9. A final discussion of the developed solver and obtained results of the validation cases is presented in chapter 10. Recommendations are given on further validation cases and possible enhancements of the developed solver.

Chapter 2

Literature study

2.1 Background

New aircraft concepts emerged in recent years which aim at improving the environmental impact of aviation, increasing the economic benefit and providing solutions for new modes of transportation. Examples of such concepts are the Flying-V (TU-Delft, n.d.), the concepts of the ZEROe program of Airbus (Airbus, n.d.) and the emerging urban air mobility (UAM) sector, with companies such as Lilium GmbH (Lilium, n.d.), Joby Aviation (Joby-Aviation, n.d.) and EHang (EHang, n.d.). Without understating the importance of advances in electrification, aircraft integration as well as new materials as enabler of these new concepts, the use of higher fidelity methods and the combination of computational tools in a multi-disciplinary framework is and will continue to be an enabler of new aerospace solutions (Slotnick et al., 2014). The importance of the former is illustrated in this chapter by showing how advancements in the current aerodynamic tools enable or at minimum accelerate the development of next generation aircrafts. After discussing the necessary advancements of current aerodynamic tools, we take a multidisciplinary look by including the structural degrees of freedom in the analysis and later the flight dynamic degrees of freedom. The former topic is part of the computational aero-elasticity (CAE) study (D. Schuster, Liu, & Huttsell, 2003) while the latter topic is part of the aero-servo-elasticity (ASE) field (Tewari, 2015).

2.1.1 A note on computational fluid dynamics

The aerodynamic analysis has advanced massively with the availability of increased computational power in the 1970 to 1990 from the use of panel methods, solving the potential flow equations, further to the solution of the inviscid Euler equations with and without boundary-layer formulations, to the solution of the Reynolds averaged Navier Stokes (RANS) equations (Slotnick et al., 2014). The use of scale-resolving techniques, such as large-eddy simulations (LES), wall-modeled LES and hybrid RANS-LES has increased

significantly since the year 2000, but is at the time of writing not seen as the preferred choice for engineers during the design and validation of the aforementioned aircraft concepts. Results of LES with aircraft applications are currently mainly used for aeroacoustic analysis purposes (Khorrami & Fares, 2019) and for the design of individual components, such as aeroengine combustors (James, Anand, & Sekar, 2008). Currently, the use of LES for design purposes is constrained by the computational cost which results in slow turn-around times.
The validity of RANS simulation results is limited to attached flows. RANS solutions for detached flows are highly dependent on the implemented turbulence model and underlying flow case (Bardina, Huang, & Coakley, 1997). Therefore, the use of RANS simulation results for the analysis and design validation at off-design conditions is not feasible without the support of wind-tunnel and or flight-test measurements (Malik & Bushnell, 2012). At the same time, some newer emerging aircraft concepts rely on the expansion of the flight envelope into regions with significant flow detachment. Such concepts include the transition flight concepts of the UAM sector. While, these types of concepts have been designed with the currently available and older methods, such as the MV/CV-22 Osprey or AW-609, some significant drawbacks and program risks arise from their use: **(1)** The performance of the designed aircraft is sub-optimal due to uncertainties of the computational methods, **(2)** program delays may arise when discrepancies between wind-tunnel/flight-test data and computational methods trigger redesigns and **(3)** the testing and validation of flight control laws relies on wind-tunnel data or flight-test data as the CFD generated aerodynamic databases might be insufficient, which causes an increased development time (D. M. Schuster, 2011).
The development of future CFD software should be aimed at making scale-resolving techniques further available. Initially, for the use as a validation tool prior to wind-tunnel and flight testing to reduce development time and risk, and, once the computational cost is deemed acceptable, integrated in the design process to improve the performance of future aircrafts.
So far, the advancements in aerodynamic methods and their use in the design process were achieved via advancements in the available computational power. Further increases in the computational power will play an important role in making the use of scale-resolving techniques feasible for the validation and design of future aircrafts. At the same time, advancements in the numerics and solver algorithms will equally play an important role (Slotnick et al., 2014). The lattice boltzmann method (LBM) is a prime example. The method gained popularity in recent years due to its formulation which is highly suitable for massively parallelized high performance computing (HPC) hardware such as graphic processing units (GPU), which have outperformed advancements of central processing units (CPU) (Obrecht, Kuznik, Tourancheau, & Roux, 2013).

2.1.2 A note on aero-structural analysis

It has been shown how advances in the aerodynamic tools aid the design of future aircrafts. The discussion is extended in the following paragraph with a look at coupled aero-structural analysis. The coupled analysis of the two disciplines predicts the structural response due to aerodynamic forces and at the same time predicts the changes in

the aerodynamic characteristics of the investigated geometry due to the structural deformations. The interested reader is referred to the book of (Wright & Cooper, 2014) for an introduction to the topic. The discussion is started on the fundamental level by illustrating how the use of coupled aero-structural methods aids the design of aircrafts without specifying the need for high-fidelity methods. Afterwards, the benefits of moving to higher fidelity tools for aero-structural analysis are shown.

The benefits of coupled aero-structural analysis are grouped into three areas: **(1)** Increased accuracy of aerodynamic performance predictions, **(2)** capability of predicting coupled phenomena and **(3)** improved efficiency of structural designs via more accurate and complete load cases.

The external shape of wings and other lifting and non-lifting surfaces of aircrafts can vary significantly due to the deformation of the structure under load in both design and off-design conditions. This introduces uncertainties in the results as the aerodynamic characteristics vary between the deformed and un-deformed shape. The coupled analysis can alleviate or fully remove these uncertainties because the aerodynamic analysis is performed on the deformed shape. The variation in the aerodynamic characteristics between deformed and un-deformed surfaces and the importance of an aero-structural analysis for the quantification of the aircraft aerodynamic characteristics will increase further with the trend towards higher aspect ratio and as a result more flexible wing designs (Kenway & Martins, 2014). The aerodynamic knowledge gathered from the coupled analysis is firstly used for more certainty in the validation of the aircraft performance and secondly used within the design process to obtain optimal aircraft designs.

Dynamic phenomena, that arise from the coupling between the aerodynamic forces and the structural response, can only be predicted and designed for with an assessment of the coupled aero-structural system. The considered phenomena are commonly considered within the field of aero-elasticity. The most common phenomena are divergence, control inversion and flutter (D. Schuster et al., 2003). The importance of the field was best demonstrated during the Tacoma Narrows bridge catastrophe in (1940) (Green & Unruh, 2006) when the coupling between aerodynamics and the structure resulted in the collapse of the bridge. The importance of the field will further increase in the future with the trend towards higher aspect ratio and more flexible wings (Palacios, Cesnik, & Reichenbach, 2007).

Related to the first two aspects of the aero-structural analysis, more efficient structural designs are achieved via the combined analysis. This is achieved through more accurate load predictions via the aerodynamic analysis of the deformed rather than the undeformed shape and a more complete set of load conditions via the prediction of both steady and unsteady load cases. The weight savings that are achieved through the efficient structural design are either turned into increased payload, reduced fuel burn or more range which contributes to the overall goals of the industry, which were introduced at the beginning of the chapter.

The discussion has presented the use and need of aero-structural analysis in the design of aircrafts. The analysis is further extended by investigating how the use of higher fidelity aerodynamic solvers aids the aero-structural analysis.

Initial improvements in the accuracy of aero-structural analysis are achieved via the move from linear aerodynamic methods (Crawley et al., 1995) to nonlinear aerodynamic methods such as unsteady RANS solvers (Baxevanou, Chaviaropoulos, Voutsinas, & Vlachos, 2008). Linear solvers have been successfully used for load predictions and aero-elasticity

analysis of aircraft (Yi & Changchuan, 2018). However, the methods tend to overpredict structural loads of high load factor maneuvers, are not applicable to stalled conditions and are not applicable for the analysis at high Mach numbers. Solutions to these conditions are achieved with the use of Euler solvers (B. Zhang, Ding, Cheng, & Zhang, 2016) and RANS based solvers (Baxevanou et al., 2008). Further improvements to the aero-structural analysis are achieved with the use of scale-resolving techniques. The advantages of scale-resolving techniques for the anlaysis of off-design conditions such as separated flow conditions has been already discussed on the aerodynamic side (P. Zhang & Huang, 2011). The increased accuracy of the aerodynamic solution leads to more accurate load predictions. Furthermore, buffeting load cases may be added to the load database which are either not predictable with linear methods or are not accurately predictable with RANS solvers (Morton, Cummings, & Kholodar, 2007; Katzenmeier, Vidy, Benassi, & Breitsamter, 2019).

2.1.3 A note on aero-servo-elasticity analysis

The rational behind high-fidelity aerodynamic simulations and the coupling of these simulations with structural solvers has been introduced up to this point. The discussion is further expanded with the coupling of the discussed aero-structural analysis with control laws and flight dynamics degrees of freedom, leading to the full analysis of the aero-servo-elastic aircraft system. It is important to note at this point, that while the integration of the control laws is crucial for the full aero-elasticity analysis, the focus of this chapter and the research objective is on the flight dynamics degrees of freedom. The reader is pointed to (Tewari, 2015) on the topic of modeling and analysis of aero-servo-elastic systems.
Three scenarios are considered within this topic: **(1)** The coupling of aero-structural analysis with control laws, **(2)** the coupling of high-fidelity aerodynamic solvers with flight dynamics degrees of freedom and flight control laws and **(3)** the combined analysis of the flight dynamics of an elastic aircraft with coupled flight control laws.
The introduction of the aircraft control laws in the aero-structural analysis has been used for active flutter suppression (Theis J. J, 2020) as well as gust load alleviation (H. Liu & Wang, 2019), which are used to expand the aircraft flight envelope, increase the aircraft component lifespan and increase passenger comfort. The former analysis is up to a certain extend achievable without introducing the flight dynamics degrees of freedom.
Simulations of the aircraft characteristics for pilot training and testing/design of the flight control laws is primarily performed based on simple but fast aerodynamic models or aerodynamic databases and surrogate models based on CFD data and experimental data (M. Kim et al., 2019). The limits of the low fidelity models have already been discussed. The use of aerodynamic databases is more suited for the analysis and design of flight control laws as they are quick and can map non-linear behavior. But a full coverage of the complete flight envelope, including control derivatives, dynamic derivatives and additional time history effects (such as hysteresis) is very expensive and up to impossible. Therefore, aerodynamic databases can not replace experimental flight testing. Consequently, the use of the proposed high-fidelity method with coupled flight/rigid body dynamics and control laws is very attractive, because flight dynamic characteristics and control laws can be assessed in regions of the flight envelope which are either computational expensive or to complex too accurately model.

However, with the trend towards higher aspect ratio and more flexible wings the wing frequencies approach the flight dynamics frequencies which results in a strong coupling between the flight dynamic degrees of freedom and elastic degrees of freedom (Yi & Changchuan, 2018). At this point the solution of the flight dynamics equations alone do not provide an accurate description of the aircraft characteristics and the elastic degrees of freedom must be included. The resulting aircraft system can be described by the theory of elastic multi-body dynamics (Shabana, 2020). (Yi & Changchuan, 2018; Dussart, Portapas, Pontillo, & Lone, 2018) present aero-servo-elastic frameworks which apply these theories, but in combination with low fidelity aerodynamic solvers.

2.1.4 Research objective

This chapter has introduced the benefits and need of high-fidelity simulations for the validation and design of future aircraft concepts. It was further shown how the coupling of high-fidelity simulations with the structural field and aero-servo-elasticity field can aid the design of aircrafts. The analysis was ended with the introduction of coupling elastic multi-body dynamics with computational fluid dynamics. This framework would allow the flight dynamics and structural analysis of elastic aircrafts in combination with highly accurate scale-resolving fluid dynamic simulations. The **research objective** is the development and validation of a multi-body solver tailored to the analysis of aircraft and the integration and coupling of the solver into a currently developed GPU based scale-resolving CFD solver.
The development of such tools is not new. (Yi & Changchuan, 2018; Dussart et al., 2018) present an aero-servo-elasticity framework for the flight dynamics and control analysis of highly flexible aircraft, (Y. Li et al., 2017) developed an aero-servo-elastic simulation framework for windturbines based on coupled fluid and mutli-body dynamics and (Yang, Bashir, Michailides, Li, & Wang, 2020) extended the aero-servo-elastic analysis of windturbines to offshore windturbines by including hydrodynamic effects in the analysis. Furthermore, the application of a variational aero-elastic framework for flexible multi-body dynamics was presented by (G. Li, Law, & Jaiman, 2019a, 2019b) for the simulation of flying animals. A delayed detached eddy simulation treatment was used for the prediction of the turbulent flow. Commercial and proprietary codes have been developed for the coupled analysis. ASTEP (Roughen, Baker, Seber, & Taylor, 2006) advertise with the capabilities of performing aerothermodynamic, servo, thermal, elastic, propulsive coupled analysis with aerodynamic solvers ranging from Euler simulations to Navier-Stokes simulations. Another commercial code SIMPACK [1] (Krüger, 2007) has been developed for simulations of multi-body systems. The solver can be coupled with low to high-fidelity aerodynamic tools.
All these methods are not optimal for the specific usecase of the developed aero-servo-elastic framework for different reasons. The presented methods are partially based on lower fidelity aerodynamic methods (Yi & Changchuan, 2018; Dussart et al., 2018), designed for high modularity and functionality (Dussart et al., 2018; Krüger, 2007) rather than low computational cost and tailored to specific applications (G. Li et al., 2019a, 2019b) and (Y. Li et al., 2017; Yang et al., 2020). A fast solution of the governing equa-

[1] https://www.3ds.com/de/produkte-und-services/simulia/produkte/simpack/

tions and efficient integration of the multi-body dynamics solver into the aerodynamic solver is crucial for the feasibility of performing high-fidelity simulations of complete maneuvers. This is only possible with a tight integration of the aerodynamic and multi-body solvers and by tailoring the numerical scheme to the specific problem of simulating the flight dynamics of an elastic aircraft. The research is aiming to answer the following research question:

What is an efficient implementation of a multi-body dynamics solver inside a GPU-based high-fidelity scale-resolving CFD solver ?

The answer to this question is split into two parts. A literature review is conducted first to research existing methods for the solution of coupled multi-body dynamics/fluid dynamics problems and guide the selection of methods for the developed framework. The results of the literature study are presented in the remainder of this chapter. The formulation and specifics of the implementation of the developed tool together with validation results are presented in the following chapters. The research field is split into three smaller fields of fluid/solid coupling methods, fluid domain modeling and solid domain modeling. The breakdown of the solvers is graphically illustrated in figure 2.1. The results of the literature review about the fluid/solid coupling methods are presented in section 2.2. The review starts with an introduction to monolithic and partitioned coupling approaches. Afterwards, a more elaborate discussion is held about coupling/interpolation of the interface solution and the temporal coupling approaches of partitioned methods. The literature review of the fluid domain is presented in section 2.3. Two topics are covered, a high level discussion of the fluid domain discretization and modeling of the turbulent flow field and a more elaborate discussion on the topic of immersed boundary methods. The results of the literature review on the modeling of the solid domain are presented in section 2.4. The review is started with a discussion of the rigid body (RB) equations of motion and the modeling and solution of constraint rigid body systems. Afterwards, the elastic degrees of freedom are introduced and different approaches for the kinematic description of elastic bodies are reviewed. The application of reduced order modeling (ROM) techniques is envisioned to reduce the number of elastic degrees of freedom. A review of these methods is shown in section 2.4.3. The discussion of the solid domain is finished with a review of time integration methods for the governing equations of both rigid and elastic multi-body systems. The final goal of the developed framework is the aero-servo-elastic analysis of the elastic aircraft. However the implementation of the control laws and modeling of aircraft sensors is not part of the research project.

2.2 Coupling approach

The review of the computational fluid-structure interaction methods is started with a discussion of possible fluid/solid coupling approaches. The coupling approach is selected first because it has large effects on the selection of the numerical methods for the fluid and solid domains, the transfer of the solution between the domains and the time integration of the resulting system.
Today's approaches are commonly grouped into two categories. Category **1** contains methods based on monolithic coupling approaches (Blom, 1998; J. Liu, Jaiman, & Gurugubelli,

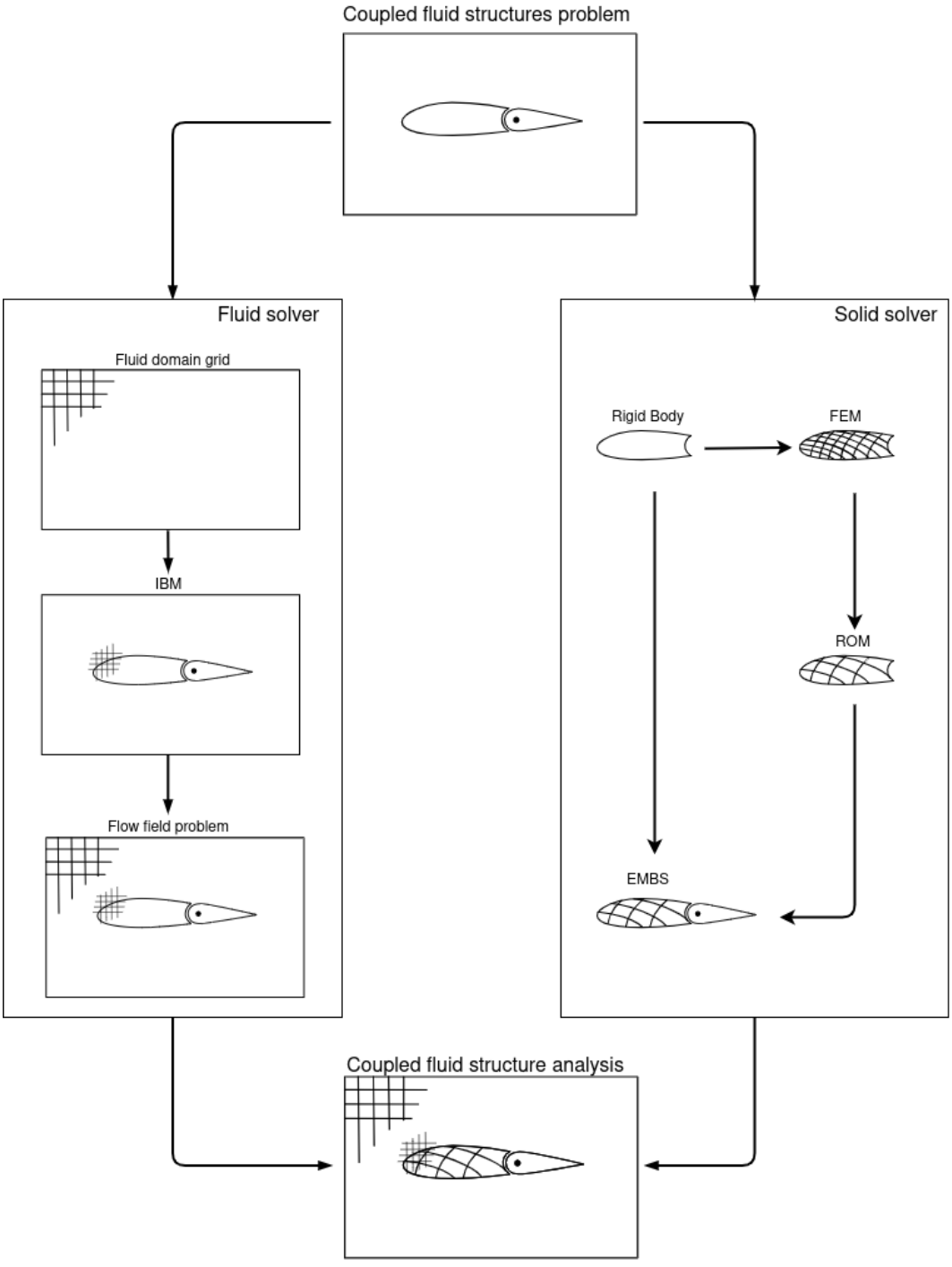

Figure 2.1: Graphical representation of the solver break down.

2014), category **2** collects coupling methods based on a staggered or partitioned approach (Felippa, Park, & Deruntz, 1977; Farhat, Lesoinne, & Maman, 1995; Farhat & Lesoinne, 2000).

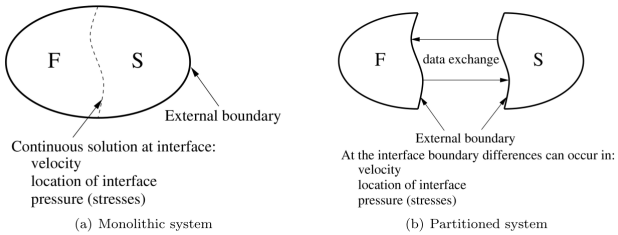

Figure 2.2: Graphical representation of a monolithic and partitioned approach (Zuijlen, 2006, p. 2).

The monolithic approach assembles the governing equations of the fluid and solid domains into a single block (He & Zhang, 2017) and integrates the single block in time with a selected time integration scheme. The fully coupled approach results in superior stability properties and excellent conservation of energy. The method is therefore suitable for a wide range of fluid-structure problems including problems with low solid-fluid mass ratios (Turek et al., 2010). The development and application of a monolithic algorithm is presented in Blom (1998), together with a comparison of the monolithic and staggered algorithms via the piston problem.
The improved stability and energy conserving properties of the monolithic approach come at the cost of removing the modularity of the fluid and structural solvers due to the entanglement of the governing equations and combined time integration. As a result, significant recasting efforts of existing codes are required for the coupling of the fluid and solid domains (He & Zhang, 2017). The monolithic approach is depicted in figure 2.2 (a). In the partitioned approach, the fluid and solid domains are solved separately. The approach dates back to the early work of Felippa et al. (1977) in the 1970s. A coupling algorithm is introduced to (1) interpolate and transfer the motion and forces between the separated domains and (2) advance the solution in the domains in a coupled fashion (Zuijlen, 2006). The approach is depicted in figure 2.2 (b). The method is further divided into explicit and implicit coupling algorithms. Farhat and Lesoinne (2000) show the development of an explicit staggered algorithm and its application to the AGARD 445.6 flutter problem. Farhat et al. (1995) describe the implementation of implicit and explicit partitioned schemes and apply them to the instability analysis of flat panels submerged in supersonic flow. The explicit method solves the coupling problems in a sub-iteration free fashion which results in a lag of the structural problem behind the fluid solution and the violation of the equilibrium condition at the interface (He & Zhang, 2017). This may lead to spurious solution errors or divergence of the numerical solution. The stability issues of the method come apparent once the density of the solid domain approaches the density of the fluid domain (Van Brummelen, 2009; Causin, Gerbeau, & Nobile, 2005). The implementation of the implicit staggered algorithm alleviates the problems of the explicit method and results in a strongly coupled system but it does require additional sub-iterations leading to increased computational cost. The following two sections provide

a more detailed discussion about the spatial coupling schemes and the temporal coupling schemes of the partitioned approach.

2.2.1 Spatial coupling

In either approach, monolithic and partitioned, an interface problem may arise for the transfer of the solution between the solid and fluid either across conformal or non-conformal meshes. The equations that arise from the interface problem either take an interpolation and data transfer role within partitioned approaches, or act as additional constraint equations in the monolithic approaches for the augmentation of the system matrix.
As discussed, with the use of the partitioned approach existing solvers and meshes can be used for the specific domain needs. But the use of the partitioned domains introduces a new problem of transferring the load and motion information between two or more domains.
This problem is mathematically expressed via a set of two algebraic equations that must be satisfied at the interface, given by

$$\begin{aligned} \mathbf{x}^f &= \mathbf{x}^s \\ \sigma^f \cdot \mathbf{n}^i &= \sigma^s \cdot \mathbf{n}^i, \end{aligned} \tag{2.1}$$

where $\mathbf{x}$ denotes the position of the interface surfaces on fluid and solid side, σ denotes the stress tensor on both sides of the interface and $\mathbf{n}$ denotes the normal vector of the fluid and solid interface boundaries. Equality 1 equates the displacement field of the fluid and solid domains at the interface. Equality 2 equates the tractions on the solid and fluid domain wetted surfaces at the interface.
A comprehensive review and comparison of existing solutions for the interface problem can be found in Boer, Zuijlen, and Bijl (2007). Perhaps the simplest approach for the interpolation of data between two meshes is the nearest neighbor (NN) approach (Thévenaz, Blu, & Unser, 2000). With this approach the load on the structural nodes is equal to the load on the nearest fluid node and the motion of the fluid nodes is equal to the nearest structural node. The approach globally conserves forces but is only first order accurate (Boer et al., 2007).
An improved and higher order method is achieved with the use of projection (Cebral & Lohner, 1997; Farhat, Lesoinne, & Le Tallec, 1998). The projection method projects the fluid side stresses onto the wetted surfaces of the structural mesh and integrates the projected values with the shape function of the elements. Equally the displacement of the fluid nodes is derived by projecting them onto the wetted surface of the structural mesh. However, as shown by Farhat et al. (1998), the original formulation of the method is not conservative. At the same time, Cebral and Lohner (1997); Farhat et al. (1998) have presented implementations of the projection which are conservative but not consistent. The conservative projection method of Farhat et al. (1998) is used for the prediction of the flutter speed index polar of the AGARD Wing 445.6 in Farhat and Lesoinne (2000).
A third method for the solution of the coupling problem was developed based on radial basis function interpolation (Beckert & Wendland, 2001; Rendall & Allen, 2009). The method is especially attractive for problems involving largely non-matching interfaces

such as the coupling of aerodynamic surfaces to structural beam models (Rendall & Allen, 2008; G. Li et al., 2019b). A limiting factor of the method is its computational cost. The method requires the inversion and storage of a full matrix with size $N_A \times N_S$, where N_A denotes the number of surface nodes of the fluid mesh and N_S denotes the number of wetted structural nodes. The computational cost of the method was significantly reduced recently by introducing local interpolation problems, where aerodynamic points only depend on their N_{sp} nearest structural points (Rendall & Allen, 2009; Murray, Thornber, Flaig, & Vio, 2019). The local support of the aerodynamic nodes may lead to non-smooth surfaces. Therefore Rendall and Allen (2009) introduced an additional smoothing function based on the nearest aerodynamic points. G. Li et al. (2019a) applies the radial basis function interpolation for the interpolation and transfer of the aerodynamic forces and structural displacements within their aero-elastic framework for flexible multi-body dynamics.
The methods that have been presented up to this point are commonly known as direct coupling methods. A different solution to the spatial coupling problem was derived from the structural analyses field were partitioned structural domains are coupled via the introduction of Lagrange multipliers (Barlow, 1982). The mortar method (Bernardi, Maday, & Patera, 1993, n.d.) is based on this idea. Within this method, Lagrange multipliers are used for the coupling of the interface displacement fields via a weigthed residual equation. The method is mathematically superior to the projection method as it does not lead to a decrease of the discretization order across the interface (Farhat et al., 1998), but the computational cost of the original method is comparable to the cost of the structural problem (Farhat et al., 1998) and not attractive for fluid-structure interaction problems. Further work was conducted on the Mortar method to improve its scale-ability and applicability to fluid-structure interaction problems. Wohlmuth (2000) presents a Mortar method with shape functions that are only supported by few local elements. The method leads to a diagonal matrix which is computational more attractive than the linear matrix of the original Mortar method (Bernardi et al., 1993, n.d.). Traditional methods are based on a two field approach where the interface mesh is equal to the surface mesh of one of the domains, denoted as master. The Lagrange multipliers are introduced to couple the master and conformal interface to the slave surface. These methods suffer from a master-slave bias (Zhou, Zhang, Chen, Peng, & Fang, 2020). Three field approaches instead introduce an additional interface field which is independently meshed from either domain. The domains are coupled to the interface field via Lagrange multipliers whereby the master-slave bias is eliminated. Such an approach is discussed in Park, Felippa, and Ohayon (2001) and Gerstenberger and Wall (2008).

2.2.2 Temporal coupling

With the staggered approach the integration of the fluid and structure domains is decoupled, which enables the use of different integration schemes and time steps. An overall coupled solution is achieved by communicating the motion and forces at the interface between the domains. The coupling approach dictates the direction and point in time of the communication between the coupled domains.
The elementary explicit coupling approach for the solution of fluid interaction problems is the conventional serial staggered (CSS) approach (Farhat & Lesoinne, 2000). The approach is shown in figure 2.3 with additional subcycling on the fluid side. The illustration

shows the states of the structural field U, the aerodynamic field W and the mesh state x.

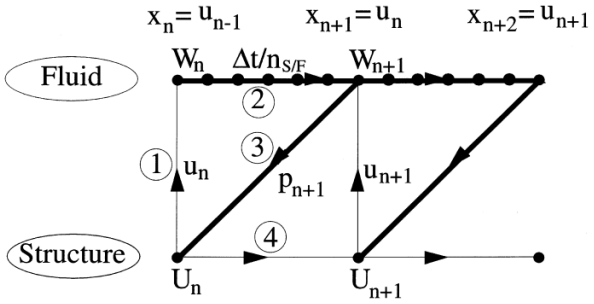

Figure 2.3: Illustration of the conventional serial staggered procedure with subcycling. (Farhat & Lesoinne, 2000, p. 503).

Figure 2.3 shows two important characteristics of the CSS approach: (1) The explicit and serial characteristics of the approach are illustrated by showing how first the fluid solution is advanced in time and later the structural solution, and (2) it illustrates the time lag of the communicated input of the fluid solution which receives the structural deformation x of the previous time step. The time lag of the communicated interface solution results in a first order accuracy of the coupled system in time (Farhat et al., 1995), independent of the time discretization of the partitioned domains. Furthermore, the CSS suffers from numerical instabilities due to the artificial added-mass effect (Van Brummelen, 2009; Causin et al., 2005).

Different approaches have been presented in literature to solve the drawbacks of the convential staggered scheme.

A possible solution to these issues is the implementation of an implicit staggering approach. The implicit staggering approach removes the time lag between the structural displacement and flow solution. An implicit problem arises due to the removal of the time lag because the fluid equations must be solved on a yet unknown deformed mesh. The implicit problem can be solved with the use of block-Jacobi and block-Gauss-Seidel processes (Le Tallec & Mouro, 2001) and also using more sophisticated block-Newton methods (Matthies & Steindorf, 2003). The implicit methods are attractive as they maintain modularity of the coupled solvers, achieve the temporal accuracy of the coupled solvers and achieve the same results as monolithic solvers (Matthies & Steindorf, 2003). The implicit method is not attractive from a computational view point due to the increased computational cost for each time step.

An explicit improved serial staggered (ISS) coupling approach was proposed by Farhat and Lesoinne (2000) by shifting the structural solution by half a time step. The analysis of the resulting coupling approach showed improved robustness and accuracy. Farhat, Zee, and Geuzaine (2006) later proved that the ISS coupling approach is second order accurate in time. A novel coupling method for solvers with second and higher order temporal accuracy was proposed by Zuijlen (2006). The proposed mixed implicit/explicit (IMEX) scheme can couple systems of any order (Zuijlen, 2006) and is highly suitable for the coupling of high order codes. An explicit scheme is used for the integration of the coupling term which results in a conditionally stable scheme even if implicit uncondition-

ally stable schemes are used in the individual partitions.
While the two presented approaches maintain a second order or higher temporal accuracy, they may suffer from numerical instabilities due to the added-mass effect. The added mass arises from the effect of the fluid on the structure, which can be represented as an additional structural mass in the higher frequencies (Van Brummelen, 2009). The effect increases with decreasing mass ratios between the structural and fluid domains. Causin et al. (2005) further showed that the added-mass effect not only leads to instabilities of explicit methods but also results in poor convergence properties of the presented implicit schemes for strongly coupled systems. Significant differences were also found between the added-mass effect in incompressible and compressible flow. It was proven that for compressible flows staggered approaches are stable for an sufficiently small time step, while for incompressible flows the stability of the solution may not be guaranteed independent of the selected time step (Van Brummelen, 2009).
This led to the development of the added-mass partitioned (AMP) coupling approach. For the simulation of lightweight or zero-weight rigid bodies in compressible flow (J. Banks, Henshaw, & Sjögreen, 2013) and also for the simulation of linear elastic bodies (J. W. Banks, Henshaw, & Schwendeman, 2012) and non-linear solids (J. W. Banks, Henshaw, Kapila, & Schwendeman, 2016). The stabilty of the above methods is achieved by introducing a fluid-solid Riemann problem into the treatment of the interface.
The approach was further used to stabilize staggered fluid-structure simulation for incompressible flow as presented by J. W. Banks, Henshaw, and Schwendeman (2014); Serino, Banks, Henshaw, and Schwendeman (2019) and the references within.

2.2.3 Discussion

Spatial and temporal coupling schemes for fluid and solid domains have been presented. The coupling schemes were primarily split into partitioned and monolithic coupling approaches. The literature research has shown that monolithic approaches have superior stability and accuracy characteristics over partitioned approaches by assembling the equations of either domain into a single block and integrating the resulting system. The superior characteristics of the monolithic approach come at the cost of less modularity and reduced flexibility in the development of the individual solvers.
The partitioned approach separates the computation of the individual domains. Coupling between the domains is introduced in the domain specific boundary conditions which are derived from the interface conditions. It was further presented that the partitioned approach is separated into explicit and implicit methods. Implicit methods have characteristics similar to the monolithic approach in terms of stability and accuracy but come at an increased computational cost. Explicit methods are computationally inexpensive but may become unstable for low solid fluid mass ratios.
A partitioned approach is selected for the coupling scheme of the GPU-based CFD solver and multi-body solver. The numerics of the flow solver have been developed prior to this thesis without consideration of the multi-body solver and optimised for GPU based HPC hardware. The integration of the numerics of the monolithic approach into the current fluid solver would significantly reduce the efficiency of the flow solution. Moreover, the time integration of the fluid and solid domain can not be separated in the monolithic approach. The time scales of the fluid flow are significantly smaller than the time scales of interest in the solid domain. With the partitioned approach the time integration of the

solid region is decoupled from the fluid domain and significantly higher time steps may be taken during the integration of the equations. Finally, the coupled solvers are used for the simulation of air and solid domains only. Solid-fluid mass ratios for most aerospace vehicles are significantly above one. Therefore, stability issues are not expected with the explicit partitioned approach.
A radial basis function (RBF) approach is used for the spatial coupling of the fluid and solid domains. Mortar based methods are not selected due to the increased computational cost that arises from the introduction of additional degrees of freedom at the interface. Projection based methods are conservative or consistent but do not offer the flexibility of RBF methods because a projection result may not be found if the fluid and structure surfaces meshes are significantly misaligned. As is the case with simple structural beam models.
Two schemes are considered for the temporal coupling of the fluid and solid domains. Initially the conventional serial staggered approach is implemented with additional sub-cycling on the fluid side. The approach is only first order accurate in time but was shown to be sufficiently accurate for the simulation of the Agard 445.6 wing (Farhat & Lesoinne, 2000).

2.3 Fluid solver

2.3.1 Fluid domain modeling and discretization

A wide range of aerodynamic methods have been used for fluid-structure and aero-servo-elasticity problems, ranging from low fidelity potential flow methods to high-fidelity scale-resolving methods.
Yi and Changchuan (2018) present the use of a doublet lattice method for the prediction of the aerodynamic forces in their aero-servo-elasticity framework.
B. Zhang et al. (2016) developed a method based on the Euler equations for the solution of transonic flutter problems and applied the method to the Agard 445.6 wing.
Yang et al. (2020) discuss the development and application of an aero-hydro-servo-elastic coupling framework for the analysis of offshore wind turbines. The framework employs the blade element momentum theory with a generalized wake model for the prediction of the aerodynamic forces.
G. Li et al. (2019b) use a hybrid RANS/LES model based on the delayed detached eddy DDES treatment for the solution of the flow around a flapping bat wing which is modeled via a flexible multi-body system and Roughen et al. (2006) describe the availability of different flow solvers ranging from RANS to LES in the proprietary ASTEP software tool for the aerothermodynamic, servo, thermal, elastic, propulsive coupled analysis.
As discussed in the introduction, a scale-resolving approach is selected for the developed aero-servo-elasticity framework, inline with the CFD 2030 goals (Slotnick et al., 2014). A review of the fluid model, turbulence closure and spatial/temporal discretization of the governing equations is outside the scope of this review. Instead, the already selected models and methods are presented. The governing equations are discretized on an adaptive Cartesian mesh using the finite volume method. The mesh is generated and updated with a forest of octree adaptive mesh refinement library (Burstedde, Wilcox, & Ghattas, 2011). The selected mesh is ideal for GPU based numerical solvers. Very low memory

requirements for the mesh allow the solution of large problems on GPU which are commonly bound by memory limitation. Reduced memory requests and efficient caching of the partially structured data during the computation reduce overall computational cost. The spatial discretization and explicit time integration scheme are proprietary and are not discussed further. A wall-modeled LES approach is selected for the modeling of the subgrid terms and modeling of the near-wall flow field. The presence of geometries in the flow field is modeled via the immersed boundary method. An elaborate discussion of this method is presented in the following paragraphs.

2.3.2 Immersed boundary method

Arbitrary Lagrangian Eulerian (ALE) (Hirt, Amsden, & Cook, 1974) methods are commonly used for fluid-structure interaction problems. These methods use body fitted meshes for the discretization of the flow field. During the simulation the body fitted meshes are deformed to fit the deformed shape of the structural domain. ALE methods are not suitable for the developed solver due to the non-body conforming Cartesian mesh, which is used for the discretization of the governing equations. Further, ALE methods are not applicable to problems with large deformations (Sahin & Mohseni, 2009) without expensive remeshing efforts. Consequently, these methods are not suitable for the solution of rigid body motion which is an intended use of the developed solver.
Instead, an immersed boundary method is implemented to model the presence of the geometry in the flow. A method later referenced as immersed boundary method was initially introduced by Peskin (1973) for the simulation of flow patterns around heart valves. Comprehensive reviews of immersed boundary methods can be found in Mittal and Iaccarino (2005); Sotiropoulos and Yang (2014); W. Kim and Choi (2019).
The method is divided into continuous forcing approaches and discrete forcing approaches. The continuous forcing approach (Peskin, 1973) adds a forcing term to the continuous formulation of the Navier Stokes equations. It is therefore independent of the discretization. The method was initially implemented for the simulation of elastic boundaries (Peskin, 1973, 1982).
Conceptually, the method works in the following way. The elastic boundary is discretized by a set of Lagrange markers, which move with the flow. A force is computed based on the elastic properties and relative displacement of Lagrange markers. The force is applied to the fluid field via a distribution function (Beyer, 1992; Lai & Peskin, 2000; Saiki & Biringen, 1996).
The method has been applied to the solution of flows around rigid bodies by introducing a spring forcing term which is based on the displacement of the Lagrange markers with respect to their equilibrium position (Beyer, 1992; Lai & Peskin, 2000). However, for an accurate respresentation of the boundary high spring constants are necessary which lead to very stiff systems of equations which introduce stability issues (Lai & Peskin, 2000). Improvements were achieved by introducing damping terms to the Lagrange force (Goldstein, Handler, & Sirovich, 1993). However, also here high spring stiffnesses and damping constants are required for an accurate representation of the boundary.
The inability of the method to accurately represent rigid bodies and the stability concern together with the need to manually specify the stiffness of the boundary renders it not suitable for the simulation of flow around aircraft components.
Instead, a discrete forcing approach is considered for the immersed boundary method

which derives the forcing term from the discretized form of the Navier Stokes equations. The discrete forcing approach is split into indirect methods and direct methods which are further explained in the next paragraphs.

Indirect methods

The continuous Navier Stokes equations can not be integrated analytically, which prevents the derivation of a forcing term which satisfies the boundary condition of the immersed boundary (Mittal & Iaccarino, 2005). However, as shown by Mohd-Yusof (1997), a forcing term can be derived from the discretized Navier Stokes equations for each time step by computing a priori velocity field. That is a velocity field that does not account for the presence of the immersed boundary.
Following his initial publication, Mohd-Yusof, Orlandi, and Haworth (1998) applied an indirect forcing approach in LES of internal flow in piston engines. Identical to the continuous forcing approach introduced by Peskin (1973), an interpolation function is used for the interpolation of the flow variables on the surface and the spreading of the surface forces onto the fluid. Different forms of a discrete delta function used by Peskin (1973) are commonly used for the interpolation of the velocity on the surface and the distribution of the forces onto the fluid.
Mohd-Yusof et al. (1998) linearly interpolate the force between the boundary and the inner flow field in line with the central discretization scheme. A more conventional approach is the use of a discrete form of the Dirac's delta function. Roma, Peskin, and Berger (1999) proposed a 3 point version of the discrete Dirac's delta function. Uhlmann (2005); Kempe and Fröhlich (2012) use the discrete form of the Dirac's delta function proposed by Roma et al. (1999) for the modeling and simulation of flow around finite particles.
The indirect forcing approach has two significant advantages over the direct forcing approaches. (1) Volume geometry information such as expensive levelset information (Katopodes & Katopodes, 2019) is not required by the method and (2) the method is easily extended to moving geometries without spurious oscillations at the immersed boundaries (Luo et al., 2012). However, the method is less applicable to high Reynolds number flow due to the spreading of the body forces across the grid nodes in the vicinity of the boundary which removes the sharpness of the boundary (Mittal & Iaccarino, 2005) and the explicit nature of the method leads to slip velocities at the immersed boundary. Recent studies have presented ways to increase the sharpness and accuracy of the method. Vanella and Balaras (2009) presented a novel interpolation for the velocities and forces based on moving least squares and Shi, Yang, Jin, He, and Wang (2019) present the use of the indirect forcing method for wall-modelled high Reynolds number LES.
The numerical errors due to the slip velocity at the immersed boundary have been removed by introducing multi-step methods (Kempe & Fröhlich, 2012) or by introducing an implicit problem for the magnitude and distribution of the forcing terms (Pinelli, Naqavi, Piomelli, & Favier, 2010). More recently Gsell and Favier (2021) proposed a priori correction term for the correction of the slip velocity.

Direct methods

The indirect forcing method was presented previously. As discussed, this method is not well suited for the simulation of sharp interfaces due to the diffusive nature of spreading a forcing term over multiple cells in the vicinity of the boundary. The method is therefore generally said to be applicable only to low or moderate Reynolds number flows. Direct methods have been developed for the simulation of sharp interfaces and for the solution of high Reynolds number flows. The most common method is the ghost-cell method (Fedkiw, Aslam, Merriman, & Osher, 1999; Tseng & Ferziger, 2003; Ghias, Mittal, & Lund, 2004) which applies corrections directly to the flow variables in the cells and the cut-cell method (Clarke, Salas, & Hassan, 1986) which adapts the finite volumes in the vicinity of the boundary.

Ghost-cell method

Ghost-cell methods are fundamentally derived from the domain boundary conditions of finite difference and finite volume methods, where values in stencil nodes outside the numerical domain are set based on the imposed boundary condition and fluid side solution. Ghost-cell methods apply this principle to immersed boundaries which are not necessarily grid aligned. Ghost cells are generally defined as solid cells with at least one fluid side neighbor (Mittal & Iaccarino, 2005). Additional layers of ghost cells may be introduced on the solid side of the immersed boundary for higher order stencils. The flow quantities in the ghost cells are derived by introducing two additional points. The boundary intercept which defines the normal and boundary value associated with the ghost cell and the image point, which is used to interpolate the fluid side solution associated with the ghost cell. The three points/cells ghost cell, boundary intercept and image point are illustrated in figure 2.4.

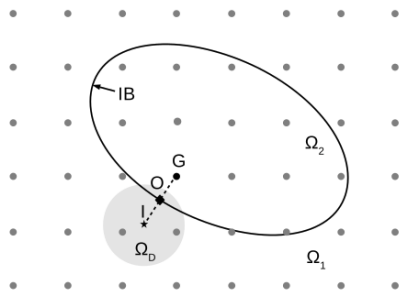

Figure 2.4: Schematic diagram of Catesian-grid-based computational domain with immersed boundary, [Nomenclature: **G**, ghost node; **O**, boundary point; **I**, image point; $\mathbf{\Omega_D}$, domain of dependence; $\mathbf{\Omega_1}$, fluid domain; $\mathbf{\Omega_2}$, solid domain; **IB**, immersed boundary], taken and modified from Mo et al. (2018, p. 3).

Various interpolation schemes have been introduced for the interpolation of the fluid solution at the image points. Linear and bilinear interpolation schemes have been applied by Majumdar, Iaccarino, and Durbin (2002); Ghias et al. (2004). The interpolation can be extended to a trilinear interpolation for three-dimensional flows as shown by Majumdar et al. (2002). The linear interpolation schemes work well when the image point sits within the

viscous sublayer of the boundary layer, but leads to wrong predictions for higher Reynolds numbers (Mittal & Iaccarino, 2005). Directional interpolation schemes were proposed to obtain more accurate solution of higher Reynolds number flows. Furthermore, Tseng and Ferziger (2003) present the use of polynomials for the reconstruction of the ghost cell values and estimation of the forcing term. Kapahi, Sambasivan, and Udaykumar (2013) propose the use of least squares for the interpolation of the image point values. The use of inverse distance methods was first introduced by Tseng and Ferziger (2003) and further developed by Gao, Tseng, and Lu (2007) and Mo et al. (2018). The presented interpolation methods can be used for higher order methods with the introduction of additional ghost cell layers. However, to maintain high numerical accuracy, a high order reconstruction of the ghost cell values is required in combination with the high order numerics of the flow field (Baeza, Mulet, & Zorío, 2016). The ghost-cell methods deliver accurate results for low and high Reynolds number flows with a sharp representation of the boundary. The method may lead to spurious oscillations in the flow field once geometries start moving. This is caused by a switch in the states of the cells in the numerical domain from ghost cell to fluid cell and vise-versa (Luo et al., 2012). Luo et al. (2012) propose a blending approach where cells in the first fluid layer of the wall are smoothly transitioned into the ghost cell values. Lee and You (2013) propose a novel approach for the interpolation of multiple layers of fresh fluid cells, cells that switched from solid state to fluid state.
The ghost-cell method is applicable to low and high Reynolds number flow with a sharp representation of the boundary. Compared to the indirect forcing method the ghost-cell method requires additional computational resources for the calculation of geometry information such as the levelset function in the vincinity of the boundary. The levelset function is used to compute the boundary intercepts of the ghost cells and to subsequently locate the image point.

Cut cell method

The presented IB methods do not satisfy the underlying conservation of mass and momentum close to the surface. A finite volume approach at the IB should be selected to satisfy the conservation laws within the flow field and at the immersed boundary (Mittal & Iaccarino, 2005). This forms the main motivation for the cut-cell methodology. Clarke et al. (1986) introduced the method for the simulation of inviscid flow around multi-element airfoils. The method was further applied to viscous flows by H. Udaykumar, Shyy, and Rao (1996); H. S. Udaykumar, Mittal, Rampunggoon, and Khanna (2001) as discussed in Mittal and Iaccarino (2005). The cut-cell method truncates the cells that are cut by

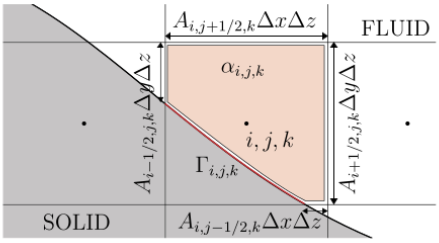

Figure 2.5: Two-dimensional sketch of a cut-cell, taken from Örley et al. (2015, p. 5).

the immersed boundary. The cutting of the finite volume cells results in new trapezoidal

cells in the two-dimensional case as shown in figure 2.5.
The problem that arises from these new cells is the reconstruction of the fluxes at the irregular cell faces. A common approach is the use of interpolation functions to approximate the flux at the face based on the cell values of the solution (Ye, Mittal, Udaykumar, & Shyy, 1999). Mittal, Seshadri, and Udaykumar (2004) shows the application of this cut-cell method to free falling objects.
However, while the truncation of the volumes leads to sharp interfaces and conservative properties which are ideal for LES, the method may generate very small cells which lead to stability issues in explicit and poor convergence performance in implicit methods. Different approaches have been implemented to alleviate the problem of the small cut-cells. Ye et al. (1999) and Bayyuk, Powell, and Leer (1993) employ a cell merging technique where small cells are merged with larger neighboring cells at the cost of additional complexity due to the need to change the stencil of all neighboring cells. Another approach referred to as flux redistribution was introduced by Pember, Bell, Colella, Curtchfield, and Welcome (1995); Colella, Graves, Keen, and Modiano (2006).
The application of the method to multi-dimensional compressible flow has been presented by Lauer, Hu, Hickel, and Adams (2012) for the simulation of bubble dynamics and by Pasquariello et al. (2016) for the solution of fluid-structure interaction problems between compressible flow and deformable bodies. The volume preserving properties of the cut-cell method comes at the cost of significant geometrical computation. Both the cut surface areas of the geometry and the cut cell faces must be computed as well as the cut volumes. This leads to significant additional computational costs for both stationary and moving geometries.

2.3.3 Discussion

The review of the fluid solver has been started with an overview of various flow solvers that have been used for fluid-structure interaction simulations. It was stated that the selection of spatial and temporal discretization methods and the modeling techniques for the turbulent flow are outside the scope of this project. Instead, a top level description of the selected models was given.
The selection of an adaptive Cartesian mesh for the discretization of the fluid equations ruled out the use of the conventional ALE methods and introduced the need for an immersed boundary approach to model the presence of the moving and flexible aircraft components in the flow field. The review of immersed boundary approaches formed the main focus of this section. Based on the knowledge gathered from the literature review a selection of an appropriate immersed boundary approach was made. The result of the selection is discussed in the section.
The review of the immersed boundary methods was started at the origin of the method with a discussion of the continuous forcing approach introduced by Peskin (1973). The review of the method showed that it is suitable for the simulation of flexible bodies in the flow field such as heart valves. The method is not well suited for the simulation of rigid bodies. Multiple attempts have been made to apply the method to simulations of rigid bodies, however these often resulted in stiff problems with low stability and time step limits. Moreover, these approaches generally relied on user-defined spring and damping coefficients. The inability to efficiently model rigid bodies combined with the need for user specified boundary coefficients already rule out the method for the aero-servo-elasticity

framework.
Subsequently, the discrete forcing approach was introduced. The methods of the discrete forcing approach were classified either as indirect or direct methods. The direct methods were further split into the ghost-cell method and cut-cell method.
The review showed that the indirect methods are conceptually derived from the continuous forcing approach but the forcing term is derived from the discretized form of the Navier Stokes equations, which eliminates the need of user specified parameters and enables the simulation of rigid bodies. Similar to the continuous approach a distribution kernel is used to spread the boundary force over the flow field in the vicinity of the boundary. Advantages of the indirect forcing approach were pointed out to be smooth flow solution for stationary as well as moving geometries and generally low computational cost as only little geometry information is required for the method. However, the method is generally said to not be applicable for high Reynolds number flow due to the diffusive nature of spreading the boundary force in the vicinity of the boundary and a true no slip boundary either requires the use of more expensive multi-step methods or the solution of an implicit problem.
A sharp interface is achievable with direct forcing methods such as ghost-cell or cut-cell methods. Ghost-cell methods set the numerical solution in cells which are located outside of the fluid domain but within the numerical stencil. These are usually defined by cells with at least one fluid cell neighbor but multiple ghost cell layers may be required for high order spatial schemes. The numerical solution of the ghost cell is set based on the boundary intercept and fluid flow solution at the image point which may not coincide with the numerical grid. Interpolation methods were introduced for the interpolation of the flow solution at the image point. The review showed that proposed interpolation schemes range from simple and computationally inexpensive inverse distance weighting methods to computationally more expensive tri-linear interpolation methods and regression methods. The ghost-cell method is applicable to high Reynolds number flows and does suffer from numerical inaccuracy due to residual slip velocities such as the indirect methods. However, the method may cause spurious oscillation in the flow field when applied to moving geometries. Further, the method does require additional geometric information which results in additional computational cost.
Numerically superior to the above two methods is the cut-cell method which achieves sharp interfaces and further conserves mass and momentum. The cut-cell method truncates cells by cutting them with the immersed boundary. Interpolation techniques must be employed to compute the correct fluxes of the truncated cells. Further, cell merging techniques must be used to eliminate stability issues arising from small cells. The calculation of the correct face fluxes of the truncated cells and additional cell merging or similar techniques increase the computational overhead of the method.
The ghost-cell method is selected for the immersed boundary method inside the code for the simulation of stationary or moving geometries. The method is computationally more expensive than the indirect method, but the literature review showed that the indirect forcing approach is not well suited for the simulation of high Reynolds number wall-bounded flows. Therefore the use of the ghost-cell based approach is deemed more suitable for the aero-servo-elasticity framework used for the simulation of aircraft flight dynamics. The numerically superior cut-cell method is not considered due to its high computational cost.

2.4 Motion solver

The motion solver of the aero-servo-elasticity framework covers three types of problems: **(1)** The solution of the rigid body equations of motion for the aircraft in order to predict the trajectory and movement (translation and rotation) of the aircraft and control surfaces, **(2)** the solution of the elastic deformation problem of aircraft components in the inertial frame due to aerodynamic, thrust and other forces and **(3)** the solution of the combined problem of elastic deformation and large translational and rotational movement. The solution to the third problem is subject of the flexible mutli-body dynamics field of study Shabana (1997). A review of methods for the solution of the mentioned problems is given in this section. The review starts with a discussion of the rigid body equation of motions and the solution to the motion problem of constrained bodies. Afterwards, the discussion is extended to the motion of elastic bodies with special attention to the modeling of elastic bodies that undergo large translational and rotational motion. The chapter is concluded with a discussion of reduced order model techniques for the reduction of the governing equation to computational acceptable levels and a discussion of time integration methods for the constructed system of equations.

2.4.1 Rigid body motion

The motion of a rigid body is governed by Newton's second law of motion. The governing equations relate the translational and rotational acceleration of the body to the inertia properties and applied external forces. The governing equations of a single body (Shabana, 2020, p. 133), under the assumption that the center of rotation is aligned with the centroid of the body is written as

$$\begin{bmatrix} \mathbf{m}_{RR} & 0 \\ 0 & \mathbf{m}_{\theta\theta} \end{bmatrix} \begin{bmatrix} \ddot{\mathbf{x}} \\ \boldsymbol{\theta} \end{bmatrix} = \mathbf{Q}_e + \mathbf{Q}_v, \tag{2.2}$$

where $\mathbf{m_{RR}}$ denotes the inertia matrix of the translational degrees of freedom given by the product of the body mass and a square identity matrix, with size equal to the number of translational degrees of freedom, $\mathbf{m}_{\theta\theta}$ is the inertia matrix derived from the mass moment of intertia of the body and rotational degrees of freedom. Vector $\mathbf{x}$ denotes the translational degrees of freedom and vector θ contains the rotational degrees of freedom of the body which are defined via Euler parameters, Rodriguez parameters or Euler angles (Shabana, 2020, p. 55). Vector $\mathbf{Q}_e$ is the combined vector of external forces and moments with contributions from the aerodynamic, thrust and gravitational forces and moments. Vector $\mathbf{Q}_v$ is denoted as quadratic velocity vector defined by the non-linear terms of the equations of motion.
The governing equations form an initial value problem, which is solved by integrating the governing equations in time twice. An extensive review of the numerical integration methods is presented in section 2.4.4.
While simple, the presented equations for the motion of a single body enables a wide range of studies. Mittal et al. (2004) studied the phenomenon of flutter and tumble of objects in free fall, where the motion of the objects is governed by the presented rigid body equations of motion and the presence of the objects in the flow field is modeled via a cut-cell immersed boundary approach (Mittal & Iaccarino, 2005). The oscillations and

flow field around a sprung mounted cylinder is another well studied case. Jauvtis and Williamson (2003, 2004) performed experimental studies on the motion of a sprung cylinder with two degrees of freedom. Kang, Zhang, Ma, and Ni (2018); Sarkar and Schlüter (2013); J. Zhang and Dalton (1996) present numerical results of the flow field and motion of sprung cylinder with one and two degrees of freedom. Alonso and Jameson (1994) performed aero-elastic airfoil simulations of the NACA64A010 profile to investigate the transient response and flutter boundaries at transonic speeds. Baxevanou et al. (2008) present an aero-elastic numerical model for the study of flutter characteristics of a wind turbine profile in stalled conditions.

As shown, the solution of the rigid body equations of motion for a single body already enables a large range of studies. For an accurate simulation of the full aircraft system the equation of motion (2.2) must be evaluated for each component and constraint equations must be implemented to link the motion of the individual bodies.

Two approaches are feasible. Under the assumption that the control surfaces do not contribute significantly to the aircraft mass and inertia and under the assumption that only the flight dynamics are of interest, a mass-less approach may be taken. With this approach the equations of motion are only solved for the aircraft body. The effect of the control surfaces are modeled via aerodynamic reaction forces and moments. This approach is very common in the study of flight dynamics (Stengel, 2004, p. 147).

The mass-less approach may not be taken if the dynamics of the control surfaces or the coupled dynamics of control surface and aircraft are of interest (Tewari, 2015, p. 7) and if the control surfaces contribute significantly to the mass and inertia of the aircraft, as given by some novel aircraft concepts (Lilium, n.d.).

In those cases the equations of motion must be solved for the aircraft and control surface plus constraint equations must be implemented to link the motion of the aircraft components. The resulting multi-body system takes the form of a tree like structure (F. Amirouche, 2006, p. 107) with the fuselage as the root and flaps, control surfaces and spoilers as branches of the tree system. An additional layer of branches may be build from additional trim surfaces attached to the control surfaces.

The introduction of the constraints introduces additional equations which must be solved in conjunction with the equations of motion. The constraint equations are either in the form of holonomic constraints or nonholonomic constraints. Holonomic constraints constrain the position and orientation of rigid bodies. These constraints are further divided into constraints that explicitly depend on time, rheonomic, and those which do not depend on time, scleronomic constraints (F. Amirouche, 2006, p. 320). The constraint equation of holonomic constraints can be written in the form of

$$\phi_i(x_1, x_2, ..., x_n, t) = 0 \quad (i = 1, 2, ..., m) \tag{2.3}$$

Examples of holonomic constraints include any type of relative position constraint such as joints, hinges and fixation constraints between two bodies. Nonholonomic can not be written in the form of equation (2.3). The contact constraint of the aircraft landing gear with the ground forms a nonholonomic constraint as it can not be brought into the form of equation (2.3). Other examples of nonholonomic constraints are presented in Swaczyna (2011).

The governing equations of the resulting constraint multi-body system are commonly written in the Lagrange multiplier form, where the presence of the constraints is introduced via Lagrange multipliers which represent unknown constraint forces (Gavrea, Negrut, &

Potra, 2005).
Two solution approaches are commonly used for the solution of the constraint equations. Approach one, the augmented method, combines the Lagrange multiplier form with the constraint equations into a single block. The resulting index 3 differential-algebraic equation (DAE) is integrated via methods proposed in Ascher and Petzold (1998); Gavrea et al. (2005); Wang and Li (2015).
A second approach, the coordinate reduction method, introduces a transformation matrix. The transformation matrix is designed such that when multiplied with the Lagrange multiplier form of the governing equations, the unknown Lagrange multipliers are removed and the number of equations of motion are reduced by the number of constraint equations. Different approaches have been proposed in literature for the derivation of the transformation matrix. F. M. L. Amirouche and Jia (1988) proposed the Pseudo Upper Triangular Decomposition (PUTD) approach for the computation of the transformation. An alternative approach for the computation of the transformation matrix was introduced by Steeves and Walton (1969) with the use of the zero-Eigenvalue Theorem.
Many libraries and software packages have been developed for the solution of the described multi-body dynamics problem. Besides many proprietary and commercial tools, two open-source tools are worth mentioning, namely HOTINT [2] and MBDyn [3]. The coupling of multi-body dynamics with aerodynamics has been done in past, but commonly in combination with the elastic degrees of freedom, which are discussed in the following section. A constraint multi-body approach without elastic degrees of freedom was taken by Vierendeels, Dumont, and Verdonck (2008) for the fluid-structure simulations of an heart valve leaflet.

2.4.2 Elastic multi-body systems

Up to this point the discussion focused on the study of rigid body motion with and without constraints. The modeling of flexible bodies such as high aspect ratio wings as rigid bodies results in inaccurate results as the deflection and twisting of the wing result in significant changes in the aerodynamic characteristics (Kenway & Martins, 2014). Furthermore, the natural frequencies of highly flexible wings approach the flight dynamics frequencies of the aircraft which results in strong interactions between the flight dynamics and structural degrees of freedom (Yi & Changchuan, 2018). These aspects show the need to model the aircraft components as linked flexible bodies.
The deformation of structures is governed by a set of linear or nonlinear differential equations which relate the deformation of the structure to external and internal forces, material properties and mass properties. The finite element method (FEM) is commonly used for the spatial discretization of these equations in space. Time integration is performed with the methods presented in section 2.4.4. Other methods have been used for the discretization of solids such as mode based methods (Sharifnia & Akbarzadeh, 2017), finite segment methods (Adamiec-Wójcik & Wojciech, 2018) or mesh-less methods (Xie, Jian, & Wen, 2017). A full discussion of these methods is outside the scope of this review. Furthermore, the following paragraphs were written based on the assumption that a FEM is used for the discretization of the solid domains.

[2] https://hotint.lcm.at/
[3] https://www.mbdyn.org/

An introduction to the FEM for linear and also non-linear solids and structures is given in Nikishkov (2004); Krenk (2009); Neto, Amaro, Roseiro, Cirne, and Leal (2015). A full review of the modeling approaches of geometrical and material linear or non-linear behavior and the finite element (FE) discretization approach is out of the scope of this review. Instead, the review concentrates on the specifics of FEM formulations of elastic multi-body systems EMBS, which were defined by Shabana (1997)

> Flexible multi-body dynamics is the subject concerned with the computer modeling and analysis of constrained deformable bodies that undergo large displacements, including large rotations.

Extensive reviews of modeling approaches for flexible multi-body systems have been presented by Shabana (1997) and more recent by Rong, Rui, Tao, and Wang (2019). Rong et al. (2019) identifies the two core problems of EMBS as the description of the flexible kinematics and the subsequent derivation of the governing equations of motion. Different approaches have been proposed for the description of the kinematics of the elastic bodies. The most commonly used approach is the floating frame of reference (FFR) approach (Shabana, 1997). The approach was initially introduced within the aerospace sector with contributions from Likins (1967); Frisch and Center. (1975). Two sets of coordinates are introduced (Shabana, 1997). One set describes the orientation and position of the body reference frame, the second set describes the deformation of the body within the body reference frame. This is illustrated in figure 2.6 for a two-dimensional beam. The

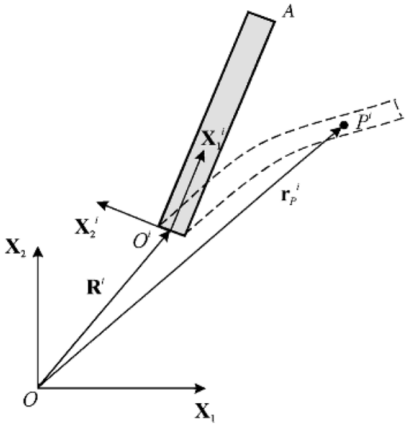

Figure 2.6: Illustration of the floating reference frame, taken from (Shabana, 2020, p. 184).

position of the reference frame may be selected arbitrarily. However, reference conditions must be defined between the reference frame and the deformation degrees of freedom to eliminate the rigid body motion modes (Rong et al., 2019). Generally, reference frames that satisfy the mean axis conditions show preferable characteristics (Agrawal & Shabana, 1985), as they lead to a weak coupling between the reference motion and elastic deformation (Shabana, 1997).
The derivation of the governing equations of motion based on this and the later approaches is discussed at the end of this section. The equations of motion based on the FFR approach are characterized by a highly non-linear mass matrix due to the coupling between

the reference motion and elastic deformation (Shabana, 1997). At the same time the stiffness matrix is identical to the stiffness matrix of the pure structural dynamics problem due to the definition of the degrees of freedom within the floating reference frame.
Existing finite element codes may be used for the construction of the mass matrix components and stiffness matrix. Furthermore, the FFR formulation is well suited for the use of model order reduction techniques applied to the deformation degrees of freedom (Nowakowski, Fehr, Fischer, & Eberhard, 2012). The full elimination/reduction of the elastic degrees of freedom reduces the system matrix to the rigid body equations of motion presented in section 2.4.1.
The floating reference frame formulation as discussed in Shabana (2020, p. 179) may only be used for isoparametric elements as the shape functions and nodal coordinates of these elements can describe rigid body motion (Shabana, 2020, p. 294). The often used non-isoparametric beam, plate and shell elements can not describe rigid body motion, due to the use of infinitesimal small rotations as nodal coordinates (Shabana, 1997). Subsequently, these elements produce non-zero strain under arbitrary rigid body displacements (Shabana, 1997).
The incremental finite element approach was introduced to use non-isoparametric elements in bodies that undergo large rotations (Shabana, 1997). Additional element coordinate systems are introduced to separate the rigid-body and strain-producing deformation components (Campanelli, Berzeri, & Shabana, 1999). A convected coordinate system approach was used initially for the definition of the element coordinate system (Belytschko & Hsieh, 1973; Argyris et al., 1979). A co-rotational approach was introduced by (Rankin & Brogan, 1986). The approach allows the use of existing finite elements in the large rotation analysis. In either approach the element shape function is used to describe the small rotation of the body, which leads to a linearization of the rotation in the equations of motion. As a consequence the incremental finite element method is unable to model exact rigid body motion (Campanelli et al., 1999). Shabana (1996b) solved this issue by introducing an additional intermediate element coordinate system.
A different approach, based on an absolute nodal coordinate formulation (ANCF), was proposed by Shabana (1996a). The approach differs significantly from the FFR approach. The element nodal coordinates are defined in the inertial frame instead of the local element frame and the rigid body modes are incorporated into the shape function (Shabana, 2020, p. 298). Furthermore, the inifinitesimal small rotation nodal coordinates are replaced by absolute slopes and position nodal cooradinate. This combined with the consistent mass approach (Shabana, 2020, p. 296) allows the method to exactly model rigid body motion. Different from the FFR formulation, the ANCF results in a linear mass matrix and highly non-linear stiffness matrix. Yet as shown by Shabana and Schwertassek (1998) both methods lead to identical dynamic relationships. They further show an approach for the derivation of the non-linear mass matrix of the FFR approach from the linear mass matrix of the ANCF approach.
The derivation of the equations of motion of the flexible multi-body system follows similar methodologies used for the derivation of the rigid body equations of motion shown in section 2.4.1. The use of Hamilton's principle (J. Kim, 2012) and Lagrange's equation (Shabana, 2020, p. 211) are the most common methods for the derivation of the equations of motion from the selected description of the kinematics. The kinematic constraints between bodies appear in the form of Lagrange multiplier which represent the reaction loads of the constraints. The augmented matrix approach may be used for the solution

of constraint motion of the multi-body system which results in a non-linear index 3 DAE (Gavrea et al., 2005) or the coordinate reduction approach as discussed in section 2.4.1. Other methods have been proposed in literature based on Kane's method (Kane, Likins, & Levinson, 1983), those methods are not further discussed in this review.
Elastic multi-body systems have been coupled with aerodynamic solvers for various purposes. Y. Li et al. (2017) present coupled computational fluid dynamics/multi-body dynamics method for aero-servo-elastic simulations of wind turbines. Additional drivetrain dynamics are included in the framework. An augmented matrix method is used to handle the constraints between the wind-turbine components. Yang et al. (2020) present a framework for aero-hydro-servo-elasticity simulations of offshore windturbines. The use of a co-rotational finite element method in combination with an aero-elastic framework for the simulation of bat-like wings was presented by G. Li et al. (2019a). The use of the floating frame of reference formulation for the aero-servo-elasticity analysis of flexible aircraft has been presented by Yi and Changchuan (2018).

2.4.3 Reduced order model

The discretization of the elastic bodies with the FEM leads to many additional elastic degrees of freedom in addition to the rigid body degrees of freedom. This may bring the computational cost of the motion solver within the aero-servo-elasticity framework to unacceptable levels. Model order reduction (ROM) techniques are one method to reduce the number of unknowns and reduce the computational cost to acceptable levels. These techniques are widely used in the aero-elasticity analysis (Dowell & Hall, 2001; Debrabandere, Tartinville, Hirsch, & Coussement, 2012), but have also been used to reduce the cost of EMBS simulations as shown by Fehr and Eberhard (2010, 2011); Fischer and Eberhard (2014).
Two model reduction techniques are common in combination with structural dynamics simulations: The mode superposition methods and variants thereof (Geradin, Rixen, & Gaeradin, 2015) and the component mode synthesis techniques (Craig & Bampton, 1968). All mode superposition methods describe the displacement of the solid and structure with a finite number of free vibration modes (Besselink et al., 2013). The mode displacement method represents the most basic method of the superposition methods. The displacement field is described via the vibration modes corresponding to the lowest (Rayleigh, 1945) or lowest N eigenfrequencies of the solid or structure, as those modes typically contain the highest amount of energy. The vibration modes belonging to the higher frequencies are truncated.
The simple truncation of the higher frequencies leads to an incorrect response of the lower frequencies as the effect of the truncated frequencies onto the lower frequencies is removed (Besselink et al., 2013). The mode acceleration method as proposed by Williams (1945) is an improved version of the mode displacement method which takes the static effect of the truncated modes on the lower frequencies into account (Soriano & Filho, 1988). This correction factor takes the form of a static correction displacement vector which is added to the predicted displacement field. The mode acceleration method improves the prediction of the low frequency mode response but does not improve prediction in the higher frequency range as only the static effect of the truncated modes is considered. The modal truncation augmentation method was subsequently introduced by Dickens and Pool (1992) to capture parts of the dynamic effect of the truncated frequencies. The

method augments the modal expansion of the displacement field with the static correction field of the mode acceleration method. An orthogonal set is derived with a mathematically consistent Rayleigh-Ritz approximation (Dickens, Nakagawa, & Wittbrodt, 1997). Dickens et al. (1997) show that the mode augmentation method significantly improves the prediction of higher frequencies by estimating the average dynamic response of the truncated modes.
The presented mode superposition methods consider the complete finite element structure (Besselink et al., 2013). A partitioned based approach was proposed in literature with the component mode synthesis method. Within this approach the finite element structural domain is divided into N connected finite element substructures (J.-G. Kim & Lee, 2015). The degrees of freedom of each substructure are reduced with the modal superposition approaches discussed above. The general method of component mode synthesis was proposed by Hurty (1965) and Guyan (1965). Craig and Bampton (1968) derived from this idea the well known Craig-Bampton method. The method divides the degrees of freedom of the substructures into interface and non-interface degrees of freedom. The modal reduction of the substructures is performed on the non-interface degrees of freedom. In that way the exact interface conditions between the substructures are maintained. The method is also referred to as fixed-interface reduction method (Besselink et al., 2013). The approach was further advanced with the work of MacNeal (1971) and Rubin (1975) who released the fixed interface degrees of freedom of the Craig-Bampton method. This approach is also referred to as free-interface method (Besselink et al., 2013). An extensive review of the component mode synthesis technique is presented in Klerk, Rixen, and Voormeeren (2008).
In all presented methods the solution of either the complete structure or set of substructures is expressed via modes. The calculation of these modes defined via a shape function and associated frequency (Arnold, Citerley, Chargin, & Galant, 1985) has not been discussed up to this point. Perhaps the most well known approach for the calculation of the modes is the use of the dynamic system eigenvectors. Numerical techniques have been developed for the calculation of the eigenvector and eigenvalues, such as the Arnoldi method (Arnoldi, 1951). Ritz presented a more accurate and superior definition of the frequencies and modes denoted as Ritz vectors (Arnold et al., 1985). Wilson, Yuan, and Dickens (1982) were the first to report the application of the Ritz vectors to the dynamic analysis of large structures.
The use of model order reduction techniques within the simulation of elastic multi-body systems is discussed extensively in Fischer and Eberhard (2014) and in Nowakowski et al. (2012) for the elastic multi-body system which used the floating reference formulation.

2.4.4 Time integration

The constrained rigid body equations of motion and discretized equations of the elastic mutlibody system result in a set of second order differential algebraic equations or ordinary differential equations. These equations must be integrated in time to obtain the temporal response of the system.
Various approaches have been developed and presented in literature for the integration of these equations. These approaches are grouped into implicit, explicit and mixed implicit/explicit (IMEX) approaches and may be further divided into direct and indirect time integration schemes. They also differ by their integration order and the numerical

damping, which can either be controlled or not.
Without going into detail on the various schemes a high level decision is made on the overall scheme of the aero-servo-elasticity framework. Explicit schemes are suitable for simulations concerned with the propagation of high frequency waves such as shocks (Dokainish & Subbaraj, 1989). The methods are further characterized by low stability margins which permit only small time steps resulting in increased computational time (Dokainish & Subbaraj, 1989). Implicit methods on the other side are often numerically stable and permit large time steps (Subbaraj & Dokainish, 1989) but require the solution of a matrix system. The aero-servo-elasticity framework is not concerned with the response of the high frequencies of the structure and further large time steps are preferred to reduce the overall computational cost of the structural problems. Therefore, the review focuses on implicit time integration methods only. Furthermore, direct methods (Wilson, 1968; Newmark, 1959) integrate the DAE or second order ordinary differential equations directly, while indirect methods convert the second order ordinary differential equations into a set of first order ordinary differential equations and integrate the resulting sytem in time. Indirect methods significantly increase the size of the system due to the addition of the first time derivative of the degrees of freedom as unknowns. A direct integration method is therefore selected for the aero-servo-elasticity framework. What follows is a review of the common direct integration schemes. A broader review of time integration methods may be found in Subbaraj and Dokainish (1989); Dokainish and Subbaraj (1989) and more recent in Rong et al. (2019) for elastic multi-body systems.
The most widely used methods, according to Subbaraj and Dokainish (1989) are the Newmark, Houbolt and Wilson-θ method. These direct methods make an assumption on the variation of the acceleration over the integration interval and with that derive expressions for the velocity and position. These expressions are used in combination with the governing equations of motion to derive an implicit expression for the acceleration. The Newmark method (Newmark Nathan, 1959) employs a linear acceleration assumption. An additional parameter is included for the control of the dissipation and related stability. Two parameters control the numerical dissipation and stability of the method. However, only one combination of the two parameters leads to second order accuracy. Increased dissipation and stability leads to reduction of the integration order of the method. The Wilson-θ method (Wilson, 1968) was later introduced as a second order method with increased numerical dissipation and improved stability characteristics. This method assumes a linear acceleration over the time integral. The method is characterized by a integration step that is larger than the time step. The solution at the selected time step is computed from the solution at the integration step. Hilber, Hughes, and Taylor (1977) proposed a Newmark method referred to as α-method. The method is second order accurate and does give control over numerical damping characteristics with a decrease of the integration order. The methods were initially developed for linear structural dynamics problem and not for the integration of elastic multi-body systems. Gavrea et al. (2005) presents the application of the Newmark integration method to the integration of a multi-body system. Later Wang and Li (2015) presents the application of the α-method to the integration of a flexible multi-body system.

2.4.5 Discussion

The chapter introduced the modeling and solution aspects of the solid domain. These ranged from the introduction of unconstrained and constrained rigid body equations of motion and their extension to elastic multi-body systems, further to reduction modeling techniques and closed with a discussion of the time integration methods for solid domains.
The review was started with a discussion of the rigid body equations of motion and the introduction of constraints for the simulation of systems of constrained rigid bodies. Two common methods were introduced. Approach 1, the augmented method combines the equations of motion and constraint equations into a single system and integrates the resulting system of equations in time. Approach 2, reduces the number of degrees of freedom based on the given constraints. The reduced set of degrees of freedom should result in a lower computational cost. However, the derivation of the reduced system introduces additional complexity and might not be well suited for the GPU based HPC hardware. In the author's opinion the augmented system approach is more suited for the used hardware and this approach was selected for the framework.
The review of the solid domain methods was continued with an introduction to elastic multi-body systems and their solution. The review showed that the floating frame of reference formulation can be used as a natural extension to the rigid body framework, where additional elastic degrees of freedom are introduced to the already existing rigid body degrees of freedom. The finite elements of existing FEM codes may be used for the discretization of the body. However, non-isoparametric elements such as shell and beam elements can not be used with the FFR approach. Approaches such as the incremental finite element approach and absolute nodal coordinate formulation were therefore introduced. The resulting stiffness and mass matrices of these approaches vary significantly from the FFR approach and they can not be seen as a natural extension of the rigid body equations of motion. The FFR approach is selected for the aero-servo elasticity framework. The approach is selected due to its compatibility with the developed rigid body solver, its ability to use elements of existing finite element solvers, and the straight forward implementation of ROM techniques.
Two reduced order modeling approaches were discussed, the common mode displacement technique and partitioned based mode synthesis approach. The implementation of the reduced order modeling approach is beyond the scope of the thesis project. However, a mode displacement technique is envisioned for the aero-servo-elasticity framework in the future. The method is less flexible than the mode synthesis approach because it considers the complete finite element structure, while the mode synthesis approach can be tailored to specific geometric features. However, in the author's opinion the mode displacement method is sufficient for the initial implementation of the aero-servo-elasticity and it has been used in many other aero-structural analysis tools. Additional treatments of the truncated frequencies are not considered for the initial implementation but may be added to the solver if required.
The review of the time integration schemes has shown that implicit direct schemes should be favored for the developed framework. The discussion of the other schemes is not repeated in this section. Three direct implicit schemes were presented, the Newmark method, Wilson-θ and α-method. The Newmark method is selected for the initial implementation of the aero-servo elasticity framework, as it is second order accurate with low numerical dissipation. Additionally, if required the damping can be introduced into the

system at the cost of a reduced integration order. The method may be extended later to the α-method if damping is required and the reduced order of accuracy is not sufficient for accurate results. The Wilson-θ method is not considered as it is known to have a high dissipation.

2.5 Conclusion

A literature review on the three fundamental aspects of a fluid-structure interaction tool for the coupled analysis of multi-body systems with fluid flow has been presented. After discussing the need for high-fidelity coupled simulations for the design and analysis of future and novel aircraft concepts, the review focused on the selection of suitable methods for the framework. The selection of the methods was performed based on two criteria. Their applicability to the simulation of the physics of the fluid and solid domains and their computational cost.
Based on the review a partitioned approach is selected for the coupling of the fluid and solid domains. The approach has been successfully used in literature for the simulation of fluid-structure interaction problems with high solid fluid mass ratios. It is therefore suitable for the simulation of the aircraft components in the flow field. The decoupling of the time integration and spatial discretization of the domains allows the individual optimization of either solver. Further the time integration of the domains may be separated and tailored to the time scales of interest of either domain.
The ghost-cell approach has been selected for the immersed boundary method which is used for the simulation of stationary and moving geometries in the flow field. While the indirect method is computationally less expensive, it has not been selected due to its inability to accurately model sharp interfaces. The cut-cell immersed boundary approach has not been selected due to the significant computational cost of the method.
The floating frame of reference approach has been selected for the kinematic description of the aircraft components. The approach is selected as it is applicable to both the kinematic description of rigid and elastic bodies. The resulting system of equations is integrated with the Newmark time integration scheme. The review has shown that the integration scheme is most applicable to the time scales expected in the solid domain and further has been successfully used for the simulation of elastic multi-body systems. The implementation of the elastic degrees and reduced order modeling is outside the scope of this thesis. However, the mode superposition is proposed for the reduced order modeling approach of future developments. The selection of the presented methods should form an efficient framework for the aero-servo-elastic analysis of aircrafts. The suitability of the methods for the accurate analysis is assessed with validation cases in the final parts of this thesis.

Chapter 3

Immersed boundary method

A ghost-cell based immersed boundary condition is implemented in the present solver. It is derived from the domain boundary conditions of finite difference methods where values in the stencil nodes outside the fluid domain are set based on the imposed boundary conditions. This allows the use of the interior numerical stencil at the domain boundaries without adaptation. The results of the literature review on the topic of immersed boundary conditions and ghost-cell immersed boundaries was presented in section 2.3. Various ghost-cell based immersed boundary conditions have been proposed in literature. The research on ghost-cell immersed boundaries is primarily focused on the interpolation of the flow solution at the image point. But topics such as mass conservation and spurious oscillations in the flow field for moving immersed boundaries were brought up in the reviewed literature.

The presented ghost-cell methods were primarily used for no-slip boundary conditions on solid walls. That is, Dirichlet boundary conditions for the velocity or momentum terms and Neumann boundary conditions for internal energy. No-slip boundary conditions may be used for low and mid Reynolds number flows when the numerical mesh resolves the boundary layer down to the viscous sublayer. The method may be applied to high Reynolds number flows but comes at significant numerical costs as the grid requirements for wall-resolved LES are proportional to $Re^{1.8}$ (Chapman, 1979). A wall-modeled LES (WMLES) framework is therefore targeted during the development of the present code. A wall-stress based wall modeling technique is selected for this purpose. The details of the selection of an appropriate wall-modeling approach is outside the scope of this thesis. But the development of a ghost-cell method for wall-modeled LES is presented in this chapter. A second topic of the development which was raised in literature as well, is the appearance of spurious oscillations at the immersed boundary for moving geometries. Similar oscillations were found during the development of the immersed boundary method for the fluid model and numerics of the present solver. An approach to limit the oscillations at the boundary of moving geometries for the developed immersed boundary method is presented in this chapter. The topics may be summarized as the development of a ghost-cell based immersed boundary method for wall-modeled LES of moving geometries. The discussion of the ghost-cell immersed boundary is started with the derivation

of the ghost-cell value. This is followed by a discussion on the image or probing point placement in the flow field and the presentation of the interpolation scheme. Afterwards, the implementation of the ghost-cell immersed boundary for no-slip and wall-modeled solid boundaries is presented. The documentation of the immersed boundary method is concluded with the reduction of the spurious oscillations for moving geometries.

3.1 Ghost-cell method

The key idea of the presented ghost-cell method does not differ from the various ghost-cell methods presented in literature. The nomenclature of the ghost cells, boundary intercept points and image points is illustrated in figure 3.1. To reiterate, ghost cells are defined as cells or points that are outside the fluid domain but are inside the numerical stencil of the interior discretization scheme. For each ghost cell $\mathbf{x}_{GP}$, a boundary intercept point $\mathbf{x}_{BI}$ and one or multiple image or probing points $\mathbf{x}_{IP}$ are defined. The boundary intercept point is defined as the point on the surface of the geometry which is closest to the ghost cell. The point is defined as

$$\mathbf{x}_{BI} = \mathbf{x}_{GP} + \Delta_{GP}\mathbf{n}. \tag{3.1}$$

$\mathbf{n}$ defines the normal vector of the surface of the immersd boundary at the boundary intercept and Δ_{GP} is the distance between the ghost cell and boundary intercept. The image point is defined as a function of the boundary intercept

$$\mathbf{x}_{IP} = \mathbf{x}_{BI} + \Delta_{IP}\mathbf{n}, \tag{3.2}$$

with Δ_{IP} being equal to the distance between the boundary intercept and image point. For later reference either distance Δ_{GP} and Δ_{IP} are of order $\mathcal{O}(\Delta)$, with Δ being equal to the cell edge length of the numerical grid.

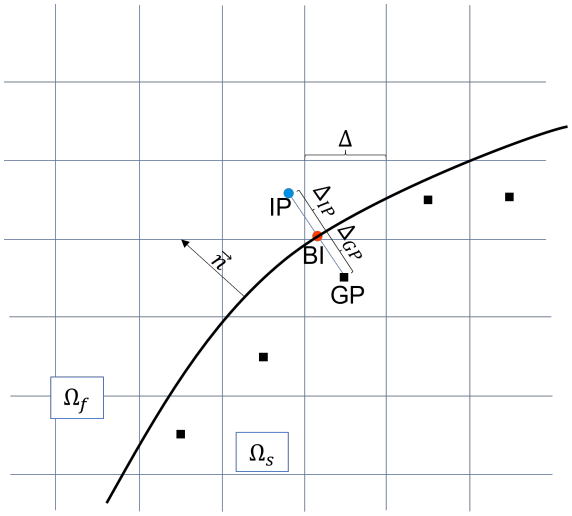

Figure 3.1: Schematic diagram of Catesian-grid-based computational domain with immersed boundary; Nomenclature: **GP**, ghost cell; **BI**, boundary intercept; **IP**, image point; $\mathbf{\Omega_s}$, solid domain; $\mathbf{\Omega_f}$, fluid domain.

Any field Ψ may be expanded around the boundary intercept to reconstruct the image point and ghost cell solution. The spatial coordinate η is introduced for this purpose to

define a position along the normal vector of the surface. $\eta = 0$ defines the position of the boundary intercept, $\eta = \Delta_{IP}$ the position of the image point and $\eta = -\Delta_{GP}$ the position of the ghost cell. The expansion of the solution towards the ghost cell yields

$$\Psi_{GP} = \Psi(-\Delta_{GP}) = \Psi_{BI} - \left.\frac{d\Psi}{d\eta}\right|_{BI} \Delta_{GP} + \frac{1}{2} \left.\frac{d^2\Psi}{d\eta^2}\right|_{BI} \Delta_{GP}^2 - \mathcal{O}(\Delta_{GP}^3). \tag{3.3}$$

Equally, the solution at the image point is reconstructed by

$$\Psi_{IP} = \Psi(\Delta_{IP}) = \Psi_{BI} + \left.\frac{d\Psi}{d\eta}\right|_{BI} \Delta_{IP} + \frac{1}{2} \left.\frac{d^2\Psi}{d\eta^2}\right|_{BI} \Delta_{IP}^2 + \mathcal{O}(\Delta_{IP}^3). \tag{3.4}$$

The reconstruction of the ghost cell and image point solution is used to define equations for the ghost-cell solution based on the boundary condition applied at the boundary intercept BI. Two boundary conditions are considered here, a Dirichlet boundary condition defined by

$$\Psi_O = f \tag{3.5}$$

and a Neumann boundary condition defined by

$$\left.\frac{\partial\Psi}{\partial n}\right|_O = g. \tag{3.6}$$

Given the Dirichlet boundary condition on the immersed boundary, the ghost-cell solution is given by

$$\begin{aligned} \Psi_{GP} = (2f - \Psi_{IP}) &+ \left.\frac{d\Psi}{d\eta}\right|_{BI} (-\Delta_{GP} + \Delta_{IP}) \\ &+ \frac{1}{2} \left.\frac{d^2\Psi}{d\eta^2}\right|_{BI} \left(\Delta_{GP}^2 + \Delta_{IP}^2\right) + \mathcal{O}\left(-\Delta_{GP}^3 + \Delta_{IP}^3\right). \end{aligned} \tag{3.7}$$

Given the Neumann boundary condition on the immersed boundary, the ghost-cell solution is given by

$$\begin{aligned} \Psi_{GP} = \Psi_{IP} &- g\left(\Delta_{GP} + \alpha\Delta\right) \\ &+ \frac{1}{2} \left.\frac{d^2\Psi}{d\eta^2}\right|_{BI} \left(\Delta_{GP}^2 - \alpha^2\Delta^2\right) - \mathcal{O}\left(\Delta_{GP}^3 + \alpha^3\Delta^3\right). \end{aligned} \tag{3.8}$$

The derivation of the ghost cell values for Dirichlet and Neumann boundary condition above was performed indepedent of the interpolation scheme for the image point and independent of the image point placement. These two topics are discussed in the following section.

3.2 Image/probing point placement

The placement of the image/probing points follows two common approaches. As discussed in Mittal et al. (2008) the image point may be defined as the mirror point of the ghost-cell around the boundary intercept. This leads to $\Delta_{IP} = \Delta_{GP}$. Replacing the image point distance Δ_{IP} with the ghost cell distance Δ_{GP} in the equations (3.7) and (3.8) yields

$$\Psi_{GP} = 2f - \Psi_{IP} + \left.\frac{d^2\Psi}{d\eta^2}\right|_{BI} \Delta_{GP}^2, \tag{3.9}$$

$$\Psi_{GP} = 2f - \Psi_{IP} + \mathcal{O}\left(\Delta^2\right), \tag{3.10}$$

for the Dirichlet boundary condition and similarly for the Neumann boundary condition

$$\Psi_{GP} = \Psi_{IP} - 2g\Delta_{GP} + \mathcal{O}\left(\Delta^3\right). \tag{3.11}$$

The Dirichlet and Neumann boundary conditions are thus second order and third order accurate when the mirror point is used as image point for the ghost cell. A second approach used in literature is the placement of the image point or probing point at a constant wall distance defined as $\Delta_{IP} = \alpha\Delta$. The image point distance is again in the order of $\mathcal{O}(\Delta)$. The ghost cell value for a Dirichlet boundary condition with constant image point distance is given by

$$\begin{aligned}\Psi_{GP} = (2f - \Psi_{IP}) + \left.\frac{d\Psi}{d\eta}\right|_{BI} (-\Delta_{GP} + \alpha\Delta) \\ + \frac{1}{2}\left.\frac{d^2\Psi}{d\eta^2}\right|_{BI} \left(\Delta_{GP}^2 + (\alpha\Delta)^2\right) + \mathcal{O}\left(-\Delta_{GP}^3 + (\alpha\Delta)^3\right).\end{aligned} \tag{3.12}$$

The gradient of the solution at the boundary intercept is approximated by the fluid side gradient

$$\left.\frac{d\Psi}{d\eta}\right|_{BI} = \frac{\Psi_{IP} - f}{\alpha\Delta} - \mathcal{O}(\alpha\Delta). \tag{3.13}$$

Substituting the estimation of the gradient into equation (3.12) yields

$$\begin{aligned}\Psi_{GP} = (2f - \Psi_{IP}) + \left(\frac{\Psi_{IP} - f}{\alpha\Delta} - \mathcal{O}(\alpha\Delta)\right) (-\Delta_{GP} + \alpha\Delta) \\ + \frac{1}{2}\left.\frac{d^2\Psi}{d\eta^2}\right|_{BI} \left(\Delta_{GP}^2 + (\alpha\Delta)^2\right) + \mathcal{O}\left(-\Delta_{GP}^3 + (\alpha\Delta)^3\right),\end{aligned} \tag{3.14}$$

$$\begin{aligned}\Psi_{GP} = f - \frac{\Psi_{IP} - f}{\alpha\Delta}\Delta_{GP} + \mathcal{O}(-\alpha\Delta_{GP}\Delta + \alpha^2\Delta^2) \\ + \frac{1}{2}\left.\frac{d^2\Psi}{d\eta^2}\right|_{BI} \left(\Delta_{GP}^2 + (\alpha\Delta)^2\right),\end{aligned} \tag{3.15}$$

$$\Psi_{GP} = f - \frac{\Delta_{GP}}{\alpha\Delta}\left(\Psi_{IP} - f\right) + \mathcal{O}(\Delta^2). \tag{3.16}$$

For Neumann boundary conditions the analysis yields

$$\Psi_{GP} = \Psi_{IP} - g\left(\Delta_{GP} + \alpha\Delta\right) + \mathcal{O}\left(\Delta^2\right). \tag{3.17}$$

The analysis shows that the constant image point distance leads to a second order accuracy for both Dirichlet and Neumann boundary conditions. The constant image point method is selected for the immersed boundary method in the present code as the second order accuracy for both Dirichlet and Neumann boundary conditions is deemed sufficient. Further, the constant image point simplifies the interpolation of the flow solution as the boundary intercept solution may be excluded in the interpolation.

3.3 Image/probing point interpolation

Various image point interpolation techniques were tested during the development of the immersed boundary method. The tested approaches were part of the families of trilinear interpolation approaches, inverse distance interpolation approaches and moving least squares approaches. A detailed discussion of each approach is outside the scope of this thesis. At the end, the moving least squares approach was selected as it is a fluid side only interpolation method, as the method may be extended to higher orders easily and cells can be easily excluded or included in the interpolation. The following section presents the derivation of the moving least squares method which is implemented in the present solver. The approach follows largely the derivation of Vanella and Balaras (2009) The solution at any point in the flow field may be approximated by the following weighted sum

$$\Psi(\mathbf{x}) = \sum_j p_j(\mathbf{x})\alpha_j(\mathbf{x}) = \mathbf{p}^T(\mathbf{x})\boldsymbol{\alpha}(\mathbf{x}). \tag{3.18}$$

where $\mathbf{p}(\mathbf{x})$ defines a vector of basis functions and $\boldsymbol{\alpha}(\mathbf{x})$ their corresponding weights. A linear polynomial is chosen for the basis function of the interpolation

$$f(x) = \alpha_0 + \alpha_1 x + \alpha_2 y + \alpha_3 z. \tag{3.19}$$

The basis function vector $\mathbf{p}^T(\mathbf{x})$ is thus defined as

$$\mathbf{p}(\mathbf{x}) = \begin{bmatrix} 1 & x & y & z \end{bmatrix}^T \tag{3.20}$$

With the approximation of the flow solution $\Psi(\mathbf{x})$, the following L2-norm between the approximation and the discrete flow solution Ψ^k is defined

$$J = \sum_{k=0} w(\mathbf{x} - \mathbf{x}^k) \left(\mathbf{p}^T(\mathbf{x}^k)\alpha(\mathbf{x}) - \Psi^k \right)^2. \tag{3.21}$$

Superscript k denotes the discrete locations $\mathbf{x}^k$ and values ψ^k of the numerical solution in the support domain of the interpolation. $w(\mathbf{x} - \mathbf{x}^k)$ defines the weight assigned to the k'th location in the support domain. The solution of the basis function weights $\alpha(\mathbf{x})$ is the minimizer of the L2-norm. An equation for the minimizer is obtained by taking the derivative of the L2-norm with respect to the basis function weights and setting the resulting equation equal to zero

$$\mathbf{0} = \frac{\partial J}{\partial \alpha} = 2 \sum_{k=0} w(\mathbf{x} - \mathbf{x}^k)\mathbf{p}(\mathbf{x^k}) \left(\mathbf{p}^T(\mathbf{x}^k)\alpha(\mathbf{x}) - \Psi^k \right), \tag{3.22}$$

$$\mathbf{0} = \sum_{k=0} w(\mathbf{x} - \mathbf{x}^k)\mathbf{p}(\mathbf{x^k})\mathbf{p}^T(\mathbf{x}^k)\alpha(\mathbf{x}) - \sum_{k=0} w(\mathbf{x} - \mathbf{x}^k)\mathbf{p}(\mathbf{x^k})\Psi^k. \tag{3.23}$$

The equation may be simplified by introducing the matrices $\mathbf{A}$ and $\mathbf{B}$ which are defined by

$$\mathbf{A} = \sum_{k=0} w(\mathbf{x} - \mathbf{x}^k)\mathbf{p}(\mathbf{x^k})\mathbf{p}^T(\mathbf{x}^k) \tag{3.24}$$

and

$$\mathbf{B} = \begin{bmatrix} w(\mathbf{x} - \mathbf{x}^0)\mathbf{p}(\mathbf{x^0}) & w(\mathbf{x} - \mathbf{x}^1)\mathbf{p}(\mathbf{x^1}) & \dots & w(\mathbf{x} - \mathbf{x}^k)\mathbf{p}(\mathbf{x^k}) \end{bmatrix}. \tag{3.25}$$

The system of equations then reads

$$\mathbf{0} = \mathbf{A}\boldsymbol{\alpha}(\mathbf{x}) - \mathbf{B}\boldsymbol{\Psi}, \tag{3.26}$$

which may be solved for the unknown basis function weights $\boldsymbol{\alpha}(\mathbf{x})$

$$\boldsymbol{\alpha}(\mathbf{x}) = \mathbf{A}^{-1}\mathbf{B}\boldsymbol{\Psi}. \tag{3.27}$$

Using equation (3.18) the interpolation of the point $\mathbf{x}$ may be expressed as a weighted sum of the discrete solution Ψ^k or $\boldsymbol{\Psi}$ in the support domain. The solution of the basis function weights $\boldsymbol{\alpha}(\mathbf{x})$ is subsituted into equation (3.18)

$$\Psi(\mathbf{x}) = \mathbf{p}^T(\mathbf{x})\mathbf{A}^{-1}\mathbf{B}\boldsymbol{\Psi}. \tag{3.28}$$

The weights assigned to the discrete solutions in the support domain may then be defined as

$$\boldsymbol{\phi}^T = \mathbf{p}^T(\mathbf{x})\mathbf{A}^{-1}\mathbf{B} \tag{3.29}$$

and the interpolation of the solution at locati on $\mathbf{x}$ may be expressed as

$$\Psi(\mathbf{x}) = \boldsymbol{\phi}^T\boldsymbol{\Psi}. \tag{3.30}$$

The weighting function of the L2-norm is used to define the support radius of the interpolation and ensure that the interpolation function is continuous. The interpolation is performed on the numerical solution which is solved on the isotropic Cartesian mesh. A cubic support domain is therefore preferable over a spherical support domain. The support domain is defined by a cube with edge half length $h = 1.5\Delta$ and edge length $H = 2h$, centered around the interpolation location $\mathbf{x}$. The support domain of the interpolation thus contains $3 \times 3 \times 3 = 27$ nodes of the discretized solution. The overlay of the support domain on the cartesian mesh is illustrated in figure 3.2. Figure 3.2 further illustrates that nodes in the support domain may be part of the solid domain rather than the fluid domain. A weight of $w = 0$ is assigned to any node outside the fluid domain.

Cubic splines are used as weighting function in the interpolation, as proposed by Vanella and Balaras (2009). A weight is computed for each spatial direction i in the support domain, given by

$$w_i(r_i) = \begin{cases} 2/3 - 4r_i^2 + 4r_i^3 & \text{for} \quad r_i \leq 0.5 \\ 4/3 - 4r_i + 4r^2 - 4/3r_i^3 & \text{for} \quad 0.5 < r_i \leq 1.0 \\ 0 & \text{for} \quad r_i > 1 \end{cases} \tag{3.31}$$

with $r_i = \frac{1}{h}\left|\mathbf{x}_i^k - \mathbf{x}_i\right|$. The weight associated with the discrete solution Ψ^k is given by the root of the product

$$w(\mathbf{x} - \mathbf{x}^\mathbf{k}) = \sqrt[3]{w_x \cdot w_y \cdot w_z}. \tag{3.32}$$

The weighting function for the two-dimensional case is illustrated in figure 3.3.

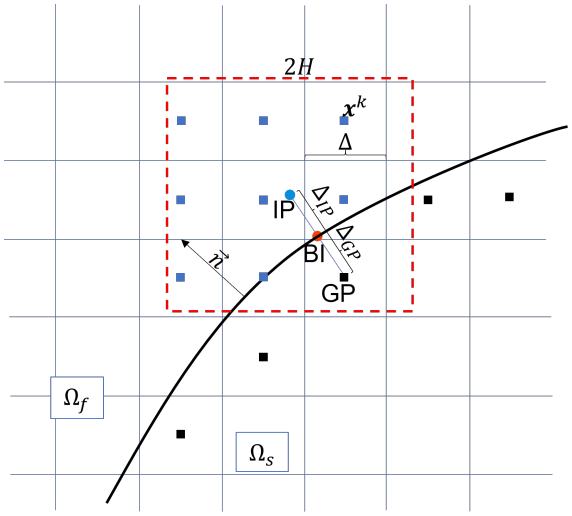

Figure 3.2: Schematic diagram of Catesian-grid-based computational domain with immersed boundary and interpolation support domain; Nomenclature: **GP**, ghost cell; **BI**, boundary intercept; **IP**, image point.

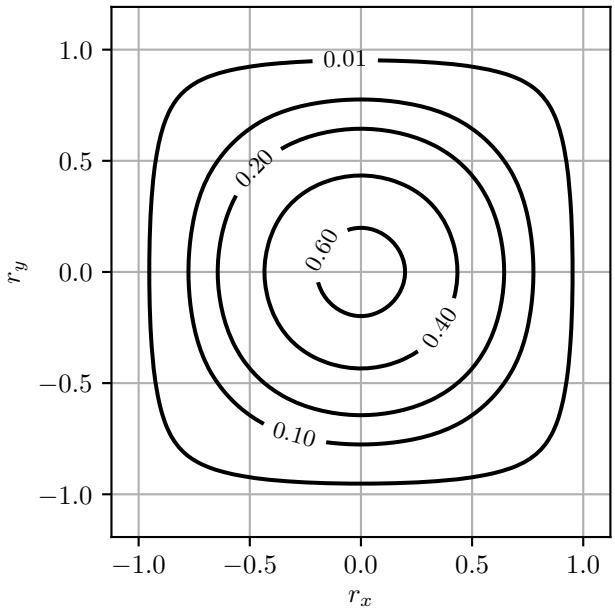

Figure 3.3: Contour-line plot of the weighting function in two dimensions.

3.4 Surface interpolation

The calculation of ghost cell values for Dirichlet and Neumann boundary conditions require information of the imposed Dirichlet boundary condition value f or gradient g at the boundary intercept. The boundary condition values are stored on the vertices of the triangulated surface mesh. An interpolation scheme is used to interpolate the solution on the vertices Ψ_i of the triangulated surface at the boundary intercept $\mathbf{x_{BI}}$.
A finite element approach with linear shape functions is used for the interpolation. The interpolation is expressed as a sum over the vertices of the triangle

$$\Psi = \sum w_i \Psi_i. \tag{3.33}$$

With the boundary intercept location given in the local triangle coordinates η, ν. The weights associated to the nodes of the triangle are given by

$$\begin{aligned} w_0 &= 1 - \eta - \nu, \\ w_1 &= \eta, \\ w_2 &= \nu. \end{aligned} \tag{3.34}$$

The triangle coordinate system $[\mathbf{e}_0, \mathbf{e}_1, \mathbf{n}]$ and boundary intercept coordinates η, ν are illustrated in figure 3.4. The coordinate axis $\mathbf{e}_0$ and $\mathbf{e}_1$ are defined with the vertices of the triangle

$$\begin{aligned} \mathbf{e}_0 &= \mathbf{v}_1 - \mathbf{v}_0, \\ \mathbf{e}_1 &= \mathbf{v}_2 - \mathbf{v}_0. \end{aligned} \tag{3.35}$$

The normal vector which defines the hypothetical $\mathbf{e}_2$ axis is defined by the cross-product of the two other axis vectors

$$\mathbf{n} = \mathbf{e}_2 = \mathbf{e}_1 \times \mathbf{e}_0. \tag{3.36}$$

The boundary intercept coordinate may be expressed in terms of the triangle coordinate system, which yields

$$\mathbf{x_{BI}} = \mathbf{x}_0 + \mathbf{e}_0\eta + \mathbf{e}_1\nu + \mathbf{n}\xi, \tag{3.37}$$

where $\mathbf{x}_0$ denotes the origin of the triangle system which is equal to vertex 0, $\mathbf{x}_0 = \mathbf{v}_0$.
The third term in the equation is removed as the solution of η and ν are independent of ξ since the vectors $\mathbf{e}_0$ and $\mathbf{e}_1$ are orthogonal to the normal axis. We may write the equation therefore in matrix form given by

$$\mathbf{x_{BI}} - \mathbf{x}_0 = \begin{bmatrix} \mathbf{e}_0 & \mathbf{e}_1 \end{bmatrix} \begin{bmatrix} \xi \\ \nu \end{bmatrix} = \mathbf{A} \begin{bmatrix} \xi \\ \nu \end{bmatrix}. \tag{3.38}$$

A least squares solution approach is used for the solution of the image point coordinates in the triangle reference frame

$$\begin{bmatrix} \xi \\ \nu \end{bmatrix} = (\mathbf{A}^T\mathbf{A})^{-1}\mathbf{A}^T(\mathbf{x_{BI}} - \mathbf{x}_0). \tag{3.39}$$

The least squares approach is selected to reduce the matrix inverse from a 3×3 matrix to a 2×2 matrix.

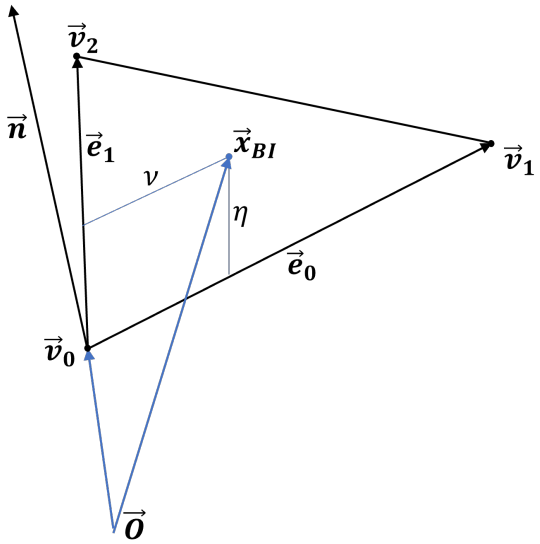

Figure 3.4: Schematic drawing of the coordinate system of a single triangle of the geometry surface mesh.

3.5 Wall boundary conditions

Two wall boundary conditions, a no-slip wall boundary condition and a wall-modeled wall boundary condition, are implemented in the ghost-cell immersed boundary framework. A slip wall boundary condition is also available within the wall-modeled framework when a zero-stress wall-model is selected.
For no-slip wall boundary conditions the image point is placed at a constant distance of

$$\Delta_{IP} = \alpha\Delta, \quad with \quad \alpha = 0.5. \tag{3.40}$$

With the placement of the image point at $\Delta_{IP} = 0.5$, the immersed boundary condition converges to the domain boundary condition when the immersed boundary is face aligned. Dirichlet boundary conditions are applied on the momentum terms, given by

$$\rho u_i|_{GP} = \rho u_i|_{BI} - \frac{2\Delta_{GP}}{\Delta}(\rho u_i|_{IP} - \rho u_i|_{BI}) \tag{3.41}$$

The solution of the momentum terms at the image point $\rho u_i|_{IP}$ is obtained with the presented moving least squares interpolation. The boundary intercept solution is split into the velocity and density term. The velocity term is interpolated on the triangulated surface mesh using triangular shape functions. The pressure and density is interpolated from the fluid solution using the zero gradient Neumann boundary conditions:

$$\rho|_{BI} = \rho|_{IP}\,. \tag{3.42}$$

A zero gradient Neumann boundary condition $\frac{\partial \Psi}{\partial n}\big|_O = 0$ is applied as

$$\rho|_{GP} = \rho|_{IP}\,. \tag{3.43}$$

The no-slip boundary can not be used in the wall-model framework as the grid is to coarse too resolve the inner layer of the turbulent boundary layer and therefore insufficient to

resolve the velocity profile. The numerical errors of the no-slip boundary condition on the coarse grid would violate the shear stress balance and thereby results in large errors in the flow-field solution. A detailed discussion on this topic is held in Tamaki and Kawai (2021). The conclusion of the discussion is two fold. The Dirichlet boundary condition of the convective terms should be replaced by a partial-slip boundary condition and the shear stress approximated by a suitable wall-model and applied either via an additional shear stress term or via the eddy viscosity in the near-wall cells.
For the partial slip boundary condition a similar approach to the one proposed in Noordt, Ganju, and Brehm (2021) is used. The Dirichlet boundary condition of the convective terms is replaced by a Neumann boundary condition for the wall tangential terms and a no penetration Dirichlet boundary condition for the wall-normal term. A probing point is introduced for the input to the wall-model. The image point and probing point location is illustrated in figure 3.5. The partial slip velocity results in an incorrect resolved shear stress. A wall-model is therefore employed to estimate the shear stress based on the near-wall flow solution. The wall shear stress may be applied to the numerical solution through a modified turbulent viscosity in the near-wall cells, or by adding a shear stress term to the equations. The turbulent viscosity treatment is known to lead to log-law mismatches (Tamaki & Kawai, 2021). Thus the shear stress source term approach is selected.

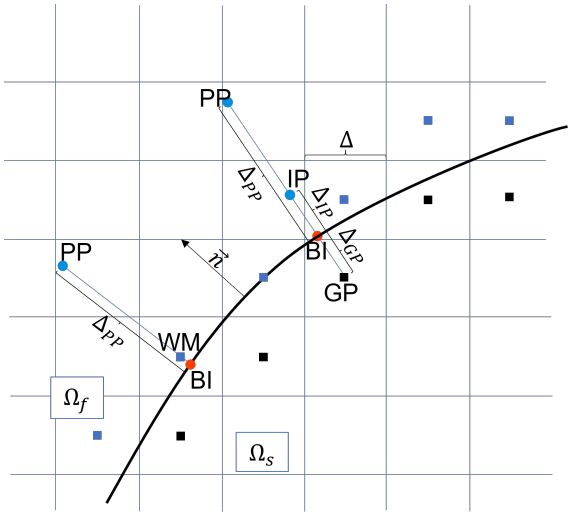

Figure 3.5: Schematic diagram of Catesian-grid-based computational domain with immersed boundary; Nomenclature: **GP**, ghost cell; **BI**, boundary intercept; **IP**, image point.

3.6 Hybrid ghost-cell method

As shown by Luo et al. (2012), the use of ghost-cell type immersed boundary techniques for the solution of moving geometries can lead to spurious oscillations as the numerical solution in the ghost cell might experience an instantaneous change. A so called hybrid-cell treatment has been subsequently implemented into the ghost-cell immersed boundary method based on the idea of Luo et al. (2012). The ghost-cell method with hybrid-cell treatment will be referred to as hybrid ghost-cell method. The hybrid-cell treatment

blends an interpolated solution in cells, marked as hybrid cells, with the numerical solution of the time integrated equations. Hybrid cells are defined as all fluid cells with solid cells or equivalently ghost cell neighbors. These cells may become a ghost cell in the following time step and can suffer from a discontinuous solution in time. A solution to this problem is a blending between the numerical solution and an interpolated solution. The ghost cell value converges to the the boundary condition when the ghost cell approaches the boundary,

$$\Psi_{GP} = \lim_{\boldsymbol{\Delta}_{GP} \to 0} \left(f - \frac{\Delta_{GP}}{\alpha \Delta} \left(\Psi_{IP} - f \right) \right) = f. \tag{3.44}$$

Equally, the flow solution is expected to approach the ghost cell value and the Dirichlet boundary condition when the fluid cell approaches the wall. For under-resolved flow cases the numerical solution might violate this condition which leads to a temporal discontinuity in the cell value once the fluid cell crosses the immersed boundary and switches to a ghost cell. This discontinuity leads to spurious oscillations or waves in the flow field.
The ghost cell value of the Dirichlet boundary condition is linear and further valid for cells inside the solid as well as in the fluid. We may therefore compute a ghost cell value for any hybrid-cell in the flow field. The interpolated solution in the hybrid cell is defined by

$$\Psi_{HB} = f - \frac{\Delta_{HB}}{\alpha \Delta} \left(\Psi_{IP} - f \right). \tag{3.45}$$

The interpolation at the image point might include hybrid cells, which leads to an implicit problem for the solution of the hybrid cell values. To prevent the implicit problem, the interpolation of the image point value for the hybrid cells is performed on the flow solution of the previous time step t_{i-1}.
With the definition of the interpolated hybrid cell value, which is defined in the following as $\Psi^{HB}_{interpolated}$, we can now define the blending between the interpolated solution and the time integrated solution of the image point denoted in the following by $\Psi^{HB^*}_{t+1}$. The blending is designed in such a way that the solution of hybrid cells approaches the fully interpolated and correct boundary intercept solution when the hybrid cells approach the immersed boundary and that the solution is fully given by the numerically advanced solution when the hybrid cells are at the limit of becoming a regular fluid cell. The blending between the two solutions is given by

$$\Psi^{HB}_{t+1} = (1 - \alpha) \Psi^{HB^*}_{t+1} + \alpha \Psi^{HB}_{interpolated} \tag{3.46}$$

The blending function is defined by a three-point version of the discrete Dirac's delta function given by

$$\alpha(r_i) = \begin{cases} 2/3 - 4r^2 + 4r^3 & \text{for} \quad r \leq 0.5 \\ 4/3 - 4r + 4r^2 - 4/3r^3 & \text{for} \quad 0.5 < r \leq 1.0 \\ 0 & \text{for} \quad r > 1 \end{cases}. \tag{3.47}$$

The coordinate r of the Dirac's delta function is defined via the signed distance function of the hybrid cell. The equation for the coordinate r is given by

$$r = \frac{2}{\sqrt{2}} \frac{|\boldsymbol{\Delta}_{HB}|}{\Delta}, \tag{3.48}$$

where Δ defines the size of the hybrid cell. The normalization length $\frac{\sqrt{2}}{2}\Delta$ is derived based on a two dimensional assessment of the location of regular fluid cells. Only one cell layer is currently marked as hybrid cells. Under this condition the lowest *sdf* of a fluid cell is $\frac{\sqrt{2}}{2}\Delta$. The normalization length ensures that any fluid cell that transitions to a hybrid cell has an initial blending weight of $\alpha = 0$.
Neumann type boundary conditions do not cause spurious oscillations in the flow field because, based on the definition of the ghost cell value, the image point and ghost cell values will always be identical which prevents the temporal discontinuity. Therefore, the hybrid cell approach is only applied to the Dirichlet type boundary conditions.

Chapter 4

Multi-body solver

A rigid body solver is integrated in the present code for the simulation of aircraft flight dynamics. With the implemented rigid body solver the aircraft and its components are modeled as multi-body systems. Absolute and relative constraint formulations are available to constrain bodies to the inertial reference frame and to specify constraints between bodies. The derivation of the equations of motion and constraint implementations are presented in this chapter. Moreover, the time integration of the equations of motion is addressed, and a control strategy of bodies and constraints based on the time integration scheme is presented. The chapter is started with the definition of the rigid body position and orientation which form the state vector of every rigid body in the system. The introduction to the position and orientation definition is given in section 4.1. The derivation of the equations of motion of a single rigid body is presented in section 4.2. The chapter is continued with the derivation of the absolute and relative constraints in section 4.4. Combined, these sections form the complete definition of the multi body system. The time integration of the constraint equations of motion is presented in section 4.5. The discretized equations of motion form a system of non-linear equations. The solution procedure for the non-linear equations is presented in section 4.6. The chapter is closed with the derivation of the control strategy which is used to constrain rigid bodies and constraints to prescribed paths defining the position and orientation.

4.1 Floating frame of reference for rigid bodies

The chapter starts with the derivation of the equations of motion. The derivation of the equations of motion of a single rigid body requires the definition of the body state that is the definition of the body position and orientation in space. The floating frame of reference approach has been used for this purpose as this approach can easily be extended to elastic bodies. A review of different approaches has been presented in section 2.4. The derivation shown in this and later sections follows largely the work of Shabana (2020). The input and output of the present code uses the Euler angle convention commonly used in flight dynamics. The definition of the Euler angles used in the present code is shown

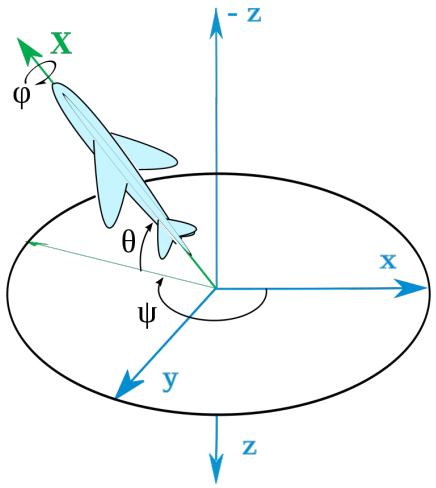

Figure 4.1: Definition of the Euler orientation angles, taken from (Sempere, 2009).

in figure 4.1. In case of an aircraft, the angles are referred to as roll ϕ, pitch θ and yaw angle ψ. Following the floating frame of reference formulation the position of any material point of the aircraft or any type of rigid body in the inertial reference frame $\mathbf{r}_P^i$ is defined by

$$\mathbf{r}_P^i = \mathbf{R} + \mathbf{A}(\mathbf{u}_s^i - \mathbf{u}_o^i), \tag{4.1}$$

as shown in figure 4.2. $\mathbf{R}$ denotes the position of the aircraft reference frame origin within the inertial coordinate system. $\mathbf{u}_o^i$ denotes the origin coordinate of the body defined in the body coordinate system. The origin defines the rotation and position reference point. The orientation coordinate is used in cases where the origin of the geometry file does not correspond to the rotation reference. $\mathbf{u}_s^i$ denotes any material point within the rigid body defined in the body coordinate system. $\mathbf{A}$ defines the transformation matrix which is derived from the presented Euler angles. For the defined Euler angles, the transfomation matrix $\mathbf{A}$ is given by

$$\mathbf{A} = \begin{bmatrix} \cos\theta\cos\psi & \sin\phi\sin\theta\cos\psi - \cos\phi\sin\psi & \cos\phi\sin\theta\cos\psi + \sin\phi\sin\psi \\ \cos\theta\sin\psi & \sin\phi\sin\theta\sin\psi + \cos\phi\cos\psi & \cos\phi\sin\theta\sin\psi - \sin\phi\cos\psi \\ -\sin\theta & \sin\phi\cos\theta & \cos\phi\cos\theta \end{bmatrix}. \tag{4.2}$$

The floating frame of reference approach is illustrated in figure 4.2 for a two-dimensional elastic body. The body coordinate system in figure 4.2 is denoted with the superscript i. The velocity of the material point is given by the time derivative of Eq. (4.1).

$$\dot{\mathbf{r}}_P^i = \dot{\mathbf{R}} + \dot{\mathbf{A}}(\mathbf{u}_s^i - \mathbf{u}_o^i). \tag{4.3}$$

The second term is rewritten to

$$\dot{\mathbf{r}}_P^i = \dot{\mathbf{R}} + \frac{\partial \mathbf{A}}{\partial \phi}(\mathbf{u}_s^i - \mathbf{u}_o^i)\dot{\phi} + \frac{\partial \mathbf{A}}{\partial \theta}(\mathbf{u}_s^i - \mathbf{u}_o^i)\dot{\theta} + \frac{\partial \mathbf{A}}{\partial \psi}(\mathbf{u}_s^i - \mathbf{u}_o^i)\dot{\psi}, \tag{4.4}$$

$$\dot{\mathbf{r}}_P^i = \dot{\mathbf{R}} + \mathbf{A}_\phi(\mathbf{u}_s^i - \mathbf{u}_o^i)\dot{\phi} + \mathbf{A}_\theta(\mathbf{u}_s^i - \mathbf{u}_o^i)\dot{\theta} + \mathbf{A}_\psi(\mathbf{u}_s^i - \mathbf{u}_o^i)\dot{\psi}, \tag{4.5}$$

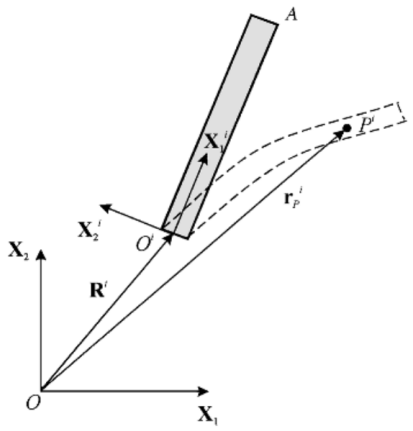

Figure 4.2: Illustration of the floating reference frame, taken from (Shabana, 2020, p. 184).

The derivatives of the matrices are given by

$$\mathbf{A}_\phi = \begin{bmatrix} 0 & \cos\phi\sin\theta\cos\psi + sin\phi\sin\psi & -\sin\phi\sin\theta\cos\psi + \cos\phi\sin\psi \\ 0 & \cos\phi\sin\theta\sin\psi - \sin\phi\cos\psi & -\sin\phi\sin\theta\sin\psi - \cos\phi\cos\psi \\ 0 & \cos\phi\cos\theta & -\sin\phi\cos\theta \end{bmatrix}, \tag{4.6}$$

$$\mathbf{A}_\theta = \begin{bmatrix} -\sin\theta\cos\psi & \sin\phi\cos\theta cos\psi & \cos\phi\cos\theta\cos\psi \\ -\sin\theta\sin\psi & \sin\phi\cos\theta\sin\psi & \cos\phi\cos\theta\sin\psi \\ -\cos\theta & -\sin\phi\sin\theta & -\cos\phi\sin\theta \end{bmatrix}, \tag{4.7}$$

$$\mathbf{A}_\psi = \begin{bmatrix} -\cos\theta\sin\psi & -\sin\phi\sin\theta\sin\psi - cos\phi\cos\psi & -\cos\phi\sin\theta\sin\psi + \sin\phi\cos\psi \\ \cos\theta\cos\psi & \sin\phi\sin\theta\cos\psi - \cos\phi\sin\psi & \cos\phi\sin\theta\cos\psi + \sin\phi\sin\psi \\ 0 & 0 & 0 \end{bmatrix}. \tag{4.8}$$

4.1.1 Euler parameters

The use of Euler angles in the rigid body solver leads to a singularity in the equations of motion if the pitch angle θ is equal to $\theta \pm \frac{\pi}{2}$. This lead to the introduction of the Euler parameters for the solution of the rigid body equations and for the calculation of body material points.

$$\boldsymbol{\theta} = \begin{bmatrix} \theta_0 & \theta_1 & \theta_2 & \theta_3 \end{bmatrix}^T \tag{4.9}$$

The transformation matrix $\mathbf{A}$ is defined in terms of Euler parameters as

$$\mathbf{A} = \begin{bmatrix} 2\left[(\theta_0)^2 + (\theta_1)^2\right] - 1 & 2(\theta_1\theta_2 - \theta_0\theta_3) & 2(\theta_1\theta_3 + \theta_0\theta_2) \\ 2(\theta_1\theta_2 + \theta_0\theta_3) & 2\left[(\theta_0)^2 + (\theta_2)^2\right] - 1 & 2(\theta_2\theta_3 - \theta_0\theta_1) \\ 2(\theta_1\theta_3 - \theta_0\theta_2) & 2(\theta_2\theta_3 + \theta_0\theta_1) & 2\left[(\theta_0)^2 + (\theta_3)^2\right] - 1 \end{bmatrix}. \tag{4.10}$$

The transformation matrix $\mathbf{A}$ may be defined as a product of two transformation matrices $\mathbf{E}$ and $\bar{\mathbf{E}}$ (Shabana, 2020). The matrices $2\mathbf{E} = \mathbf{G}$ and $2\bar{\mathbf{E}} = \bar{\mathbf{G}}$ are defined by

$$\mathbf{E} = \frac{\mathbf{G}}{2} = \begin{bmatrix} -\theta_1 & \theta_0 & -\theta_3 & \theta_2 \\ -\theta_2 & \theta_3 & \theta_0 & -\theta_1 \\ -\theta_3 & -\theta_2 & \theta_1 & \theta_0 \end{bmatrix} \tag{4.11}$$

and

$$\bar{\mathbf{E}} = \frac{\bar{\mathbf{G}}}{2} = \begin{bmatrix} -\theta_1 & \theta_0 & \theta_3 & -\theta_2 \\ -\theta_2 & -\theta_3 & \theta_0 & \theta_1 \\ -\theta_3 & \theta_2 & -\theta_1 & \theta_0 \end{bmatrix}, \tag{4.12}$$

The product of the matrices may be written as

$$\mathbf{A} = \mathbf{E}\bar{\mathbf{E}}^T. \tag{4.13}$$

As defined later in this chapter material point velocities of the body may be defined by

$$\dot{\mathbf{r}}_P = \dot{\mathbf{R}} - \mathbf{A}\tilde{\mathbf{u}}\bar{\mathbf{G}}\dot{\boldsymbol{\theta}}. \tag{4.14}$$

The use of the Euler parameters introduces an additional unknown in the equations of motion. At the same time the number of equations describing the motion of one rigid body does not change. The system is therefore under-determined. An additional constraint equation must be satisfied with the use of the Euler parameters. The constraint equation of the Euler parameters reads

$$\boldsymbol{\theta}^T\boldsymbol{\theta} = 1. \tag{4.15}$$

4.1.2 Transformation between Euler angles and Euler parameters

As discussed in the previous sections the Euler angles are used for the input and output of the present code as they follow the common aircraft flight dynamics definition. Internally, the Euler parameters are used to describe the orientation of the rigid bodies to prevent singularities in the equations of motion. The transformation of the Euler angles into Euler parameters is performed internally during the initialization of the simulation. The Euler parameters may be expressed as a function of the Euler angles of the body

$$\theta_i = \theta_i(\phi, \theta, \psi), \tag{4.16}$$

with

$$\begin{aligned} \theta_0 &= \cos\phi/2\cos\theta/2\cos\psi/2 + \sin\phi/2\sin\theta/2\sin\psi/2, \\ \theta_1 &= \sin\phi/2\cos\theta/2\cos\psi/2 - \cos\phi/2\sin\theta/2\sin\psi/2, \\ \theta_2 &= \cos\phi/2\sin\theta/2\cos\psi/2 + \sin\phi/2\cos\theta/2\sin\psi/2, \\ \theta_3 &= \cos\phi/2\cos\theta/2\sin\psi/2 - \sin\phi/2\sin\theta/2\cos\psi/2. \end{aligned} \tag{4.17}$$

Given the function $\theta_i(\phi, \theta, \psi)$ the first and second time derivatives of the Euler parameters may be written as

$$\dot{\theta}_i = \frac{\partial\theta_i}{\partial\phi}\dot{\phi} + \frac{\partial\theta_i}{\partial\theta}\dot{\theta} + \frac{\partial\theta_i}{\partial\psi}\dot{\psi} \tag{4.18}$$

and

$$\ddot{\theta}_i = \frac{d}{dt}\left(\frac{\partial\theta_i}{\partial\phi}\dot{\phi}\right) + \frac{d}{dt}\left(\frac{\partial\theta_i}{\partial\theta}\dot{\theta}\right) + \frac{d}{dt}\left(\frac{\partial\theta_i}{\partial\psi}\dot{\psi}\right), \tag{4.19}$$

$$\ddot{\theta}_i = \frac{d}{dt}\left(\frac{\partial \theta_i}{\partial \phi}\right)\dot{\phi} + \frac{\partial \theta_i}{\partial \phi}\ddot{\phi} + \frac{d}{dt}\left(\frac{\partial \theta_i}{\partial \theta}\right)\dot{\theta} + \frac{\partial \theta_i}{\partial \theta}\ddot{\theta} + \frac{d}{dt}\left(\frac{\partial \theta_i}{\partial \psi}\right)\dot{\psi} + \frac{\partial \theta_i}{\partial \psi}\ddot{\psi}. \tag{4.20}$$

The time derivative terms may be written as

$$\frac{d}{dt}\left(\frac{\partial \theta_i}{\partial \phi}\right) = \frac{\partial^2 \theta_i}{\partial \phi \partial \phi}\dot{\phi} + \frac{\partial^2 \theta_i}{\partial \theta \partial \phi}\dot{\theta} + \frac{\partial^2 \theta_i}{\partial \psi \partial \phi}\dot{\psi}, \tag{4.21}$$

$$\frac{d}{dt}\left(\frac{\partial \theta_i}{\partial \theta}\right) = \frac{\partial^2 \theta_i}{\partial \phi \partial \theta}\dot{\phi} + \frac{\partial^2 \theta_i}{\partial \theta \partial \theta}\dot{\theta} + \frac{\partial^2 \theta_i}{\partial \psi \partial \theta}\dot{\psi}, \tag{4.22}$$

and

$$\frac{d}{dt}\left(\frac{\partial \theta_i}{\partial \psi}\right) = \frac{\partial^2 \theta_i}{\partial \phi \partial \psi}\dot{\phi} + \frac{\partial^2 \theta_i}{\partial \theta \partial \psi}\dot{\theta} + \frac{\partial^2 \theta_i}{\partial \psi \partial \psi}\dot{\psi}. \tag{4.23}$$

The partial derivatives of the Euler parameters are presented in appendix A

4.2 Equations of motion of rigid bodies

The equations of motion of rigid bodies are derived from the definition of the material points of the rigid body in the floating frame of reference formulation. $\tilde{()}$ and $\bar{()}$ symbols are used in the derivation. The $\tilde{()}$ symbol defines skew symmetric matrices which are used to rewrite cross products between two vectors as matrices and the $\bar{()}$ symbol is used to define variables in the local body reference frame and to define matrices which transform vectors into the local body axis system. We recall the equation for the material point $\mathbf{r}_P$ in the floating frame of reference

$$\mathbf{r}_P = \mathbf{R} + \mathbf{A}\bar{\mathbf{u}} \quad with \quad \bar{u} = \mathbf{u}_s - \mathbf{u}_o. \tag{4.24}$$

The orientation matrix was defined in the preceding chapter by equation (4.2). The velocity of the material point is defined by the time derivative of the position equation

$$\dot{\mathbf{r}}_P = \dot{\mathbf{R}} + \dot{\mathbf{A}}\bar{\mathbf{u}}. \tag{4.25}$$

A slightly different approach is taken for the expansion of the time derivative of the orientation matrix. As discussed in Shabana (2020) the dot product of the orientation matrix and material coordinate in the body frame of reference $\mathbf{u}$ may be expressed by

$$\dot{\mathbf{A}}\bar{\mathbf{u}} = \mathbf{A}(\bar{\boldsymbol{\omega}} \times \bar{\mathbf{u}}). \tag{4.26}$$

The evaluation of the cross product on the right hand side yields the following expression

$$\bar{\boldsymbol{\omega}} \times \bar{\mathbf{u}} = -\tilde{\bar{\mathbf{u}}}\bar{\boldsymbol{\omega}}. \tag{4.27}$$

$\tilde{\mathbf{u}}$ is defined by the skew symmetric matrix

$$\tilde{\bar{\mathbf{u}}} = \begin{bmatrix} 0 & -\bar{x}_3 & \bar{x}_2 \\ \bar{x}_3 & 0 & -\bar{x}_1 \\ -\bar{x}_2 & \bar{x}_1 & 0 \end{bmatrix}. \tag{4.28}$$

With the above definitions the velocity of the material point may be defined by

$$\dot{\mathbf{r}}_P = \dot{\mathbf{R}} - \mathbf{A}\tilde{\bar{\mathbf{u}}}\bar{\boldsymbol{\omega}}. \tag{4.29}$$

The angular velocity of the body may be defined via the time derivatives of the orientation angles

$$\bar{\boldsymbol{\omega}} = \bar{\mathbf{G}}\dot{\boldsymbol{\theta}}. \tag{4.30}$$

The transformation matrix $\bar{\mathbf{G}}$ is shown in the preceding chapter. This leads to the final definition of the material point velocity $\dot{\mathbf{r}}_P$

$$\dot{\mathbf{r}}_P = \dot{\mathbf{R}} - \mathbf{A}\tilde{\bar{\mathbf{u}}}\bar{\mathbf{G}}\dot{\boldsymbol{\theta}}, \tag{4.31}$$

which can be written in a partitioned form as

$$\dot{\mathbf{r}}_P = \begin{bmatrix}\mathbf{I} & -\mathbf{A}\tilde{\bar{\mathbf{u}}}\bar{\mathbf{G}}\end{bmatrix}\begin{bmatrix}\dot{\mathbf{R}} \\ \dot{\boldsymbol{\theta}}\end{bmatrix}. \tag{4.32}$$

Kinetic Energy

The mass matrix of the rigid body is derived from the definition of the kinetic energy $T = \frac{1}{2}\int_V \rho\dot{\mathbf{r}}_P\dot{\mathbf{r}}_P dV$. Substituting the definition of the material point velocity into the definition of the kinetic energy yields

$$T = \frac{1}{2}\int_V \rho \begin{bmatrix}\dot{\mathbf{R}}^T & \dot{\boldsymbol{\theta}}^T\end{bmatrix}\begin{bmatrix}\mathbf{I} & -\mathbf{A}\tilde{\bar{\mathbf{u}}}\bar{\mathbf{G}} \\ symmetric & \bar{\mathbf{G}}^T\tilde{\bar{\mathbf{u}}}^T\tilde{\bar{\mathbf{u}}}\bar{\mathbf{G}}\end{bmatrix}\begin{bmatrix}\dot{\mathbf{R}} \\ \dot{\boldsymbol{\theta}}\end{bmatrix} dV. \tag{4.33}$$

The definition of the kinetic energy may be rewritten in the form of

$$T = \frac{1}{2}\begin{bmatrix}\dot{\mathbf{R}}^T & \dot{\boldsymbol{\theta}}^T\end{bmatrix}\left\{\int_V \rho\begin{bmatrix}\mathbf{I} & -\mathbf{A}\tilde{\bar{\mathbf{u}}}\bar{\mathbf{G}} \\ symmetric & \bar{\mathbf{G}}^T\tilde{\bar{\mathbf{u}}}^T\tilde{\bar{\mathbf{u}}}\bar{\mathbf{G}}\end{bmatrix} dV\right\}\begin{bmatrix}\dot{\mathbf{R}} \\ \dot{\boldsymbol{\theta}}\end{bmatrix}. \tag{4.34}$$

The equation may further be reduced to

$$T = \frac{1}{2}\dot{\mathbf{q}}^T\mathbf{M}\dot{\mathbf{q}}, \tag{4.35}$$

with

$$\mathbf{q} = \begin{bmatrix}\mathbf{R} & \boldsymbol{\theta}\end{bmatrix}^T \tag{4.36}$$

and

$$\mathbf{M} = \int_V \rho\begin{bmatrix}\mathbf{I} & -\mathbf{A}\tilde{\bar{\mathbf{u}}}\bar{\mathbf{G}} \\ symmetric & \bar{\mathbf{G}}^T\tilde{\bar{\mathbf{u}}}^T\tilde{\bar{\mathbf{u}}}\bar{\mathbf{G}}\end{bmatrix} dV. \tag{4.37}$$

The mass matrix is further simplified to

$$\mathbf{M} = \begin{bmatrix}\mathbf{m}_{RR} & \mathbf{m}_{R\theta} \\ symmetric & \mathbf{m}_{\theta\theta}\end{bmatrix}, \tag{4.38}$$

with

$$\mathbf{m}_{RR} = \int_V \rho\mathbf{I}dV = m\mathbf{I}, \tag{4.39}$$

$$\mathbf{m}_{R\theta} = -\int_V \rho \mathbf{A}\tilde{\mathbf{u}}\bar{\mathbf{G}} dV \tag{4.40}$$

and

$$\mathbf{m}_{\theta\theta} = \int_V \rho \bar{\mathbf{G}}^T \tilde{\mathbf{u}}^T \tilde{\mathbf{u}} \bar{\mathbf{G}} dV = \bar{\mathbf{G}}^T \bar{\mathbf{I}}_{\theta\theta} \bar{\mathbf{G}}. \tag{4.41}$$

Two variables were introduced. (1) The mass of the body m and (2) the mass moment of inertia matrix $\mathbf{I}_{\theta\theta}$. The mass moment of inertia matrix $\mathbf{I}_{\theta\theta}$ may be written as

$$\mathbf{I}_{\theta\theta} = \int_V \rho \tilde{\mathbf{u}}^T \tilde{\mathbf{u}} dV = \begin{bmatrix} I_{xx} & I_{xy} & I_{xz} \\ & I_{yy} & I_{yz} \\ sym. & & I_{zz} \end{bmatrix}. \tag{4.42}$$

Potential Energy

The potential energy of the rigid body is defined by all external forces and moments times their respective translational and rotational displacements.

$$W_e = \mathbf{Q}_e \mathbf{q}, \tag{4.43}$$

which are further divided into

$$W_e = \begin{bmatrix} (\mathbf{Q}_R)_e^T & (\mathbf{Q}_\theta)_e^T \end{bmatrix} \begin{bmatrix} \mathbf{R} \\ \boldsymbol{\theta} \end{bmatrix}. \tag{4.44}$$

Vector $(\mathbf{Q}_R)_e$ holds all external forces which are applied to the rigid body. Vector $(\mathbf{Q}_\theta)_e$ holds all external moments which are applied to the rigid body. Both vectors are defined in the inertial reference frame.

Lagrange's equation

Lagrange's equation is used to derive the equations of motion. Lagrange's equation is defined by

$$\frac{d}{dt}\frac{\partial L}{\partial \dot{\mathbf{q}}} - \frac{\partial L}{\partial \mathbf{q}} = 0, \tag{4.45}$$

where L is the energy of the system defined by the sum of the kinetic and potential energy. Crucial to the derivation of the equations of motion is that the center of rotation is aligned with the center of gravity of the rigid body. Substituting the derived definition of the kinetic and potential energy into Lagrange's equation yields

$$\frac{d}{dt}\frac{\partial}{\partial \dot{\mathbf{q}}}(T + W_e) - \frac{\partial}{\partial \mathbf{q}}(T + W_e) = 0. \tag{4.46}$$

The evaluation of the potential energy part yields

$$\frac{d}{dt}\frac{\partial T}{\partial \dot{\mathbf{q}}} - \frac{\partial T}{\partial \mathbf{q}} = \mathbf{Q}_e. \tag{4.47}$$

The evaluation of the kinetic energy yields

$$\frac{d}{dt}\frac{\partial}{\partial \dot{\mathbf{q}}}\left(\frac{1}{2}\dot{\mathbf{q}}^T \mathbf{M} \dot{\mathbf{q}}\right) - \frac{\partial}{\partial \mathbf{q}}\left(\frac{1}{2}\dot{\mathbf{q}}^T \mathbf{M} \dot{\mathbf{q}}\right) = \mathbf{Q}_e, \tag{4.48}$$

$$\frac{d}{dt}\left(\mathbf{M}\dot{\mathbf{q}}\right) - \frac{\partial}{\partial q}\left(\frac{1}{2}\dot{\mathbf{q}}^T\mathbf{M}\dot{\mathbf{q}}\right) = \mathbf{Q}_e, \tag{4.49}$$

$$\mathbf{M}\ddot{\mathbf{q}} + \dot{\mathbf{M}}\dot{\mathbf{q}} - \frac{\partial}{\partial q}\left(\frac{1}{2}\dot{\mathbf{q}}^T\mathbf{M}\dot{\mathbf{q}}\right) = \mathbf{Q}_e, \tag{4.50}$$

$$\mathbf{M}\ddot{\mathbf{q}} = \mathbf{Q}_e - \dot{\mathbf{M}}\dot{\mathbf{q}} + \frac{\partial}{\partial q}\left(\frac{1}{2}\dot{\mathbf{q}}^T\mathbf{M}\dot{\mathbf{q}}\right). \tag{4.51}$$

The non-linear velocity terms on the right hand side are combined in the quadratic velocity vector $\mathbf{Q}_v$. The equation then reads

$$\mathbf{M}\ddot{\mathbf{q}} = \mathbf{Q}_e + \mathbf{Q}_v \quad with \quad \mathbf{Q}_v = -\dot{\mathbf{M}}\dot{\mathbf{q}} + \frac{\partial}{\partial \mathbf{q}}\left(\frac{1}{2}\dot{\mathbf{q}}^T\mathbf{M}\dot{\mathbf{q}}\right). \tag{4.52}$$

The expansion of term 1 of the quadratic velocity term reads

$$\dot{\mathbf{M}}\dot{\mathbf{q}} = \begin{bmatrix}\dot{\mathbf{m}}_{RR}\dot{\mathbf{R}}\\ \dot{\mathbf{m}}_{\theta\theta}\dot{\boldsymbol{\theta}}\end{bmatrix} = \begin{bmatrix}\mathbf{0}\\ \dot{\mathbf{m}}_{\theta\theta}\dot{\boldsymbol{\theta}}\end{bmatrix} = \begin{bmatrix}\mathbf{0}\\ \frac{d}{dt}(\bar{\mathbf{G}}^T\bar{\mathbf{I}}_{\theta\theta}\bar{\mathbf{G}})\dot{\boldsymbol{\theta}}\end{bmatrix} = \begin{bmatrix}\mathbf{0}\\ \dot{\bar{\mathbf{G}}}^T\bar{\mathbf{I}}_{\theta\theta}\bar{\mathbf{G}}\dot{\boldsymbol{\theta}} + \bar{\mathbf{G}}^T\bar{\mathbf{I}}_{\theta\theta}\dot{\bar{\mathbf{G}}}\dot{\boldsymbol{\theta}}\end{bmatrix}. \tag{4.53}$$

The expansion of the second term of the quadratic velocity vector is given by

$$\frac{\partial}{\partial \mathbf{q}}\left(\frac{1}{2}\dot{\mathbf{q}}^T\mathbf{M}\dot{\mathbf{q}}\right) = \begin{bmatrix}\mathbf{0}\\ \frac{1}{2}\frac{\partial}{\partial\boldsymbol{\theta}}(\dot{\boldsymbol{\theta}}^T\mathbf{m}_{\theta\theta}\dot{\boldsymbol{\theta}})\end{bmatrix} \tag{4.54}$$

The equations are significantly simplified with the use of identities of the Euler parameters. The first term is simplified to

$$\dot{\bar{\mathbf{G}}}^T\bar{\mathbf{I}}_{\theta\theta}\bar{\mathbf{G}}\dot{\boldsymbol{\theta}} + \bar{\mathbf{G}}^T\bar{\mathbf{I}}_{\theta\theta}\dot{\bar{\mathbf{G}}}\dot{\boldsymbol{\theta}} = \dot{\bar{\mathbf{G}}}^T\bar{\mathbf{I}}_{\theta\theta}\bar{\mathbf{G}}\dot{\boldsymbol{\theta}}, \tag{4.55}$$

using the Euler parameter identity $\dot{\bar{\mathbf{G}}}\dot{\boldsymbol{\theta}} = 0$. The second term may be simplified to

$$\frac{1}{2}\frac{\partial}{\partial\boldsymbol{\theta}}(\dot{\boldsymbol{\theta}}^T\mathbf{m}_{\theta\theta}\dot{\boldsymbol{\theta}}) = -\dot{\bar{\mathbf{G}}}^T\bar{\mathbf{I}}_{\theta\theta}\bar{\mathbf{G}}\dot{\boldsymbol{\theta}}, \tag{4.56}$$

using equation (4.41) and the Euler parameter identity $\dot{\bar{\mathbf{G}}}\boldsymbol{\theta} = \bar{\mathbf{G}}\dot{\boldsymbol{\theta}}$. The equations of motion of a single rigid body are given in terms of Euler parameters as

$$\begin{bmatrix}\mathbf{m}_{RR} & 0\\ 0 & \mathbf{m}_{\theta\theta}\end{bmatrix}\begin{bmatrix}\ddot{\mathbf{R}}\\ \ddot{\boldsymbol{\theta}}\end{bmatrix} = \mathbf{Q}_e - \begin{bmatrix}\mathbf{0}\\ 2\dot{\bar{\mathbf{G}}}^T\bar{\mathbf{I}}_{\theta\theta}\bar{\mathbf{G}}\dot{\boldsymbol{\theta}}\end{bmatrix}. \tag{4.57}$$

4.3 Constraint equation for Euler parameters

The equations of motion in terms of Euler parameters must be satisfied in combination with the constraint equation

$$\boldsymbol{\theta}^T\boldsymbol{\theta} = 1. \tag{4.58}$$

In acceleration terms the equation might be expressed via

$$\boldsymbol{\theta}^T\ddot{\boldsymbol{\theta}} = -\dot{\boldsymbol{\theta}}^T\dot{\boldsymbol{\theta}}. \tag{4.59}$$

The constraint equation of the Euler parameters is integrated into the inertia matrix of the rigid body by introducing an additional Lagrange multiplier unknown:

$$\begin{bmatrix} \mathbf{m}_{\theta\theta} & \boldsymbol{\theta} \\ \boldsymbol{\theta}^T & \mathbf{0} \end{bmatrix} \begin{bmatrix} \ddot{\boldsymbol{\theta}} \\ \lambda \end{bmatrix} = \begin{bmatrix} \mathbf{Q}_e - 2\dot{\bar{\mathbf{G}}}^T \bar{\mathbf{I}}_{\theta\theta} \bar{\mathbf{G}} \dot{\boldsymbol{\theta}} \\ -\dot{\boldsymbol{\theta}}^T \dot{\boldsymbol{\theta}} \end{bmatrix}. \tag{4.60}$$

The solution of the augmented system is consistent but the numerical discretization error of the time integration schemes lead to the violation of the constraint equation $\boldsymbol{\theta}^T\boldsymbol{\theta} = 1$. Normalization of the Euler parameters after each integration step removes the constraint violation in terms of the Euler position parameters but does not prevent the violation of the constraint equation in terms of the Euler velocity parameters $\dot{\boldsymbol{\theta}}$. Long running simulations have shown that the normalization of the Euler parameters without treatment of the Euler velocity can lead to instability and divergence of the solution. A revised Euler parameter constraint implementation was derived based on the path following algorithm presented in section 4.7. We start by rewriting the constraint equation with an unknown right hand side value c

$$\boldsymbol{\theta}^T\boldsymbol{\theta} = c. \tag{4.61}$$

The time derivative of the constraint equation then becomes

$$\dot{\boldsymbol{\theta}}^T\boldsymbol{\theta} = \frac{1}{2}\dot{c} \tag{4.62}$$

and

$$\boldsymbol{\theta}^T\ddot{\boldsymbol{\theta}} + \dot{\boldsymbol{\theta}}^T\dot{\boldsymbol{\theta}} = \frac{1}{2}\ddot{c}. \tag{4.63}$$

The equation may be used to compute the current state of the constraint in terms of the position, velocity and acceleration terms, subscript $(.)_n$. The current state of the constraint equation and the target values of the constraint $c = 1$ and $\dot{c} = 0$ may be used in combination with the controller strategy, discussed in section 4.7, to define the acceleration state of the constraint at the new time step $\ddot{c}_{n+1}$. Applying the path-following equation to the constraint state results in

$$\begin{bmatrix} 1 \\ 0 \end{bmatrix} - \begin{bmatrix} 1 & 2c_0 & c_1 + c_0 \cdot d_0 \\ 0 & 1 & d_0 \end{bmatrix} \begin{bmatrix} c_n \\ \dot{c}_n \\ \ddot{c}_n \end{bmatrix} = \begin{bmatrix} c_2 + c_0 \cdot d_1 + c_1 & c_2 \\ d_0 + d_1 & d_1 \end{bmatrix} \begin{bmatrix} \ddot{c}_{n+1} \\ \ddot{c}_{n+2} \end{bmatrix}. \tag{4.64}$$

The augmented equation in the non discretized form reads

$$\begin{bmatrix} \mathbf{m}_{\theta\theta} & \boldsymbol{\theta} \\ \boldsymbol{\theta}^T & \mathbf{0} \end{bmatrix} \begin{bmatrix} \ddot{\boldsymbol{\theta}} \\ \lambda \end{bmatrix} = \begin{bmatrix} \mathbf{Q}_e - 2\dot{\bar{\mathbf{G}}}^T \bar{\mathbf{I}}_{\theta\theta} \bar{\mathbf{G}} \dot{\boldsymbol{\theta}} \\ -\dot{\boldsymbol{\theta}}^T \dot{\boldsymbol{\theta}} + 0.5\ddot{c} \end{bmatrix}. \tag{4.65}$$

4.4 Constraints

The rigid body equations of motion may be solved in combination with holonomic fixation constraints with respect to the inertial frame or between two rigid bodies. Holonomic constraints, (F. Amirouche, 2006, p. 319), are constraints which can be written in the form of

$$f(q_0, q_1, q_2, ..., q_n, t) = 0. \tag{4.66}$$

The augmented method is used for the solution of the constraint equations of motion. The method augments the mass matrix with constraint equations and introduces the constraint forces via Lagrange multipliers λ, similar to the implementation of the Euler parameter constraint. As discussed before the constraint equation must be written in the acceleration form, which is obtained by differentiating the constraint equation in time. The differentiation of the constraint equation is discussed in the individual constraint sections 4.4.1 and 4.4.2. In general the constraint equation can be written in the form of

$$\mathbf{C}_q \ddot{\mathbf{q}} = \mathbf{q}_c(\mathbf{q}, \dot{\mathbf{q}}). \tag{4.67}$$

The system of equations defines constraint equations of the individual position and rotation degrees of freedom as a function of the acceleration state and a vector consisting of position and velocity terms. The augmented system matrix is derived from a simplified form of the equations of motion

$$\left[\mathbf{m}\right]\left[\ddot{\mathbf{q}}\right] = \left[\mathbf{Q}\right], \tag{4.68}$$

which reads in the augmented form

$$\begin{bmatrix} \mathbf{m} & \mathbf{C}_q^T \\ \mathbf{C}_q & \mathbf{0} \end{bmatrix} \begin{bmatrix} \ddot{\mathbf{q}} \\ \boldsymbol{\lambda} \end{bmatrix} = \begin{bmatrix} \mathbf{Q} \\ \mathbf{q}_c \end{bmatrix}. \tag{4.69}$$

In the above form the constraint equation constrains all translation and rotation degrees of freedom, yielding 6 equations per constraint. However, specific constraints such as hinge constraints do not require a constraint equation for each degree of freedom. These constraint equations may be removed from the system or replaced by other equations. The current implementation introduces a fixation matrix $\mathbf{C}_{qs}$ to deal with fixed and free degrees of freedom in constraints. Instead of removing unused constraint equations, the equation is modified by constraining the specific Lagrange multiplier to zero. The system then reads

$$\begin{bmatrix} \mathbf{m} & \mathbf{C}_q^T \\ \mathbf{C}_q & \mathbf{C}_{qs} \end{bmatrix} \begin{bmatrix} \ddot{\mathbf{q}} \\ \boldsymbol{\lambda} \end{bmatrix} = \begin{bmatrix} \mathbf{Q} \\ \mathbf{q}_c \end{bmatrix}. \tag{4.70}$$

4.4.1 Inertial constraints

The degrees of freedom of the rigid bodies may be decreased by enforcing inertial constraints. The constraint prescribes the position and orientation of any point, defined in the body reference frame, in the inertial frame. The constraint equation for the translational degrees of freedom is derived from the definition of the material point velocity by differentiating the equation in time once. The resulting equation yields the definition of the material point acceleration in the inertial reference frame.

$$\ddot{\mathbf{r}}_p = \frac{d}{dt}\left(\dot{\mathbf{R}} - \mathbf{A}\tilde{\bar{\mathbf{u}}}\bar{\mathbf{G}}\dot{\boldsymbol{\theta}}\right) = \ddot{\mathbf{R}} - \mathbf{A}\tilde{\bar{\mathbf{u}}}\bar{\mathbf{G}}\ddot{\boldsymbol{\theta}} - \dot{\mathbf{A}}\tilde{\bar{\mathbf{u}}}\bar{\mathbf{G}}\dot{\boldsymbol{\theta}} - \mathbf{A}\tilde{\bar{\mathbf{u}}}\dot{\bar{\mathbf{G}}}\dot{\boldsymbol{\theta}} \tag{4.71}$$

The definition of the material point acceleration may be applied to any point $\bar{\mathbf{u}}$ in the body reference frame, which is constraint to the inertial frame of reference. The acceleration

of the point may be prescribed in the inertial frame. The constraint equation for the translational degrees of freedom reads

$$\begin{bmatrix} \ddot{r}_x^{pres} \\ \ddot{r}_y^{pres} \\ \ddot{r}_z^{pres} \end{bmatrix} = \ddot{\mathbf{R}} - \mathbf{A}\tilde{\mathbf{u}}\bar{\mathbf{G}}\ddot{\boldsymbol{\theta}} - \dot{\mathbf{A}}\tilde{\mathbf{u}}\bar{\mathbf{G}}\dot{\boldsymbol{\theta}} - \mathbf{A}\tilde{\mathbf{u}}\dot{\bar{\mathbf{G}}}\dot{\boldsymbol{\theta}}. \tag{4.72}$$

The equation may be simplified using identities of the Euler parameters $\dot{\bar{\mathbf{G}}}\dot{\boldsymbol{\theta}} = 0$ and $\dot{\mathbf{A}} = \mathbf{A}\tilde{\boldsymbol{\omega}}$

$$\begin{bmatrix} \ddot{r}_x^{pres} \\ \ddot{r}_y^{pres} \\ \ddot{r}_z^{pres} \end{bmatrix} + \mathbf{A}\tilde{\boldsymbol{\omega}}\tilde{\mathbf{u}}\bar{\mathbf{G}}\dot{\boldsymbol{\theta}} = \ddot{\mathbf{R}} - \mathbf{A}\tilde{\mathbf{u}}\bar{\mathbf{G}}\ddot{\boldsymbol{\theta}}. \tag{4.73}$$

In a similar fashion the constraint equation of the rotational degrees of freedom is derived. The angular velocity of the body in the inertial reference frame is defined by

$$\boldsymbol{\omega} = \mathbf{G}\dot{\boldsymbol{\theta}}. \tag{4.74}$$

The derivative of the equation yields the angular acceleration around the inertial axis system

$$\dot{\boldsymbol{\omega}} = \boldsymbol{\alpha} = \frac{d}{dt}\left(\mathbf{G}\dot{\boldsymbol{\theta}}\right), \tag{4.75}$$

$$\boldsymbol{\alpha} = \mathbf{G}\ddot{\boldsymbol{\theta}} + \dot{\mathbf{G}}\dot{\boldsymbol{\theta}}, \tag{4.76}$$

using $\dot{\mathbf{G}}\dot{\boldsymbol{\theta}} = 0$

$$\begin{bmatrix} \alpha_x^{pres} \\ \alpha_y^{pres} \\ \alpha_z^{pres} \end{bmatrix} = \mathbf{G}\ddot{\boldsymbol{\theta}} \tag{4.77}$$

The final form of the fixation constraint equation is given by the combination of the translational and rotational constraints

$$\begin{bmatrix} \mathbf{I} & \mathbf{A}\tilde{\mathbf{u}}\bar{\mathbf{G}} \\ \mathbf{0} & \mathbf{G} \end{bmatrix} \begin{bmatrix} \ddot{\mathbf{R}} \\ \ddot{\boldsymbol{\theta}} \end{bmatrix} = - \begin{bmatrix} \mathbf{A}\tilde{\boldsymbol{\omega}}\tilde{\mathbf{u}}\bar{\mathbf{G}}\dot{\boldsymbol{\theta}} \\ \mathbf{0} \end{bmatrix} + \begin{bmatrix} \ddot{\mathbf{r}}^{pres} \\ \boldsymbol{\alpha}^{pres} \end{bmatrix}. \tag{4.78}$$

Springs

Any rigid body in the simulation may be constrained to the inertial frame via a set of springs, three translational and three torsional. The translational and torsional springs are aligned with the x,y,z axis of the inertial frame independent of the position and displacement of the body. The forces of the springs and later defined dampers are introduced as force vector on the right hand side of the equations of motion. The force of the translational springs may be expressed by

$$\mathbf{F}_r = -\left(\mathbf{K}_r\left(\mathbf{r}' - \mathbf{r}_0\right)\right). \tag{4.79}$$

Matrix $\mathbf{K}_r$ holds the spring stiffnesses of the three translational springs

$$\mathbf{K}_r = \mathbf{K}_r^T = \begin{bmatrix} k_x & 0 & 0 \\ 0 & k_y & 0 \\ 0 & 0 & k_z \end{bmatrix}. \tag{4.80}$$

Vectors $\mathbf{r}'$ and $\mathbf{r}_0$ define the current and rest position of the spring anchor point in the inertial frame. The position vector of the elastic anchor point $\mathbf{r}$ is defined with the floating frame of reference approach which was introduced during the derivation of the equations of motion. The definition of the elastic anchor point is given by

$$\mathbf{r}' = \mathbf{R} + \mathbf{A}\bar{\mathbf{u}}_e, \tag{4.81}$$

where $\bar{\mathbf{u}}_e$ is the position of the elastic anchor point in the body reference frame. Substituting the definition of $\mathbf{r}'$ into the spring force equation yields

$$\mathbf{F}_r = -\left(\mathbf{K}_r\left(\mathbf{R} + \mathbf{A}\bar{\mathbf{u}}_e - \mathbf{r}_0\right)\right) \tag{4.82}$$

The moment of the force $\mathbf{F}_r$ may be defined via the cross product of the moment arm and the force. The moments are given by the distance of the elastic anchor point and center of gravity which is defined by the vector $\bar{\mathbf{u}}_e$.

$$\mathbf{M}_r = \mathbf{A}\bar{\mathbf{u}}_e \times \mathbf{F}_r \tag{4.83}$$

The moment is defined within the x,y,z frame and must be transferred into Euler parameters with the transformation matrix $\mathbf{G}$. Given the spring force and moment the external spring force vector $\mathbf{Q}_s^r$ is defined by

$$\mathbf{Q}_s^r = -\begin{bmatrix} \mathbf{K}_r\left(\mathbf{R} + \mathbf{A}\bar{\mathbf{u}}_e\right) \\ \mathbf{G}^T\left(\mathbf{A}\bar{\mathbf{u}}_e \times \mathbf{K}_r\left(\mathbf{R} + \mathbf{A}\bar{\mathbf{u}}_e\right)\right) \end{bmatrix} + \begin{bmatrix} \mathbf{K}_r\mathbf{r}_0 \\ \mathbf{G}^T\left(\mathbf{A}\bar{\mathbf{u}}_e \times \mathbf{K}_r\mathbf{r}_0\right) \end{bmatrix}. \tag{4.84}$$

The moment of an external torsional spring is defined by the Euler angles of the body

$$\mathbf{M}_r = -\mathbf{K}_\theta\left(\boldsymbol{\theta}' - \boldsymbol{\theta}_0\right), \tag{4.85}$$

with

$$\mathbf{K}_\theta = \begin{bmatrix} k_\phi & 0 & 0 \\ 0 & k_\theta & 0 \\ 0 & 0 & k_\psi \end{bmatrix} \tag{4.86}$$

The moment of the torsional springs are defined around the x,y,z axis of the inertial reference frame. In matrix form the external torsional spring vector is given by

$$\mathbf{Q}_s^\theta = -\begin{bmatrix} \mathbf{0} \\ \mathbf{G}^T\mathbf{K}_\theta\left(\boldsymbol{\theta} - \boldsymbol{\theta_0}\right) \end{bmatrix}. \tag{4.87}$$

Damper

The forces and moments of the translational and torsional dampers are derived from Rayleigh's dissipation function (Minguzzi, 2015) and are given by

$$\mathbf{Q}_c^r = -\begin{bmatrix} \mathbf{C}_r\dot{\mathbf{r}} \\ \mathbf{G}^T\left(\mathbf{A}\bar{\mathbf{u}}_e \times \left(\mathbf{C}_r\dot{\mathbf{r}}\right)\right) \end{bmatrix} = -\begin{bmatrix} \mathbf{C}_r\left(\dot{\mathbf{R}} + \mathbf{A}\tilde{\bar{\mathbf{u}}}_e\mathbf{G}\dot{\boldsymbol{\theta}}\right) \\ \mathbf{G}^T\left(\mathbf{A}\bar{\mathbf{u}}_e \times \mathbf{C}_r\left(\dot{\mathbf{R}} + \mathbf{A}\tilde{\bar{\mathbf{u}}}_e\mathbf{G}\dot{\boldsymbol{\theta}}\right)\right) \end{bmatrix} \tag{4.88}$$

$$\mathbf{Q}_c^\theta = -\begin{bmatrix} \mathbf{0} \\ \mathbf{G}^T\mathbf{C}_\theta\mathbf{G}\dot{\boldsymbol{\theta}} \end{bmatrix} \tag{4.89}$$

4.4.2 Relative constraints

The multi-body model of the aircraft follows a tree-structure (F. Amirouche, 2006, p. 107). In combination with the tree-structure a master slave approach is used for relative constraints between bodies. Identical to the inertial constraints the constraint equation operates on the acceleration level. For relative constraints the translational and rotational accelerations are matched. The master-slave approach is used to define the owner of the axis system of the constraint origin.
At the time of writing prismatic and slider constraints were not required. Therefore, relative constraints constrain all translational degrees of the freedom which makes the definition of the coordinate system for the translational coordinates obsolete. The acceleration of a material point in the rigid body has been defined before. With the definition of the material point one can define the relative acceleration of two rigid bodies at the constraint anchor point

$$\Delta\ddot{\mathbf{r}}^{pres} = \ddot{\mathbf{r}}^{slave} - \ddot{\mathbf{r}}^{master}. \tag{4.90}$$

Reduced for better readability

$$\Delta\ddot{\mathbf{r}}^{p} = \ddot{\mathbf{r}}^{s} - \ddot{\mathbf{r}}^{m} \tag{4.91}$$

with

$$\ddot{\mathbf{r}}^{s/m} = \ddot{\mathbf{R}} - \mathbf{A}\tilde{\mathbf{u}}\bar{\mathbf{G}}\ddot{\boldsymbol{\theta}} - \mathbf{A}\tilde{\boldsymbol{\omega}}\tilde{\mathbf{u}}\bar{\mathbf{G}}\dot{\boldsymbol{\theta}}. \tag{4.92}$$

$$\ddot{\mathbf{r}}^{s/m} = \ddot{\mathbf{R}} - \mathbf{A}\tilde{\mathbf{u}}\bar{\mathbf{G}}\ddot{\boldsymbol{\theta}} + \mathbf{Q}_r^{s/m} \quad with \quad \mathbf{Q}_r^{s/m} = -\mathbf{A}\tilde{\boldsymbol{\omega}}\tilde{\mathbf{u}}\bar{\mathbf{G}}\dot{\boldsymbol{\theta}}. \tag{4.93}$$

The constraint of the rotational degrees of freedom introduces a coordinate system, which resides in the reference frame of one of the rigid bodies. The coordinate system is used to constrain individual rotational degrees of freedom between the bodies and model fix, hinge, and joint constraints. A unit normal vector in the coordinate system $\bar{\bar{\mathbf{v}}}$ may be transformed to the body and inertial reference frame via

$$\bar{\mathbf{v}} = \bar{\mathbf{A}}\bar{\bar{\mathbf{v}}} \tag{4.94}$$

and

$$\mathbf{v} = \mathbf{A}\bar{\mathbf{v}} = \mathbf{A}\bar{\mathbf{A}}\bar{\bar{\mathbf{v}}}, \tag{4.95}$$

which is nothing else but two successive rotations. The new matrix $\bar{\mathbf{A}}$ desribes the orientation of the coordinate system in the rigid body reference frame.
The angular velocity of the body in the inertial reference frame is given by

$$\boldsymbol{\omega} = \mathbf{A}\bar{\boldsymbol{\omega}} = \mathbf{A}\bar{\mathbf{G}}\dot{\boldsymbol{\theta}} = \mathbf{G}\dot{\boldsymbol{\theta}} \tag{4.96}$$

With this the angular velocity of the master and slave bodies may be defined

$$\begin{aligned} \boldsymbol{\omega}^m &= \mathbf{A}^m\bar{\boldsymbol{\omega}}^m, \\ \boldsymbol{\omega}^s &= \mathbf{A}^s\bar{\boldsymbol{\omega}}^s. \end{aligned} \tag{4.97}$$

The relative angular velocity of the bodies is given by

$$\Delta\boldsymbol{\omega}^p = \boldsymbol{\omega}^s - \boldsymbol{\omega}^m \tag{4.98}$$

The two angular velocities may be equated around any axis $\mathbf{v}$ in the inertial reference frame. Further the axis may be defined with the unit vector of the constraint coordinate system of the master body

$$\mathbf{A}^m \bar{\mathbf{A}}^m \bar{\bar{\mathbf{v}}}^m \cdot \mathbf{A}^m \bar{\boldsymbol{\omega}}^m + \Delta\boldsymbol{\omega}^p = \mathbf{A}^m \bar{\mathbf{A}}^m \bar{\bar{\mathbf{v}}}^m \cdot \mathbf{A}^s \bar{\boldsymbol{\omega}}^s, \tag{4.99}$$

$$\mathbf{A}^m \bar{\mathbf{A}}^m \bar{\bar{\mathbf{v}}}^m \cdot \mathbf{A}^m \bar{\mathbf{G}}^m \dot{\boldsymbol{\theta}}^m + \Delta\boldsymbol{\omega}^p = \mathbf{A}^m \bar{\mathbf{A}}^m \bar{\bar{\mathbf{v}}}^m \cdot \mathbf{A}^s \bar{\mathbf{G}}^s \dot{\boldsymbol{\theta}}^s, \tag{4.100}$$

$$\left(\bar{\mathbf{A}}^m\right)^T \left(\mathbf{A}^m\right)^T \mathbf{G}^s \dot{\boldsymbol{\theta}}^s = \left(\bar{\mathbf{A}}^m\right)^T \bar{\mathbf{G}}^m \dot{\boldsymbol{\theta}}^m + \Delta\boldsymbol{\omega}^p. \tag{4.101}$$

The constraint equation is again derived by taking the derivative in time

$$\begin{aligned} \left(\bar{\mathbf{A}}^m\right)^T \left(\mathbf{A}^m\right)^T \mathbf{G}^s \ddot{\boldsymbol{\theta}}^s + \frac{d}{dt}\left(\left(\bar{\mathbf{A}}^m\right)^T \left(\mathbf{A}^m\right)^T \mathbf{G}^s\right) \dot{\boldsymbol{\theta}}^s \\ = \left(\bar{\mathbf{A}}^m\right)^T \bar{\mathbf{G}}^m \ddot{\boldsymbol{\theta}}^m + \left(\bar{\mathbf{A}}^m\right)^T \dot{\bar{\mathbf{G}}}^m \dot{\boldsymbol{\theta}}^m + \Delta\boldsymbol{\alpha}^p, \end{aligned} \tag{4.102}$$

$$\begin{aligned} &\left(\bar{\mathbf{A}}^m\right)^T \left(\mathbf{A}^m\right)^T \mathbf{G}^s \ddot{\boldsymbol{\theta}}^s + \mathbf{Q}_\theta^s \\ &\qquad = \left(\bar{\mathbf{A}}^m\right)^T \bar{\mathbf{G}}^m \ddot{\boldsymbol{\theta}}^m + \mathbf{Q}_\theta^m + \Delta\boldsymbol{\alpha}^p \quad with \\ &\qquad \mathbf{Q}_\theta^s = \left(\bar{\mathbf{A}}^m\right)^T \left(\dot{\mathbf{A}}^m\right)^T \mathbf{G}^s \dot{\boldsymbol{\theta}}^s = \left(\bar{\mathbf{A}}^m\right)^T \left(\tilde{\bar{\boldsymbol{\omega}}}^m\right)^T \left(\mathbf{A}^m\right)^T \mathbf{G}^s \dot{\boldsymbol{\theta}}^s \\ &\qquad \mathbf{Q}_\theta^m = \mathbf{0}. \end{aligned} \tag{4.103}$$

Combining the constraint equation of the translational and rotational degrees of freedom between the master and slave body results in the final definition of the relative constraint equation

$$\begin{bmatrix} \mathbf{I} & -\mathbf{A}^s \tilde{\bar{\mathbf{u}}}^s \bar{\mathbf{G}}^s & -\mathbf{I} & +\mathbf{A}^m \tilde{\bar{\mathbf{u}}}^m \bar{\mathbf{G}}^m \\ \mathbf{0} & \left(\bar{\mathbf{A}}^m\right)^T \left(\mathbf{A}^m\right)^T \mathbf{G}^s & \mathbf{0} & -\left(\bar{\mathbf{A}}^m\right)^T \bar{\mathbf{G}}^m \end{bmatrix} \begin{bmatrix} \ddot{\mathbf{R}}^s \\ \ddot{\boldsymbol{\theta}}^s \\ \ddot{\mathbf{R}}^m \\ \ddot{\boldsymbol{\theta}}^m \end{bmatrix} = \begin{bmatrix} \mathbf{Q}_r^m - \mathbf{Q}_r^s \\ \mathbf{0} - \mathbf{Q}_\theta^s \end{bmatrix} + \begin{bmatrix} \Delta\ddot{\mathbf{r}}^{pres} \\ \Delta\boldsymbol{\alpha}^{pres} \end{bmatrix}. \tag{4.104}$$

4.4.3 Constraint controller

The inertial and relative constraints may be controlled via target translational and rotational accelerations as presented in the preceding sections. The accelerations are derived from user-prescribed position and orientation paths. This feature is used to prescribe dynamic control deflections in aircraft flight dynamics simulations. The derivation of the acceleration based on the prescribed paths is discussed in section 4.7. It assumes that the state of the acceleration, position and orientation is known at the current time step. This holds true for rigid bodies as the state is defined by the degrees of freedom of the rigid body. However, this assumption is not valid for relative constraints and must be derived from the states of the constraint bodies. The derivation of the constraint state of relative constraints is presented in this section. The relative position of the constraint coordinate systems is easily defined via the material point definition

$$\Delta\mathbf{r} = \mathbf{R}^s + \mathbf{A}^s \bar{\mathbf{u}}^s - \mathbf{R}^m - \mathbf{A}^m \bar{\mathbf{u}}^m, \tag{4.105}$$

$$\Delta\dot{\mathbf{r}} = \dot{\mathbf{R}}^s - \mathbf{A}^s\tilde{\mathbf{u}}^s\bar{\mathbf{G}}^s\dot{\boldsymbol{\theta}}^s - \dot{\mathbf{R}}^m + \mathbf{A}^m\tilde{\mathbf{u}}^m\bar{\mathbf{G}}^m\dot{\boldsymbol{\theta}}^m \tag{4.106}$$

and

$$\Delta\ddot{\mathbf{r}} = \left(\ddot{\mathbf{R}}^s - \mathbf{A}^s\tilde{\mathbf{u}}^s\bar{\mathbf{G}}^s\ddot{\boldsymbol{\theta}}^s - \mathbf{A}^s\tilde{\boldsymbol{\omega}}^s\tilde{\mathbf{u}}^s\bar{\mathbf{G}}^s\dot{\boldsymbol{\theta}}^s\right) - \left(\ddot{\mathbf{R}}^m - \mathbf{A}^m\tilde{\mathbf{u}}^m\bar{\mathbf{G}}^m\ddot{\boldsymbol{\theta}}^m - \mathbf{A}^m\tilde{\boldsymbol{\omega}}^m\tilde{\mathbf{u}}^m\bar{\mathbf{G}}^m\dot{\boldsymbol{\theta}}^m\right) \tag{4.107}$$

The orientation of the constraint coordinate systems may be expressed via the Euler identity

$$\boldsymbol{\theta}^{c_s} = \mathbf{H}^{c_m}\Delta\boldsymbol{\theta}, \tag{4.108}$$

as written in Shabana (2020), with

$$\mathbf{H}^{c_m} = \begin{bmatrix} \theta_0^{c_m} & -\theta_1^{c_m} & -\theta_2^{c_m} & -\theta_3^{c_m} \\ \theta_1^{c_m} & \theta_0^{c_m} & -\theta_3^{c_m} & \theta_2^{c_m} \\ \theta_2^{c_m} & \theta_3^{c_m} & \theta_0^{c_m} & -\theta_1^{c_m} \\ \theta_3^{c_m} & -\theta_2^{c_m} & \theta_1^{c_m} & \theta_0^{c_m} \end{bmatrix}. \tag{4.109}$$

Equally the orientation of the constraint coordinate systems in the inertial reference system may be defined by

$$\boldsymbol{\theta}^{c_s/c_m} = \mathbf{H}^{s/m}\bar{\boldsymbol{\theta}}^{c_s/c_m}, \tag{4.110}$$

where $\mathbf{H}^{s/m}$ is the above transformation matrix based on the master or slave body.
The relative velocity of the constraint coordinate systems is given by the time derivative of equation (4.108)

$$\dot{\boldsymbol{\theta}}^{c_s} = \dot{\mathbf{H}}^{c_m}\Delta\boldsymbol{\theta} + \mathbf{H}^{c_m}\Delta\dot{\boldsymbol{\theta}}, \tag{4.111}$$

and

$$\dot{\boldsymbol{\theta}}^{c_s/c_m} = \dot{\mathbf{H}}^{s/m}\bar{\boldsymbol{\theta}}^{c_s/c_m}. \tag{4.112}$$

The acceleration state of the constraint is equally found by taking the temporal derivative again.

$$\ddot{\boldsymbol{\theta}}^{c_s} = \ddot{\mathbf{H}}^{c_m}\Delta\boldsymbol{\theta} + 2\dot{\mathbf{H}}^{c_m}\Delta\dot{\boldsymbol{\theta}} + \mathbf{H}^{c_m}\Delta\ddot{\boldsymbol{\theta}} \tag{4.113}$$

$$\ddot{\boldsymbol{\theta}}^{c_s/c_m} = \ddot{\mathbf{H}}^{s/m}\bar{\boldsymbol{\theta}}^{c_s/c_m}. \tag{4.114}$$

Given the transformation matrix identity $\mathbf{H}^T\mathbf{H} = \mathbf{I}$ the relative position, velocity and acceleration state of the constraint coordinate system may be defined as

$$\Delta\boldsymbol{\theta} = \left(\mathbf{H}^{c_m}\right)^T\boldsymbol{\theta}^{c_s}, \tag{4.115}$$

$$\Delta\dot{\boldsymbol{\theta}} = \left(\mathbf{H}^{c_m}\right)^T\left(\dot{\boldsymbol{\theta}}^{c_s} - \dot{\mathbf{H}}^{c_m}\Delta\boldsymbol{\theta}\right), \tag{4.116}$$

and

$$\Delta\ddot{\boldsymbol{\theta}} = \left(\mathbf{H}^{c_m}\right)^T\left(\ddot{\boldsymbol{\theta}}^{c_s} - \ddot{\mathbf{H}}^{c_m}\Delta\boldsymbol{\theta} - 2\dot{\mathbf{H}}^{c_m}\Delta\dot{\boldsymbol{\theta}}\right). \tag{4.117}$$

4.5 Newmark time integration

The translational and rotational coordinates of all bodies are a result of the integration of the accelerations in time. The accelerations are numerically integrated with the Newmark method, (Gavrea et al., 2005), which assumes a linear acceleration in the interval $[t_n, t_{n+1}] = [t, t + \Delta t]$ which is given by

$$\ddot{\mathbf{q}}(h) = \frac{\Delta t - h}{\Delta t}\ddot{\mathbf{q}}_n + \frac{h}{\Delta t}\ddot{\mathbf{q}}_{n+1}. \tag{4.118}$$

Vector $\mathbf{q}$ is defined by the translational and rotational degrees of freedom

$$\mathbf{q} = \begin{bmatrix} \mathbf{R} \\ \boldsymbol{\theta} \end{bmatrix}. \tag{4.119}$$

The position and velocity within the integration interval are given by the Newmark equations which assume a linear acceleration in the interval $[t_n, t_n + h]$

$$\mathbf{q}(h) = \mathbf{q}_n + h\dot{\mathbf{q}}_n + \frac{h^2}{2}[(1 - 2\beta)\ddot{\mathbf{q}}_n + 2\beta\ddot{\mathbf{q}}(h)], \tag{4.120}$$

and

$$\dot{\mathbf{q}}(h) = \dot{\mathbf{q}}_n + h[(1 - \gamma)\ddot{\mathbf{q}}_n + \gamma\ddot{\mathbf{q}}(h)], \tag{4.121}$$

with $h \in [0, \Delta t]$. The equations show that the position and velocity of the bodies in the interval $[t, t + \Delta t]$ are a function of the position, velocity and acceleration at t and the acceleration at $t + \Delta t$ only. The coefficients of the scheme must satisfy the stability criteria

$$\gamma \geq 0.5, \qquad \beta \geq \frac{(\gamma + 0.5)^2}{4} \tag{4.122}$$

As discussed in Gavrea et al. (2005), the coefficient set $\gamma = 0.5$ and $\beta = 0.25$ results in a second-order scheme with low dissipation. Coefficients $\gamma = 0.75$ and $\beta = 0.390625$ result in a first-order accurate scheme. The low dissipation second order accurate coefficients $\gamma = 0.5$ and $\beta = 0.25$ are implemented in the present code.

4.6 Solution algorithm

An iterative scheme is used to solve the implicit non-linear system of equations for the unknown acceleration $\ddot{\mathbf{q}}^{t+1}$ and the Lagrange multipliers $\boldsymbol{\lambda}$. The iterative scheme combines the equations of motion with the Newmark integration method to obtain the acceleration, velocity and position of the rigid body at time $t + 1$. Assuming that the changes in the degrees of freedom over the time step Δt are small, the acceleration of the body at time step $t + 1$ may be approximated via

$$\begin{bmatrix} \mathbf{M}^i & \left(\mathbf{C}_q^T\right)^i \\ \mathbf{C}_q^i & \mathbf{0} \end{bmatrix} \begin{bmatrix} \ddot{\mathbf{q}}^{t+1} \\ \boldsymbol{\lambda} \end{bmatrix} = \begin{bmatrix} \mathbf{Q}_e^{t+1} + \mathbf{Q}_v^i \\ \mathbf{Q}_c \end{bmatrix}, \tag{4.123}$$

where index i denotes a solution between the solution at time t and $t + 1$. The resulting linear system is easily solved for the acceleration of the rigid body at time $t + 1$. The

result is used in combination with the Newmark integration scheme to obtain the position of the body at time $t+1$ via

$$\mathbf{q}^{t+1} = \mathbf{q}^t + \Delta t \dot{\mathbf{q}}^t + \frac{\Delta t^2}{2}\left[(1-2\beta)\,\ddot{\mathbf{q}}^t + 2\beta \ddot{\mathbf{q}}^{t+1}\right], \tag{4.124}$$

and

$$\dot{\mathbf{q}}^{t+1} = \dot{\mathbf{q}}^t + \Delta t\left[(1-\gamma)\,\ddot{\mathbf{q}}^t + \gamma \ddot{\mathbf{q}}^{t+1}\right]. \tag{4.125}$$

The solution of the position and velocity are used to redefine the intermediate solution via the relaxation scheme

$$\begin{aligned} \mathbf{q}^{i+1} &= (1-\tau)\mathbf{q}^i + \tau \mathbf{q}^{t+1}, \\ \dot{\mathbf{q}}^{i+1} &= (1-\tau)\dot{\mathbf{q}}^i + \tau \dot{\mathbf{q}}^{t+1}. \end{aligned} \tag{4.126}$$

The solution procedure may be summarized in the following steps:

1. Set the initial linearized solution $\mathbf{q}^i$ to the current solution $\mathbf{q}^t$.
2. Solve the linearized equations of motion to obtain the acceleration at $t+1$.
3. Compute the position and velocity of the rigid body at time $t+1$ using the Newmark integration method.
4. Update the linearized solution using the relaxation scheme.
5. Redo steps (1)-(4) until the solution converges. Convergence is determined by the residual of the acceleration at time $t+1$.

4.7 Prescribed path implementation

Prescribed paths are given as a set of translational and rotational coordinates versus time instances. The definition results in a linearization of the body motion and consequently into non-continuous body velocities and accelerations. An inverse problem has been implemented into the present solver which derives an acceleration profile based on the prescribed path which results in a continuous acceleration profile and smooth velocity and position profiles. The solution of the inverse problem is presented in this section.
The interpolation of the path profile is based on the following concept. Given a current position, velocity and acceleration $\mathbf{q}_n, \dot{\mathbf{q}}_n, \ddot{\mathbf{q}}_n$ find the acceleration of the body at $t+\Delta t$ and $t+2\Delta t$ with a given target position and velocity at $t+2\Delta t$. The target position and velocity are derived from the prescribed path.
The derivation of the solution is started from the definition of the position and velocity at $t+2\Delta t$

$$\mathbf{q}_{n+2} = \mathbf{q}_{n+1} + \Delta t \dot{\mathbf{q}}_{n+1} + \frac{\Delta t^2}{2}[(1-2\beta)\ddot{\mathbf{q}}_{n+1} + 2\beta \ddot{\mathbf{q}}_{n+2}] \tag{4.127}$$

and

$$\dot{\mathbf{q}}_{n+2} = \dot{\mathbf{q}}_{n+1} + \Delta t[(1-\gamma)\ddot{\mathbf{q}}_{n+1} + \gamma \ddot{\mathbf{q}}_{n+2}]. \tag{4.128}$$

Position and velocity terms at $t + \Delta t$ are replaced with Eq. (4.120) and Eq. (4.121). The resulting equations yield the position and velocity at $t + 2\Delta t$ as a function of the current position and the accelerations at $t + \Delta t$ and $t + 2\Delta t$

$$\begin{aligned}\mathbf{q}_{n+2} = \mathbf{q}_n + \Delta t\dot{\mathbf{q}}_n + \frac{\Delta t^2}{2}[(1-2\beta)\ddot{\mathbf{q}}_n + 2\beta\ddot{\mathbf{q}}_{n+1}] \\ + \Delta t(\dot{\mathbf{q}}_n + \Delta t[(1-\gamma)\ddot{\mathbf{q}}_n + \gamma\ddot{\mathbf{q}}_{n+1}]) + \frac{\Delta t^2}{2}[(1-2\beta)\ddot{\mathbf{q}}_{n+1} + 2\beta\ddot{\mathbf{q}}_{n+2}]\end{aligned} \tag{4.129}$$

and

$$\dot{\mathbf{q}}_{n+2} = \dot{\mathbf{q}}_n + \Delta t[(1-\gamma)\ddot{\mathbf{q}}_n + \gamma\ddot{\mathbf{q}}_{n+1}] + \Delta t[(1-\gamma)\ddot{\mathbf{q}}_{n+1} + \gamma\ddot{\mathbf{q}}_{n+2}]. \tag{4.130}$$

The following constants are defined to simplify the equations

$$\begin{aligned} c_0 &= \Delta t, \\ c_1 &= 0.5\Delta t^2(1-2\beta), \\ c_2 &= \Delta t^2\beta \end{aligned} \tag{4.131}$$

and

$$\begin{aligned} d_0 &= \Delta t(1-\gamma), \\ d_1 &= \Delta t\gamma. \end{aligned} \tag{4.132}$$

Substitution of the defined constants into the equations results in

$$\mathbf{q}_{n+2} = \mathbf{q}_n + 2c_0\dot{\mathbf{q}}_n + (c_1 + c_0 \cdot d_0)\ddot{\mathbf{q}}_n + (c_2 + c_0 \cdot d_1 + c_1)\ddot{\mathbf{q}}_{n+1} + c_2\ddot{\mathbf{q}}_{n+2}, \tag{4.133}$$

and

$$\dot{\mathbf{q}}_{n+2} = \dot{\mathbf{q}}_n + d_0\ddot{\mathbf{q}}_n + (d_0 + d_1)\ddot{\mathbf{q}}_{n+1} + d_1\ddot{\mathbf{q}}_{n+2}. \tag{4.134}$$

The equations are combined into a system of equations

$$\begin{bmatrix}\mathbf{q}_{n+2} \\ \dot{\mathbf{q}}_{n+2}\end{bmatrix} - \begin{bmatrix}1 & 2c_0 & c_1 + c_0 \cdot d_0 \\ 0 & 1 & d_0\end{bmatrix}\begin{bmatrix}\mathbf{q}_n \\ \dot{\mathbf{q}}_n \\ \ddot{\mathbf{q}}_n\end{bmatrix} = \begin{bmatrix}c_2 + c_0 \cdot d_1 + c_1 & c_2 \\ d_0 + d_1 & d_1\end{bmatrix}\begin{bmatrix}\ddot{\mathbf{q}}_{n+1} \\ \ddot{\mathbf{q}}_{n+2}\end{bmatrix}. \tag{4.135}$$

Known values are gathered on the left hand side of the equation and the unknown acclerations are gathered on the right hand side. The position and velocity at $t + 2\Delta t$ are defined by the prescribed path.The position $\mathbf{q}_{n+2}$ is linearly interpolated in the path data. The velocity at $t + 2\Delta t$ follows a linear approximation based on the positions at $t + \Delta t$ and $t + 2\Delta t$ as defined by

$$\dot{\mathbf{q}}_{n+2} = \frac{1}{\Delta t}(\mathbf{q}_{n+2} - \mathbf{q}_{n+1}) \tag{4.136}$$

The acceleration solution of the system of equations is used in combination with the Newmark time integration described in the previous section to define the position and velocity of the body in the interval $[t, t + \Delta t]$.

Chapter 5

Verification of the hybrid ghost-cell method

Two verification tests were conducted for the hybrid ghost-cell method to assess the effect of the hybrid-cell treatment discussed in section 3.6 on the numerical solution of moving geometries. The tests consist of a low Reynolds moving cylinder and a high Reynolds NACA0012 airfoil with pitch-up motion. The assessment of the hybrid-cell treatment was performed on integral forces and qualitative flow field assessments. An assessment of the hybrid ghost-cell method with static geometries was performed prior to the presented results to ensure that the treatment is not detrimental to the numerical results of the solver. The assessment of the static geometries was done for low and high Reynolds number flows. The results of the static geometries are not presented in this thesis.

5.1 Transverse oscillating cylinder

A verification test for the hybrid ghost-cell method was presented in Luo et al. (2012) who discussed hybrid-cell treatment for a ghost-cell method framework in an incompressible flow solver. The test features a circular cylinder which is oscillating either in-line with the flow direction or transverse to the flow direction. The effect of the hybrid-cell treatment is illustrated with the drag coefficient of the cylinder. The transverse version of the test case was used for the verification of the presented hybrid ghost-cell method. The simulation setup and results are discussed in the following section.

5.1.1 Simulation setup

The numerical domain of the simulation is illustrated in figure 5.1. The cylinder, with diameter d, is located in a square domain with dimensions $4d \times 4d$. Note, the test case is only used to assess the differences in the cylinder drag force with and without hybrid-cell

treatment. A small domain is therefore used for the test case to reduce the computational cost of the simulation. The motion of the cylinder is given by

$$u = u_c sin\left(2\pi f t\right). \tag{5.1}$$

The Reynolds number defined with the inflow velocity U and cylinder diameter d is equal to $Re = \frac{Ud}{\nu} = 100$. The amplitude of the cylinder velocity u_c is given by

$$u_c/U = 0.1\pi. \tag{5.2}$$

The frequency of the cylinder motion satisfies the equality

$$\frac{fd}{U} = 0.2. \tag{5.3}$$

Integrating equation (5.1) and using relations (5.2) and (5.3) yields the position of the cylinder in terms of the free stream velocity U and diameter d.

$$y = \frac{1}{4} d \cdot cos\left(\frac{2}{5}\frac{\pi U}{d} t\right). \tag{5.4}$$

A parabolic inlet velocity profile with no-slip top and bottom wall boundary conditions and a zero gradient Neumann outflow boundary condition are used in Luo et al. (2012). Instead, a uniform inflow boundary condition and slip top and bottom wall boundary conditions are used in the presented case combined with the used zero gradient Neumann boundary condition at the outflow. A comparison between the numerical results of Luo et al. (2012) is therefore not possible. However, the simplified setup of the presented simulation should be sufficient to test the hybrid-cell treatment. The flow field is initialized with the free stream velocity U. A uniform mesh is used for the discretization of the domain with a cell density of 32 cells per diameter d. The cylinder drag force D is used to assess the effect of the hybrid-cell treatment. The drag force is presented in the non-dimensional form

$$C_D = \frac{2D}{\rho U^2 d}. \tag{5.5}$$

The time axis is non-dimensionalised with

$$t' = t\frac{U}{d}. \tag{5.6}$$

5.1.2 Results

The drag force of the transverse oscillating cylinder is shown in figure 5.2 and 5.3. Figure 5.2 shows the cylinder drag coefficient without hybrid-cell treatment, and figure 5.3 shows the cylinder drag coefficient with hybrid-cell treatment. Either plot shows an initial transient, where the drag coefficient oscillates with high amplitudes. These oscillations are induced by the initialization of the flow field and are not effected by the hybrid-cell treatment. The high oscillations disappear at approximately $t' = 5$ for both methods. After the initial transient the drag force oscillates with double the frequency of the cylinder motion $f' = \frac{1}{t'_{period}} = 0.4$. Oscillations of higher frequencies are visible in either result, but the hybrid-cell treatment significantly reduces the amplitudes of these high frequencies.

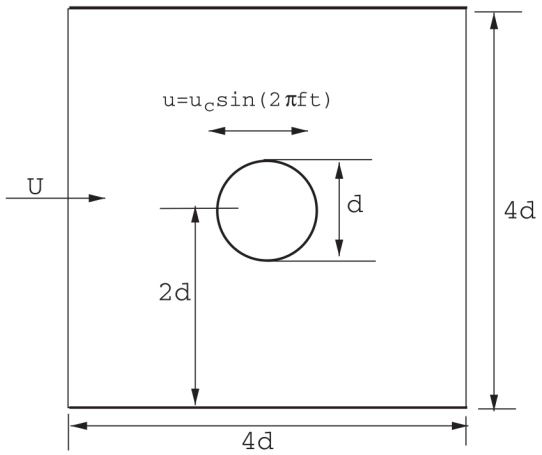

Figure 5.1: Schematic of an in-line oscillating cylinder in a channel, taken from (Luo et al., 2012).

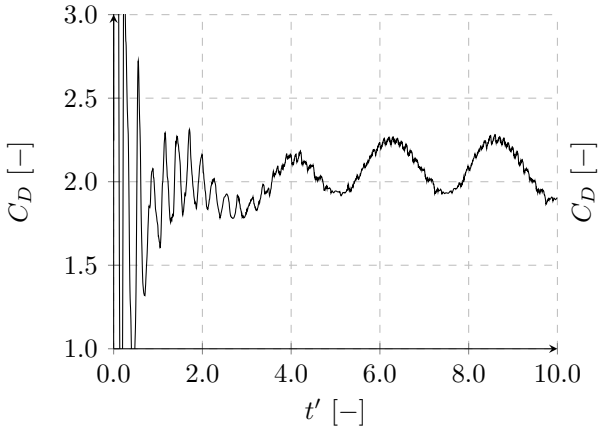

Figure 5.2: Numerical solution of the drag coefficient C_D of the transverse oscillating cylinder with no hybrid-treatment enabled.

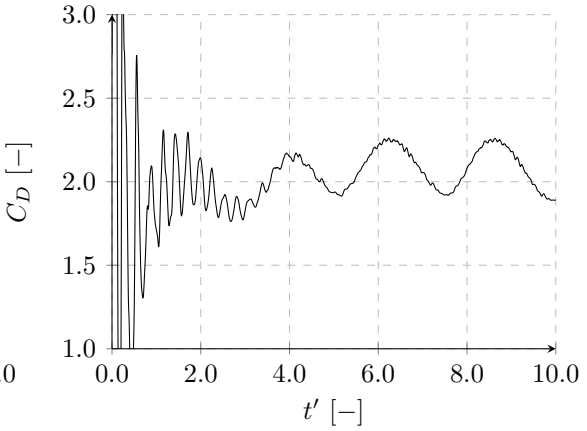

Figure 5.3: Numerical solution of the drag coefficient C_D of the transverse oscillating cylinder with hybrid-treatment enabled.

A Fast-Fourier transform is performed over one period of the cylinder oscillation in the interval $t' = [5.0, 10.0]$. The results of the Fourier transform of the two numerical results is shown in figure 5.4. The ghost-cell method and hybrid ghost-cell method predict identical force amplitudes for the frequencies associated with the motion of the cylinder $f' = 0.4$. The result indicates that the hybrid-cell treatment does not effect the solution of the low frequency scales in the laminar flow field. Differences are found at higher frequencies $f' > 10$, where the the hybrid-cell treatment suppresses the oscillations. The higher frequencies are associated with spurious numerical oscillations as these time scales corresponding to these frequencies should not be present in the laminar flow around the moving cylinder. An assessment of the Kolmogorov time scale $t_v = \left(\frac{\nu}{\epsilon}\right)^{\frac{1}{2}}$ with $\epsilon \sim \frac{U^3}{d}$ alone indicates the highest frequencies corresponding to the smallest hydrodynamic scales

in the flow field should not exceed $f'_v > 10$. This further underlines that the spurious oscillations found at frequencies above $f' > 10$ are associated with numerical effects and not physical flow features.

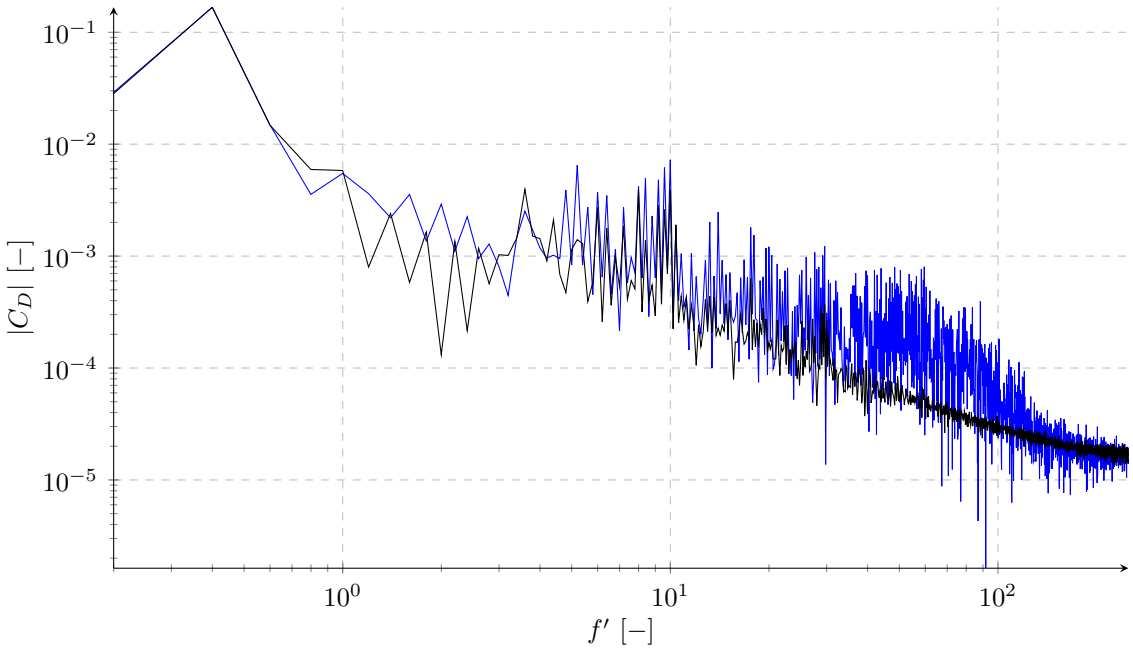

Figure 5.4: Fast-Fourier transform of the transverse oscillating cylinder over one period; (——) numerical results with not hybrid-cell treatment, (——) numerical results with hybrid-cell treatment.

5.2 Flow around NACA0012 airfoil with pitch up motion

The initial need for the hybrid ghost cell method was found in the simulation of the NACA0012 dynamic stall case. Spurious oscillations are common in in-compressible solvers with immersed boundary methods as discussed in Luo et al. (2012). They are less often reported in compressible solvers. The numerical results of the NACA0012 dynamic stall validation simulations are presented in chapter 8. In this section the numerical results of a simplified test case are presented. The test case was used to illustrate the force and flow field differences between the ghost-cell method with and without hybrid-cell treatment.

5.2.1 Simulation setup

The setup of the simulation was set based on the simulations of the NACA0012 dynamic stall case, 8. Some simplifications were implemented to reduce the computational cost of the simulation and to isolate the hybrid-cell treatment from other numerical methods in the present solver. The domain size was reduced from a width of $b = 3c$ to $b = c$ and the near-wall mesh resolution was decreased to $\Delta/c = 0.98 \cdot 10^{-3}$ by reducing the octree mesh refinement level by one. Inflow conditions were not changed for the test case. A no-slip

wall is used instead of the wall-modeled boundary condition to reduce the complexity of the numerics and focus the investigation on the hybrid-cell treatment. The NACA0012 airfoil in dynamic stall case, presented in chapter 8, follows a sinusoidal motion. The motion is simplified in the numerical verification test and plotted in figure 5.5. The time is given as the non-dimensional unit $t' = t\frac{U}{L}$. The motion is split into two parts, the airfoil remains at a constant pitch up angle of 5° for the first 8 time units. Afterwards, the pitch up angle is increased at a constant rate of 1° per time unit for the final 8 time units.

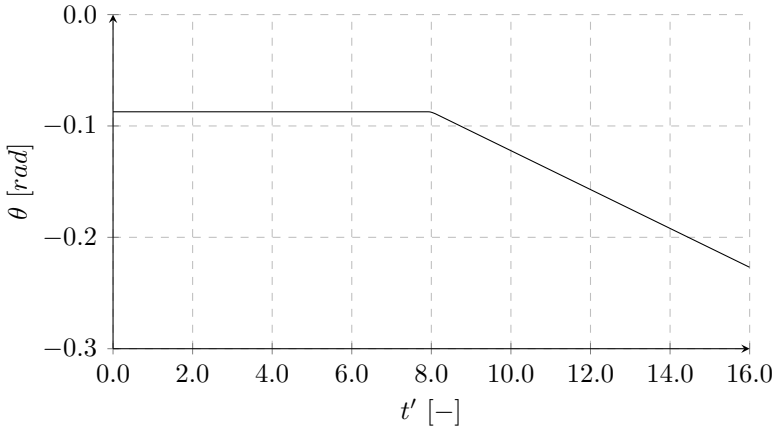

Figure 5.5: Prescribed pitch angle of the NACA0012 for the hybrid ghost-cell verification test.

5.2.2 Results

The effect of the hybrid ghost-cell method on the numerical solution of the flow field around the NACA0012 airfoil is again shown with a plot of the integral forces. In addition to the integral forces, plots of the flow field are shown around the NACA0012 airfoil to present the spurious oscillations that were found in the flow field prior to the implementation of the hybrid ghost-cell method.
The integral lift coefficient C_L of the airfoil is shown in figure 5.6 and 5.7. Figure 5.6 shows the lift coefficient of the NACA0012 airfoil versus time with no hybrid-cell treatment and figure 5.7 with hybrid-cell treatment enabled. Both plots show an initial transient in the lift coefficient characterized by oscillations with large amplitudes. The initial transient is again caused by the initialization of the flow field. The transient disappears at around $t' = 6$. The results show that the hybrid-cell treatment leads to a higher decay of the initial transient indicating an increased dissipation at the immersed boundary. The solution of the lift coefficient converges to a quasi static value before the pitch up motion is initiated at $t' = 8.0$. The lift coefficient during the pitch-up motion $t' > 8.0$ is characterized by a sudden jump in the lift coefficient $\Delta C_L = 0.1$ around $t' = 8.0$ caused by the sudden increase in the rotational velocity of the NACA0012 airfoil around the quarter chord axis. The initial jump in the lift coefficient is followed by a quasi linear increase in the lift coefficient until the end of the simulation at $t' = 16.0$. Oscillations are found around the linear trend with both immersed boundaries. These oscillations are associated

with spurious oscillations and turbulent fluctuations in the boundary layer of the airfoil. The simulations again show that the ghost-cell method without hybrid-cell treatment has significantly higher oscillations in the lift coefficient once the geometry moves. From the lift coefficient alone it is not possible to assess whether the differences in the oscillations are caused by differences in the turbulent boundary layer flow alone or differences in the spurious oscillations.

A qualitative assessment of the flow field was performed to assess whether the oscillations are associated with flow features in the density/pressure and velocity field. Slices of the velocity magnitude solution field at $t' = 4$ and $t' = 12$ are shown in figures 5.8, 5.10, 5.9 and 5.11. Figures 5.8 and 5.10 show the velocity field obtained with the ghost-cell method without hybrid-cell treatment at time $t' = 4$ and $t' = 12$, respectively. Figures 5.9 and 5.11 show the velocity field solution of the ghost-cell method with hybrid-cell treatment at time $t' = 4$ and $t' = 12$. Due to the chaotic characteristics of turbulent flow, the velocity show differences in the near-wall solution. However, the flow fields of the ghost-cell methods with and without hybrid-cell treatment do not show significant differences in the boundary layer thickness and turbulent scales. The author would like to emphasize that this is purely based on a qualitative assessment of the flow field.

Slices of the density solution field at $t' = 4$ and $t' = 12$ are shown in figures 5.12, 5.14, 5.13 and 5.15. Figures 5.12 and 5.14 show the velocity field solution of the ghost-cell method without hybrid-cell treatment at time $t' = 4$ and $t' = 12$ respectively. Figures 5.13 and 5.15 show the velocity field solution of the ghost-cell method with hybrid-cell treatment at time $t' = 4$ and $t' = 12$. The assessment of the density field at $t' = 4$ does not show significant differences in the solution. No spurious oscillations are found in the density field for either method in-line with expectations as the geometry is not moving at this point in time. Further the result indicates that the hybrid-cell treatment does not effect the numerical solution much on a qualitative level. The density solution at $t' = 12$ shows large oscillations in the flow field in the solution without hybrid-cell treatment. The oscillations are in the form of acoustic waves which originate primarily on the pressure side of the airfoil and travel into the far-field. The solution of the ghost-cell method with hybrid-cell treatment does not show any such oscillation in the flow field. The qualitative assessment of the density field thus indicates that a part of the oscillations in the lift coefficient of the airfoil is caused by spurious oscillations which are damped by the hybrid-cell treatment.

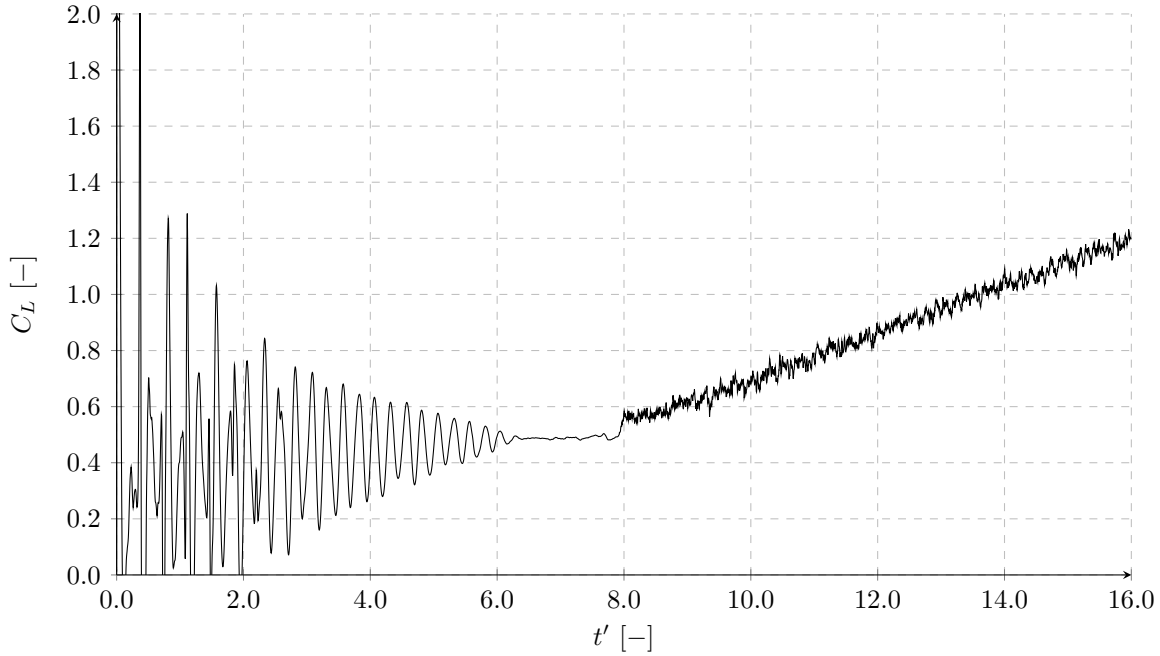

Figure 5.6: Numerical results of the NACA0012 lift coefficient C_L without hybrid-cell treatment.

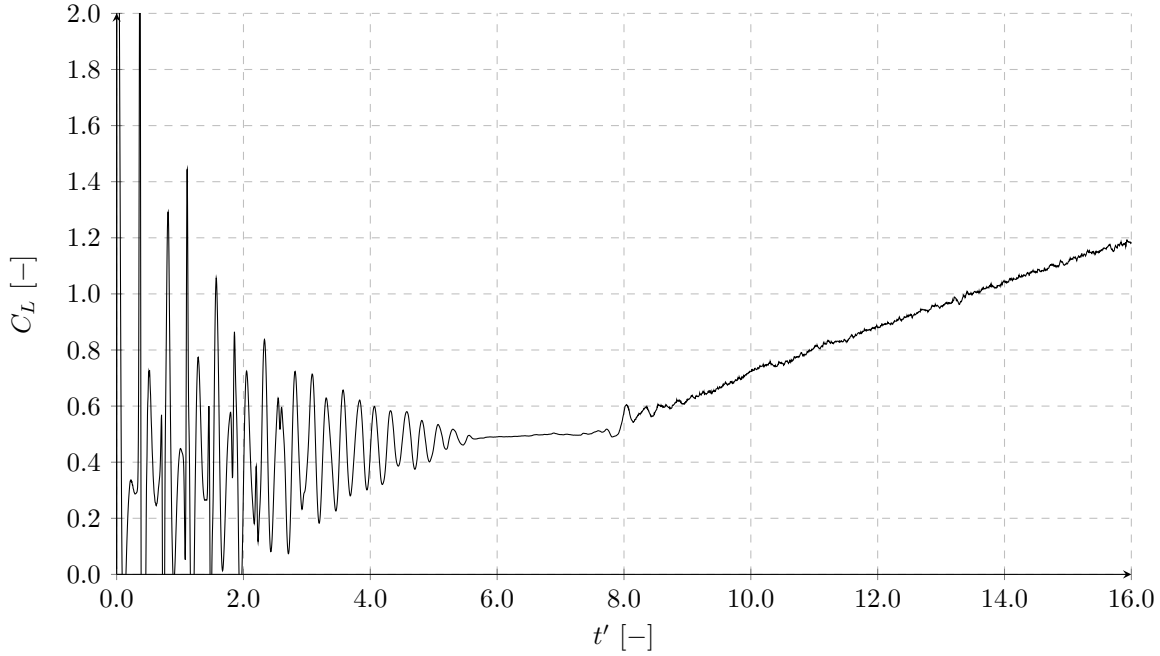

Figure 5.7: Numerical results of the NACA0012 lift coefficient C_L with hybrid-cell treatment.

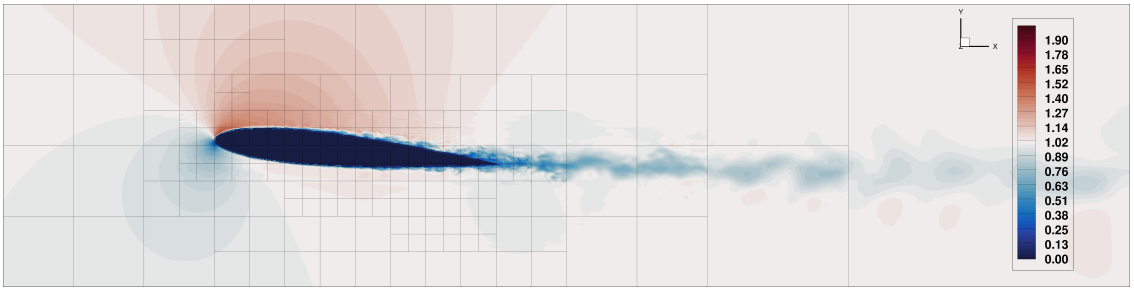

Figure 5.8: Ghost-cell method result of the instantaneous velocity magnitude field around the NACA0012 airfoil at $t' = 4$.

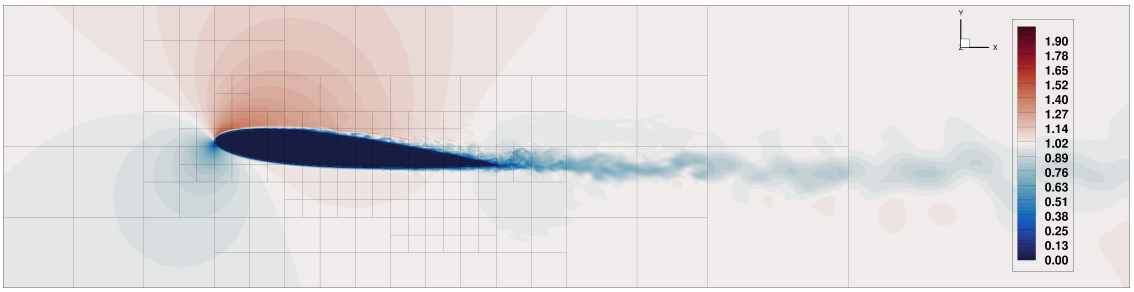

Figure 5.9: Hybrid ghost-cell method result of the instantaneous velocity magnitude field around the NACA0012 airfoil at $t' = 4$.

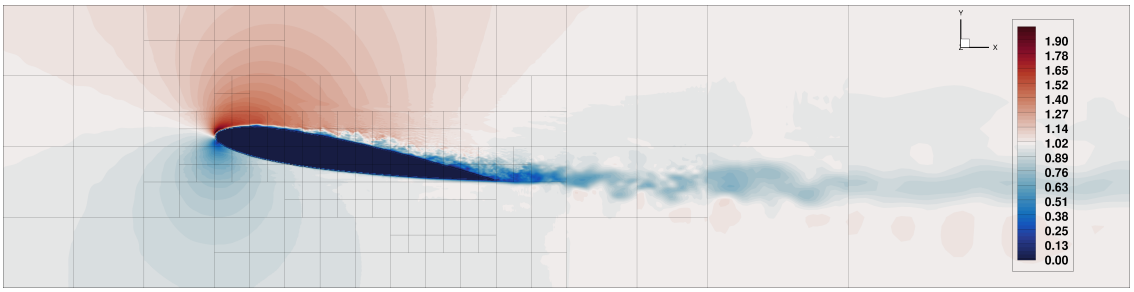

Figure 5.10: Ghost-cell method result of the instantaneous velocity magnitude field around the NACA0012 airfoil at $t' = 12$.

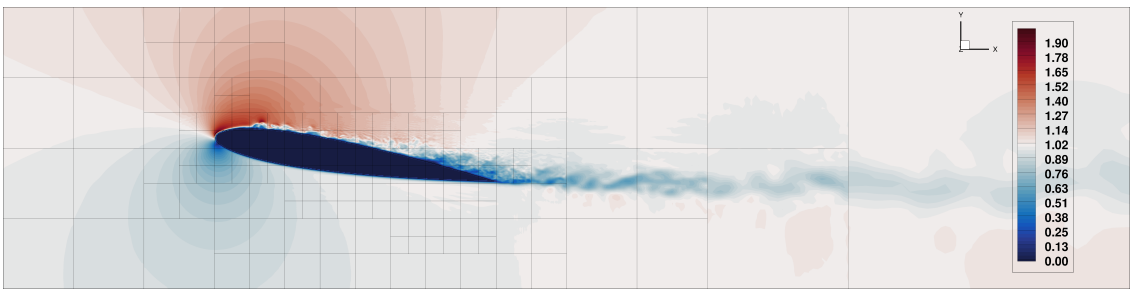

Figure 5.11: Hybrid ghost-cell method result of the instantaneous velocity magnitude field around the NACA0012 airfoil at $t' = 12$.

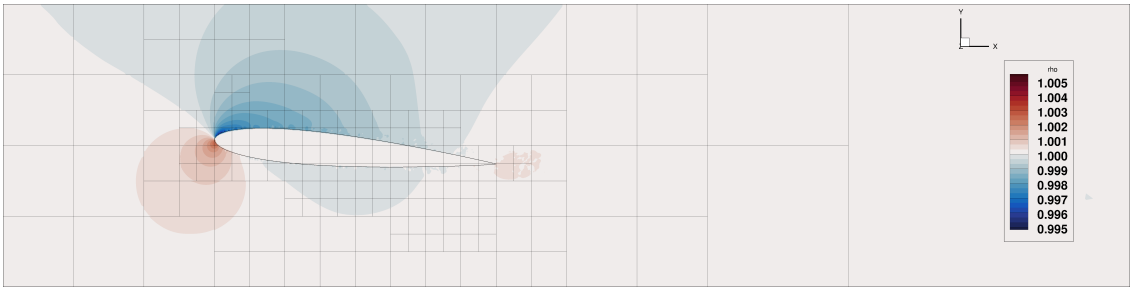

Figure 5.12: Ghost-cell method result of the instantaneous density field ρ around the NACA0012 airfoil at $t' = 4$.

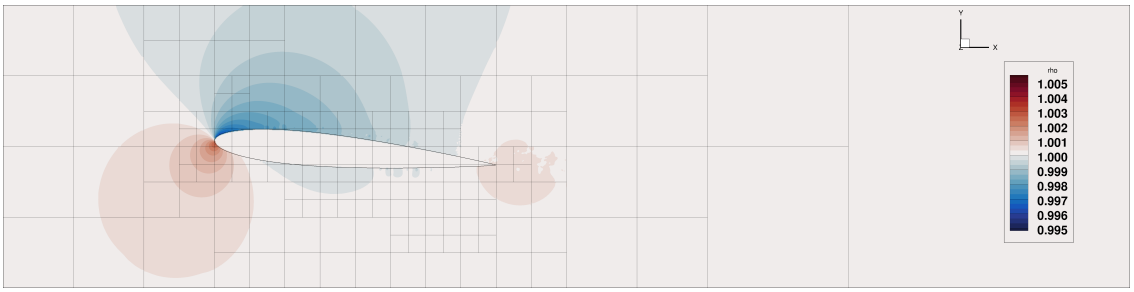

Figure 5.13: Hybrid ghost-cell method result of the instantaneous density field ρ around the NACA0012 airfoil at $t' = 4$.

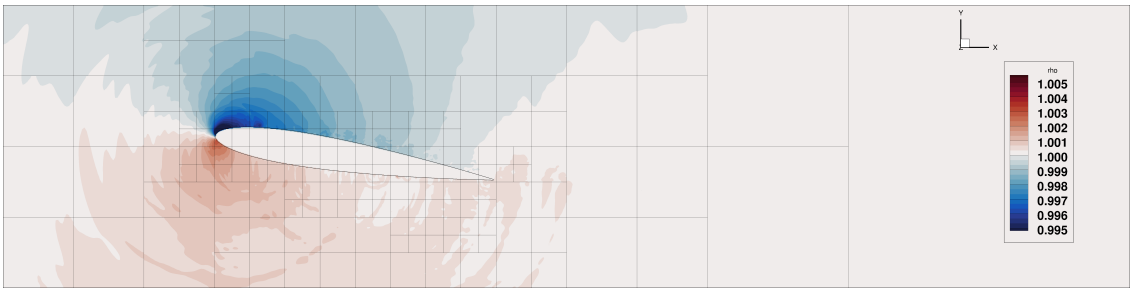

Figure 5.14: Ghost-cell method result of the instantaneous density field ρ around the NACA0012 airfoil at $t' = 12$.

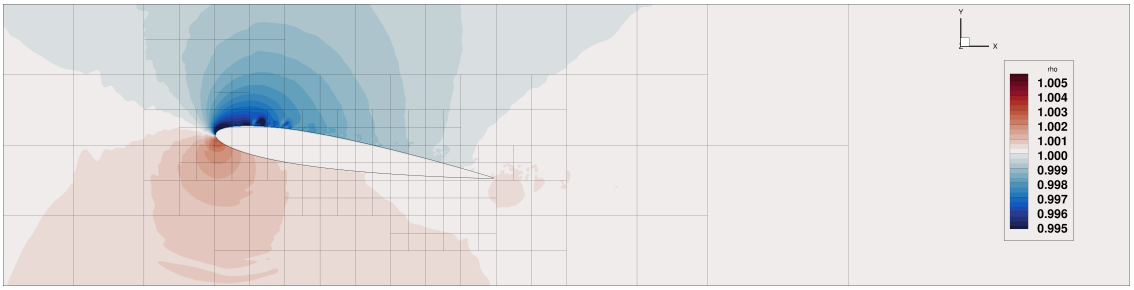

Figure 5.15: Hybrid ghost-cell method result of the instantaneous density field ρ around the NACA0012 airfoil at $t' = 12$.

5.3 Conclusion

Simulations of a transversely oscillating cylinder and a NACA0012 airfoil undergoing pitch up motion were presented in this chapter. The results of the transverse oscillating cylinder showed high oscillations in the flow field for the ghost-cell method without hybrid-cell treatment. The oscillations were associated with spurious numerical oscillations as the frequency associated with theses oscillations in the drag coefficient was above the maximum frequencies associated with the Kolmogorov time scale. The results of the flow case with the hybrid-cell treatment showed that the hybrid-cell treatment did not negatively effect the solution of the low frequencies in the transient drag coefficient of the cylinder but did significantly suppress the spurious high frequencies in the results. It is therefore concluded that the hybrid-cell treatment is a suitable method for the suppression of spurious oscillation in the present solver for moving geometries at low Reynolds numbers.
The results of the NACA0012 airfoil did show that the numerical solution of the flow field does not contain spurious oscillations when the airfoil is not moving. Oscillations were found in the pitch up motion which were associated with both turbulent fluctuations and spurious numerical oscillations. Again the ghost-cell method without hybrid-cell treatment had significantly higher amplitudes in the oscillations of the lift coefficient than the ghost-cell method with hybrid-cell treatment. A qualitative assessment was performed on the velocity magnitude and density field to associate the oscillations in the lift coefficient to flow features in the two fields. The assessment showed no significant differences in the boundary layer height and turbulent scales in the velocity field of the ghost-cell method and hybrid ghost-cell method. However, large differences were found in the solution of the density. While the solution was similar when the airfoil was not moving, large spurious oscillations in the form of acoustic waves were found in the density field once the airfoil started moving. It was concluded that these waves cause the significant increase in the amplitude of the lift coefficient oscillations with the ghost-cell method without hybrid-cell treatment. Based on the findings, it can be concluded that the hybrid ghost-cell method successfully suppresses spurious oscillation in high Reynolds number flow.
In conclusion the hybrid ghost-cell method developed in this thesis is suitable for the suppression of spurious oscillations for moving geometries in both low and high Reynolds number flows.

Chapter 6

Verification of the multi-body solver

Verification tests are performed with the developed rigid body solver. Multiple aspects of the rigid body solver are investigated with the verification tests. Simulations of a single pendulum are performed to analyze the order of accuracy of the Newmark time integration scheme and to compare the numerical results with the analytical solution of the single pendulum. Simulations of a double pendulum are performed to verify the implementation of the relative and absolute constraints and to investigate the conservation error in the system energy. The results of the single pendulum are shown in section 6.1. The results of the double pendulum are presented in section 6.2.

6.1 Single pendulum

Simulations of a single pendulum are performed. The results of the simulations are used to analyze the order of convergence of the Newmark time integration method, which is implemented in the present rigid body solver. The results are further compared to analytical results of a single pendulum. The single pendulum is illustrated in figure 6.1. The pendulum considered in the present simulations has a link length of $l = 1m$ and a mass of $m = 1kg$. The mass of the pendulum link is modeled as a point mass located at the end of the link. The angle of the pendulum link with respect to the inertial frame is defined by the angle θ_1. The pendulum is subjected to a gravitational acceleration of $g = \pi^2 m/s^2$. The analytical solution of the pendulum is derived in section 6.1.1. The numerical results of the single pendulum obtained with the present code are presented in section 6.1.1.

6.1.1 Analytical analysis

The motion of the pendulum, shown in figure 6.1, is described by the following equation of motion around the hinge point of the pendulum

$$l^2 m\ddot{\theta}_1 = -mglsin(\theta_1). \tag{6.1}$$

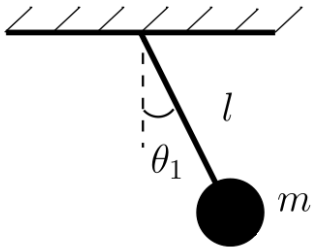

Figure 6.1: Illustration of a single pendulum, taken and modified from (Maiti et al., 2016).

The left hand side term describes the time derivative of the angular momentum of the pendulum, with l^2m equal to the angular mass moment of inertia of the pendulum around the hinge point of the pendulum. The right hand side term describes the restoring moment of the pendulum caused by the angular displacement and gravity. The equation of motion is simplified by assuming that the angle of the single pendulum remains small. Given this assumption, the $\sin(\theta_1)$ term is approximated by $\sin(\theta_1) \approx \theta_1$. The equation of motion is written as

$$\ddot{\theta}_1 + \frac{g}{l}\theta_1 = 0. \tag{6.2}$$

The solution of the linear second order ordinary differential equation is given by

$$\theta_1(t) = \theta_{1_0} \cos \omega t \quad with \quad \omega = \sqrt{\frac{g}{l}}. \tag{6.3}$$

θ_{1_0} is the initial angular displacement of the pendulum and ω is the natural frequency of the pendulum. Given the properties of the pendulum and the gravitational acceleration g, the natural frequency of the pendulum is equal to $\omega = \sqrt{\frac{g}{l}} = \pi$. The oscillation period of the pendulum T is equal to

$$T = 2\pi\sqrt{l/g} = 2s. \tag{6.4}$$

Numerical analysis

Next, the numerical solution of the single pendulum is presented. The simulations are performed with an initial pendulum displacement of $\theta_{1_0} = 1.0°$. Given the small initial displacement, the result should compare well to the derived analytical result. The link is modeled as a single rigid body with mass m and inertia terms $\mathbf{I}$. The inertia terms I_{xx}, I_{yy}, I_{zz} are set equal to $10^{-6} kgm^2$ in order to model the pendulum link as a point mass. The equations of motion of the single rigid body were presented in section 4.2. A coordinate system is added to the local reference frame of the rigid body at distance l from the center of gravity. The coordinate system is constrained with a fixation constraint to the inertial frame. The fixation constraint fixes all degrees of freedom except for the rotational degree of freedom around the out of plane axis of the pendulum. The constraint implementation of rigid bodies and the inertial frame of reference, used in the numerical simulations, is shown in section 4.4.1. Initial simulations were performed to assess the

order of convergence of the Nemark time integration scheme, 4.5. These simulations were performed over one oscillation period T. The numerical error is defined by

$$\epsilon_\theta = \sqrt{(\theta_1(t=T) - \theta_{1_0})^2}). \tag{6.5}$$

Simulations were performed with time step sizes in the range of $\Delta t = [0.00125s, 0.32s]$. The convergence plot is shown in figure 6.2. The numerical error is plotted against the number of solid time steps over one oscillation period $N_t = T/\Delta t$. First and second order convergence lines are added as reference to the plot. The convergence plot shows that the present code follows approximately the second order convergence trend line. This is in line with the Newmark time integration error for the Newmark coefficient $\beta = 0.25$ $\gamma = 0.5$ and verifies the correct implementation of the method.

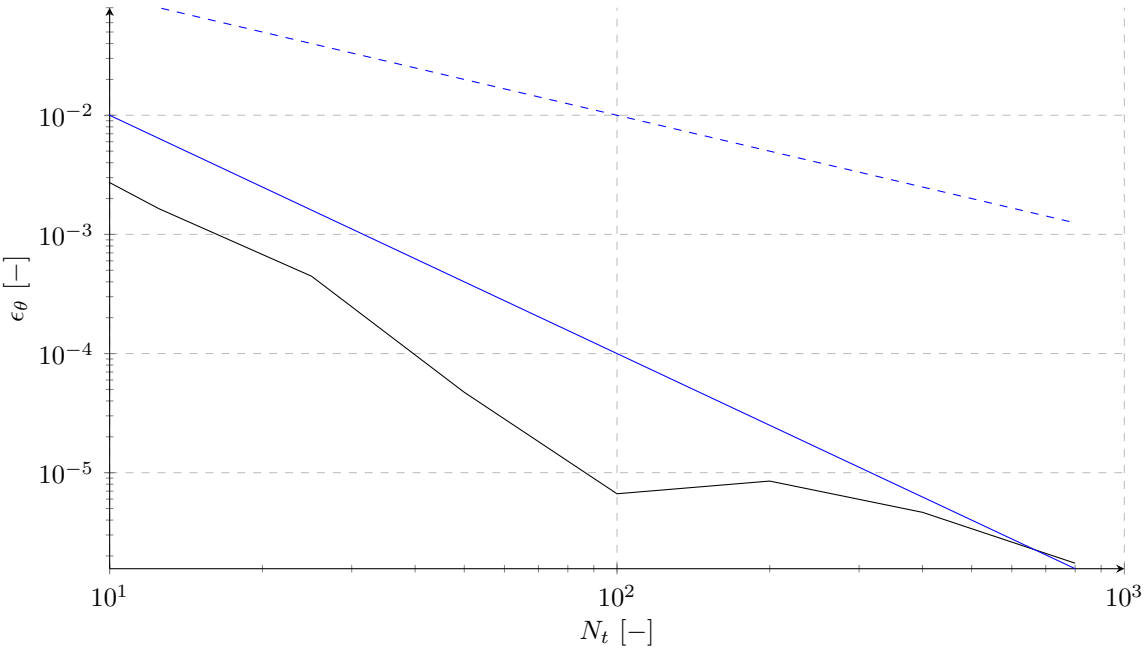

Figure 6.2: L2-norm error plot of the pendulum position after one time period; (——) solution of present code, (- - -) first order convergence reference, (——) second order convergence reference.

The pendulum displacement angle is plotted against time in figure 6.3. The trajectory of the pendulum is plotted over one oscillation period T. The analytical solution of the single pendulum is added as reference. The numerical simulation was performed with the lowest considered time step of $\Delta t = 0.00125s$. The plot shows an exact match between the numerical analytical solutions, verifying that the present solver correctly predicts the motion of a single pendulum.

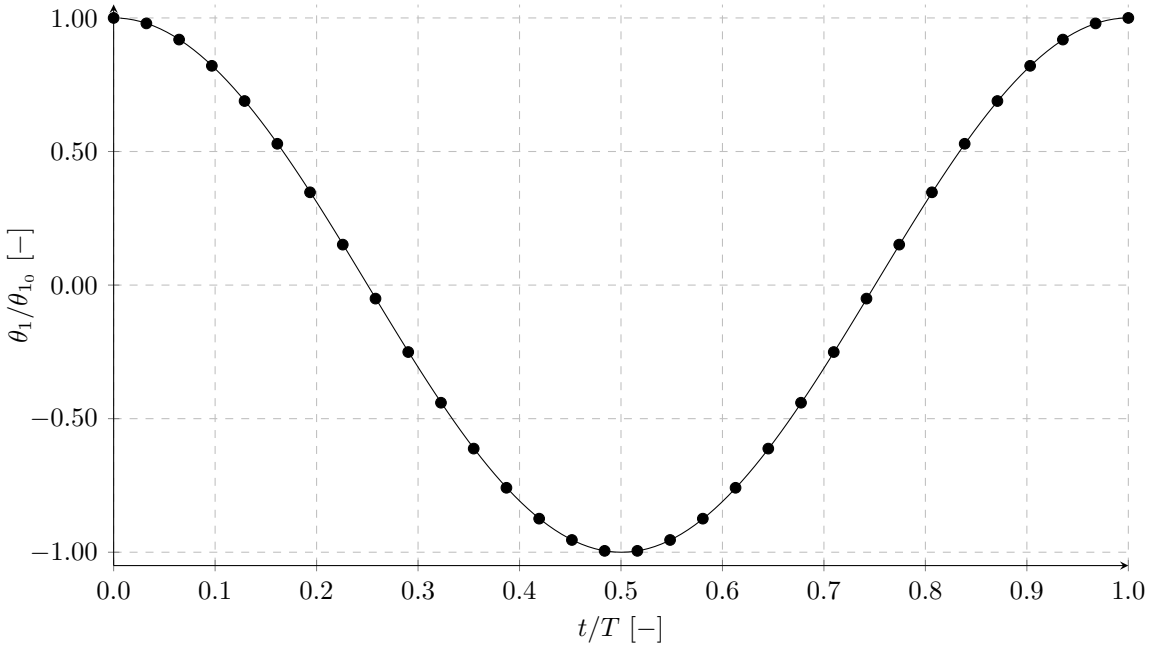

Figure 6.3: Plot of the pendulum angle θ_1 against time t; (——) solution of present code, (•) analytical solution.

6.2 Double pendulum

Simulations of a double pendulum were performed to verify the inertial and relative constraints. The double pendulum of the numerical simulation is shown in figure 6.4. The double pendulum consists out of two links. An equal length and mass is assigned to both links of the pendulum of $m = 1kg$ and $l = 1m$. A second degree of freedom is introduced into the system compared to the single pendulum considered in the previous section. The additional degree of freedom describes the angular displacement of the second link in the inertial frame of reference and is denoted as θ_2. Both links are modeled as point masses as done for the single pendulum simulations. The relative constraint implementation presented in section 4.4.2 is used to model the constrained between the two links of the pendulum.
The double pendulum is a primary example for chaotic systems (Maiti et al., 2016). The equations are non-integrable as infinitesimal changes to the initial conditions lead to significant differences in the dynamic response of the system. Therefore, convergence studies are only performed on the system energy and constraints. As regardless of the dynamic response of the system the energy should be conserved and the constraints should be satisfied. The simulations were performed over a total time of $t = 10s$. Results obtained during the simulations include plots of the two degrees of freedom and plots of the system energy. The initial condition of the system is defined by

$$\theta_{1_0} = \theta_{2_0} = 18.0°. \tag{6.6}$$

The presentation of the results is started with the convergence studies on the system energy and constraint violation. These studies are of interest as neither the constraints

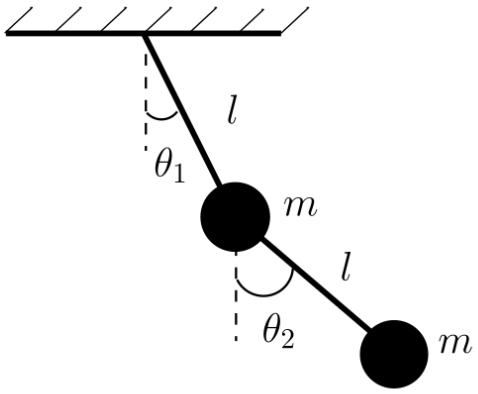

Figure 6.4: Illustration of a double pendulum, taken from and modified from (Maiti et al., 2016).

nor the system energy are conserved. The convergence analysis of the system shows the correlation between the numerical error in the system energy and constraints and the selected numerical time step. The system is simulated for a time period of $T = 10s$. The error in the system energy is defined by

$$\epsilon_E = \sqrt{(E_0 - E(t = T))^2}. \tag{6.7}$$

The constraint violation error is defined by the distance of the constraint coordinate systems Δx_i, where i indexes the three coordinate system axis $0, 1$ and 2. The error term is given by

$$\epsilon_c = \sqrt{\Delta x_0^2 + \Delta x_1^2 + \Delta x_2^2}. \tag{6.8}$$

The time step of the Newmark time integration was swept over a range of $\Delta t = [6.25 \cdot 10^{-4}s, 3.2 \cdot 10^{-1}s]$. The errors are plotted against the number of time integration steps $N_t = T/\Delta t$. The convergence plot of the system energy is plotted in figure 6.5. Trend lines of first order convergence and second order convergence characteristics are added as reference. The plot of the energy error indicates that the error converges with first order accuracy. This is expected as the energy term includes position and velocity terms. The integration of the velocity is only first order accurate with the selected Newmark time integration scheme. The error terms of the two hinge constraints is plotted in figure 6.6. The constraint of link 1 to the inertial reference frame is denoted as link 1 constraint. The relative constraint between link 1 and link 2 is denoted as link 2 constraint. The plot shows that the error of the constraint terms converges with first order accuracy.

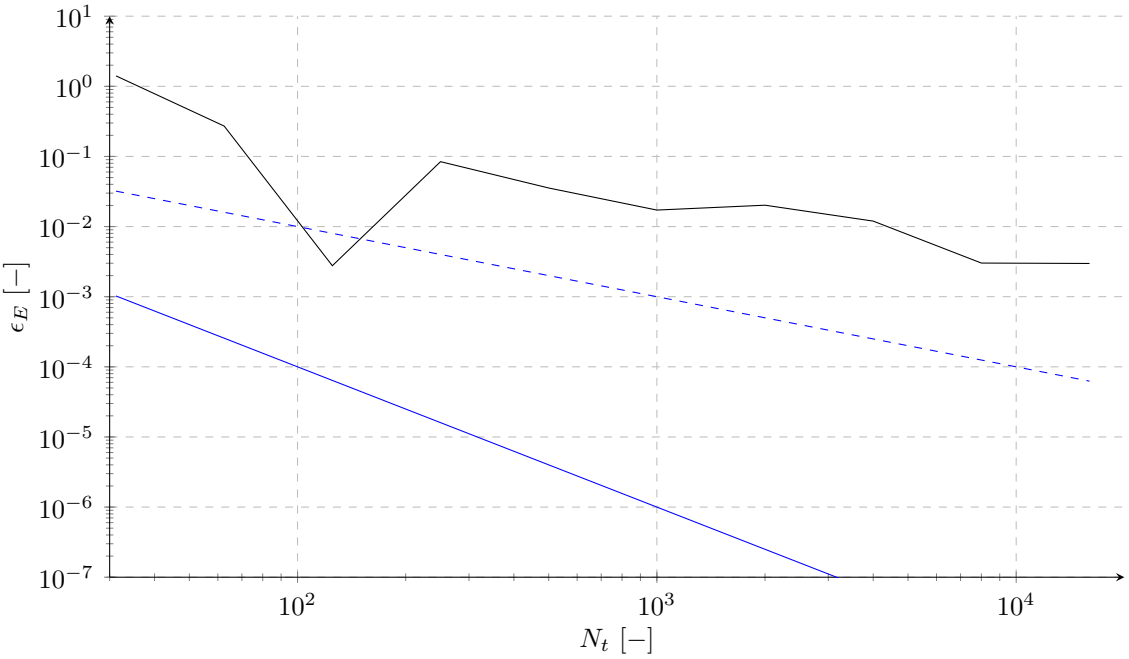

Figure 6.5: L2-norm error plot of the pendulum energy after a time period of $t = 10$; (——) solution of present code, (- - -) first order convergence reference, (——) second order convergence reference.

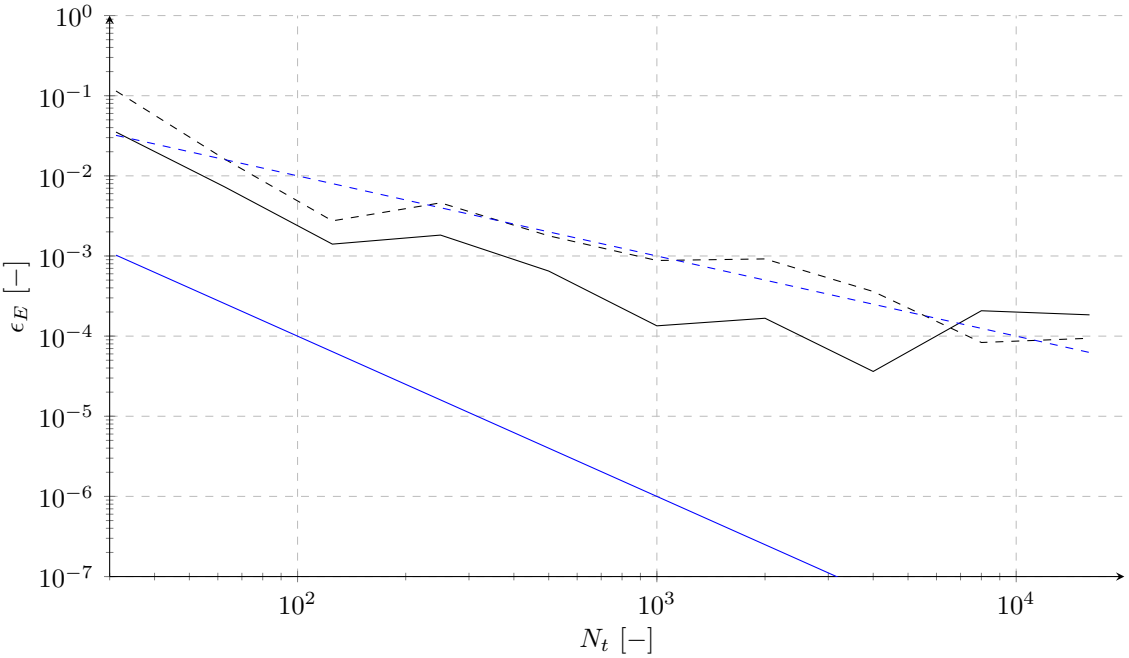

Figure 6.6: L2-norm error plot double pendulum constraints after a time period of $t = 10$; (——) link 1 constraint, (- - -) link 2 constraint, (- - -) first order convergence reference, (——) second order convergence reference.

The final simulation is performed with the smallest time step of $\Delta t = 6.25 \cdot 10^{-4}$. The simulation is performed over the time period T. The energy of the system is plotted versus time in figure 6.8. The plot clearly illustrates how the system energy is constant over time, while the energy of the two links is variable over the time period. Changes in the energy of the links is only achieved by transferring the kinetic and potential energy from one link to the other link. The simulation results further show that the energy of the second link is overall higher than the energy of the first link. This might only be true for the selected initial condition. The potential energy of link 2 is twice as high as the energy of link 1 in the initial conditions of the system. The angles of link 1 and link 2 over the time period T are plotted against each other in figure 6.7. The plot shows the quasi periodic but chaotic behavior of the pendulum motion.

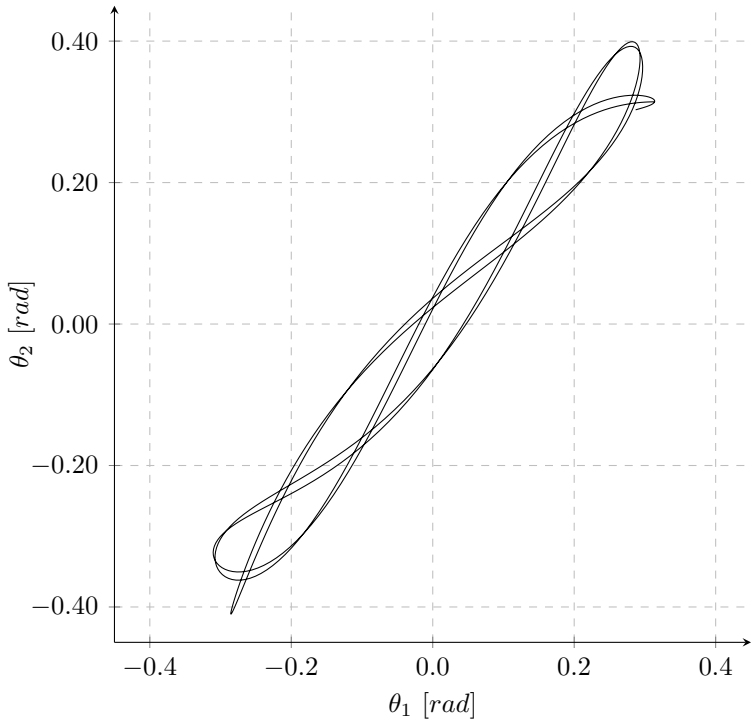

Figure 6.7: Plot of system degrees of freedom θ_1 and θ_2 over a time period of $T = 10s$.

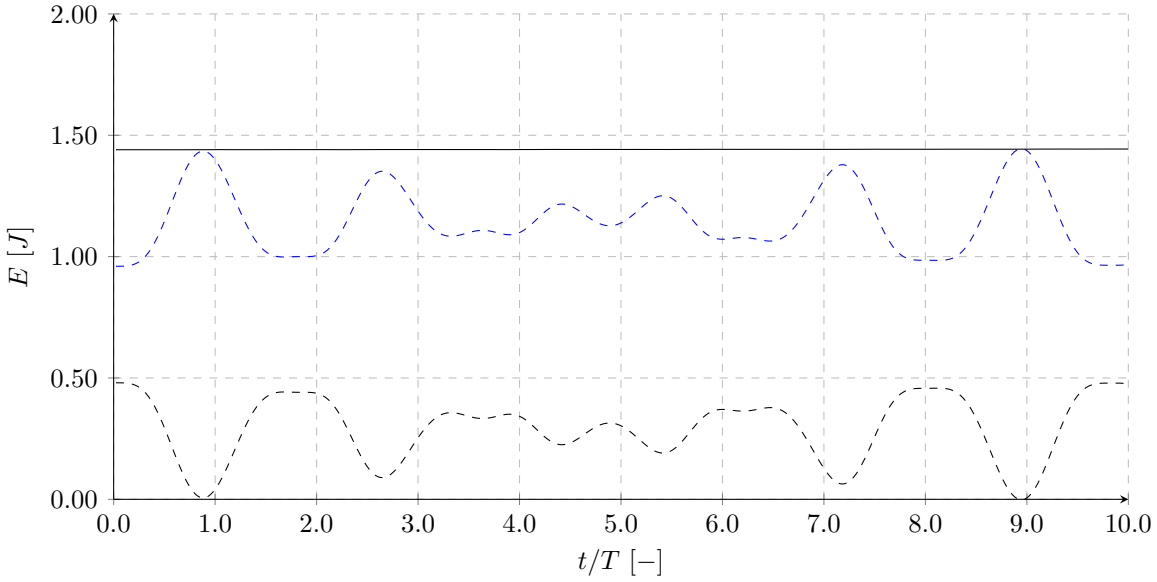

Figure 6.8: Plot of the system and links energy against time t/T; (- - -) link 1, (- - -) link 2, (——) total.

6.3 Discussion and Conclusion

Simulations of a single and double pendulum were performed to verify the components of the developed rigid body solver. The setup of the simulations included the use of the rigid body equations of motion and the modeling of bodies as point masses. The simulations further verified the implemtation of constraints between rigid bodies and the inertial frame as well as relative constraints between rigid bodies. The simulations of the single pendulum were further compared to a derived analytical solution of a pendulum with small amplitudes. The analysis of the single pendulum showed a second order convergence of the pendulum position degree of freedom which is in line with the expected time integration error expected from the Newmark integration scheme. The analysis further showed a perfect match between the analytical solution of the single pendulum and the numerical solution of the present code. The single pendulum verified the correct implementation of the time integration scheme and constraint implementation between rigid bodies and the inertial reference frame. Subsequently simulations of a double pendulum were performed. The addition of the second link leads to an additional degree of freedom. It further results in a chaotic non-integratable system. A convergence error analysis was performed on the system energy and constraint violation. Both showed first order convergence characteristics. Plots of the system energy and two degrees of freedom of the simulated time period were shown. The system energy plot showed how the system energy is correctly conserved while the energy is transferred between the two links during the motion. The plot of the two degrees of freedom showed the expected quasi-periodic but chaotic motion of the two pendulum links. The simulations and tests performed in this chapter verified the implementation of the rigid body solver components. The verified rigid body solver has been used for flutter simulations of a NACA0012 airfoil. The results of these simulations are presented in chapter 9.

Chapter 7

Laminar flow around an in-line oscillating cylinder

Örley et al. (2015) show numerical results of an in-line oscillating cylinder in both still and moving air at low Reynolds numbers. The test case was used to validate the developed cut-element based immersed boundary method. The numerical results are compared to the experimental results of Dütsch et al. (1998). The identical case was simulated with the present solver and hybrid ghost-cell immersed boundary. The results of the validation study are presented in this chapter. Sections 7.1 and 7.2 give a short introduction to the conducted experiment and flow problem at hand. Section 7.3 presents the setup of the simulation. The results of the simulation and discussion are presented in sections 7.4 and 7.5.

7.1 Experiment

The experiment of Dütsch et al. (1998) was performed to investigate the forces and flow field around an in-line oscillating cylinder in low Reynolds number flow at low Keulegan-Carpenter (KC) numbers. These studies are used to support the fundamental understanding of fluid structure interaction. The experiment was conducted in a water tank. LDA measurements were performed to obtain the velocity at selected locations. Differences in the Reynolds and Keulegan-Carpenter numbers were achieved by varying the speed of the motor drive, the amplitude of the oscillation and the diameter of the cylinder. Variations of the Reynolds and Keulegan-Carpenter number are of particular interest for this case as the vortex dynamics drastically change with these parameters. This is discussed in more detail in section 7.2. Three combinations of Reynolds and Keulegan-Carpenter numbers were investigated in the experiment. The combinations are summarized in table 7.1 together with their corresponding Stokes parameter $\beta = Re/KC$. The key numbers of the experiment, (Dütsch et al., 1998), are defined by

$$Re = \frac{U_{max} d}{\nu} \quad and \quad KC = \frac{U_{max}}{f d}. \tag{7.1}$$

U_{max} defines the maximum velocity of the oscillating cylinder. The position of the cylinder is defined by

$$x(t) = -A\sin(2\pi ft), \tag{7.2}$$

with the velocity defined by the derivative of the position function

$$u(t) = -2\pi fA\cos(2\pi ft). \tag{7.3}$$

The equation yields a maximum velocity of

$$U_{max} = 2\pi fA \tag{7.4}$$

and similar a Reynolds and Keulegan-Carpenter number of

$$Re = \frac{2\pi fAd}{\nu} \quad and \quad KC = \frac{2\pi A}{d}. \tag{7.5}$$

Test case I is selected for the simulation. This enables the comparison of the results to

Case	Re	KC	β
I	100	5	20
II	200	10	20
III	210	6	35

Table 7.1: Experiments of the in-line oscillating cylinder conducted by Dütsch et al. (1998).

both the experimental results of Dütsch et al. (1998) and the numerical results of Örley et al. (2015). Section 7.4 present measurements of the force acting on the cylinder as well as flow field measurements of the velocity at different positions. Uncertainty estimates of the measurements in the experiments were not given.

7.2 Flow problem

The oscillating cylinder sheds vortices which are convected away from the cylinder into the far field of the domain. The dynamics of these vortices is highly dependent on the Reynolds and Keulegan-Carpenter number of the specific case. As discussed in Tatsuno and Bearman (1990) different region may be defined on a Reynolds Keulegan-Carpenter plot which define the characteristics of the vortex dynamics. The various regions identified by Tatsuno and Bearman (1990) are shown in figure 7.1. The experiments of Dütsch et al. (1998) focused on regions **A**, **F** and **E**. The simulations and tests performed in region **E** were primarily conducted to compare results to previous studies as discussed by Dütsch et al. (1998). Region**A**, which is also subject of the presented numerical simulation, is characterized by a stable, symmetric and periodic vortex shedding as discussed in Dütsch et al. (1998). The vortex dynamic lead to fixed stagnation points on both sides of the cylinder. With increasing Reynolds and Keulegan-Carpenter number the vortex dynamics become more unstable. The flow field in region **F** was characterized by vortex shedding which was symmetric in the beginning but moved to non-symmetric vortex shedding with time as the shed vortices on one side of the cylinder became larger than on the other side.

The asymmetric size in the vortices led to a movement of the stagnation point and an inclination of the mean vortex shedding direction. This is discussed in detail in Dütsch et al. (1998). The reader is further directed to the work of Tatsuno and Bearman (1990) for a discussion of all regions in figure 7.1.

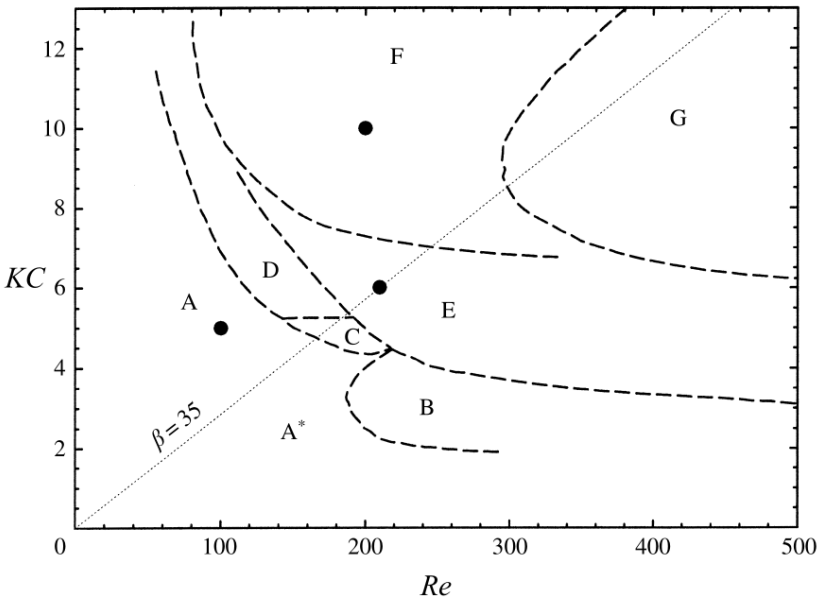

Figure 7.1: Flow regimes of the in-line oscillating cylinder as defined by Tatsuno and Bearman (1990).

7.3 Simulation setup

The setup of the numerical simulation followed the simulation of Örley et al. (2015). A square domain with size $38.4d \times 38.4d$ is used for the discretization of the flow field. Riemann boundary conditions are used at the domain boundaries to prevent reflections of waves traveling from the cylinder into the far-field. The octree based Cartesian mesh is used for the discretization of the flow field with 3 levels of refinement at the cylinder. The refinement level combined with the number of cells per block and the block size led to a mesh density of 80 cells per cylinder diameter d. This mesh density corresponds to the finest mesh used in the numerical simulations of Örley et al. (2015). To prevent compressibility effects in the results of the flow-field the setup was set such that the maximum velocity of the cylinder corresponds to a Mach number of $M = 0.2$. The simulation was run for 8 cylinder periods before gathering force and flow field data to prevent the pollution of the numerical results from transients of the initial conditions of the flow field.

7.4 Results

The results presented in Dütsch et al. (1998); Örley et al. (2015), consist of numerical and experimental results of the drag coefficient of the cylinder, numerical results of the

pressure and vorticity field and plots of horizontal and vertical velocity across different slices in the flow field at phase angle 180°. All presented results in this section are given as non-dimensional units. The drag coefficient on the cylinder is defined by

$$C_d = \frac{2D}{\rho U_{max} d}. \tag{7.6}$$

The time variable is given in the non-dimensional form of

$$t' = t \cdot f. \tag{7.7}$$

Velocities are given as a fraction of the maximum velocity of the cylinder

$$u' = u/u_{max} \quad and \quad v' = v/u_{max}. \tag{7.8}$$

Positions are given in terms of the cylinder diameter

$$x' = x/d \quad and \quad y' = y/d. \tag{7.9}$$

The integral force acting on the cylinder over one period of the cylinder oscillation is presented against the experimental results of Dütsch et al. (1998) in figure 7.2. The result of the cylinder drag coefficient shows good agreement on the phase angle between the cylinder force and cylinder oscillation. A slight under-prediction is found in the cylinder force amplitude. But, overall the results of the drag coefficient and their agreement with the results of Dütsch et al. (1998) are satisfactory.

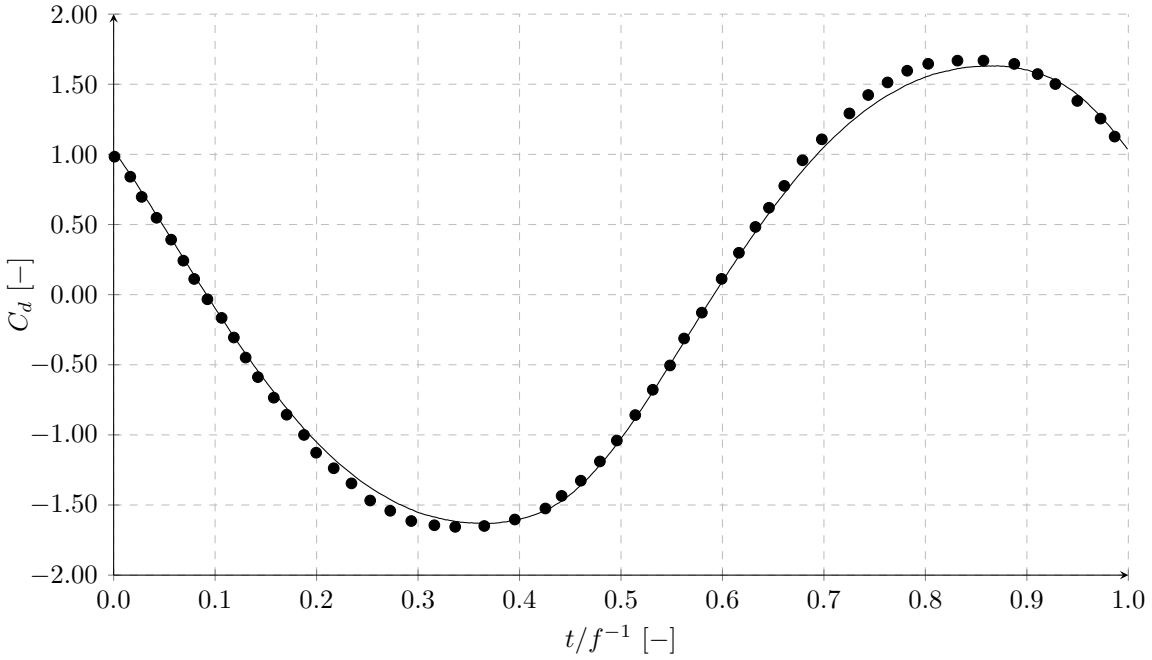

Figure 7.2: Plot of the aerodynamic forces on the cylinder surface along the x axis: (——) present code, (•) experimental results of Dütsch et al. (1998).

Iso-line plots of the vorticity and density field similar to the ones presented in Dütsch et al. (1998); Örley et al. (2015) are shown in figure 7.3. A good agreement is found

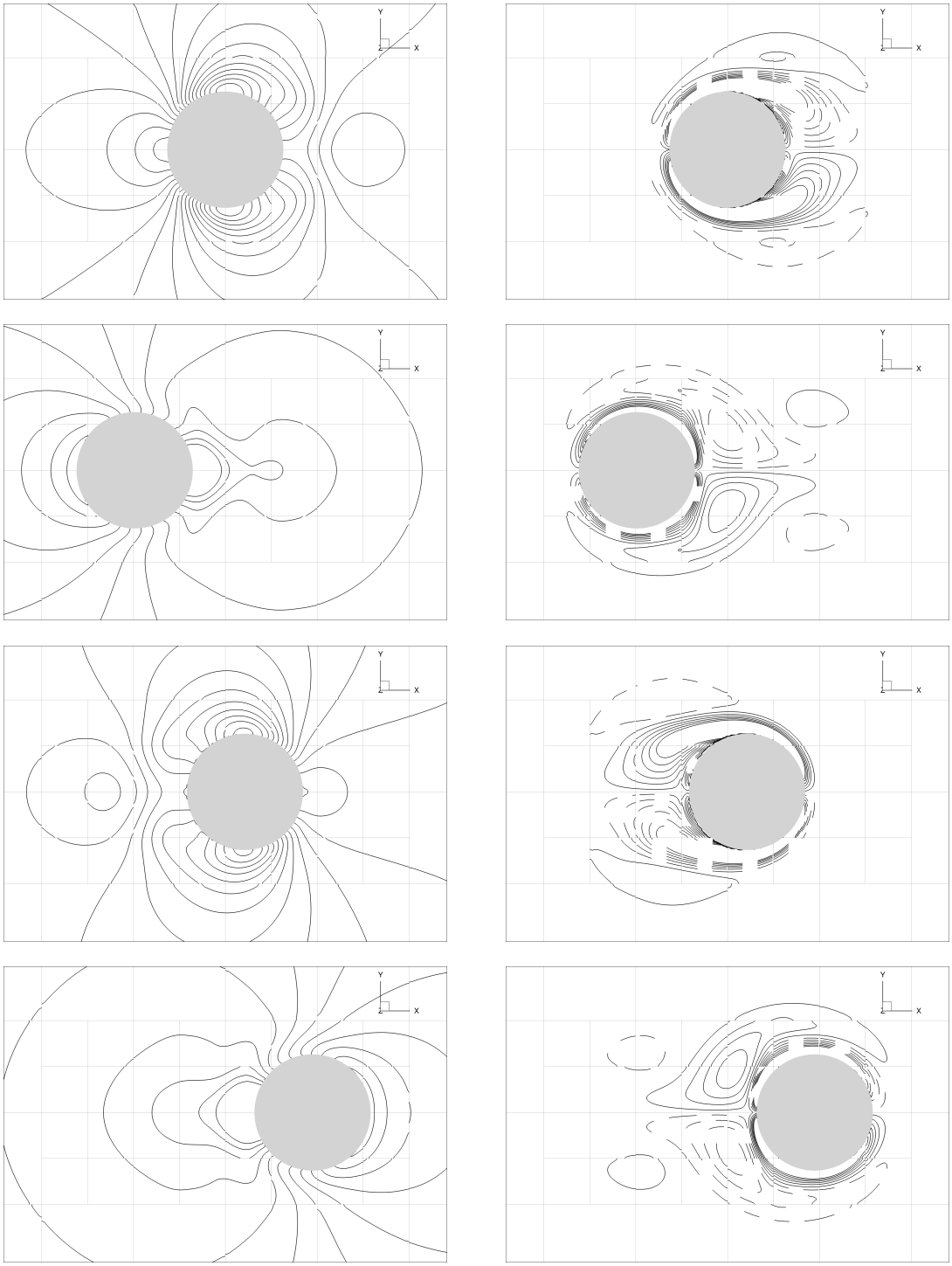

Figure 7.3: Density (left) and vorticity contours (right) of the flow field around the in-line oscillating cylinder at $Re = 100$ and $KC = 5$ at four different phase-angles (top to bottom): $0°$, $96°$, $192°$, $288°$.

between the flow fields presented in the reference and the result shown in figure 7.3. The symmetry of the shed vortices is confirmed by the plot of the vorticity field. The symmetry of the flow field plots also confirms the stationary stagnation points on both sides of the cylinder. Discontinuities in the contour plots are caused by the interpolation of the solution at block boundaries in the post processing phase. They do not indicate discontinuities in the flow field.

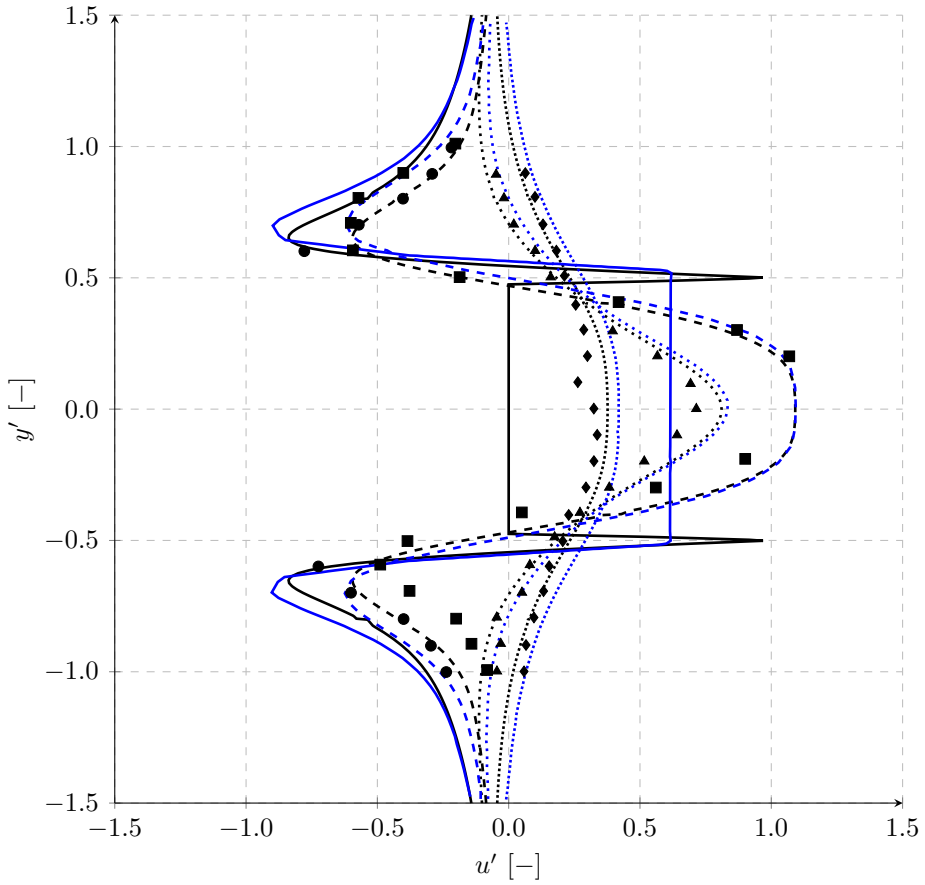

Figure 7.4: Plot of u' velocity field slices at different x' positions at phase angle 180.0° based on experiments of Dütsch et al. (1998) (Scattered values), numerical analysis of Örley et al. (2015) (Blue lines) and numerical results of the present solver (black lines): (——,——,●) slice at $x' = 0.0$, (- - -,- - -,■) slice at $x' = -0.6$, (·····,·····,▲) slice at $x' = 0.6$, (·····,·····,♦) slice at $x' = 1.2$.

Measurements of the horizontal u' and vertical v' velocity components were obtained at different location in the flow field at a phase angle of 180°. The location were defined by vertical slices at four different horizontal locations, $x' = -0.6$, 0.0, 0.6 and 1.2. The u' velocity component measurements are shown in figure 7.4. The measurements of the v' component of the velocity field are shown in figure 7.5. A good agreement is found between the numerical results of Örley et al. (2015) and the numerical results obtained with the present hybrid ghost-cell method. A slight under-prediction is found in the magnitude of the u' and v' component predicted by the present hybrid ghost-cell method. A large discrepancy is found in the $x' = 0.0$ slice between $y' = -0.5$ and $y' = 0.5$.

This discrepancy is caused by a different handling of the solid cell velocities.A velocity of $u', v' = 0.0$ is assigned in cells outside of the fluid domain. The results of Örley et al. (2015) assigned the cylinder velocity to those cells. Larger discrepancies are found between the numerical results and experimental results of Dütsch et al. (1998). The magnitude of the measured u' and v' components tends to be lower in the experimental measurements of Dütsch et al. (1998) than found in the numerical results. The large discrepancies are especially visible in the u' component of the velocity field at slice $x' = -0.6$ and $x' = 0.0$. Given the good agreement between the numerical results of Örley et al. (2015) and the present hybrid ghost-cell method and the good prediction of the vortex dynamics, the discrepancies between the experimental results and numerical results are attributed to measurement and setup uncertaintities in the experiment rather than the inability of the two numerical codes to accurately predict the physics of the flow field.

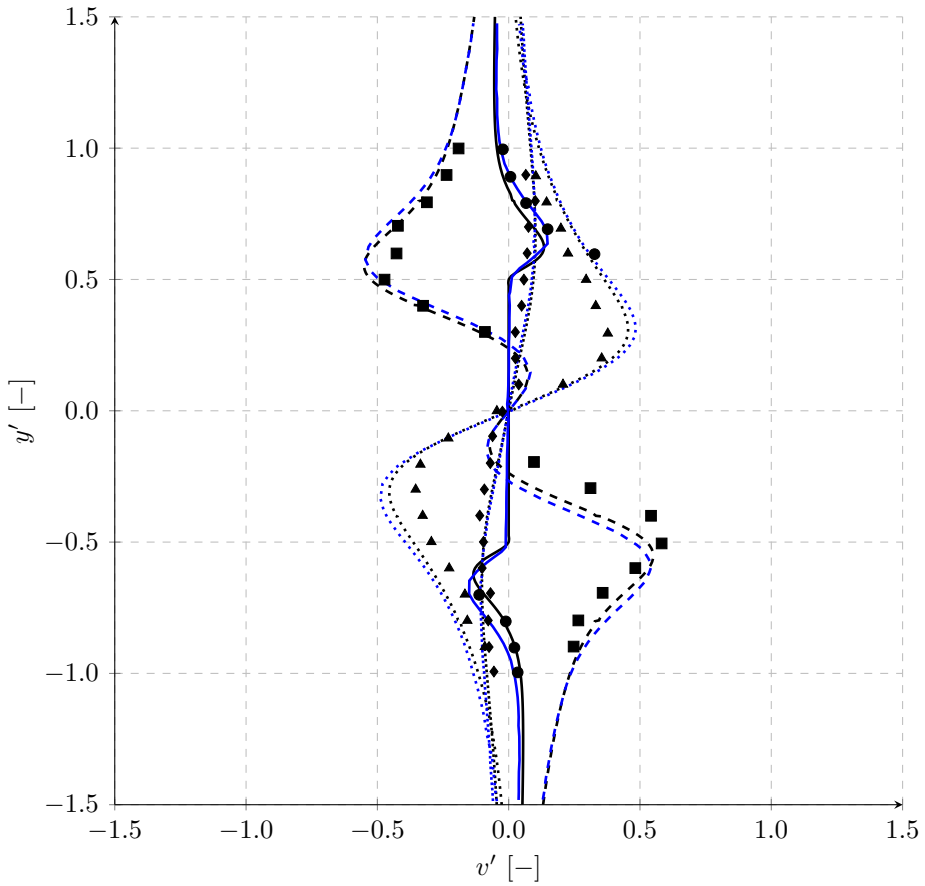

Figure 7.5: Plot of v' velocity field slices at different x' positions at phase angle $180.0°$ based on experiments of Dütsch et al. (1998) (Scattered values), numerical analysis of Örley et al. (2015) (Blue lines) and numerical results of present solver (black lines): (——,——,●) slice at $x' = 0.0$, (- - -,- - -,■) slice at $x' = -0.6$, (·····,·····,▲) slice at $x' = 0.6$, (·····,·····,♦) slice at $x' = 1.2$.

7.5 Conclusion

Numerical results of the flow field around an in-line oscillating cylinder at low Reynolds $Re = 100$ and Keulegan-Carpenter $KC = 5$ were presented. The test case was selected as validation case for the developed hybrid ghost-cell method. The numerical results were assessed with numerical and experimental results from Örley et al. (2015) and Dütsch et al. (1998) respectively. The presented results showed that the developed hybrid ghost-cell method accurately predicts the hydrodynamic forces acting on the cylinder, contour plots of the density and vorticity field further confirmed that the vortex dynamics are correctly predicted and slices of the velocity field showed a good agreement with the numerical results of Örley et al. (2015). Discrepancies with respect to the experimental results of Dütsch et al. (1998) were attributed to the unknown uncertainties of the experiment. Discrepancies with respect to the numerical results of (Örley et al., 2015) may be attributed to differences in the numerical discretization scheme of the interior flow field as well as immersed boundary treatment. In conclusion the developed hybrid ghost-cell method accurately predicts the flow around moving geometries at low Reynolds numbers. Further studies may be conducted to test the method a higher Reynolds and Keulegan-Carpenter numbers. Based on the presented results the author expects a similar accuracy for those cases.

Chapter 8

Dynamic stall of a NACA0012 airfoil

A series of experimental studies was performed in 1982 to investigate the dynamic stall behavior of helicopter blade sections. The experimental study was motivated by the high speed performance limits imposed by retreating blade stall (Mcalister et al., 1982a). The setup and results of the experimental study are documented in Mcalister et al. (1982a); Mcalister, Pucci, Mccroskey, and Carr (1982b). The experimental results of the study have been subsequently used as reference for CFD simulations with varying turbulence closure approaches such as unsteady RANS approaches, DDES approaches and large eddy turbulence closure formulations, which are further discussed in section 8.3. The availability of numerical results in addition to the experimental results of Mcalister et al. (1982a, 1982b) creates a suitable test case for the validation of the hybrid ghost-cell immersed boundary method in the present solver. Details of the experiment are presented in section 8.1. The underlying physics of dynamic stall, which must be accurately resolved or modeled to match the experimental data, are discussed in section 8.2. Afterwards, a small summary of available numerical reference data is presented in section 8.3, followed by the selected numerical setup in section 8.5. The results section of this chapter is split into two parts. An initial analysis at static angles of attack was performed to validate the hybrid ghost-cell immersed boundary method with wall-model. The simulation at static angles of attack was further used to determine an appropriate near-wall mesh resolution. These results are presented in section 8.6. The results of the dynamic stall simulation are presented in the following section, section 8.7.

8.1 Experiment

The experiment was performed in the U.S. Army Aeromechanics Laboratory wind tunnel with dimensions $2m$ by $3m$ (Mcalister et al., 1982a). The airfoil chord is $c = 0.61m$ resulting in an aspect ratio reported by Mcalister et al. (1982a) of $A = 3.5$. The objective of the experiment was the characterization of different airfoil sections in dynamic stall conditions. The wall interference effects were not part of the study but have been shown to influence the results by Ribeiro et al. (2016). However, an exact modeling of the wind

tunnel wall interference effect is difficult as wind tunnel wall boundary layer information is not available. The numerical simulation is setup with the target to investigate the airfoil characteristics noting that discrepancies between the experimental and numerical results might be caused by the wind tunnel wall interference effects.
During the experiment a total of eight airfoil sections were tested. All airfoil sections were oscillated sinusoidally around the quarter chord point. The motion of the airfoil is expressed by

$$\alpha = \alpha_0 + \alpha_{amp} sin(\omega t), \quad with \quad \omega = \frac{2U_\infty k}{c}. \tag{8.1}$$

where α_0 denotes the mean angle of the oscillation, α_{amp} denotes the amplitude of the oscillation and k denotes the reduced frequency of the oscillation. A parameter sweep was performed on all three parameters in combination with changing free stream Mach number M, up to $M = 0.3$, and Reynolds number Re, up to $Re = 4 \cdot 10^6$, and correlated free steam velocity U_∞. The experimental data selected for the numerical simulation was selected based on previous numerical simulations (Haase, Braza, & Revell, 2009; Ribeiro et al., 2016). These simulations were setup based on the NACA0012 airfoil with results collected on tape 8115. The setup is summarized in table 8.1. With a reduced frequency

Parameter	Symbol	Unit	Tape 8115
Reynolds number	Re	$[-]$	980395
Mach number	M	$[-]$	0.072
Rest pitch angle	α_0	$[^\circ]$	15.0
Pitch angle amplitutde	α_{amp}	$[^\circ]$	10.0
Reduced frequency	k	$[-]$	0.0992

Table 8.1: Experimental parameters of tape 8115 as reported by Mcalister et al. (1982a).

of $k = 0.0992$ the aerodynamic flow field around the airfoil is considered unsteady as it is above $k > 0.05$ (Leishman, 2006). The flow-field physics are further discussed in the following section. Boundary layer tripping tapes were used for selected runs but were not part of the selected run. The boundary layer transition point must therefore be predicted by the numerical simulations. Airfoil forces and moments were derived from integrated surface pressure measurements on the airfoil and phase averaged over at least 50 periods. The reported measurements ranged from airfoil suction side pressure distributions and derived lift, drag and moment coefficients (Mcalister et al., 1982b), to boundary layer measurements via hot film and hot wire measurement techniques (Mcalister, Pucci, Mccroskey, & Carr, 1982c). The surface measurements were used to investigate the boundary layer transition points, flow reversal, separation and reattachment. The results of the presented numerical simulations concentrate on the force and moment results and on a qualitative assessment of the flow field to verify the presence of the expected flow features.

8.2 Flow problem

As discussed in Carr (1988), the stall behavior of a dynamically stalling airfoil varies significantly from the stall behavior of an airfoil immersed in a quasi steady flow field. The differences in the stall behavior are caused by distinct flow features which are discussed in

this section. These flow features significantly effect the aerodynamic forces and moments. The flow field, forces and moments of a dynamically stalling airfoil are illustrated in figure 8.1. The flow field of one oscillation period is divided into five phases. The start of one oscillation period is defined as the beginning of the airfoil pitch-up motion. During the initial pitch-up motion, denoted as phase 1, the airfoil flow field and forces follow the quasi-static flow field and loading. The flow fields of the unsteady and steady case start deviating at the stall point of the steady flow case. At this point the flow field of the dynamically stalling airfoil features a growing separation zone near the leading edge region, which results in an effectively higher camber and further lift increase. This phenomena is shown in phase 2 of the oscillation period. The separation near the leading edge grows into a strong leading edge vortex which results in a low pressure zone on the top side of the airfoil and in an increased lift. The lift slope in this phase is significantly higher than the lift slope in phase 1. The vortex and associated low pressure region detaches from the leading edge and travels downstream causing a low pressure region towards the trailing edge of the airfoil. The lower pressure introduces a high pitch-down moment and a substantial increase in pressure drag, which are not present in the quasi steady stall conditions. As indicated in figure 8.1 during the pitch-down motion, denoted as phase 4, the airfoil stays detached which results in substantial hysteresis. The flow field and forces converge again once the flow reattaches which is occurring in phase 5 of the motion. In summary, the numerical simulation should show the following features in the flow field, force and moment reports. A leading edge separation region and vortex in combination with a substantial increase in the lift coefficient beyond the $C_{L_{max}}$ of the airfoil. The flow field should further show that the leading edge vortex travels downstream and causes a significant pitch-down moment and increase in pressure drag, and the flow field should show a separated airfoil suction side during the pitch-down motion resulting in substantial hysteresis.

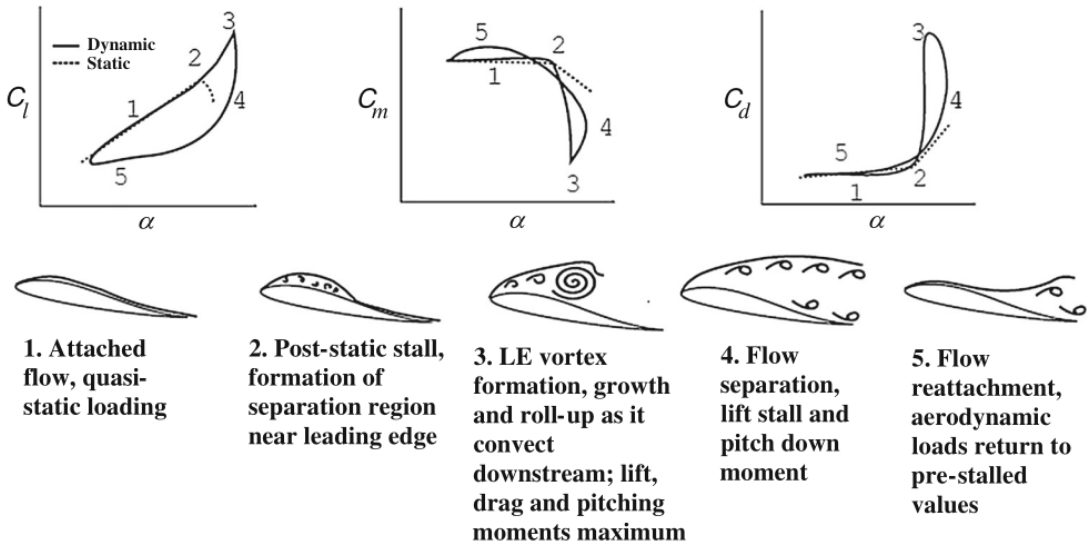

Figure 8.1: Illustration of the flow structures and correlated airfoil forces and moments taken from Carr (1988).

8.3 Reference results

Numerical results of other flow solvers and turbulence closure models were studied to aid the setup of the simulation and to aid the analysis of the results. The numerical reference results substantially decrease the efforts in sizing the numerical domain, creating an acceptable mesh and setting the boundary conditions. The findings of the reference numerical results may further be used when discussing the discrepancies between the numerical and experimental results. Numerical results of the NACA0012 test case were presented as part of the DESider project (Haase et al., 2009), as part of a feature demonstration of the commercial code XFlow in (Chávez-Modena, Martínez, Cabello, & Ferrer, 2020) and in Ribeiro et al. (2016). Combined, these three resources present a wide selection of numerics, mesh types, turbulence closure models and boundary conditions. During the DESider project (Haase et al., 2009) the test case was used to investigate the performance of Reynolds averaged Navier Stokes (RANS) turbulence closure models and detached eddy simulation (DES) formulations. The simulations were performed with finite volume based solvers on body fitted structured and unstructured meshes. Apart from the span-wise size of the domain the windtunnel size was not considered in the sizing of the domain. Wind tunnel wall boundary conditions were modeled as slip/symmetric and periodic boundary conditions. Results based on Lattice Boltzmann formulations are presented in Ribeiro et al. (2016); Chávez-Modena et al. (2020). Chávez-Modena et al. (2020) use the Lattice Boltzmann numerics in combination with a wall-modeled large-eddy simulation turbulence closure approach. The equations are solved on an Octree based lattice. The domain size is derived from the experiment but scaled down to reduce the overall cost of the simulations. The wind tunnel walls are modeled as slip walls. Ribeiro et al. (2016) present lattice Boltzmann results in combination with a very-large-eddy simulation (VLES) turbulence modeling approach. The setup of the simulation closely follows the dimensions of the windtunnel experiment and Ribeiro et al. (2016) extensively discuss the influence of the span-wise wind tunnel wall boundary conditions on the results.
The analysis of the numerical results in (Haase et al., 2009) focus on the advantages of DES approaches over URANS approaches. The analysis concluded that DES approaches generally improve the accuracy of the numerical solution during the detached flow state in the pitch-down motion and also improve the force and moment prediction around $C_{L_{max}}$. However, they also conclude that the a final decision on whether DES approaches are superior to URANS approaches is difficult due to the significantly increased computational cost and uncertainties in the experimental results. Ribeiro et al. (2016) extensively analyzed the differences between a free-slip and no-slip wall boundary condition at the wind tunnel walls. They conclude that the boundary condition at the wind-tunnel wall strongly impacts the numerical results most notable in the stalled pitch-down region. They further conclude that the no-slip boundary condition more accurately predicts the flow field and measured forces in the experiment. The improved results were associated with large coherent structures in the flow field which are present with no-slip wall boundary conditions (Ribeiro et al., 2016).
The numerical results of Ribeiro et al. (2016) are shown later in the results section in combination with the experimental results of Mcalister et al. (1982a) and the results of the developed solver.

8.4 Definition of quantities

The results of the static and dynamic simulations are presented in the form of coefficients describing the forces and moment acting on the airfoil and quantifying the airfoil surface solution. The airfoil forces are given in the form of the lift and drag coefficients C_L and C_D as defined by

$$C_L = \frac{2L}{\rho_\infty U_\infty^2 bc}, \tag{8.2}$$

and

$$C_D = \frac{2D}{\rho_\infty U_\infty^2 bc}. \tag{8.3}$$

The moment coefficient is given by

$$C_M = \frac{2M}{\rho_\infty U_\infty^2 bc^2}. \tag{8.4}$$

The moment coefficient of the presented results is defined as pitch-up positive. Skin friction and pressure coefficients are presented on the surface of the airfoil. The coefficients are defined as

$$C_p = 2\frac{p - p_\infty}{\rho U_\infty^2}, \tag{8.5}$$

and

$$C_f = 2\frac{|\tau_w|}{\rho U_\infty^2}. \tag{8.6}$$

Time, space and velocity quantities are given in non-dimensional form. All position and length measures are given in multiplies of the airfoil chord length c. Time is given in terms of airfoil flow over times defined by

$$\tau = \frac{tU_\infty}{c} \tag{8.7}$$

8.5 Simulation setup

The simulations with the commercial code Powerflow[1], as presented in Ribeiro et al. (2016), are used as baseline for the setup of the numerical domain. The simulation of Ribeiro et al. (2016) follow the dimensions of the windtunnel in the experiment of Mcalister et al. (1982a). The dimensions of the numerical domain are shown in table 8.2. An additional domain used in the commercial code XFlow[2], as presented in Chávez-Modena et al. (2020), is added as another reference in table 8.2. The numerical domain in the simulation of the present solver is identical to the dimension in all but just one dimension. The width of the numerical domain is reduced for a more efficient octree mesh blocking in the far-field of the domain.

Parameter	Symbol	Unit	Present	Powerflow	XFlow
Inlet length	l_{inlet}	$[c]$	20	20	12
Outlet length	l_{outlet}	$[c]$	50	50	20
Domain width	w	$[c]$	3	3.5	2.5
Domain height	h	$[c]$	5	5	5

Table 8.2: Numerical domain size used in the present dynamic stall simulation combined with domain sizes used in literature.

Domain boundary conditions are set in the following way. Slip boundary conditions are used for the windtunnel top, bottom and side walls. A Riemann boundary condition is used at the inlet of the windtunnel to prescribe the velocity in the domain and to damp waves inside the domain which originate from the initial condition of the flow field. A static pressure boundary condition is used at the outlet of the domain to prescribe the pressure in the flow field.
The hybrid ghost-cell immersed boundary method is used to model the NACA0012 geometry. As the mesh density is insufficient to resolve the boundary layer down to the viscous sublayer, the wall-modeled version of the hybrid ghost-cell method is used for all presented simulations. Equally a large-eddy simulation closure model is used to model the unresolved turbulent scales in the flow field. The Vreman (Vreman, 2004) turbulence closure model is selected for this purpose.
The mesh settings and estimations of the simulation length are shown in table 8.3. Results of a mesh convergence study performed on a selected static angle of attack is shown in the subsequent sections.

Parameter	Symbol	Value
Mesh spacing	$\Delta x/c$	$0.97 \cdot 10^{-3}$
Apprx. Wall spacing	y^+	42
Apprx. Time step	$\Delta t U_\infty/c$	$2.0 \cdot 10^{-5}$
Simulation time	TU_∞/c	42.0
Est. number of iterations	N_T	$2.1 \cdot 10^6$
Est. mesh cell count	N	$890 \cdot 10^6$

Table 8.3: Space and time discretization used in the dynamic stall simulations of the NACA0012 airfoil.

8.6 Static analysis

Simulations of flow around the NACA0012 profile at static angles of attack were performed as preparation for the simulation of the dynamic problem. The static simulations of the NACA0012 airfoil were performed for two purposes. A mesh study was performed on a selected static angle of attack to select an appropriate mesh for the dynamic stall simulations, and lift, drag and moment polars were generated in order to compare the

[1]https://www.3ds.com/de/produkte-und-services/simulia/produkte/powerflow/
[2]https://www.3ds.com/de/produkte-und-services/simulia/produkte/xflow/

results of the present numerical code with predictions of a fully coupled viscous inviscid panel code XFoil.[3]
The simulations were performed with a far-field domain. The width of the domain was reduced to $0.5c$ with imposed periodic boundary conditions in the span-wise direction. The rectangular domain extends 25 chord lengths in all directions. The dimensions are summarized in table 8.4. Reynolds and Mach numbers are set identical to the selected wind tunnel experiment shown in table 8.1.
The presented results cover a mesh convergence study, the lift, drag and moment polars of

Parameter	Symbol	Unit	Present
Inlet length	l_{inlet}	$[c]$	25.0
Outlet length	l_{outlet}	$[c]$	25.0
Domain width	w	$[c]$	0.5
Domain height	h	$[c]$	50.0

Table 8.4: Domain dimension of the far-field domain for the NACA0012 static analysis.

the airfoil and pressure and skin friction coefficient plots at selected angles of attack. The mesh convergence study is performed at an angle of attack of 12.5°. The following polar results are performed on the finest available mesh. The mesh settings of the mesh used for the static analysis of the NACA0012 airfoil are summarized in table 8.5. The pressure and skin friction coefficients are presented for angles of attack 5.0° and 12.5°. Surface results are presented as averaged quantities. The values were averaged over $\frac{tU_\infty}{c} = 5$ flow over periods and further spatially averaged along the airfoil span. The presentation of the results is concluded with a discussion on the differences in the modeling approaches between XFoil and the present solver and their potential effects on the accuracy of the results.

Parameter	Symbol	Value
Mesh spacing	$\Delta x/c$	$0.65 \cdot 10^{-3}$
Est. Wall spacing	y^+	30
Est. Time step	$\Delta t U_\infty/c$	$1.3 \cdot 10^{-5}$
Simulation time	TU_∞/c	25.0
Est. number of iterations	N_T	$1.9 \cdot 10^6$
Est. mesh cell count	N	$432 \cdot 10^6$

Table 8.5: Space and time discretization used in the static simulations of the NACA0012 airfoil.

8.6.1 XFoil reference

The reference results for the static simulations were performed with the coupled inviscid viscous panel code XFoil. The solver predicts the potential flow field around the airfoil using a linear vortex strength panel method. Near-wall viscous effects are predicted based on the solution of the integral boundary layer equations for both laminar and turbulent regions. The viscous boundary layer solution and potential flow field are two way coupled.

[3] https://web.mit.edu/drela/Public/web/xfoil/

The velocity and pressure of the potential flow solution is used as edge boundary condition for the boundary layer equations. The displacement effect of the viscous boundary layer is used to formulate a transpiration boundary condition on the surface of the airfoil for the potential flow solution.
Both laminar and turbulent regions of the boundary layer are predicted. The laminar-turbulent transition location on the suction and pressure side of the airfoils is predicted using the e^N method (Van Ingen, 2008). The coefficient of the viscous boundary layer equations are set to the default coefficients in the 6.99 version of the XFoil software. The exponent of the laminar turbulent transition model is set to $N = 9$ which corresponds to a 0.07% free stream turbulence intensity. Fixed laminar turbulent transition locations were not imposed in the simulation.
The XFoil code is known to give accurate airfoil lift, drag and moment results at low and medium Reynolds numbers (Drela, 1989) up to the stall point. The following analysis and comparison between the LES results of the NACA0012 airfoil and XFoil results assume that the XFoil results are accurate in the attached region and not accurate in the detached region of the airfoil polar.

8.6.2 Mesh convergence study

A mesh convergence study was performed at the static angle of attack 12.5°. The study was conducted to determine a suitable wall refinement level for the static and dynamic simulations of the NACA0012 airfoil. The mesh convergence study is conducted on the near-wall mesh resolution. Refinements of the wake are not investigated explicitly. A refinement of the near-wall region is achieved by increasing the number of cells per block and through an increased refinement level of the octree based mesh. Four near-wall mesh resolutions were investigated ranging from a coarse mesh with cell spacing $\Delta/c = 1.95 \cdot 10^{-3}$ to a fine mesh with $\Delta/c = 0.65 \cdot 10^{-3}$. The investigated near-wall mesh resolutions and associated octree refinement levels N_{ref} and per block cells N_{cells} are given in table 8.6. The wall y^+ prediction of selected meshes is presented in a later part of this section.

Δ/c	N_{ref}	N_{cells}
$0.65 \cdot 10^{-3}$	5	24^3
$0.98 \cdot 10^{-3}$	5	16^3
$1.30 \cdot 10^{-3}$	4	24^3
$1.95 \cdot 10^{-3}$	4	16^3

Table 8.6: Summary of investigated mesh sizes.

The mesh convergence of the numerical solution is judged with an assessment of the temporally averaged lift coefficient of the NACA0012 airfoil profile at 12.5°. The results of the mesh convergence study are shown in figure 8.2. The results of the XFoil numerical analysis at 12.5° is added to the plot as qualitative reference. The results of the analysis do not show an asymptotic convergence of the C_L which indicates that additional wall-resolution is required. An investigation of the surface solution and flow field was performed to investigate the causes of the C_L difference between the various near-wall mesh resolutions.

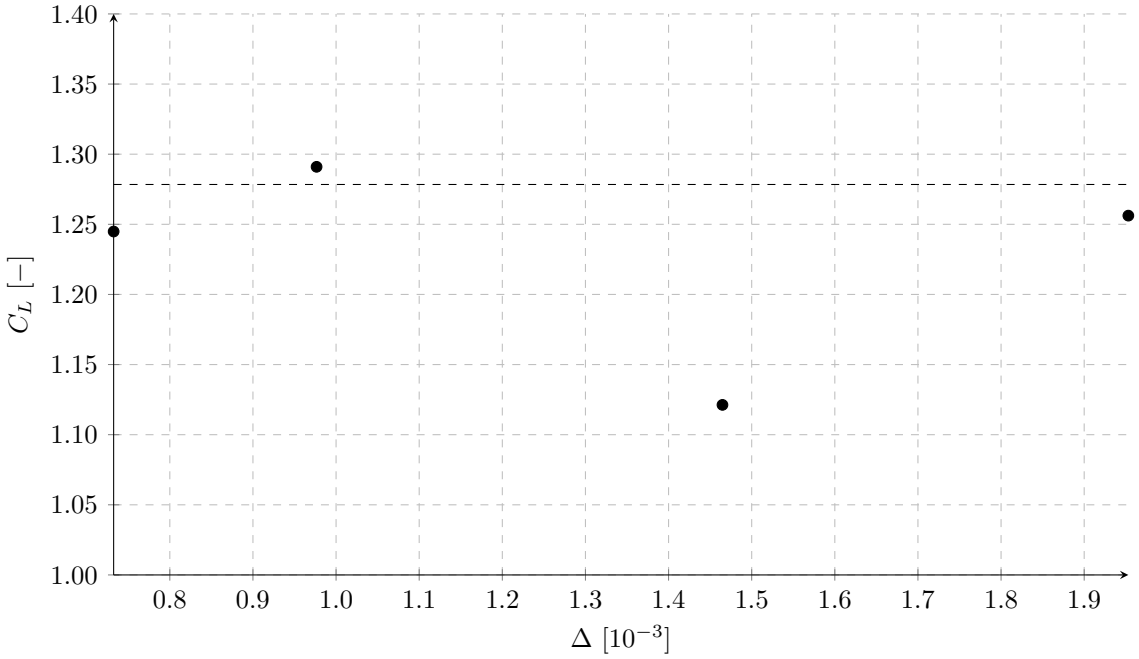

Figure 8.2: Scatter plot of C_L versus non-dimensional near-wall mesh resolution of NACA0012 at 12.5°; XFoil result added as reference: (•) numerical results of present solver, (- - -) XFoil result.

The fine $\Delta/c = 0.65 \cdot 10^{-3}$ and coarse $\Delta/c = 1.95 \cdot 10^{-3}$ mesh are used to investigate the dependency of the flow solution and near-wall mesh resolution. The following plots and discussion will cover the wall $y+$, the pressure coefficient C_P and skin friction coefficient C_f on the airfoil surface and contour plots of the instantaneous velocity magnitude field. The wall y^+ distribution of the coarse and fine mesh are plotted in figure 8.3. The y^+ value definition used in the analysis is based on the cell edge length $y^+ = \frac{u_\tau \Delta}{\nu}$. The two meshes have an average wall y^+ of approximately $y^+_{avg} = 31$ and $y^+_{avg} = 100$. A wall y^+ peak is found at the leading edge of both meshes $x/c < 0.05$ where the flow field outside the boundary layers is substantially higher than the free stream velocity due to the circulation of the airfoil profile and the boundary layer height is small due to the low chord-wise Reynolds number Re_x. Downstream of the leading edge the wall y^+ value decreases towards the trailing edge of the airfoil profile. The decrease is not monotonic as it is disrupted by the laminar turbulent transition point.

The pressure coefficient C_p of the coarse and fine mesh is shown in figure 8.4. The results indicate good agreement between the meshes on the pressure side of the airfoil. On the suction side of the airfoil the results show an underprediction of the suction peak around the leading edge on the coarse mesh. It further shows differences in the laminar turbulent transition location. The laminar turbulent transition location is indicated by a plateau in the pressure coefficient. The C_p distribution indicates that the laminar turbulent transition location is located at around $x/c = 0.1$ on the fine mesh and at approximately $x/c = 0.4$ on the coarse mesh on the suction side of the airfoil.
The skin friction coefficient C_f distribution is shown in figure 8.5. The skin friction distri-

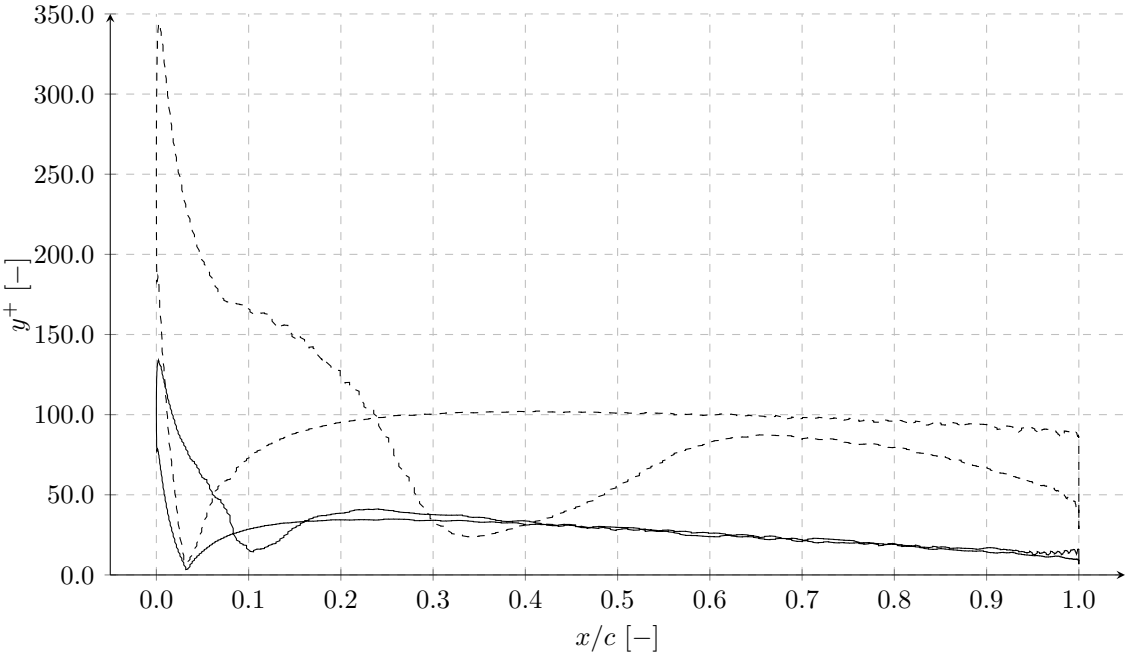

Figure 8.3: Averaged y^+ versus x/c of NACA0012 airfoil at angle of attack 12.5°: (- - -) present results with near-wall mesh resolution $\Delta/c = 1.95 \cdot 10^{-3}$, (——) present results with near-wall mesh resolution $\Delta/c = 0.65 \cdot 10^{-3}$.

bution on the airfoil surface indicates an underprediction of the skin friction around the leading edge $x/c < 0.05$ on the coarse mesh. It confirms the laminar turbulent transition location differences found in the C_p distribution with an increase in the skin friction coefficient at $x/c = 0.1$ on the fine mesh and $x/c = 0.4$ on the coarse mesh. The skin friction distribution further shows a mismatch in the skin friction coefficient on the pressure side of the airfoil. The coarse mesh overpredicts the skin friction on the pressure side of the airfoil. Neither the C_p distribution nor the skin friction distribution indicates a laminar turbulent transition on the pressure side of the airfoil.

The instantaneous velocity field on the coarse and fine mesh is sown in figures 8.6 and 8.7 respectively. The contour plots of the instantaneous velocity magnitude field support the findings of the C_p and C_f distribution. No laminar turbulent transition location is visible on the pressure side of the airfoil. An earlier laminar turbulent transition location is found on the suction side of the airfoil. Further an overall larger boundary layer thickness is found on the suction side around the trailing edge on the coarse mesh. The coarse mesh also illustrates a significantly larger increase in the boundary layer thickness at the laminar turbulent transition location.

8.6.3 Results

The static results are presented in form of the lift, drag and moment polar and surface solution at selected angles of attack. XFoil results were generated for angles of attack 0.0° up to 20.0°. Due to the limits of the XFoil modeling techniques predictions of the

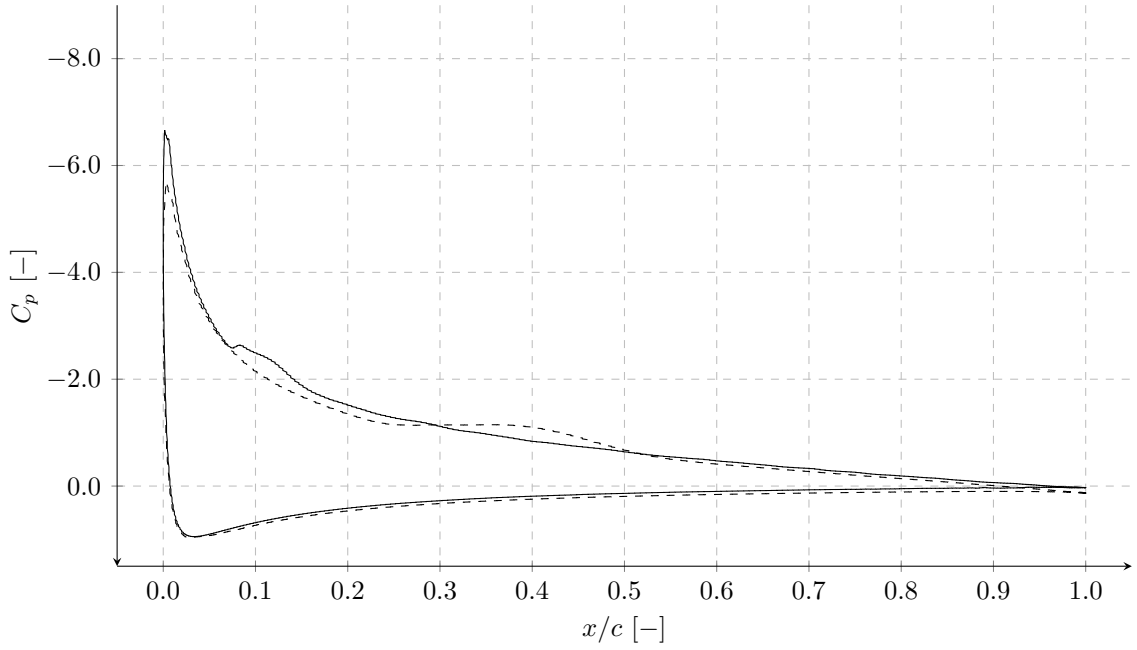

Figure 8.4: Averaged pressure coefficient C_p versus x/c of NACA0012 airfoil at angle of attack $12.5°$: (- - -) present results with near-wall mesh resolution $\Delta/c = 1.95 \cdot 10^{-3}$, (——) present results with near-wall mesh resolution $\Delta/c = 0.65 \cdot 10^{-3}$.

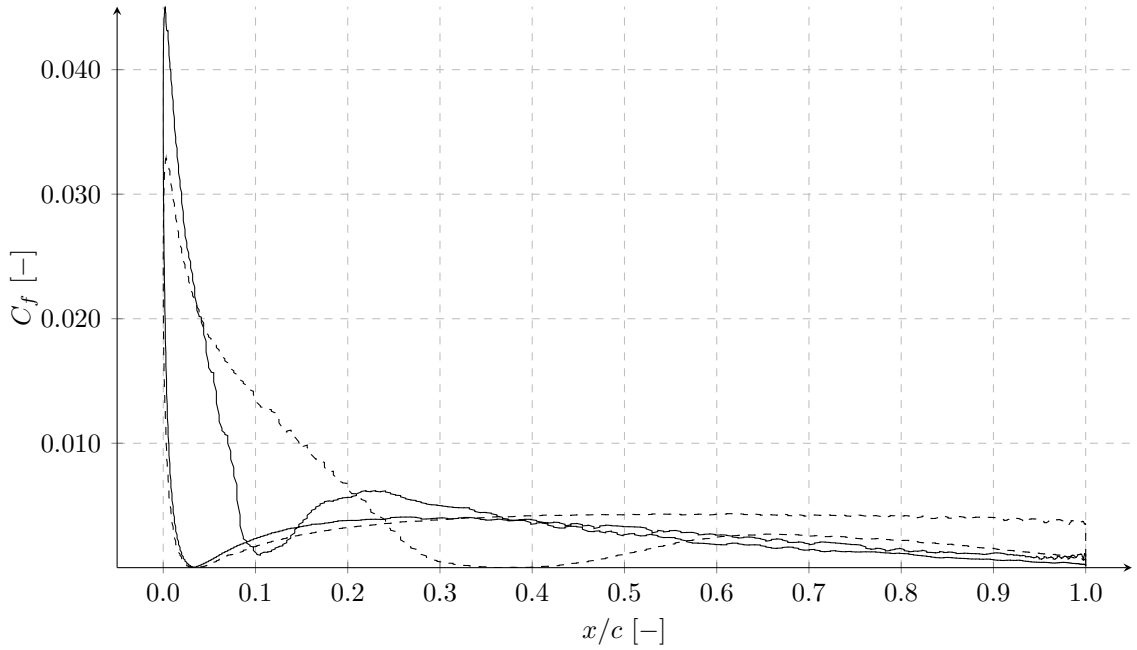

Figure 8.5: Temporally averaged pressure coefficient C_f versus x/c of NACA0012 airfoil at angle of attack $12.5°$: (——) present results with near-wall mesh resolution $\Delta/c = 1.95 \cdot 10^{-3}$, (- - -) present results with near-wall mesh resolution $\Delta/c = 0.65 \cdot 10^{-3}$.

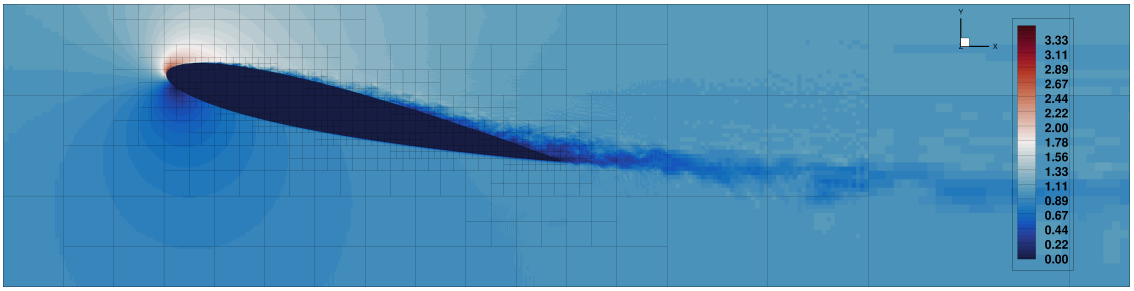

Figure 8.6: Normalized instantaneous velocity magnitude field around NACA0012 airfoil at angle of attack $12.5°$ with near wall mesh resolution $\Delta/c = 0.65 \cdot 10^{-3}$.

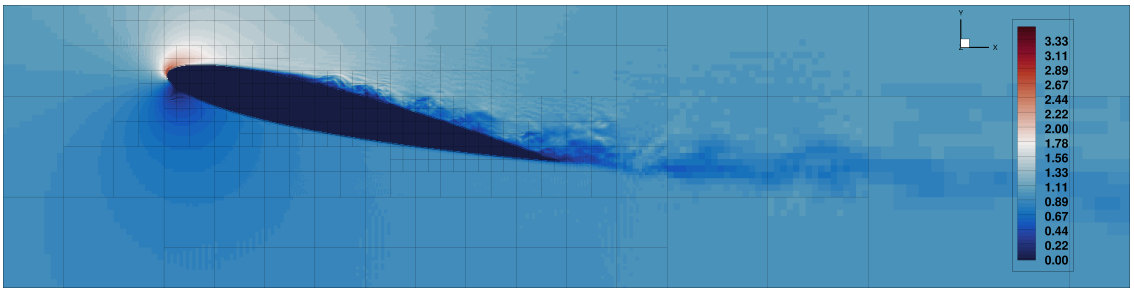

Figure 8.7: Normalized instantaneous velocity magnitude field around NACA0012 airfoil at angle of attack $12.5°$ with near wall mesh resolution $\Delta/c = 1.95 \cdot 10^{-3}$.

post-stall point should not be regarded accurate. Results were gathered for angles of attack 5.0°, 7.5°, 12.5°, 17.5° and 22.5°. The surface solution of the XFoil simulations and simulations with the present solver are shown for angles of attack 5.0° and 12.5°. As discussed in the previous chapter, the static results of the NACA0012 airfoil were performed on the fine mesh with near-wall resolution $\Delta/c = 0.65 \cdot 10^{-3}$.

Polar results

The presented polars show the three airfoil coefficients of interest, lift, drag and pitching moment. The pitching moment is measured around the quarter chord of the airfoil. The lift polar prediction of the present code and XFoil reference results are shown in figure 8.8, the drag polar is shown in 8.9 and the moment polar is shown in figure 8.10. The discussion is started with the lift polar predictions of both tools. The XFoil lift polar prediction shows a monotone nearly linear increase of the lift coefficient up to to an angle of $\alpha = 12°$. The lift coefficient deviates in between angles $\alpha = 5°$ and $\alpha = 9.0°$. The deviation of the lift coefficient from the linear slope is known to be caused by a laminar separation bubble on the suction side of the airfoil. The laminar separation bubble increases the effective airfoil camber and results in an increased lift coefficient. The results of the present solver in this range of the angles of attack do not indicate a laminar separation bubble. Angles 5.0°, 7.5° and 12.5° follow are clear linear trend. The prediction of the present solver are subsequently lower in the range $\alpha = 5.0°$ to $12.5°$. Beyond $\alpha = 12.5°$ the XFoil results predict a decrease in the lift slope $\frac{dC_l}{d\alpha}$. The maximum lift coefficient of $C_{l_{max}} = 1.35$ is predicted by XFoil at $\alpha = 15.0°$. Beyond $\alpha = 16.0°$ the airfoil enters the post stall region, based on the XFoil results. The numerical results of the present solver indicate a decrease

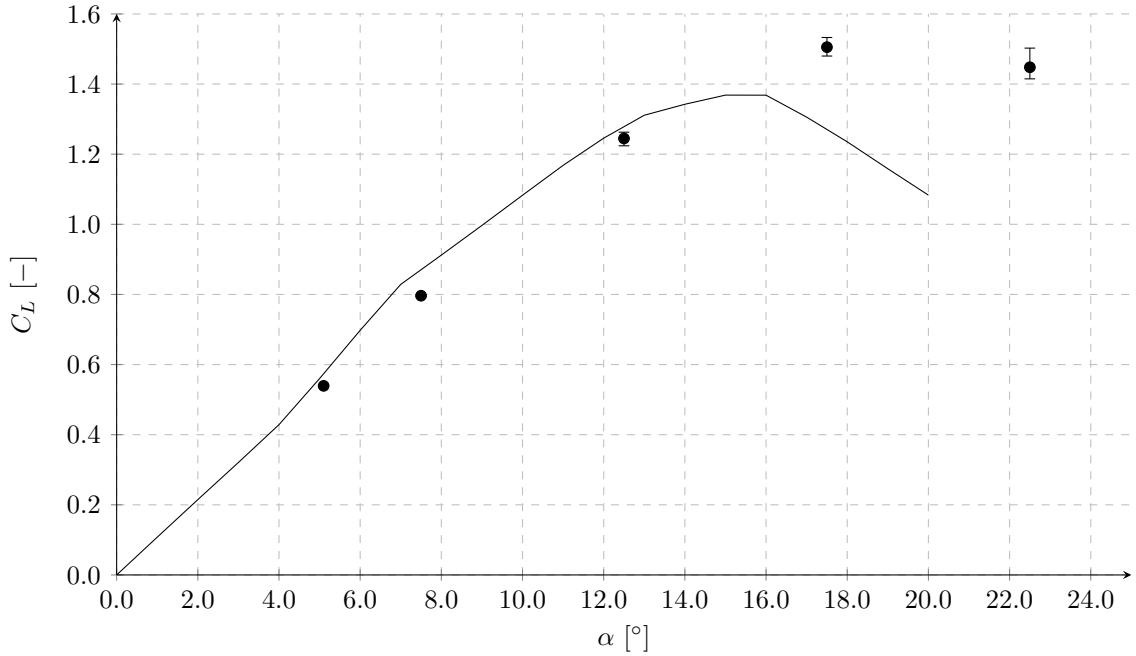

Figure 8.8: Lift coefficient C_L polar of NACA0012 airfoil at $Re = 980395$ and $Ma = 0.072$: (——) XFoil numerical results, (•) present results.

in the lift slope beyond 12.5°. The maximum lift coefficient is predicted at higher angles of 17.5°. A maximum lift coefficient of $C_{l_{max}} = 1.52$ is predicted by the present method. The results of the present solver indicate a decrease of the lift coefficient beyond an angle of attack of 17.5°. It must be stated that the prediction of the maximum angle of attack and maximum lift coefficient of the present solver contain significant uncertainties due to the sparse sampling of the lift polar at high angles of attack.

The discussion of the polar results is continued with the drag polar predictions. The drag polar predictions are shown in figure 8.9. The XFoil predictions show a slow increase in the drag coefficient in the angle of attack range $\alpha = [0.0°, 15.0°]$. A significant increase is found beyond the stall angle of the airfoil $\alpha = 15°$. From this point the drag of the airfoil increases from $C_D = 0.03$ up to a drag coefficient of $C_D = 0.16$ at an angle of attack of $\alpha = 20.0°$. The present code predicts significantly higher drag coefficients at the low angles of attack, $\alpha = 5.0°$, $\alpha = 7.5°$ and 12.5°. The drag prediction of the present code is approximately two times higher than the drag coefficient prediction of the XFoil solver. The flow field at the low angles of attack is attached. Therefore, the drag prediction discrepancies must be caused by discrepancies in skin friction rather than discrepancies in the pressure drag. The drag prediction of the present code crosses the drag polar of the XFoil code at approximately $\alpha = 17.0°$. Beyond this angle of attack the drag coefficient prediction of the present code are below the predictions of the XFoil code. However, this statement is based on a linear extrapolation of the XFoil drag polar up to an angle of attack of 22.5°. The low drag coefficient prediction at high angles of attack combined with the high lift coefficient indicate that the present code predicts smaller regions of separated flow at high angles of attack when compared to the XFoil results.

The discussion of the polar results is closed with the presentation of the pitching moment

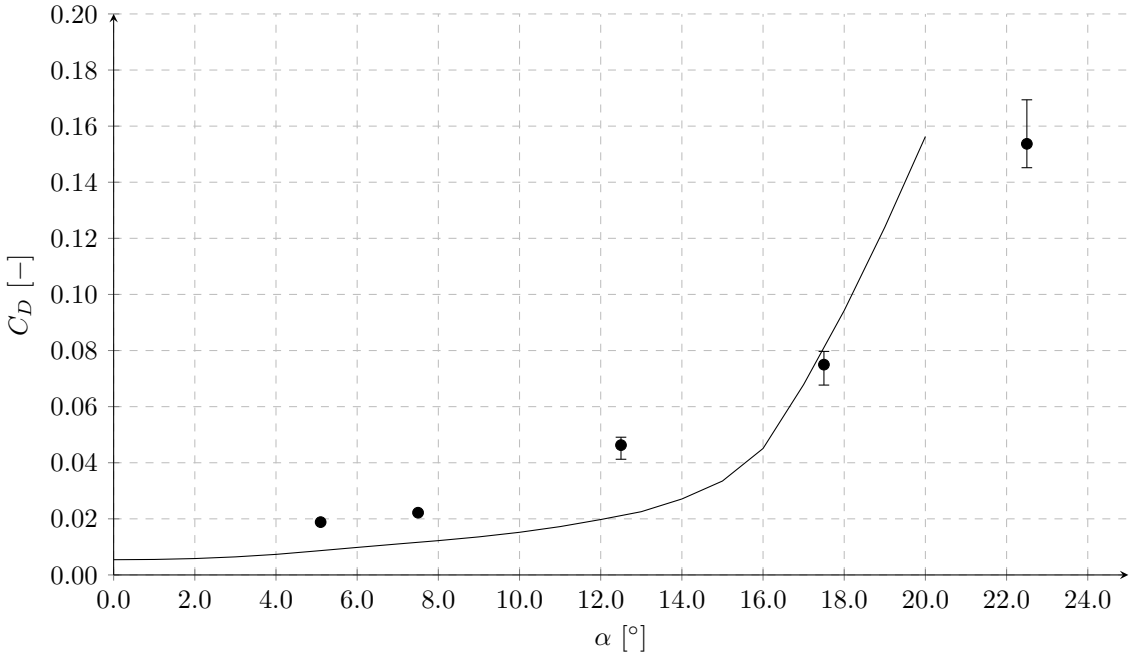

Figure 8.9: Drag coefficient C_D polar of NACA0012 airfoil at $Re = 980395$ and $Ma = 0.072$: (——) XFoil numerical results, (•) present results.

polar. The pitching moment polar is shown in figure 8.10. The pitching moment coefficient was measured around the quarter chord of the airfoil. Two significant non-linearities are found in the XFoil predictions of the pitching moment coefficient. Assuming that the airfoil pitching moment increases linearly in the angle of attack range $\alpha = [0.0°, 15.0°]$, a non-linearity is found in the angle of attack range $\alpha = [4.0°, 12.5°]$ and beyond the angle of attack associated with the maximum lift coefficient prediction $\alpha = 15.0°$. The initial non-linearity shows a significant decrease of the pitching moment coefficient with respect to the fictitious linear polar. The non-linearity is caused by the laminar separation bubble. The effective camber increase, which was introduced in the discussion of the lift coefficient polar, results in an increase in the lift coefficient but also in a significant pitch-down moment. The pitch-down moment prediction beyond $C_{L_{max}}$ are caused by the flow separation region on the suction side of the airfoil. The separation of the flow from the surface prevents the recovery of the pressure at the trailing edge. This results in a low pressure region at the trailing edge of the airfoil suction side. The low pressure region results in a significant increase in the pressure drag coefficient and in a pitch-down moment.

The present code predicts a quasi zero moment coefficient up to an angle of attack of 5.0°. Beyond 5.0°, the pitch-up moment coefficient increases up to the maximum angle of attack of 17.5°. A decrease in the pitch-up moment is found from the angle of attack 17.5° to the angle of attak of 22.5° indicating a small pitch break. The pitching moment results indicate that the present code predicts either a very small or no laminar separation bubble. Further the prediction of the pitch-down moment beyond the maximum lift coefficient is also significantly lower than the prediction obtained with the XFoil code.

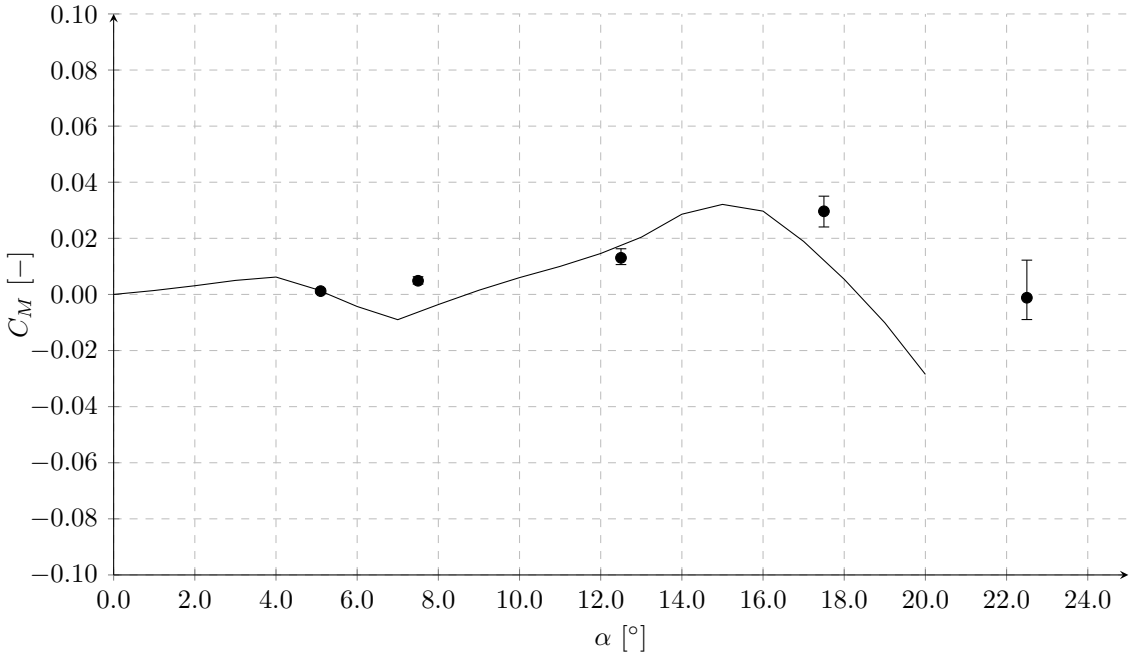

Figure 8.10: Moment coefficient C_M polar of NACA0012 airfoil at $Re = 980395$ and $Ma = 0.072$: (——) XFoil numerical results, (•) present results.

Surface solution

Predictions of the pressure coefficient and skin friction coefficient distributions were extracted from the simulation with XFoil and the present code to support the findings in the lift, drag and moment polars. The surface solutions were obtained for the selected angles of attack $\alpha = 5.0°$ and $\alpha = 12.5°$. The discussion of the surface solution is started with the pressure coefficient predictions. The pressure coefficient predictions at $\alpha = 5.0°$ are shown in figure 8.11. The pressure coefficient predictions at $\alpha = 12.5°$ are shown in figure 8.12. The pressure coefficient predictions at $\alpha = 5.0°$ indicate a good agreement between the prediction of the XFoil tool and present code. A slightly lower suction pressure peak combined with a lower pressure on the pressure side is found in the prediction of the present code. These indicate a lower circulation around the airfoil and subsequently a lower lift prediction. A lower lift prediction was found in the lift coefficient polar results. Two kinks are found in the pressure coefficient distribution predictions of the present code. The pressure coefficient plateaus at $x/c = 0.2$ on the suction side and shows a kink in the pressure distribution at $x/c = 0.47$ on the pressure side. Either kink is associated with the laminar turbulent transition location of the boundary layer. A small plateau or rather kink is found in the pressure coefficient prediction of the XFoil code on the suction side at $x/c = 0.15$.
Slightly larger discrepancies are found in the pressure coefficient predictions at $\alpha = 12.5°$. The present code predicts a significantly lower suction pressure peak of $C_{p_{min}} = -6.75$. This prediction is $\Delta C_p = 1.15$ higher than the prediction of the XFoil code. A significant pressure coefficient plateau is found in the prediction of the present solver at $x/c = [0.08, 0.16]$. The plateau indicates the laminar to turbulent transition location. The pressure coefficient plateau is found at $x/c = 0.025$ in the XFoil predictions. This

indicates that the boundary layer transition location is predicted earlier by the XFoil code at angle of attack 5.0° and 12.5°. The pressure coefficient with the reduced peak suction pressure and lower pressure side pressure coefficient confirms the lower lift coefficient found in the lift polar assessment.

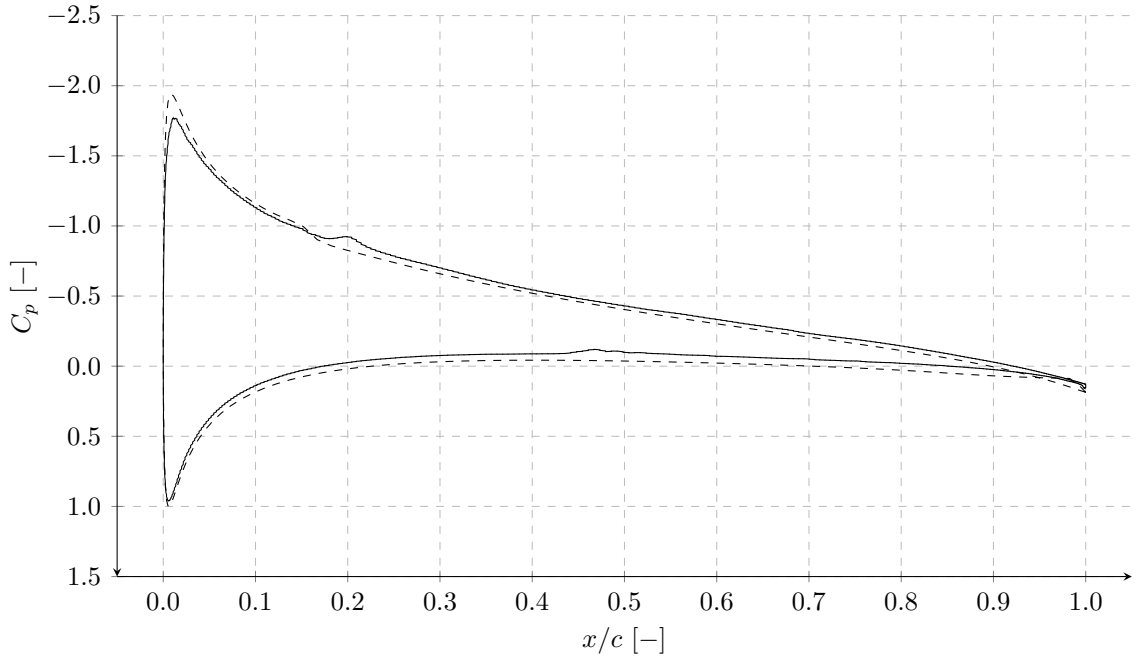

Figure 8.11: Temporally and spatially averaged pressure coefficient C_p versus x/c of NACA0012 airfoil at angle of attack $5.0°$: (——) present result, (- - -) XFoil numerical result.

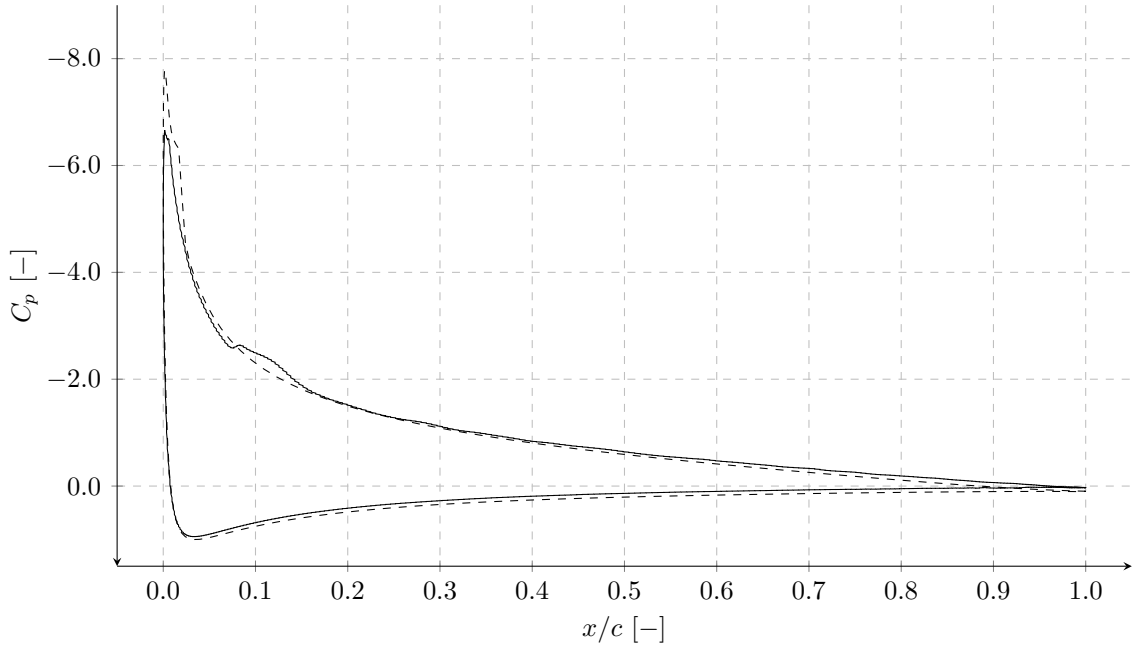

Figure 8.12: Temporally and spatially averaged pressure coefficient C_p versus x/c of NACA0012 airfoil at angle of attack $12.5°$: (——) present result, (- - -) XFoil numerical result.

The presentation of the surface solution is continued with the skin friction predictions at angles of attack $5.0°$ and $12.5°$. The skin friction coefficient predictions of the XFoil and the present code at an angle of attack of $5.0°$ are shown in figure 8.11. The XFoil predictions show a significantly higher skin friction coefficient on the suction side of the airfoil at the leading edge $x/c = 0.0$. The skin friction coefficient prediction is $\Delta C_f = 0.01$ higher than the predictions obtained with the present code. This is likely caused by an insufficiently refined mesh at the leading edge of the airfoil. The XFoil prediction indicates a sharp drop in the skin friction coefficient from it's peak at the leading edge to $x/c = 0.1$. The sharp drop in the skin friction coefficient is followed by a sharp increase in the skin friction coefficient at $x/c = 0.18$. This point indicates the laminar turbulent transition point of the suction side boundary layer. A monotone decrease of the skin friction coefficient is found in the XFoil predictions beyond $x/c = 0.2$ on the suction side. The pressure side prediction of XFoil show the initial increase in the skin friction coefficient in between the stagnation point at $x/c = 0.0$ and $x/c = 0.025$ followed by a monotone decrease towards the trailing edge. The predictions of the present solver show a quasi linear decrease of the skin friction coefficient on the suction side between the peak skin friction coefficient at $x/c = 0.01$ and $x/c = 0.21$. In the region $x/c = [0.21, 0.4]$ the skin friction coefficient increases on the suction side of the airfoil indicating the laminar to turbulent transition location. A monotone decrease is found in the skin friction coefficient prediction of the present code beyond $x/c = 0.4$. The predictions of the present solver show an increase in the skin friction coefficient on the pressure side from the stagnation point at $x/c = 0.01$ up to $x/c = 0.15$. The skin friction coefficient decreases until $x/c = 0.5$ on the pressure side, after which an increase is found in the range $x/c = [0.5, 0.7]$ followed by a further decrease until the trailing edge of the airfoil. The results show that the present code pre-

dicts that the laminar turbulent transition region is stretched over a significant portion of the airfoil. To be precise a transition region was found in the range $x/c = [0.21, 0.4]$ on the suction side and $x/c = [0.5, 0.7]$ on the pressure side. The present code predicts a laminar turbulent transition location on the pressure side which is not present in the XFoil predictions. The results further show that the predictions of the skin friction coefficient in the laminar regions of the boundary layer are significantly higher than the skin friction predictions obtained with the XFoil code. These findings lead to a significantly higher skin friction prediction on the pressure side of the airfoil and a significantly higher skin friction prediction in the laminar region of the suction side in the range $x/c = [0.02, 0.2]$. A good agreement between the XFoil predictions and the present code is only found in the turbulent boundary layer region on the suction side of the airfoil downstream of $x/c = 0.4$.

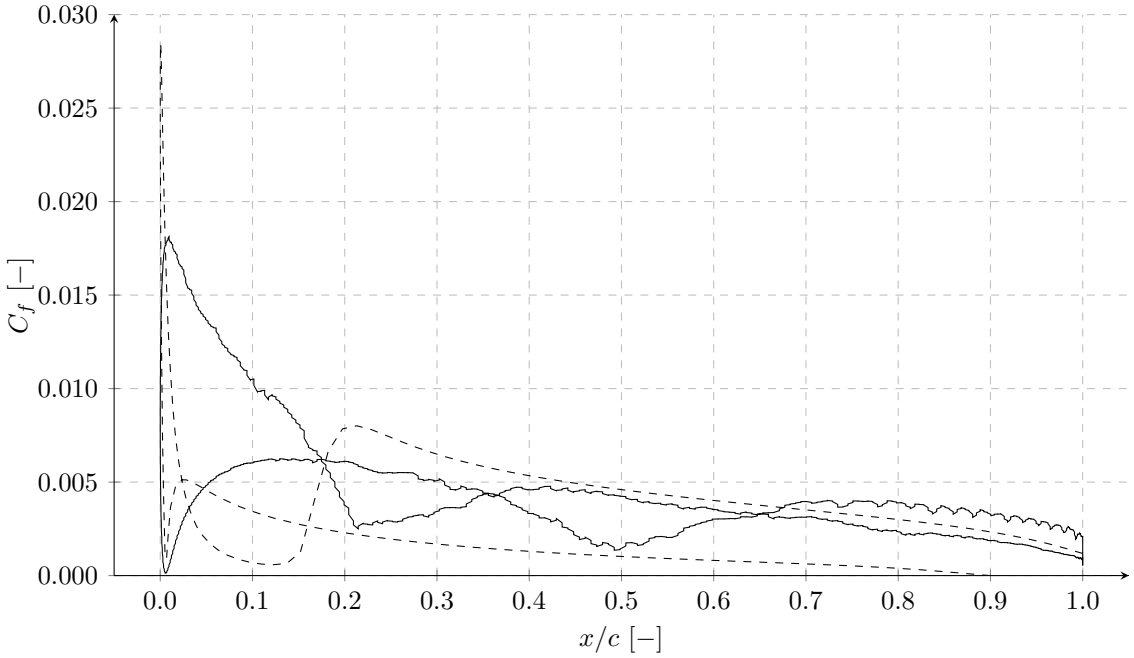

Figure 8.13: Temporally and spatially averaged skin friction coefficient C_f versus x/c of NACA0012 airfoil at angle of attack $5.0°$: (——) present result, (- - -) XFoil numerical result.

The results of the skin friction coefficient at angle of attack $12.5°$ are shown in figure 8.14. The conclusion drawn on the skin friction results at angle of attack $5.0°$ can largely be applied to the higher angle of attack as well. A significant underprediction is found in the peak skin friction coefficient at the leading edge of the airfoil. Again indicating an insufficiently refined numerical mesh in that area. Discrepancies in the prediction of the suction side laminar turbulent transition point were found in the assessment of the pressure coefficient. The skin friction coefficient preditions confirm this assessment. A laminar turbulent transition point is found at $x/c = 0.05$ in the XFoil results and in the range $x/c = [0.1, 0.22]$ in the predictions of the present code. The skin friction coefficient predictions of the present code in the laminar region are significantly higher than the predictions of the XFoil code. The skin friction prediction of the present code and XFoil

code on the suction side downstream of $x/c = 0.25$ agree well. A significantly higher skin friction prediction is found on the pressure side of the airfoil in the predictions of the present code. Neither code predicts a laminar turbulent transition region on the pressure side of the airfoil.

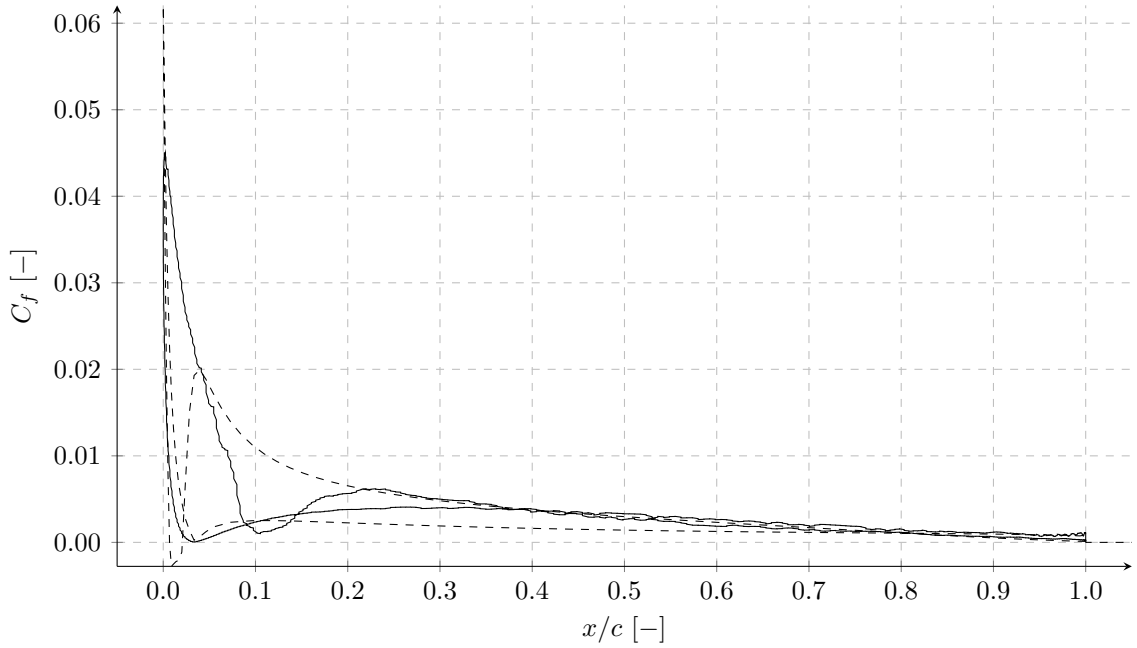

Figure 8.14: Temporally and spatially averaged skin friction coefficient C_f versus x/c of NACA0012 airfoil at angle of attack $12.5°$: (——) present result, (- - -) XFoil numerical result.

Discussion

Results of the flow field and forces of the NACA0012 airfoil at static angles of attack were shown. The results were computed with the XFoil tool and the present solver. Significant differences were found in the drag coefficient and stall predictions. All discrepancies are attributed to the prediction and modeling of the near-wall flow field. The differences in the modeling approach for the boundary layer flow field leads to differences in the shear-stress and displacement thicknesses but also differences in the flow features such as laminar turbulent transition. Experimental results are not available for the specific flow case of the NACA0012 airfoil at the selected Reynolds and Mach number. Therefore, it is not possible to conclude which prediction is more accurate. But, some drawbacks of the present flow solver for the simulation of flow around airfoils can be highlighted based on the results. The use of the equilibrium wall model without consideration of laminar and turbulent regions lead to wrong predictions of the shear-stress. The miss-predictions of the shear-stress is apparent in the laminar regions of the boundary layer on the suction and pressure side where signifcant skin friction over-predictions were found. Due to the use of the octree-based cartesian mesh a resolution of the boundary layer especially around the leading edge of the NACA0012 is not viable, as the computational cost would significantly increase. As the boundary layer in this region is below the mesh resolution,

an underprediction of the shear-stress is likely. The under-prediction of the skin friction coefficient was confirmed with the XFoil results at angles of attack 5.0° and 12.5°. The insufficient mesh resolution around the leading edge of the airfoil combined with the poor skin friction prediction in this area leads to discrepancies and likely errors in the laminar turbulent transition location prediction of the present code. A good prediction of the boundary layer characteristics is crucial for an accurate prediction of stall as the prediction of the wall model determines the amount of energy that is taken from the near-wall flow field and subsequently determine the exact separation location. Therefore the large discrepancies found in the stall predictions of XFoil and the present code should be attributed to differences in the boundary-layer predictions.
Results of a mesh convergence study were presented. The mesh convergence study did not show an asymptotic behavior of the integral lift coefficient indicating that a further mesh refinement is required to obtain a grid-converged solution in the statistical sense. The investigation of the surface solution and flow field showed that the laminar turbulent transition points were effected by the grid resolution. One can therefore argue that the near wall solution of the flow field is insufficiently refined.
A near-wall mesh resolution of $\Delta/c = 0.98 \cdot 10^{-3}$ is selected for the dynamic stall simulations. Errors are expected in the results of the dynamic stall simulation due to the insufficient mesh resolution. However, the mesh resolution is sufficient for an initial assessment of the moving immersed boundary framework for high Reynolds number flow.

8.7 Dynamic analysis

The chapter is closed with the presentation of the dynamic stall simulation results of the NACA0012 airfoil. The flow problem, simulation setup and reference results have been extensively studied in the previous sections. This section presents the results of the dynamic stall simulation and compares the results to the experimental study of Mcalister et al. (1982a) and the numerical simulations of Ribeiro et al. (2016). The section discusses the lift, drag and moment measurements over one oscillation period. Contour plots of the flow field are presented at selected time steps to assess the presence of the flow features discussed in section 8.2. The simulations were performed with two phases. In phase 1 the airfoil was kept at a static angle of attack of 5.0°, which corresponds to the minimum angle of attack of the oscillation, and in phase 2 the airfoil undergoes the prescribed sinusoidal oscillation. The initial phase was used to remove the initial part of the transient solution from the results. The initial phase was performed over approximately 11 flow over times. The integral lift, drag and moment coefficients were gathered over one period.

8.7.1 Integral forces and moments

The analysis of the dynamic stall results is started with plots of the integral lift, drag and moment coefficients of the airfoil. The integral coefficients are plotted against the pitch angle of the airfoil profile. The pitch-up motion is indicated by solid lines and filled circles. The pitch-down phase is indicated by dashed lines and hollow circles. The plot of the lift coefficient is shown in figure 8.15, the plot of the drag coefficient is shown in figure 8.16 and the moment coefficient is shown in figure 8.17.

The discussion of integral coefficient is started with the airfoil lift coefficient, shown in figure 8.15. The numerical and experimental results show that all methods agree well on the initial pitch-up motion in the angle of attack range $\alpha = [5.0°, 20.0°]$. All methods follow a quasi linear trajectory and exceed the expected maximum lift coefficient angle of attack of approximately $\alpha = 15.0°$. The numerical results of the present code and Ribeiro et al. (2016) show a slight overprediction in the C_L compared to the experimental results. The numerical results deviate at an angle of attack of $\alpha = 20.0°$. The numerical results of Ribeiro et al. (2016) follow the experimental results more closely. The experimental results and numerical results show the distinct lift increase caused by the leading edge vortex. A maximum lift coefficient of $C_L = 2.15$ is found in the experimental and reference numerical results. The numerical results of the present code show an initial flattening of the lift slope and a distinct increase in the lift coefficient only at $\alpha = 24.8°$. A similar maximum lift coefficient is found in the results of the present code. The results indicate that the present code predicts the separation of the leading edge vortex at significantly higher angles of attack than the experimental and reference numerical results. Beyond the stall point all methods predict a significant decrease in the lift coefficient. The experimental results and numerical results of the present code predict a lift coefficient post stall $\alpha = 25.0°$ of around $C_L = 1.0$. Slightly higher predictions are given by the numerical reference results. All results show an increase in the lift coefficient after the initial stall break. The experimental and numerical results show an increase of the lift to $C_L = 1.5$. The present numerical results predict an increase of the C_L to 1.3. More importantly, however, is a phase shift in the C_L increase. The experimental and reference numerical results show the C_L increase during the pitch-down motion close to the maximum angle of attack of $\alpha = 25.0°$. The numerical results of the present code show the increase in the lift coefficient at a later point during the pitch-down motion at $\alpha = 23.0°$.

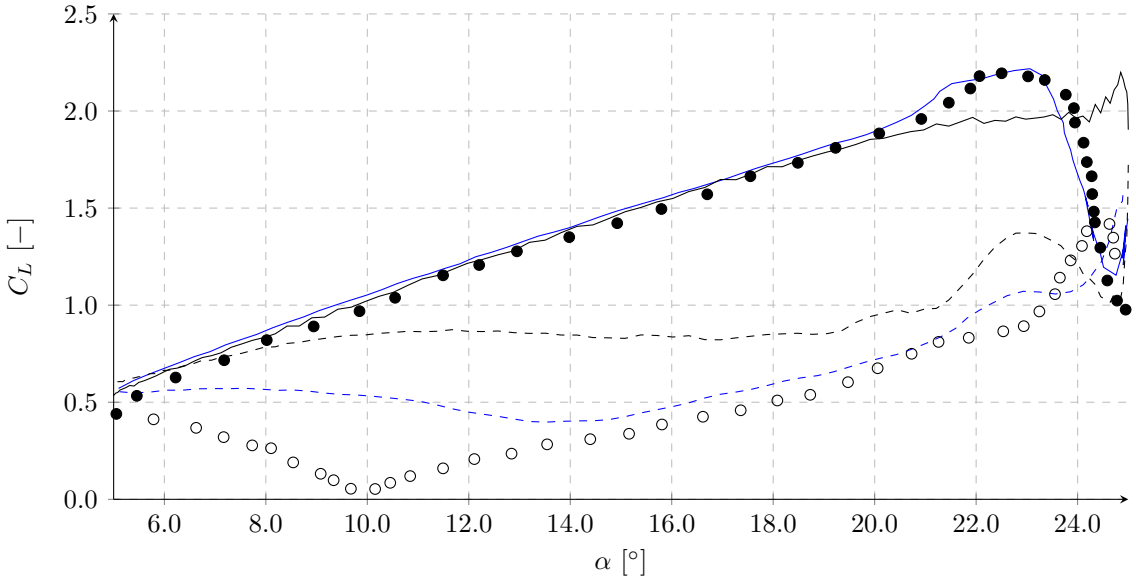

Figure 8.15: Plot of the lift coefficient C_L versus airfoil pitch-up angle α based on: (•) experimental results of Mcalister et al. (1982a), (——) numerical results of Ribeiro et al. (2016) and (——) present results. If available solid lines and markers indicate pitch-up movement, dashed lines and hollow markers indicate pitch-down movement.

The numerical and experimental results differ significantly in the post stall region $\alpha < 23.0°$. All results show deviations in the C_L between the pitch-up and pitch-down motion of the oscillation which indicates significant hysteresis in the airfoil flow field. The magnitude of the lift coefficient differs significantly between the numerical and experimental results. The numerical results of the present code predict a minimum lift coefficient of $C_L = 0.8$ in the post stall region. The reattachment of the flow field is found at approximately $\alpha = 8.0°$ where the C_L curves of the pitch-up and pitch-down motion converge. The reference numerical results show a minimum lift coefficient of $C_L = 0.4$ in the post stall region. The reference numerical results follow the experimental results closely down to an angle of $\alpha = 14.0°$. The prediction depart at this point. The C_L prediction of the reference numerical results flatten and return to the C_L of the pitch-up motion. The C_L converges with the C_L of the pitch-up motion at an angle of attack of $\alpha = 5.0°$. The experimental results show a further decay in the C_L within the post stall region. The C_L reaches a value of $C_L = 0.0$ at $\alpha = 10.0°$. An increase is found in the C_L below 10.0°. The C_L converges with the C_L of the pitch-up motion at an angle of attack of $\alpha = 5.0°$. The discrepancies between the numerical results of the present code and the numerical results of Ribeiro et al. (2016) have been in partly assessed in Ribeiro et al. (2016). Ribeiro et al. (2016) investigated the effect of the windtunnel wall boundary condition on the numerical results. They concluded that slip and no-slip wall boundary condition lead to substantial differences in the post stall lift coefficient prediction. Therefore the differences in the windtunnel wall boundary condition combined with the prediction of the stall flow field are likely the cause of the large discrepancies in the numerical results. No explanation can be given for the large discrepancies between the reference numerical results and the experimental results in the pitch-down phase below $\alpha = 14.0°$. Non of the other reference

numerical results have predicted lift coefficient as low as the ones found in the experimental study.
The discussion is now directed to the moment coefficient results of the numerical and experimental studies. The moment coefficient predictions are shown in figure 8.17. The predictions and measurements show a good agreement in the initial pitch-up motion of the airfoil up to an angle of attack of 18.0°. The pitching moment predictions follow a linear trend. The numerical results show slightly lower pitching moment predictions than the experimental measurements. The predictions and measurements depart at $\alpha = 18.0°$. All predictions show a drop in the moment coefficient beyond $\alpha = 18.0°$. However, the location of the minimum moment coefficient prediction differ. The numerical results of Ribeiro et al. (2016) predict the minimum moment coefficient at $\alpha = 23.5°$ with a value of $C_M = -0.48$. The experimental measurements show the minimum moment coefficient at $\alpha = 24.0°$, with a value of $C_M = -0.4$. The numerical results of the present code predict the minimum moment coefficient at an angle of $\alpha = 25.0°$, with a value of $C_M = -0.45$. The results show that the strength of the leading edge vortex and the separation angle of the leading edge vortex varies significantly between the numerical and experimental simulations. The predictions and measurements align well with results of the lift coefficient. Lower discrepancies are found in the pitch-down part of the airfoil motion. The numerical results converge at an angle of 12.0° and show no discrepancies in the angle range $\alpha = [5.0°, 12.0°]$. A significant pitch-up is found in the experimental results in the pitch-down part of the oscillation at $\alpha = 10.0°$. The angle of the maximum moment coefficient in the experiment is aligned with the angle of the minimum lift coefficient. The findings in the results of the moment coefficient align well with the findings in the lift coefficient plot. The pitch-down break of the airfoil is signifcantly delayed due to the late separation of the leading edge vortex. The same mechanism led to a late prediction of the maximum lift coefficient.

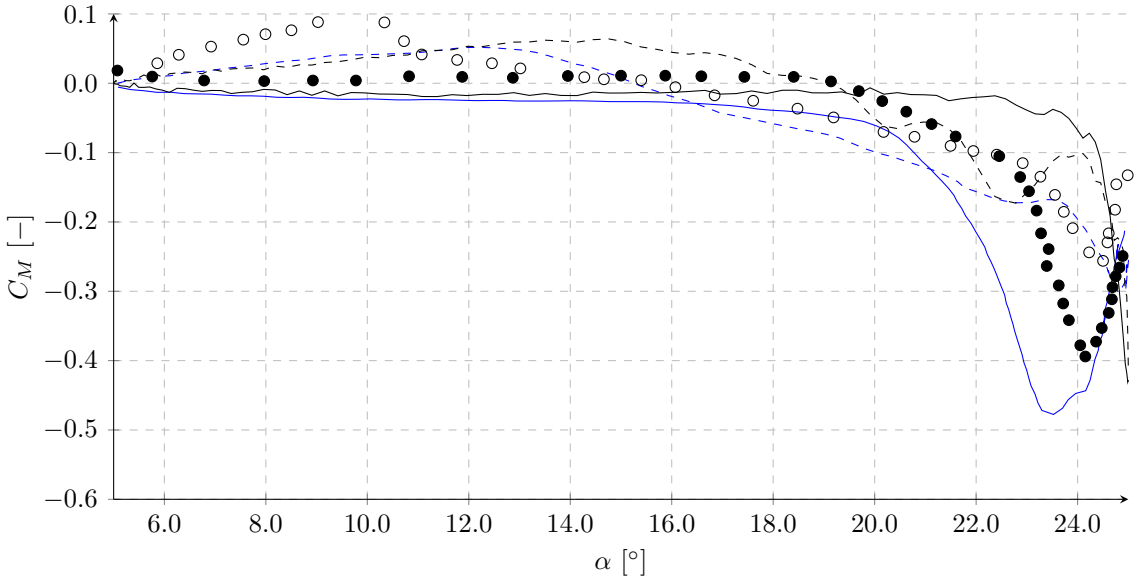

Figure 8.16: Plot of the moment coefficient C_M versus airfoil pitch-up angle α based on: (•) experimental results of Mcalister et al. (1982a), (——) numerical results of Ribeiro et al. (2016) and (——) present results. If available solid lines and markers indicate pitch-up movement, dashed lines and hollow markers indicate pitch-down movement.

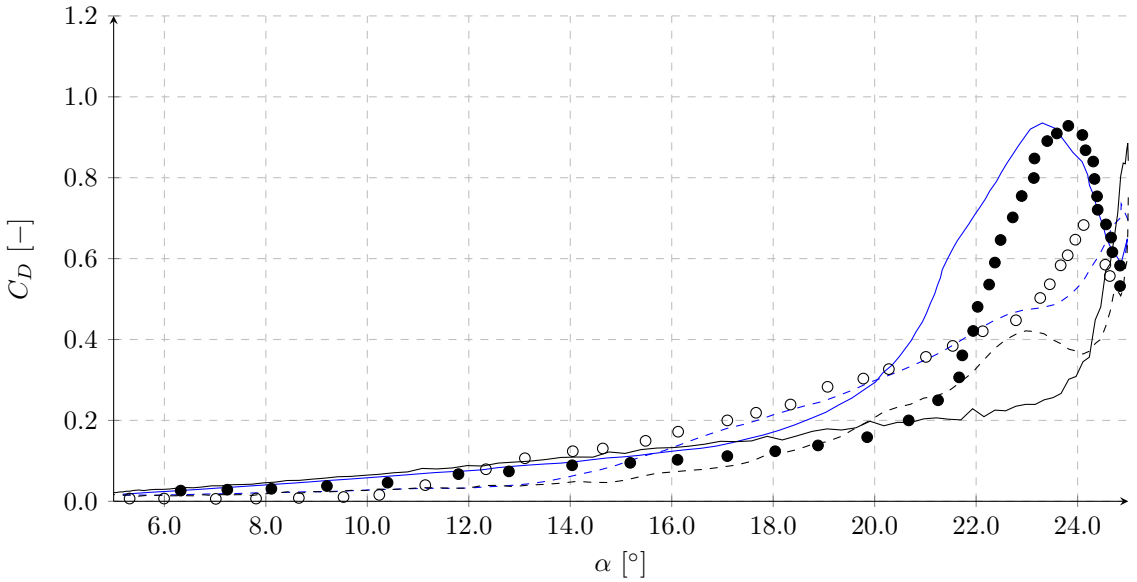

Figure 8.17: Plot of the drag coefficient C_D versus airfoil pitch-up angle α based on: (•) experimental results of Mcalister et al. (1982a), (——) numerical results of Ribeiro et al. (2016) and (——) present results. If available solid lines and markers indicate pitch-up movement, dashed lines and hollow markers indicate pitch-down movement.

The discussion of the integral coefficients is finished with an assessment of the drag coef-

ficient. The drag coefficient predictions and measurements are shown in figure 8.16. The findings are very similar to the findings in the lift and moment coefficient plots. A good agreement is found in the initial part of the pitch-up motion, $\alpha = [5.0°, 18.0°]$, between the numerical and experimental results. Discrepancies in the prediction of the leading edge vortex strength and separation angle leads to differences in the maximum drag coefficient both in the magnitude and angle of attack. A maximum drag coefficient of $C_D = 0.95$ is found in the reference numerical results and experimental measurements. The maximum drag coefficient is located at $\alpha = 23.0°$ in the reference numerical results and $\alpha = 24.0°$ in the experimental measurements. The results of the present code show a late maximum drag coefficient with a value of $C_D = 0.9$ at an angle of $\alpha = 25.0°$. The pitch-down motion shows a good agreement between the reference numerical results and experimental results. An under-prediction of the drag coefficient is found in the results of the present code. The numerical results agree well in the later part of the pitch-down motion $\alpha < 14.0°$.
The integral lift, drag and moment coefficient of the airfoil have been shown over one period of the airfoil oscillation. The results showed that the experimental and the numerical results of the present code and Ribeiro et al. (2016) predict the key flow features. The predictions and measurements showed the expected linear increase in the lift coefficient up to to the maximum lift coefficient of the NACA0012 airfoil at static angles. The results showed a further increase in the lift coefficient beyond the maximum lift coefficient of the NACA0012 airfoil. The distinct lift increase was found close to the maximum angle of attack in the pitch-up motion caused by the formation of the leading edge vortex. Further, the drop in the lift coefficient was shown in all results and a substantial hysteresis region was present in all numerical predictions and measurements. The pitch-down break of the airfoil associated with the leading edge vortex separating from the leading edge was found in all measurements and predictions and the significant pressure drag increase caused by the vortex was found in the results.
The results showed significant differences in the prediction of the airfoil stall point. The results of the present code showed a significant delay of the airfoil stall similar to the one found in the static analysis. The mechanism which lead to the delayed stall estimation is likely identical to the ones discussed in the static analysis. The delayed stall prediction of the present code were identified in all three integral coefficients as they resulted in a delayed prediction of the maximum lift coefficient a delayed prediction in the airfoil pitch break and delayed prediction in the maximum drag coefficient. Substantial differences were also found in the post stall region of the airfoil oscillation. The C_L prediction between the numerical and experimental results differed significantly. The present code predicted high lift coefficients in the post stall region. The differences in the numerical results of the present code and numerical results of Ribeiro et al. (2016) were connected to the differences in the windtunnel wall boundary conditions. The difference between the experimental results and reference numerical results could not be attributed to any concrete modeling errors.

8.7.2 Flow field

Slices of the velocity field are extracted from the numerical simulations. The contour plots of the velocity are extracted at specific points in time to show the prediction of the significant flow features. A discussion of the flow features in the dynamic stall problem is

held in section 8.2. The presented plots follow one period of the airfoil oscillation. Figure 8.18 shows the flow field in phase 1 of the airfoil motion. The flow field is attached and the lift, drag and moment coefficient follow the NACA0012 airfoil at static angles of attack. The flow field at an angle of attack beyond the maximum angle of attack of the airfoil is shown in figure 8.19. The flow field corresponds to phase 2 of the airfoil oscillation. The flow field shows that the suction side is separated. The separation location is at the leading edge of the airfoil. The flow field is shown at an angle of attack of $\alpha = 23.7°$. The detachment of the leading edge vortex is shown in figure 8.20. The leading edge vortex is highly distorted and mixed by the turbulence in the flow field. The flow field was extracted at $\alpha = 25.0°$. The flow field corresponds to phase 3 of the dynamic stall problem. The post stall flow field is shown in figures 8.21 and 8.22. Figure 8.21 shows the flow field around the airfoil in the pitch-down part of the oscillation at $\alpha = 20.0°$. The flow field corresponds to phase 4 of the dynamic stall flow problem. A large separation is seen on the suction side of the airfoil. Large turbulence scales are seen in the wake of the airfoil, likely part of the leading edge vortex. The reattachment of the boundary layer on the airfoil surface is shown in 8.22. Figure 8.22 shows the flow field around the NACA0012 airfoil at $\alpha = 15.0°$. Large parts of the boundary layer are attached on the airfoil suction side. The turbulent scales in the wake of the airfoil remain large.
The plots of the flow field around the airfoil confirm that the present code is able to predict the key flow features of the dynamic stall problem.

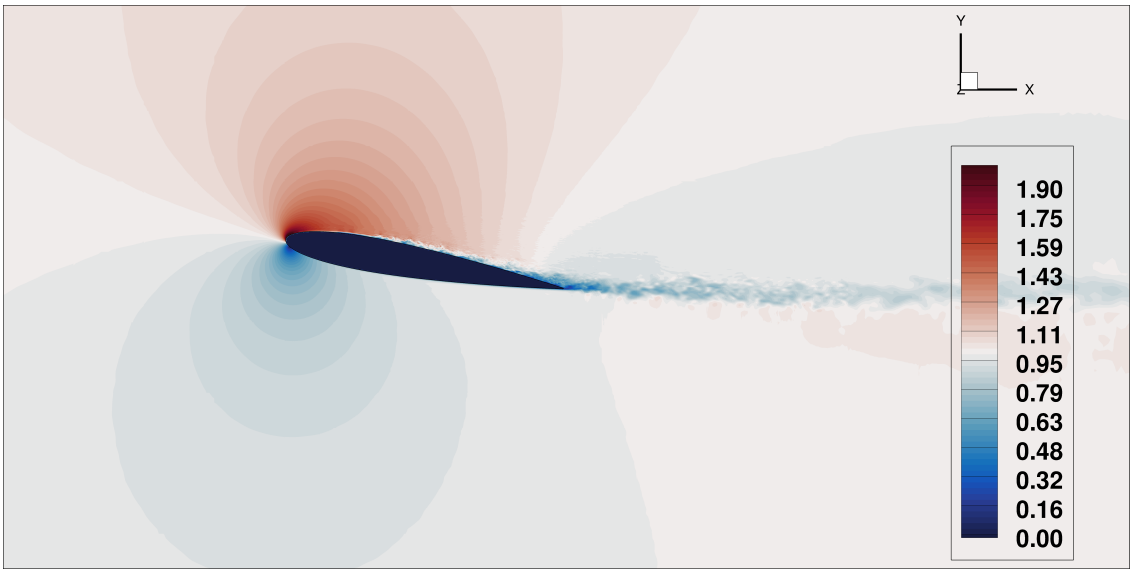

Figure 8.18: Slice of normalized velocity magnitude field $|\mathbf{U}|/U_\infty$ around NACA0012 airfoil at $10.0°$ angle of attack during the pitch-up movement for the illustration of the flow structures corresponding to phase 1 of the dynamic stall problem.

8.8 Discussion and Conclusion

The experimental studies of Mcalister et al. (1982a) on dynamic stall of helicopter blade sections have been used to define a validation case for the present code. The validation case is used to validate the hybrid ghost-cell method for moving geometries at high Reynolds

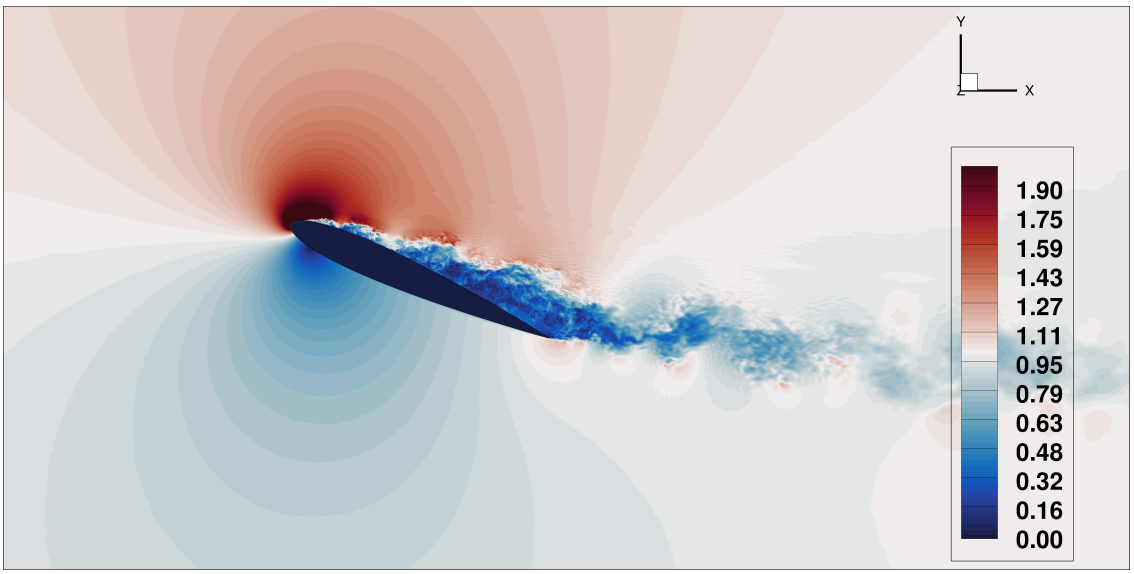

Figure 8.19: Slice of normalized velocity magnitude field $|\mathbf{U}|/U_\infty$ around NACA0012 airfoil at $23.7°$ angle of attack during the pitch-up movement for the illustration of the flow structures corresponding to phase 2 of the dynamic stall problem.

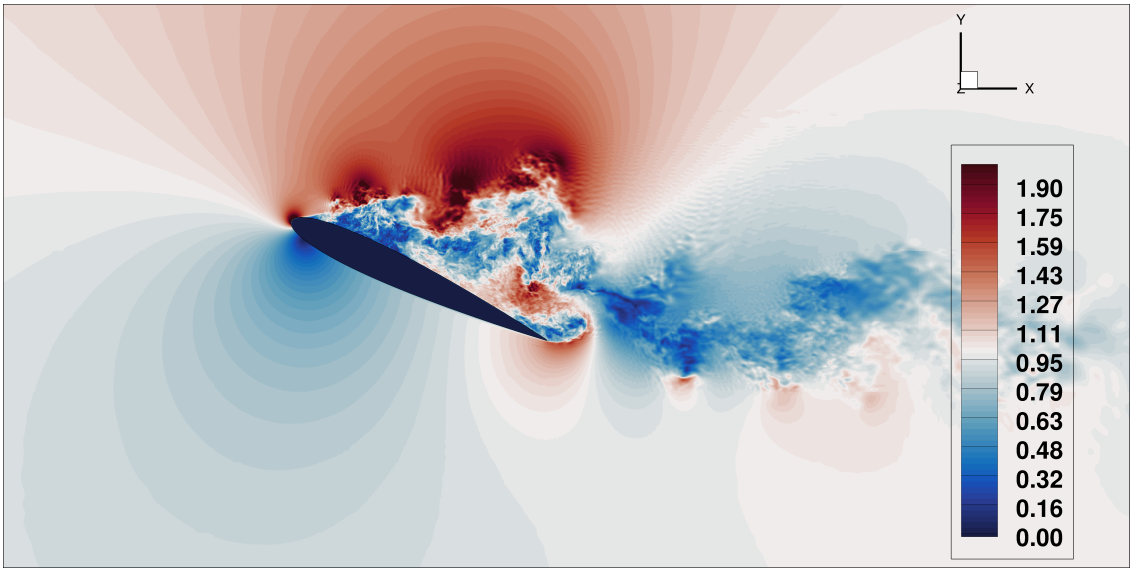

Figure 8.20: Slice of normalized velocity magnitude field $|\mathbf{U}|/U_\infty$ around NACA0012 airfoil at $25.0°$ angle of attack during the pitch-up movement for the illustration of the flow structures corresponding to phase 3 of the dynamic stall problem.

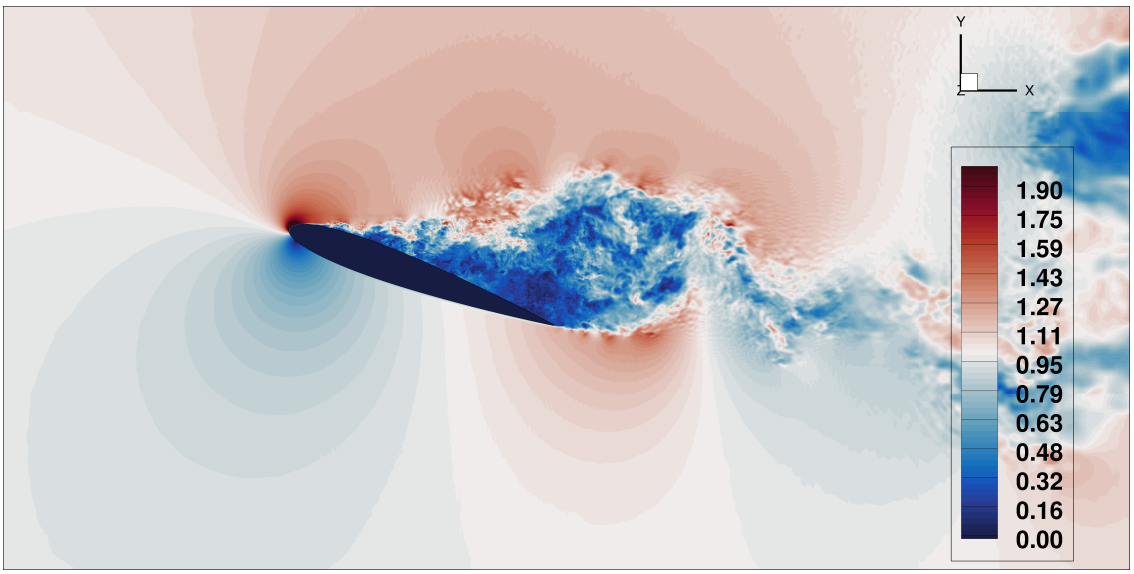

Figure 8.21: Slice of normalized velocity magnitude field $|\mathbf{U}|/U_\infty$ around NACA0012 airfoil at $20.0°$ angle of attack during the pitch-down movement for the illustration of the flow structures corresponding to phase 4 of the dynamic stall problem.

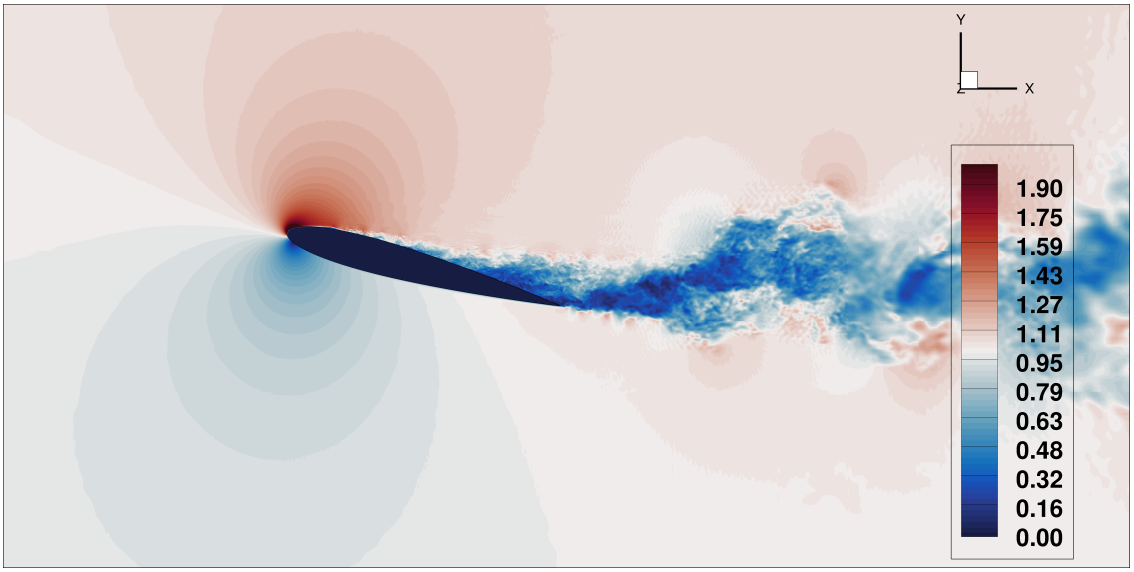

Figure 8.22: Slice of normalized velocity magnitude field $|\mathbf{U}|/U_\infty$ around NACA0012 airfoil at $15.0°$ angle of attack during the pitch-up movement for the illustration of the flow structures corresponding to phase 5 of the dynamic stall problem.

numbers. The validation case consists of a NACA0012 airfoil at $Re = 1 \cdot 10^6$ and $Ma = 0.072$. The NACA0012 airfoil undergoes an oscillation motion which results in an unsteady flow field and results in a dynamic stall problem. The case was extensively investigated with numerical tools in literature. The numerical simulations in literature have been used as reference for the setup of the numerical simulation with the present solver. The numerical results of Ribeiro et al. (2016) have been used in combination with experimental results in the discussion of the numerical results of the present code.
Simulations at static and dynamic angles of attack were performed. Data for the static angles of attack was not given in either reference. Therefore, XFoil simulations have been performed to verify the present code with results from other numerical codes. The numerical results at static angles of attack showed good agreement in the attached flow region of the airfoil polar, but significant differences in the maximum lift coefficient and associated angle of attack. Further, analysis of the polars and surface solution indicated significant deficits in the resolution and modeling of the near-wall flow solution. Deficits in the mesh resolution were indicated by a significant underprediction of the skin friction coefficient around the leading edge of the airfoil and the inability of the simulations to accurately predict the laminar-turbulent separation bubble. Moreover, no asymptotic behavior was found in the mesh convergence study, which further indicates that additional mesh resolution is required in the near-wall flow field. Deficits in the near-wall modeling were found in the shear-stress prediction. The present code does not make a distinction between laminar and turbulent flow in the wall-modeling approach. This resulted in a significant over-prediction of the skin friction coefficient and airfoil drag at low angles of attack.
The simulation of the NACA0012 in dynamic stall conditions was subsequently performed. The information of the mesh convergence study and the setup of the reference numerical results of Ribeiro et al. (2016) have been used to appropriately size the numerical domain and mesh. Results of the lift, drag and moment coefficient were shown over one period of the airfoil oscillation. Additionally, plots of the velocity magnitude were shown at selected times over one period of the airfoil oscillations. The flow field showed that the present code is able to predict the presence of the 5 phases of the dyanmic stall cases. The most important being the substantial increase in the lift coefficient due to a leading edge vortex at the stall condition and a large hysteresis region in the post stall region. The lift, drag and moment coefficient plots indicated significant discrepancies around the stall region of the airfoil and in the lift coefficient in the post stall region. The lift, drag and moment coefficients did show the important features that are expected from the dynamic stall problem, which are the distinct increase in the lift coefficient caused by the leading edge vortex. The substantial drop in the lift coefficient once the leading edge vortex detaches from the airfoil combined with a significant increase in drag and a pitch-down moment, and the signicant hysteresis in the lift coefficient in the post stall state of the airfoil flow field. The results indicated that the present code mispredicts the exact point of stall. This leads to a significant misprediction of the angle of attack of the maximum lift coefficient in the dynamic stall condition. The maximum lift coefficient was found at significant higher angles of attack then in the reference numerical and experimental results. The misprediction of the stall point led to a phase shift in the flow features and forces in the post stall region. Both the pitch break and significant increase in the airfoil drag were found at significant higher angles of attack and further in the beginning of the pitch-down part of the motion. The misprediction of the lift coefficient in the post-stall

state was largely attributed to the difference in the modeling of the wind tunnel walls. It was concluded that the insufficiently refined mesh in combination with the deficit in the near-wall modeling approach, that caused the misprediction in the static stall condition, have equally caused the misprediction in the dynamic stall case.

Chapter 9

Flutter of a sprung airfoil

Flutter is an aero-elastic phenomenon in which a structure oscillates/vibrates in an uncontained manner due to the coupling of aerodynamic and elastic forces. The criticality of studying aero-elastic phenomena such as flutter was illustrated in the Tacoma Narrows bridge catastrophe in 1940 (Green & Unruh, 2006), where the coupling between the structural response of the bridge and wind resulted in the collapse of the bridge. For design purposes or for the fundamental study of flutter phenomena the aero-elastic problem may be simplified to a mass-spring model. Such models have been extensively studied experimentally and numerically in literature. For the study of vortex induced vibrations of spring-mounted cylinders and square cylinders have been studied. Khalak and Williamson (1999) experimentally studied the motion of a sprung mounted cylinder with one degree of freedom at low mass damping. Later Jauvtis and Williamson (2003) studied the vortex-induced vibration of a cylinder with two degrees of freedom experimentally. Similar problems were also studied numerically by Evangelinos, Lucor, and Karniadakis (2000) who performed direct numerical simulations of the flow around a flexible cylinder subject to vortex-induced vibrations and Guilmineau and Queutey (2002) analyzed the vortex shedding of an oscillating circular cylinder numerically.
A more suitable problem for the developed code is the study of spring-mounted airfoils and the computation of the flutter boundary of those. Schwarz et al. (2009) performed high-fidelity numerical simulations of the flow around a spring-mounted airfoil in transonic flow. Experiments and numerical simulations were performed at lower Mach number and in the transitional Reynolds number regime by Poirel, Harris, and Benaissa (2006, 2008) and Métivier, Dumas, and Poirel (2008); Métivier, Dumas, and Poitrel (2009) respectively. A more recent study on a NACA0012 airfoil with two degrees of freedom in the transitional Reynolds number regime was performed by Wood et al. (2020); De Nayer, Breuer, and Wood (2020). Wood et al. (2020) studied the problem experimentally, while De Nayer et al. (2020) provided numerical simulations to support the experimental results of Wood et al. (2020). The experiment consists of a NACA0012 airfoil which undergoes both pitch and heave motions. The airfoil is mounted with two springs, a torsional spring for the pitch axis and a plate spring for the heave motion of the airfoil. The aero-elastic problem with the relevant parameters is illustrated in figure 9.1.

The well documented simulation setup and material properties in combination with the supporting numerical simulations by De Nayer et al. (2020) provide a good validation test case for the rigid body solver and the fluid-solid coupling scheme implemented in the present solver. This chapter presents numerical results of the present solver for the experiment of Wood et al. (2020).
Section 9.1 discusses the experimental setup of Wood et al. (2020) and the numerical simulation of De Nayer et al. (2020) in more detail, followed by a discussion on the aero-elastic problem in section 9.2. A dimensional analysis was performed to derive a non-dimensional setup for the simulation with acceptable computational cost. The results of this analysis are presented in section 9.3. With the derived non-dimensional setup the simulation domain, boundary conditions and discretization was set. The setup of the simulation is presented in section 9.4. The result section is split into two parts. Simulation in still air were performed first to validate the rigid body solver. Finally the results of the still air simulations are presented in section 9.5. The free-oscillation results of the NACA0012 airfoil under wind load are presented in section 9.6.

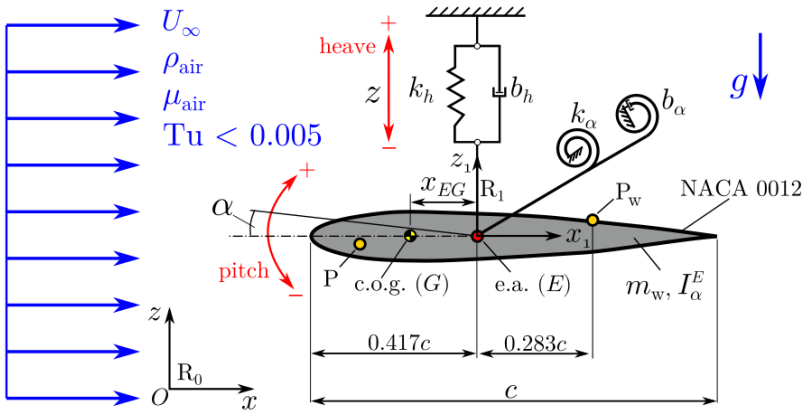

Figure 9.1: Schematic representation of the investigated FSI case with all relevant parameters, taken from Wood et al. (2020).

9.1 Experiment and numerical simulation

The experiment of Wood et al. (2020) was conducted to create a validation case for FSI tools. Therefore, a lot of attention was paid on the documentation of the boundary condition and characterization of the structural model. The test article consisted of a wing with $b = 600mm$ span and $c = 100mm$ chord. Only $500mm$ of the wing span was effectively submerged in the flow field given the $500mm$ width of the test section (Wood et al., 2020). The symmetric NACA0012 airfoil is used to define the profile of the planar wing. The test article is elastically mounted with two springs. A rotational spring for the airfoil pitch and a plate spring for the heave motion. The spring stiffness and damping are discussed in a later section of this chapter. The elastic axis is located at $x_e = 0.417$, as illustrated in figure 9.1. An additional movable weight was added to the experimental setup. Using the weight, the center of gravity of the test article was moved relative to the elastic center. Three positions were investigated and are denoted

as case I,II and III. In case I the center of gravity is located at the elastic axis, in case II upstream of the elastic axis and in case III downstream of the elastic axis. Only case I is considered in the present numerical studies. The wind speed and corresponding Reynolds number was changed during the experiment in the range from $Re = 9.66 \times 10^3$ up to $Re = 8.77 \times 10^4$. Initial still air measurements were performed to determine the spring stiffness and spring damping coefficients of the airfoil mount. Measurements consisted of one-point and two-point measurements to obtain the time and frequency response of the airfoil heave and pitch motion. Furthermore, hot-wire measurements were obtained in the wake of the airfoil in both rigid and oscillating configurations to correlate frequencies in the structural response to frequencies of flow features.
Subsequent to the experiment of Wood et al. (2020), numerical simulations were performed by the same team of researchers. The numerical simulations are discussed in De Nayer et al. (2020). The numerical simulations are performed with a body fitted mesh. An infinite aspect ratio was assumed for the sizing of the domain simplifying the problem to quasi two-dimensional. The Arbitrary Lagrangian-Eulerian formulation is used to account for the deformation of the fluid domain due to the movement of the geometry. A loose coupling FSI scheme is used, motivated by the high solid to fluid density ratio. The Smagorinsky turbulence closure model (Smagorinsky, 1963) is used to model the unresolved scales in the flow field. No slip boundary conditions are used on the wall without a wall-modeling approach, enabled by the mesh resolution which is well below $y^+ = 5$ for all considered Reynolds numbers. The results of the numerical simulation included results for the still air configuration to validate or potentially correct the spring stiffness and damping ratios found in the experiment and included results for the one and two point measurements to compare the time and frequency response of the pitch and heave motions to the ones found in the experiment of Wood et al. (2020).

9.2 Aero-elastic problem

Four motion types were found in the numerical assessment and experiments by De Nayer et al. (2020) and Wood et al. (2020). A damped stable motion at low Reynolds numbers, limit cycle oscillations with small and high amplitudes with increasing Reynolds number and flutter at high Reynolds numbers. At low Reynolds numbers and low dynamic pressures any perturbation in the airfoil pitch orientation and heave position is damped and the airfoil positions converge to the rest position. Due to the low dynamic pressure the aerodynamic forces acting on the surface of the airfoil are insufficient to destabilize the motion. The frequencies of the airfoil pitch and heave oscillations are identical to the frequencies found in the still air experiments and numerical simulation. Limit cycle oscillations with small amplitudes were found at increasing Reynolds number in the experiments of Wood et al. (2020) and numerical results of De Nayer et al. (2020). The small-amplitude oscillations (SAO) were also found at the smallest Reynolds number in the numerical results of De Nayer et al. (2020). It was concluded that the amplitude of the limit cycle oscillations at low Reynolds numbers was too small to be detected during the experiment of Wood et al. (2020). The SAO are caused by a small separation region at the trailing edge of the airfoil. The separation region alternates between either side of the airfoil.
An increase of the SAO is found with a further increase in the Reynolds number and

dynamic pressure of the free-stream. The experimental and numerical results further showed that the pitch and heave frequencies converge with increasing Reynolds number. At a sufficiently high Reynolds number the airfoil experiences limit cycle oscillations with significantly larger amplitudes denoted as large-amplitude oscillations (LAO). The oscillations were characterized by a significant increase in the pitch and heave motion of the airfoil. The flow field was characterized by flow separation at a chord-wise location of approximately $c = 2/3$ which alternates between either side of the airfoil. The separation region was characterized by distinct vortices which are shed from the airfoil surface. The frequency response showed only one distinct frequency with the large-amplitude oscillations. A further increase in the Reynolds number results in a flutter response of the airfoil. In this region the amplitude of the airfoil pitch and heave diverge. During the experiment the motion of the airfoil was manually stopped to not exceed the limits of the mounting system, the numerical simulation diverged due to the significant deformation of the numerical grid. As discussed in De Nayer et al. (2020) the frequencies of the pitch and heave motion are identical in the flutter region of the airfoil.
The present case is of particular difficulty as the characteristics of the airfoil motion are not only driven by the inertial forces of the flow field. An analysis of the flow field using potential or inviscid method may provide results for the stable and flutter region of the airfoil motion but is not able to predict the limit cycle oscillation of either magnitude. The experiments of Wood et al. (2020) and De Nayer et al. (2020) showed that these oscillations are driven by the viscous effects in the flow field, more particular by the flow separation of the boundary layer. The results therefore suggest that a good resolution of the near-wall flow field is necessary to accurately predict the motion characteristics of the airfoil in the transitional flow field.

9.3 Dimensional analysis

The results of De Nayer et al. (2020) are given in the dimensional units of the experiments of Wood et al. (2020). While not stated explicitly in the work of De Nayer et al. (2020), the simulation were potentially also carried out with a dimensional setup. With the given inflow boundary condition very low Mach numbers are present in the flow field. The maximum inflow Mach number is $M = 0.016$. The simulation of the low Mach number flow with an explicit time marching scheme combined with the large time scales of the structural problem leads to an excessive number of time integration steps and excessive numerical simulation time. This can be shown with the following relations. The time step of the numerical simulation must satisfy the CFL condition for stability. The time step size is proportional to

$$\Delta t \sim \frac{\Delta x}{c_{air} + |\mathbf{u}|}, \tag{9.1}$$

where Δt is the time step of the explicit time integration, Δx is the mesh spacing, c_{air} is the speed of sound and $|\mathbf{u}|$ is the local magnitude of the velocity. Based on equation (9.1) a decrease of the speed of sound relative to the velocity of the flow speed increases the time step. This is equivalent to increasing the Mach number of the flow field.
A non-dimensional setup is derived from the experimental setup based on Buckingham's Pi theorem. Sequentially, the Mach number in the non-dimensional setup is increased to reduce the computational cost of the simulation to acceptable levels. The Mach number

is kept below $M = 0.3$ to remain in the incompressible regime. Thus the increase of the Mach number should have a minimum effect on the numerical results of the problem. A list of all relevant parameters based on figure 9.1 is shown in table 9.1.

Variable	Unit	Description
t	$[T]$	Time
U_∞	$[L/T]$	Free-stream velocity
ρ_{air}	$[M/L^3]$	Free-stream density
ν_{air}	$[L^2/T]$	Free-stream viscosity
c	$[L]$	Airfoil chord
b	$[L]$	Airfoil span
h	$[L]$	Airfoil heave position
$\dot{h}$	$[L/T]$	Airfoil heave velocity
α	$[-]$	Airfoil pitch angle
$\dot{\alpha}$	$[1/T]$	Airfoil pitch rate
m_w	$[M]$	Airfoil/wing mass
I_α^e	$[ML^2]$	Airfoil/wing inertia around elastic axis
k_h	$[M/T^2]$	Heave spring stiffness
b_h	$[M/T]$	Heave spring damping
k_α	$[ML^2/T^2]$	Torsional spring stiffness
b_α	$[ML^2/T]$	Torsional spring damping
g	$[L/T^2]$	Gravity

Table 9.1: Tabulated list of all relevant parameters with units.

The free stream velocity U_∞, the free stream density ρ_{air} and airfoil chord c are used as independent variables. Using Buckingham's Pi theorem 11 dimensionless parameters are defined for the flow cases. The parameters are tabulated in table 9.2.

Variable	Π_i	Definition
t	Π_0	$U_\infty/c \cdot t$
ν_{air}	Π_1	$U_\infty c/\nu$
b	Π_2	b/c
z_s	Π_3	z_s/c
m_s	Π_4	$m_s/(\rho_{air}c^3)$
I_s	Π_5	$I_s/(\rho_{air}c^5)$
k_h	Π_6	$k_h/(U_\infty^2\rho_{air}c)$
b_h	Π_7	$b_h/(U_\infty\rho_{air}c^2)$
k_α	Π_8	$k_\alpha/(\rho_{air}c^3U_\infty^2)$
b_α	Π_9	$b_\alpha/(\rho_{air}c^4U_\infty)$
g	Π_{10}	$g/(U_\infty^2/c)$

Table 9.2: Tabulated list of dimensionless parameters of the FSI test case.

9.4 Simulation setup

The numerical simulations of De Nayer et al. (2020) are used as a reference for the numerical setup of the present simulation. A C-type domain with dimensions r for the radius, w for the wake length and l_c for the width of the domain has been used by De Nayer et al. (2020). A rectangular domain is used in the present simulation as the C-type domain used in the numerical simulation of De Nayer et al. (2020) is not achievable with the block mesh type of the present code. The domain dimensions are listed in table 9.3. The height of the domain was slightly increased from $7.2c$ to $8c$ for the present numerical simulation. The wake length was increased from $5c$ to $8c$ and the inlet length was set to $8c$ resulting in a square domain. The width of the domain is equal to the width chosen by De Nayer et al. (2020). Riemann boundary conditions are used for the inlet, top and bottom of the domain. A static pressure boundary condition is used at the outlet of the domain. Periodic boundary conditions are imposed in the span-wise direction of the domain.

A uniform mesh is used in the region were the airfoil is moving with a mesh spacing of

Parameter	Symbol	Unit	Present	De Nayer et al. (2020)
Domain radius/height	r	$[c]$	8	7.2
Wake length	w	$[c]$	8	5
Width	l_c	$[c]$	0.25	0.25

Table 9.3: Domain dimension for the NACA0012 2-DOF simulation.

$\Delta x = 0.002c$. The mesh spacing is equivalent to $\Delta x = 2mm$ in the numerical simulation of De Nayer et al. (2020), which results in an approximate wall to first grid point spacing of $1mm$. While larger than the selected $0.65mm$ first grid point spacing in the reference numerical results the mesh resolution is deemed sufficient for an initial set of simulations. The unresolved turbulent scales are modeled with the Vreman model (Vreman, 2004).
The airfoil is modeled as a single rigid body with all six degrees of freedom. A fixation constraint is used to fix all degrees of freedom apart from the heave and pitch motion of the airfoil. The fixation constraint follows the formulation presented in section 4.4.1. The spring damper system of the experiment is modeled using the methods described in section 4.4.1.
The one-point measurements for the time and frequency analysis were performed based on a probing point located at $x/c = 0.283$ downstream of the elastic axis as illustrated in figure 9.1. The equations of motion of the NACA0012 were integrated with a time step of $\Delta tU/c = 0.01$, which is equivalent to $N_t = 200$ time steps over one oscillation period of the airfoil.

9.5 Free-oscillations in still air

Simulations in still air or rather vacuum were carried out to validate the implementation of the rigid body equations of motion and spring/damper constraints in the present solver. The initial excitement of the system was achieved by applying rotational and translational displacements to the system with respect to the rest position. The displacements were sized in such a way that the displacement of the probing point is roughly equal in all

three considered cases.
The system parameters used for the still air simulation are based on the experiments performed by Wood et al. (2020). The position of the centre of gravity was taken from the numerical simulation of De Nayer et al. (2020). The system parameters are listed in table 9.4. All simulations were performed for $t = 22s$ to obtain sufficient data for the time and frequency analysis.

Parameter	Symbol	Unit	Value
Distance between c.o.g. and e.a	x_{EG}/c	[-]	0.006
Mass moment of inertia	I_α^E	$[kg\ m^2]$	1.399×10^{-4}
Mass of dynamic system	m_w	$[kg]$	0.33521
Bending stiffness	k_h	$[N/m]$	698
Torsional stiffness	k_α	$[N/rad]$	0.3832
Bending spring damping	b_h	$[Ns/m]$	9.72×10^{-2}
Torsional spring damping	b_α	$[Nm/s]$	3.70×10^{-5}

Table 9.4: System parameters for the still air simulations.

Three simulations were performed. Simulation I was performed to investigate the frequency and damping ratio of the heave motion. This was done by fixing the pitch degree of freedom. Simulation II was performed to investigate the frequency and damping ratio of the pitch motion by fixing the heave degree of freedom and simulation III was performed to investigate the response of the two-degree of freedom system by neither fixing the heave motion nor the pitch motion. The responses of the one-degree of freedom system is shown in figure 9.2 and 9.3. Both results show a single distinct frequency in the frequency analysis indicating the eigenfrequency of the one-degree of freedom system.

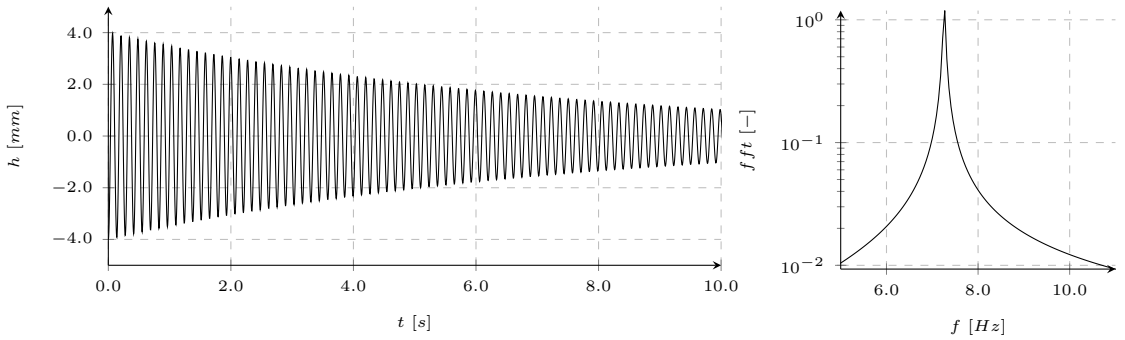

Figure 9.2: Time and frequency response of the spring-mounted airfoil in still air, pitch degree of freedom locked.

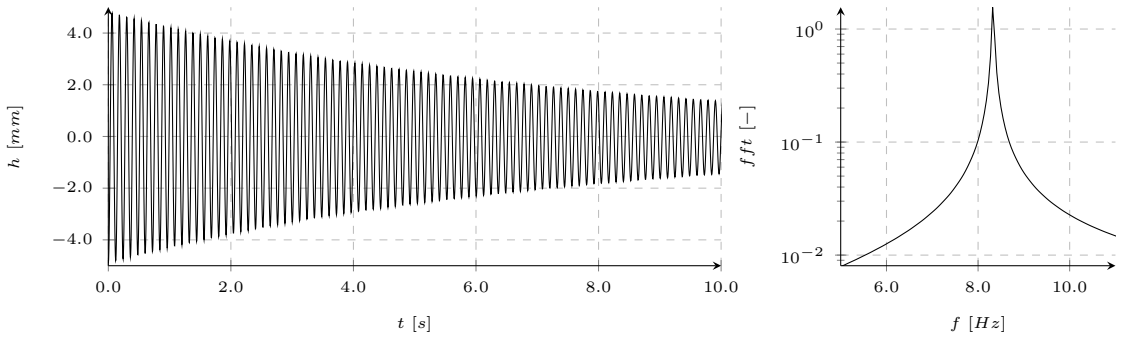

Figure 9.3: Time and frequency response of the spring-mounted airfoil in still air, heave degree of freedom locked.

The results of the two-degree of freedom system are shown in figure 9.4. Two significant frequencies are found in the frequency analysis of the motion. The frequencies correspond to the heave and pitch motion of the airfoil.

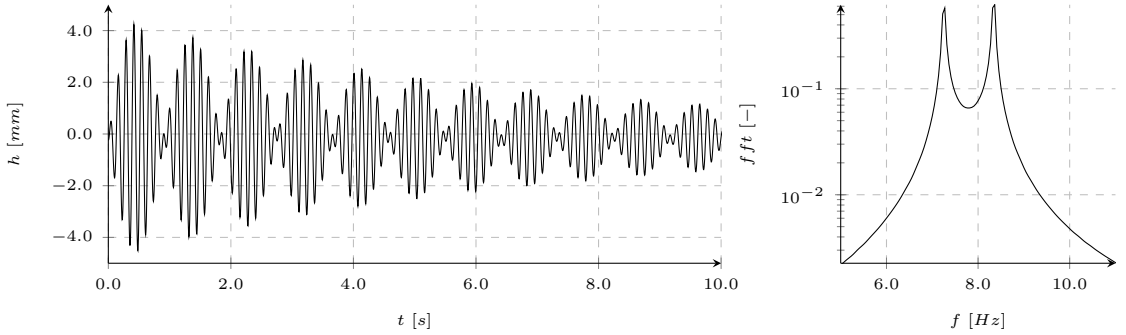

Figure 9.4: Time and frequency response of the spring-mounted airfoil in still air, both degrees of freedom unlocked.

The numerical results of the system frequencies of the one-degree of freedom and two-degree of freedom systems are summarized in table 9.5. The present results are compared to the experimental results of Wood et al. (2020) and De Nayer et al. (2020). The results show a close agreement between the numerical results of the present method and the experimental results of Wood et al. (2020). The errors found in the frequencies do not exceed those found between the experimental results of Wood et al. (2020) and the numerical results of De Nayer et al. (2020).

The damping ratios of the one-degree of freedom system were determined based on the method discussed in Wood et al. (2020). The results for the damping ratios are shown in table 9.6. The results indicate that the damping ratios predicted by the present method are lower than the damping ratios found in the experiment of Wood et al. (2020).

9.6 Free-oscillations under wind load

Simulations with wind load were performed at five Reynolds numbers ranging from $Re = 9660$ to $Re = 36000$. The Reynolds number range includes the stable, limit cycle

Parameter	Symbol	Unit	Wood et al. (2020)	De Nayer et al. (2020)	Present
Translation eigenfrequency 1-DOF	f_h^{1-DOF}	$[Hz]$	7.26	7.25	7.27
Rotational eigenfrequency 1-DOF	f_α^{1-DOF}	$[Hz]$	8.33	8.33	8.32
Translation eigenfrequency 2-DOF	f_h^{2-DOF}	$[Hz]$	7.31	7.25	7.27
Rotaitonal eigenfrequency 2-DOF	f_h^{2-DOF}	$[Hz]$	8.38	8.33	8.36
Frequency difference 2-DOF	Δf^{2-DOF}	$[Hz]$	1.07	1.08	1.09
Frequency ratio 1-DOF	$f_h^{1-DOF}/f_\alpha^{1-DOF}$	$[-]$	0.872	0.870	0.874
Frequency ratio 2-DOF	$f_h^{2-DOF}/f_\alpha^{2-DOF}$	$[-]$	0.872	0.870	0.870

Table 9.5: Tabulated frequency results of the still air simulations.

Parameter	Symbol	Unit	Wood et al. (2020)	Present
Total translational damping	$D_h^{1-DOF,tot}$	$[-]$	3.18×10^{-3}	2.993×10^{-3}
Total torsional damping	$D_\alpha^{1-DOF,tot}$	$[-]$	2.53×10^{-3}	2.406×10^{-3}

Table 9.6: Total damping ratios determined in the experiment of Wood et al. (2020) and obtained in present numerical simulations.

oscillations and flutter regions of the airfoil motion response. This section presents the numerical results of the present code in form of the time and frequency responses. The results are further tabulated and compared to the numerical and experimental results of Wood et al. (2020) and De Nayer et al. (2020). The time and frequency responses of the five Reynolds numbers are shown in figures 9.5 to 9.9.

The response of the airfoil at $Re = 9660$ is shown in figure 9.5. The results show limit cycle oscillations with small magnitudes in the time response plot of the motion. The frequency results show two distinct frequencies associated with the pitch and heave motion of the airfoil. Limit cycle oscillations were also found in the numerical results of De Nayer et al. (2020). However, the magnitude was reported to be significantly below $1mm$. The experiments of Wood et al. (2020) did not report limit cycle oscillations. De Nayer et al. (2020) concluded that limit cycle oscillations are present in the flow field, but the magnitude is below the measurable amplitudes of the experiment. Therefore, the present code correctly predicts small limit cycle oscillations, however the magnitude of the limit cycle oscillations are overpredicted.

The response of the airfoil motion at $Re = 16500$ is shown in figure 9.6. The time response shows a stable motion. The initial excitation of the airfoil decays towards zero. This is inline with the findings reported in the numerical results of De Nayer et al. (2020) and Wood et al. (2020). The frequency response shows that the frequencies of the heave and pitch motion converge towards each other which is also inline with the reported reference numerical and experimental results.

The response of the airfoil at $Re = 23900$ is shown in figure 9.7. The time response of the airfoil shows small limit cycle oscillations with magnitudes of approximately $1mm$. A further convergence of the heave and pitch frequencies is seen in the frequency response. The experimental and numerical reference results show a stable motion with limit cycle oscillations with very small amplitudes $h < 1mm$. Further a strongly damped heave motion is reported in the experimental results of Wood et al. (2020). The strongly damped heave motion is not seen in the results of the present code. The results again indicate an

overprediction of the small limit cycle oscillations.
The response of the airfoil at $Re = 30600$ is shown in figure 9.8. The response shows larger limit cycle oscillations with amplitudes of $2mm$ to $2.5mm$. The motion is further characterized by only one significant frequency, as shown in the frequency response plot. The results of the present code are inline with the reported findings of Wood et al. (2020). Both the existence of limit cycle oscillations with large amplitudes and the existence of a single significant frequency are correctly predicted by the present code.
The response of the airfoil at $Re = 36000$ is shown in figure 9.9. The response shows large limit cycle oscillations until $t = 10s$. Beyond $t = 10s$ the oscillations of the airfoil diverge inline with the motion of an airfoil post the flutter boundary. The motion is again characterized by one distinct frequency. The result is inline with the findings of the experiment of Wood et al. (2020) and the numerical results of De Nayer et al. (2020). Both, reported flutter at a Reynolds number of $Re = 36000$.

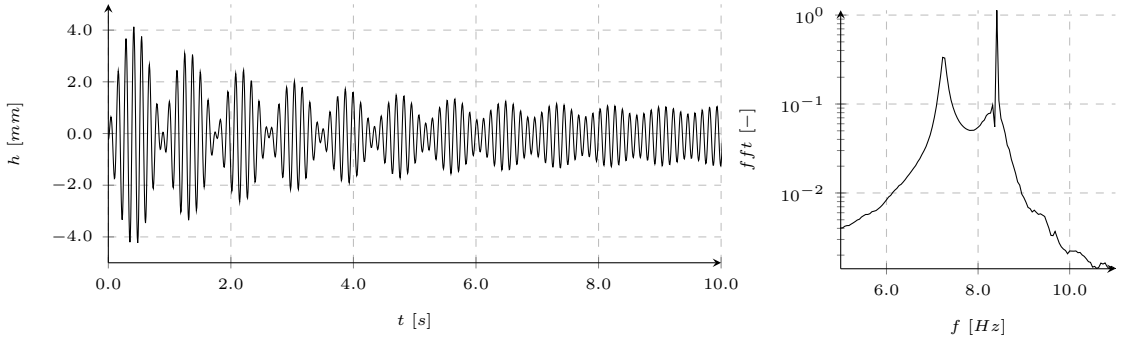

Figure 9.5: Time and frequency response of the spring-mounted airfoil at Reynolds number $Re = 9660$.

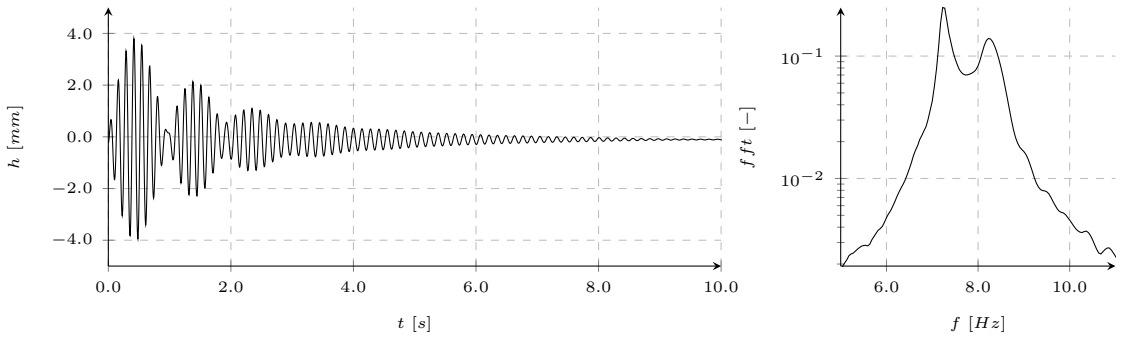

Figure 9.6: Time and frequency response of the spring-mounted airfoil at Reynolds number $Re = 16500$.

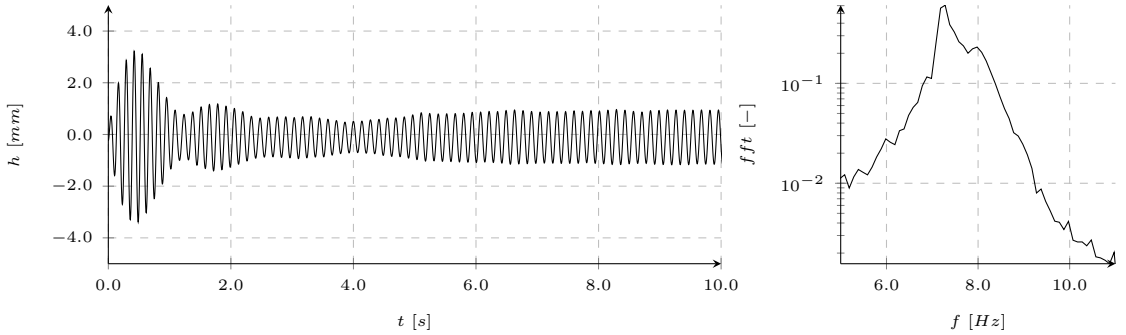

Figure 9.7: Time and frequency response of the spring-mounted airfoil at Reynolds number $Re = 23900$.

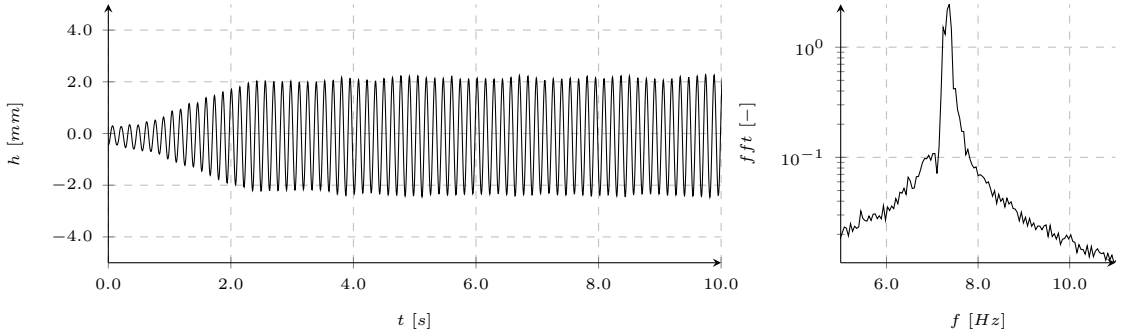

Figure 9.8: Time and frequency response of the spring-mounted airfoil at Reynolds number $Re = 30600$.

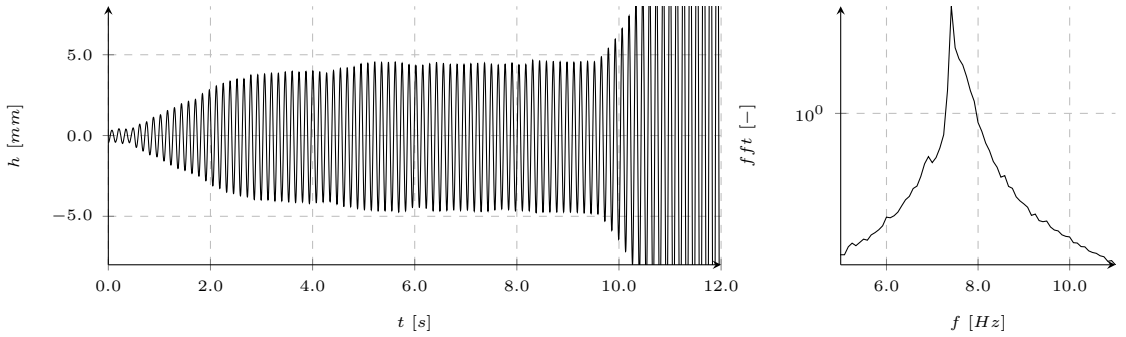

Figure 9.9: Time and frequency response of the spring-mounted airfoil at Reynolds number $Re = 36000$.

The relevant frequencies of the motion are shown in table 9.7 for all five Reynolds numbers. The frequencies are compared to the measurements of Wood et al. (2020) and predictions of De Nayer et al. (2020). Starting with the lowest Reynolds number $Re = 9660$, the results show a slight under-prediction of the heave frequency and slight over-prediction of the pitch frequency. At $Re = 16500$, the present code correctly predicts the convergence of the frequencies associated with the heave and pitch motion. A slight under-prediction is found in the frequency associated with the heave motion. The frequency associated

with the pitch motion is inline with the reported measurements of Wood et al. (2020). At $Re = 23900$, a close agreement is found in the frequency predictions of De Nayer et al. (2020) and the present code. A slight under-prediction is seen in the frequency associated with the pitch motion of the airfoil when compared to the experimental results of Wood et al. (2020). The heave motion is heavily damped in the experimental results of Wood et al. (2020) and no frequency was measured. At Reynolds numbers $Re = 30600$ and $Re = 36000$ the airfoil motion is characterized by only one distinct frequency. The results show an under-prediction of the present results and results of De Nayer et al. (2020). Both methods under-predict the frequency of the motion compared to the experimental results of Wood et al. (2020), while a larger under-prediction is found in the results of the present code.

	$Re = 9660$	$Re = 16500$	$Re = 23900$	$Re = 30600$	$Re = 36000$
Experimental (Wood et al., 2020)	7.31/8.33	7.35/8.24	−/8.06	−/7.93	−/7.79
Numerical (De Nayer et al., 2020)			7.30/7.93	−/7.77	−/7.63
Present	7.23/8.41	7.23/8.23	7.28/7.97	−/7.27	−/7.42

Table 9.7: Tabulated frequency results of the NACA0012 airfoil under wind load corresponding to the heave (left) and pitch (right) degree of freedom.

9.7 Flow field and response at Reynolds 30600

The results at $Re = 30600$ are selected for a further analysis of the response of the airfoil and flow field. The time response of the airfoil is splitted into the displacement of the probing point caused by the heave and pitch motion of the airfoil. The analysis is used to determine the phase shift between the pitch and heave motion. The response is plotted in figure 9.11. A significant phase shift is found in the numerical results of the present code with $\Phi = 220°$. The phase shift between the pitch and heave motion is significantly over-predicted compared to the numerical results of De Nayer et al. (2020) and experimental results of Wood et al. (2020). Wood et al. (2020) measured a phase shift of $\Phi = 130°$. De Nayer et al. (2020) reported a phase shift prediction of $\Phi = 138°$.
The flow field around the NACA0012 airfoil over one period is shown in figure 9.10, where t_0 and T denote the start and length of the oscillation period. The flow field slice shows the velocity magnitude field around the NACA0012 airfoil. The plots show the airfoil undergoing large limit cycle oscillations as previously discussed. Flow separation is found alternating between either side of the airfoil in combination with the turbulent vortex shedding. The results are inline with the reported findings of De Nayer et al. (2020).

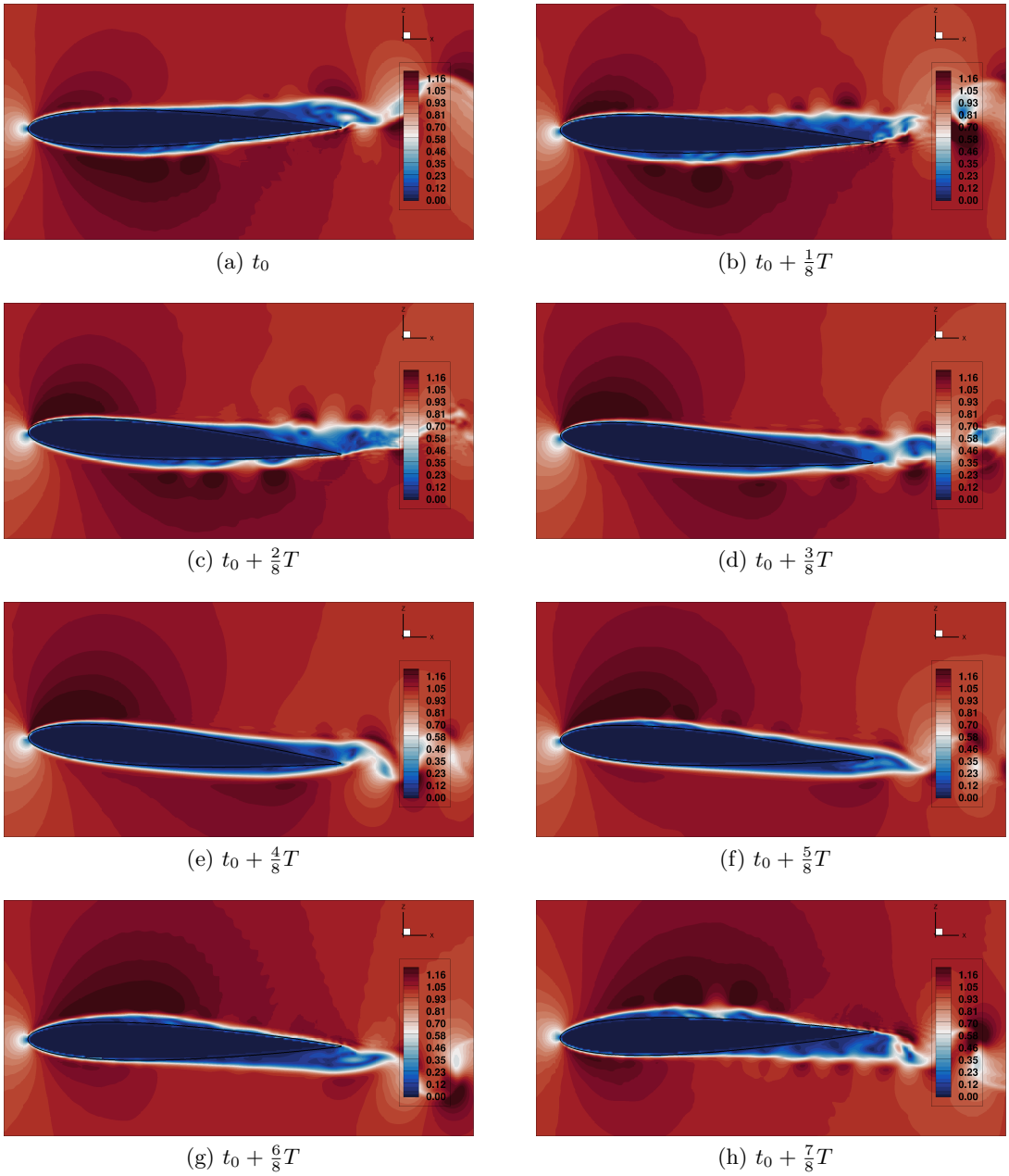

(a) t_0 (b) $t_0 + \frac{1}{8}T$

(c) $t_0 + \frac{2}{8}T$ (d) $t_0 + \frac{3}{8}T$

(e) $t_0 + \frac{4}{8}T$ (f) $t_0 + \frac{5}{8}T$

(g) $t_0 + \frac{6}{8}T$ (h) $t_0 + \frac{7}{8}T$

Figure 9.10: Slices of the velocity magnitude field over one oscillation period of the airfoil.

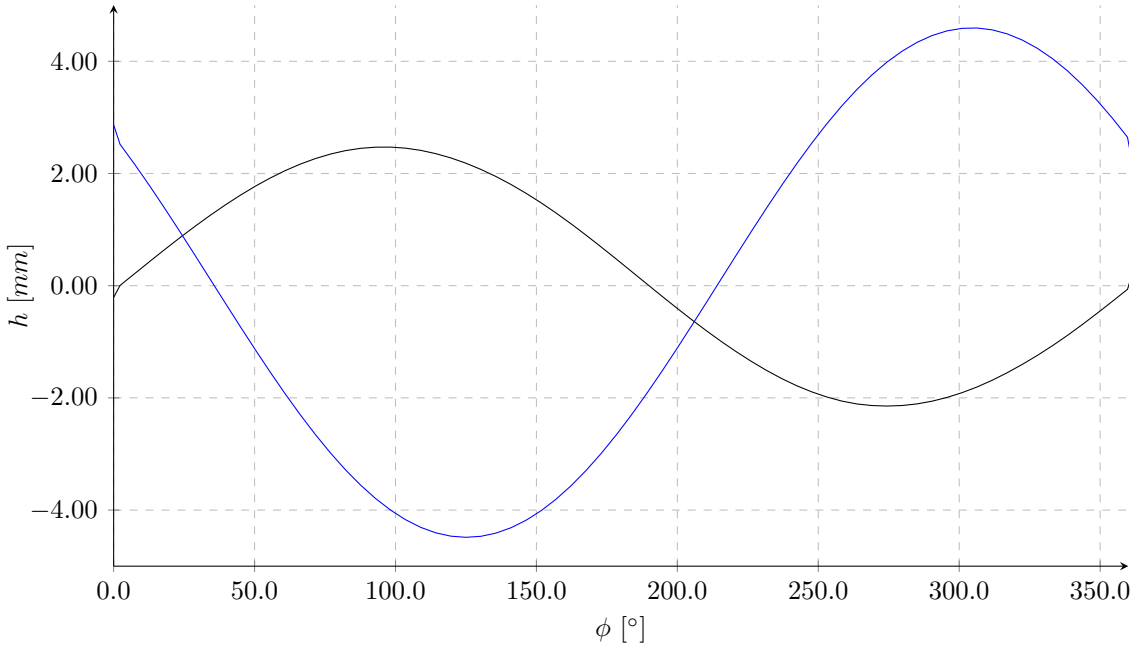

Figure 9.11: Probing point displacement h caused by the heave (——) and pitch (——) motion over one oscillation period.

9.8 Discussion

Simulations of a NACA0012 airfoil with two degrees of freedom were performed. The NACA0012 airfoil was mounted in the inertial reference frame with a translational and rotational spring damper system. The simulations were performed based on the numerical and experimental results of Wood et al. (2020) and De Nayer et al. (2020). The results are used to validate the implementation of the rigid body solver and loose fluid solid coupling scheme. An initial set of still air simulations were performed to validate the correct setup of the mass-spring system. The simulations showed a good agreement in the pitch and heave frequencies for both single degree of freedom motions and two degree of freedom motions. An under-prediction was found in the damping coefficients between the results of the present code and the experimental reference results.
Subsequently simulations with wind load were performed. The simulations showed that the present method captures the three motion patterns of the sprung NACA0012 airfoil, which are a stable damped motion, limit cycle oscillations of small and large amplitudes and flutter. Quantitative differences were found in the amplitude of the small limit cycle oscillations at low Reynolds numbers. The amplitude of the small limit cycle oscillations were over-predicted by the present code. Two possible causes were identified, the near-wall mesh resolution and the under-predicted damping ratio. The near-wall mesh resolution might cause an under-prediction in the fluid damping, subsequent mesh convergence studies are proposed to investigate this hypothesis. Further, the still air simulations indicate an under-prediction of the spring damping coefficient. This may have caused an insufficient damping of the small limit cycle oscillations. Subsequent studies on the damping coefficients are proposed.

Under-predictions were also found in the frequencies associated with the large limit cycle oscillations and flutter. The proposed studies on the mesh convergence and spring damping coefficient should also be applied to the higher Reynolds numbers.
The flow field around the NACA0012 over one oscillation period was plotted at a Reynolds number of $Re = 30600$. The motion at this Reynolds number is characterized by large limit cycle oscillations. The flow field showed an accurate prediction of the flow separation inline with the prediction of the reference numerical results. The displacement of the probing point associated with heave and pitch motion were plotted at $Re = 30600$ over one oscillation period to measure the phase shift between the two motions. A significant over-prediction was found in the phase shift between the heave and pitch motion compared to the numerical and experimental reference results.
In conclusion, the present code accurately predicts the different motion patterns of the sprung NACA0012 airfoil, but large discrepancies were found in the quantitative assessment of the airfoil.

Chapter 10

Conclusion

The development and validation of an aero-servo-elasticity solver was presented. The development and validation of this solver formed the main topic of the thesis project. The research objective of the thesis project aimed to find an efficient implementation of a multi-body dynamics solver inside a high-fidelity GPU-based computational fluid dynamics solver. The development was performed under the constraint of achieving high-fidelity with only minimal computational cost. The use of high-fidelity tools was shown to be beneficial and crucial for the development of future aircraft concepts. It was further shown that the objective of high efficiency and high fidelity is not met by currently available tools, which motivated the development of a new computational tool. A quantitative assessment of the efficiency of the developed tool and a comparison of the efficiency to other tools was not presented. A fair quantitative assessment is prevented due to different numerics and fidelity of reference computational tools as well as differences in the computational hardware. Instead, a careful selection of numerical methods was performed during the literature review based on the requirements of finding methods with suitable fidelity but low reported computational cost. The selected methods were combined into the fluid-structure interaction tool and the accuracy of the tool was verified and validated with existing numerical and experimental data. The scope of the project covered the development of a hybrid ghost-cell method for the simulation of moving boundaries in both low and high Reynolds number flows, the development of a multi-body solver for the simulation of aircrafts as tree-like multi-body systems and the implementation of the fluid-structure coupling method for the simulation of fluid-structure interaction problems.

The presented work was started with the mathematical formulation of the immersed boundary method and multi-body solver. A hybrid ghost-cell immersed boundary method was presented for the simulation of moving geometries in low and high Reynolds number flow. A hybrid-cell treatment was developed for the suppression of spurious oscillations in the flow field of moving geometries. Simulations of high Reynolds number flow was achieved with the implementation of a wall-modeling approach in the hybrid ghost-cell method. Verification and validation tests were performed in the subsequent chapters to assess the predictions of the developed immersed boundary method. The verification

tests proofed the effectiveness of the developed method in the suppression of spurious pressure waves in both low and high Reynolds number flow. Two validation tests were performed. The flow around an in-line oscillating cylinder at low Reynolds number flow was simulated. The results showed an excellent agreement between the numerical and experimental results of the cylinder forces and flow features. Small discrepancies were found between the numerical results in the velocity field around the cylinder. Simulations around an oscillating airfoil in high Reynolds number flow were performed and compared to numerical and experimental reference results. The numerical results of the present code showed that the developed methods predict the characteristic flow features of the dynamic stall problem. Discrepancies were found in the integral forces of the airfoil between the results of the present code and reference results. The discrepancies were attributed to an insufficiently resolved near-wall region and simplistic near-wall modeling approach.
A broad introduction was given in the mathematical formulation of the multi-body solver. The developed solver enables the simulation of tree-like multi-body systems. A control strategy was presented based on the time integration scheme. The control strategy is used to prescribe position and orientation states of rigid bodies and constraints dynamically. Verification and validation cases were performed to assess the multi-body solver and coupled multi-body and fluid solver. The verification of the solver was performed with simulations of a single and double pendulum. The fluid-structure interaction tool was validated with simulations of a NACA0012 airfoil with two degrees of freedom. The simulations were performed with increasing inflow speed to capture all three regions of the airfoil motion, stable, limit cycle oscillations and flutter. The results showed the correct prediction of the three motion states. Discrepancies were found in the prediction of the oscillation frequencies and in the amplitude of the small limit cycle oscillations. Two causes were identified, the near-wall mesh resolution for the frequency discrepancies at high Reynolds numbers and the under-prediction of the spring damping ratio for the over-prediction of the small limit cycle oscillations.
The presented verification and validation cases for the immersed boundary, multi-body and combined fluid-structure interaction tool demonstrated the correct implementation of the selected methods. The presence of case specific flow features and motion patterns were correctly predicted by the developed tool in the presented verification and validation cases. Discrepancies were found on the quantitative level between the numerical results of the present code and numerical and experimental reference results. In either case the discrepancies were attributed to insufficient resolution in the near-wall region.
Based on the presented results further investigations are necessary in the 2-DOF NACA0012 flow case to understand the causes of the discrepancies. Further improvements in the near-wall resolution and an improved modeling of the near-wall flow field should be the focus on future work to improve the prediction of high Reynolds number flow fields around moving geometries. Future research and development should focus on the extension of the developed multi-body solver to elastic bodies and the implementation of the control laws to complete the aero-servo-elasticity framework. The presented work showed that the selection of efficient methods is appropriate for the high-fidelity simulation of fluid-structure interaction problems.

References

Adamiec-Wójcik, I., & Wojciech, S. (2018, September). Application of the finite segment method to stabilisation of the force in a riser connection with a wellhead. *Nonlinear Dynamics*, *93*, 1853–1874.

Agrawal, O. P., & Shabana, A. A. (1985). Dynamic analysis of multibody systems using component modes. *Computers & Structures*, *21*(6), 1303–1312.

Airbus. (n.d.). *Airbus.* https://www.airbus.com/newsroom/press-releases/en/2020/09/airbus-reveals-new-zeroemission-concept-aircraft.html. (Accessed: 2021-01-25)

Alonso, J., & Jameson, A. (1994). Fully-implicit time-marching aeroelastic solutions. In *32nd Aerospace Sciences Meeting and Exhibit.*

Amirouche, F. (2006). *Fundamentals of Multibody Dynamics. Theory and Applications.* Birkhäuser.

Amirouche, F. M. L., & Jia, T. (1988, January). Pseudouptriangular decomposition method for constrained multibody systems using Kane's equations. *Journal of Guidance, Control, and Dynamics*, *11*(1), 39–46.

Argyris, J. H., Balmer, H., Doltsinis, J. S., Dunne, P. C., Haase, M., Kleiber, M., et al. (1979). Finite element method – the natural approach. *Computer Methods in Applied Mechanics and Engineering*, *17-18*, 1–106.

Arnold, R. R., Citerley, R. L., Chargin, M., & Galant, D. (1985). Application of Ritz vectors for dynamic analysis of large structures. *Computers & Structures*, *21*(3), 461–467.

Arnoldi, W. E. (1951). The principle of minimized iterations in the solution of the matrix eigenvalue problem. *Quarterly of Applied Mathematics*, *9*, 17-29.

Ascher, U. M., & Petzold, L. R. (1998). *Computer methods for ordinary differential equations and differential-algebraic equations.* Philadelphia: Society for Industrial and Applied Mathematics.

Baeza, A., Mulet, P., & Zorío, D. (2016). High Order Boundary Extrapolation Technique for Finite Difference Methods on Complex Domains with Cartesian Meshes. *Journal of Scientific Computing*, *66*(2), 761–791.

Banks, J., Henshaw, W., & Sjögreen, B. (2013, Jul). A stable FSI algorithm for light rigid bodies in compressible flow. *Journal of Computational Physics*, *245*, 399–430.

Banks, J. W., Henshaw, W. D., Kapila, A. K., & Schwendeman, D. W. (2016). An added-mass partition algorithm for fluid-structure interactions of compressible fluids and nonlinear solids. *Journal of Computational Physics*, *305*, 1037–1064.

Banks, J. W., Henshaw, W. D., & Schwendeman, D. W. (2012). Deforming composite grids for solving fluid structure problems. *Journal of Computational Physics*, *231*(9), 3518–3547.

Banks, J. W., Henshaw, W. D., & Schwendeman, D. W. (2014). An analysis of a new stable partitioned algorithm for FSI problems. Part I: Incompressible flow and elastic solids. *Journal of Computational Physics*, *269*, 108–137.

Bardina, J., Huang, P., & Coakley, T. (1997, 05). *Turbulence Modeling Validation, Testing, and Development* (NASA Technical Memorandum No. 19970017828). Ames Research Center.

Barlow, J. (1982, April). Constraint relationships in linear and nonlinear finite element analyses. *Int. J. Numer. Meth. Engng.*, *18*(4), 521–533.

Baxevanou, C. A., Chaviaropoulos, P. K., Voutsinas, S. G., & Vlachos, N. S. (2008). Evaluation study of a Navier-Stokes CFD aeroelastic model of wind turbine airfoils in classical flutter. *Journal of Wind Engineering and Industrial Aerodynamics*, *96*(8), 1425–1443.

Bayyuk, S., Powell, K., & Leer, B. van. (1993, July). A Simulation Technique for 2-D Unsteady Inviscid Flows Around Arbitrarily Moving and Deforming Bodies of Arbitrary Geometry. In *11th Computational Fluid Dynamics Conference* (pp. 1013–1024).

Beckert, A., & Wendland, H. (2001). Multivariate interpolation for fluid-structure-interaction problems using radial basis functions. *Aerospace Science and Technology*, *5*(2), 125–134.

Belytschko, T., & Hsieh, B. J. (1973, January). Non-linear transient finite element analysis with convected co-ordinates. *International Journal for Numerical Methods in Engineering*, *7*(3), 255–271. Available from https://doi.org/10.1002/nme.1620070304

Bernardi, C., Maday, Y., & Patera, A. (n.d.). A New Nonconforming Approach to Domain Decomposition : The Mortar Element Method. In *Nonlinear partial differential equations and their applications* (Vol. XI, pp. 13–51).

Bernardi, C., Maday, Y., & Patera, A. T. (1993). Domain decomposition by the mortar element method. In H. G. Kaper, M. Garbey, & G. W. Pieper (Eds.), *Asymptotic and Numerical Methods for Partial Differential Equations with Critical Parameters* (pp. 269–286). Dordrecht: Springer Netherlands.

Besselink, B., Tabak, U., Lutowska, A., Wouw, N. van de, Nijmeijer, H., Rixen, D. J., et al. (2013). A comparison of model reduction techniques from structural dynamics, numerical mathematics and systems and control. *Journal of Sound and Vibration*, *332*(19), 4403–4422.

Beyer, R. P. (1992). A computational model of the cochlea using the immersed boundary method. *Journal of Computational Physics*, *98*(1), 145–162.

Blom, F. J. (1998). A monolithical fluid-structure interaction algorithm applied to the piston problem. *Computer Methods in Applied Mechanics and Engineering*, *167*(3), 369–391.

Boer, A. de, Zuijlen, A. H. van, & Bijl, H. (2007). Review of coupling methods for non-matching meshes. *Computer Methods in Applied Mechanics and Engineering*, *196*(8), 1515–1525.

Burstedde, C., Wilcox, L. C., & Ghattas, O. (2011). `p4est`: Scalable Algorithms for Parallel Adaptive Mesh Refinement on Forests of Octrees. *SIAM Journal on Scientific Computing*, *33*(3), 1103-1133.

Campanelli, M., Berzeri, M., & Shabana, A. A. (1999, September). Performance of the Incremental and Non-Incremental Finite Element Formulations in Flexible Multibody Problems. *J. Mech. Des*, *122*(4), 498–507.

Carr, L. W. (1988, January). Progress in analysis and prediction of dynamic stall. *Journal of Aircraft*, *25*(1), 6–17.

Causin, P., Gerbeau, J. F., & Nobile, F. (2005). Added-mass effect in the design of partitioned algorithms for fluid-structure problems. *Computer Methods in Applied Mechanics and Engineering*, *194*(42), 4506–4527.

Cebral, J. R., & Lohner, R. (1997). Conservative Load Projection and Tracking for Fluid-Structure Problems. *AIAA Journal*, *35*(4), 687–692.

Chapman, D. R. (1979, December). Computational Aerodynamics Development and Outlook. *AIAA Journal*, *17*(12), 1293–1313.

Chávez-Modena, M., Martínez, J. L., Cabello, J. A., & Ferrer, E. (2020). Simulations of Aerodynamic Separated Flows Using the Lattice Boltzmann Solver XFlow. *Energies*, *13*(19).

Clarke, D. K., Salas, M. D., & Hassan, H. A. (1986, March). Euler calculations for multielement airfoils using Cartesian grids. *AIAA Journal*, *24*(3), 353–358.

Colella, P., Graves, D. T., Keen, B. J., & Modiano, D. (2006). A Cartesian grid embedded boundary method for hyperbolic conservation laws. *Journal of Computational Physics*, *211*(1), 347–366.

Craig, R. R., & Bampton, M. C. C. (1968, July). Coupling of substructures for dynamic analyses. *AIAA Journal*, *6*(7), 1313–1319.

Crawley, E. F., Curtiss, H. C., Peters, D. A., Scanlan, R. H., Sisto, F., & Dowell, E. H. (1995). *A Modern Course in Aeroelasticity.* Dordrecht: Springer Netherlands.

Debrabandere, F., Tartinville, B., Hirsch, C., & Coussement, G. (2012, June). Fluid-Structure Interaction Using a Modal Approach. *J. Turbomach*, *134*(5).

De Nayer, G., Breuer, M., & Wood, J. N. (2020). Numerical investigations on the dynamic behavior of a 2-DOF airfoil in the transitional Re number regime based on fully coupled simulations relying on an eddy-resolving technique. *International Journal of Heat and Fluid Flow*, *85*, 108631.

Dickens, J. M., Nakagawa, J. M., & Wittbrodt, M. J. (1997). A critique of mode acceleration and modal truncation augmentation methods for modal response analysis. *Computers & Structures*, *62*(6), 985–998.

Dickens, J. M., & Pool, K. V. (1992). Modal truncation vectors and periodic time domain analysis applied to a cyclic symmetry structure. *Computers & Structures*, *45*(4), 685–696.

Dokainish, M., & Subbaraj, K. (1989). A survey of direct time-integration methods in computational structural dynamics—I. Explicit methods. *Computers & Structures*, *32*(6), 1371 - 1386.

Dowell, E. H., & Hall, K. C. (2001, January). Modeling of Fluid-Structure Interaction. *Annu. Rev. Fluid Mech.*, *33*(1), 445–490.

Drela, M. (1989). XFOIL: An Analysis and Design System for Low Reynolds Number Airfoils. In T. J. Mueller (Ed.), *Low Reynolds Number Aerodynamics* (pp. 1–12). Berlin, Heidelberg: Springer Berlin Heidelberg.

Dussart, G., Portapas, V., Pontillo, A., & Lone, M. (2018). Flight dynamic modelling and simulation of large flexible aircraft. In K. Volkov (Ed.), *Flight physics* (chap. 3). Rijeka: IntechOpen. Available from https://doi.org/10.5772/intechopen.71050

Dütsch, H., Durst, F., Becker, S., & Lienhart, H. (1998). Low-Reynolds-number flow around an oscillating circular cylinder at low Keulegan-Carpenter numbers. *Journal of Fluid Mechanics*, *360*(1), 249-271.

EHang. (n.d.). *Ehang.* https://www.ehang.com/index.html. (Accessed: 2020-01-28)

Evangelinos, C., Lucor, D., & Karniadakis, G. (2000). DNS-derived force distribution on flexible cylinders subject to vortex-induced vibration. *Journal of Fluids and Structures*, *14*(3), 429 - 440.

Farhat, C., & Lesoinne, M. (2000). Two efficient staggered algorithms for the serial

and parallel solution of three-dimensional nonlinear transient aeroelastic problems. *Computer Methods in Applied Mechanics and Engineering*, *182*(3), 499–515.

Farhat, C., Lesoinne, M., & Le Tallec, P. (1998). Load and motion transfer algorithms for fluid/structure interaction problems with non-matching discrete interfaces: Momentum and energy conservation, optimal discretization and application to aeroelasticity. *Computer Methods in Applied Mechanics and Engineering*, *157*(1), 95–114.

Farhat, C., Lesoinne, M., & Maman, N. (1995, November). Mixed explicit/implicit time integration of coupled aeroelastic problems: Three-field formulation, geometric conservation and distributed solution. *Int. J. Numer. Meth. Fluids*, *21*(10), 807–835.

Farhat, C., Zee, K. G. van der, & Geuzaine, P. (2006). Provably second-order time-accurate loosely-coupled solution algorithms for transient nonlinear computational aeroelasticity. *Computer Methods in Applied Mechanics and Engineering*, *195*(17), 1973–2001.

Fedkiw, R. P., Aslam, T., Merriman, B., & Osher, S. (1999). A Non-oscillatory Eulerian Approach to Interfaces in Multimaterial Flows (the Ghost Fluid Method). *Journal of Computational Physics*, *152*(2), 457–492.

Fehr, J., & Eberhard, P. (2010, May). Error-Controlled Model Reduction in Flexible Multibody Dynamics. *J. Comput. Nonlinear Dynam*, *5*(3).

Fehr, J., & Eberhard, P. (2011). Simulation process of flexible multibody systems with non-modal model order reduction techniques. *Multibody System Dynamics*, *25*(3), 313–334.

Felippa, C., Park, K. C., & Deruntz, J. (1977, January). Stabilization of staggered solution procedures for fluid-structure interaction analysis. *American Society of Mechanical Engineers, Applied Mechanics Division, AMD*, *26*.

Fischer, M., & Eberhard, P. (2014). Linear model reduction of large scale industrial models in elastic multibody dynamics. *Multibody System Dynamics*, *31*(1), 27–46.

Frisch, H. P., & Center., G. S. F. (1975). *A vector-dyadic development of the equations of motion for N-coupled flexible bodies and point masses.* Washington, D.C.; [Springfield, Va.]: National Aeronautics and Space Administration.

Gao, T., Tseng, Y.-H., & Lu, X.-Y. (2007, December). An improved hybrid Cartesian/immersed boundary method for fluid-solid flows. *Int. J. Numer. Meth. Fluids*, *55*(12), 1189–1211.

Gavrea, B., Negrut, D., & Potra, F. (2005, 01). The Newmark Integration Method for Simulation of Multibody Systems: Analytical Considerations. In (Vol. 118).

Geradin, M., Rixen, D. J., & Gaeradin, M. (2015). *Mechanical Vibrations : Theory and Application to Structural Dynamics.* New York, United Kingdom: John Wiley & Sons, Incorporated.

Gerstenberger, A., & Wall, W. A. (2008). An eXtended Finite Element Method/Lagrange multiplier based approach for fluid-structure interaction. *Computer Methods in Applied Mechanics and Engineering*, *197*(19), 1699–1714.

Ghias, R., Mittal, R., & Lund, T. (2004). A Non-Body Conformal Grid Method for Simulation of Compressible Flows with Complex Immersed Boundaries. In *42nd AIAA Aerospace Sciences Meeting and Exhibit* (pp. 1–10).

Goldstein, D., Handler, R., & Sirovich, L. (1993). Modeling a No-Slip Flow Boundary with an External Force Field. *Journal of Computational Physics*, *105*(2), 354-366.

Green, D., & Unruh, W. G. (2006, July). The failure of the Tacoma Bridge: A physical model. *American Journal of Physics*, *74*(8), 706–716.

Gsell, S., & Favier, J. (2021). Direct-forcing immersed-boundary method: A simple correction preventing boundary slip error. *Journal of Computational Physics*, *435*, 110265.

Guilmineau, E., & Queutey, P. (2002). A Numerical Simulation of vortex shedding from an oscillating circular cylinder. *Journal of Fluids and Structures*, *16*(6), 773 - 794.

Guyan, R. J. (1965, February). Reduction of stiffness and mass matrices. *AIAA Journal*, *3*(2), 380–380.

Haase, W., Braza, M., & Revell, A. (2009). *DESider : a European effort on hybrid RANS-LES modelling : results of the European Union funded project, 2004-2007.* Berlin: Springer.

He, T., & Zhang, K. (2017). An Overview of the Combined Interface Boundary Condition Method for Fluid-Structure Interaction. *Archives of Computational Methods in Engineering : State of the Art Reviews*, *24*(4), 891-934.

Hilber, H. M., Hughes, T. J. R., & Taylor, R. L. (1977). Improved numerical dissipation for time integration algorithms in structural dynamics. *Earthquake Engineering & Structural Dynamics*, *5*(3), 283-292.

Hirt, C. W., Amsden, A. A., & Cook, J. L. (1974). An arbitrary Lagrangian-Eulerian computing method for all flow speeds. *Journal of Computational Physics*, *14*(3), 227–253.

Hurty, W. C. (1965, April). Dynamic analysis of structural systems using component modes. *AIAA Journal*, *3*(4), 678–685.

James, S., Anand, M. S., & Sekar, B. (2008, 06). *Towards Improved Prediction of Aero-Engine Combustor Performance Using Large Eddy Simulations* (Vols. Volume 3: Combustion, Fuels and Emissions, Parts A and B).

Jauvtis, N., & Williamson, C. (2003). Vortex-induced vibration of a cylinder with two degrees of freedom. *Journal of Fluids and Structures*, *17*(7), 1035 - 1042.

Jauvtis, N., & Williamson, C. H. K. (2004). The effect of two degrees of freedom on vortex-induced vibration at low mass and damping. *Journal of Fluid Mechanics*, *509*, 23–62.

Joby-Aviation. (n.d.). *Joby aviation.* https://www.jobyaviation.com/. (Accessed: 2020-01-28)

Kane, T. R., Likins, P. W., & Levinson, D. A. (1983). *Spacecraft Dynamics.* McGraw Hill.

Kang, Z., Zhang, C., Ma, G., & Ni, W. (2018). A numerical investigation of two-degree-of-freedom VIV of a circular cylinder using the modified turbulence model. *Ocean Engineering*, *155*, 211 - 226.

Kapahi, A., Sambasivan, S., & Udaykumar, H. S. (2013). A three-dimensional sharp interface Cartesian grid method for solving high speed multi-material impact, penetration and fragmentation problems. *Journal of Computational Physics*, *241*, 308–332.

Katopodes, N. D., & Katopodes, N. D. (2019). Chapter 13 - level set method. In *Free-Surface Flow* (pp. 804–828). Butterworth-Heinemann.

Katzenmeier, L., Vidy, C., Benassi, L., & Breitsamter, C. (2019, June). Prediction of Horizontal Tail Buffeting Loads Based on URANS and DES Approaches. In *Proceed-*

ings of conference International Forum on Aeroelasticity and Structural Dynamics (IFASD).

Kempe, T., & Fröhlich, J. (2012). An improved immersed boundary method with direct forcing for the simulation of particle laden flows. *Journal of Computational Physics*, *231*(9), 3663–3684.

Kenway, G., & Martins, J. (2014, January). Multi-Point High-Fidelity Aerostructural Optimization of a Transport Aircraft Configuration. *Journal of Aircraft*, *51*, 144–160.

Khalak, A., & Williamson, C. (1999). Motions, forces and mode transitions in vortex-induced vibrations at low mass-damping. *Journal of Fluids and Structures*, *13*(7), 813 - 851.

Khorrami, M. R., & Fares, E. (2019). Toward noise certification during design: airframe noise simulations for full-scale, complete aircraft. *CEAS Aeronautical Journal*, *10*(1), 31–67.

Kim, J. (2012, 04). *Lecture notes on Extended Hamilton's principle.* Department of Mechanical and Aerospace Engineering University at Buffalo.

Kim, J.-G., & Lee, P.-S. (2015, July). An enhanced Craig-Bampton method. *International Journal for Numerical Methods in Engineering*, *103*(2), 79–93.

Kim, M., Tyan, M., Juliawan, N., Kim, S., Chung, J., & Lee, J.-W. (2019, July). Data Fusion Method for Constructing Fighter Aircraft Aerodynamic Database Using Variable Fidelity and Space Mapping Techniques. In *In proceedings of Conference: 8th european conference for aeronautics and space sciences.*

Kim, W., & Choi, H. (2019). Immersed boundary methods for fluid-structure interaction: A review. *International Journal of Heat and Fluid Flow*, *75*, 301–309.

Klerk, D. de, Rixen, D. J., & Voormeeren, S. N. (2008, May). General Framework for Dynamic Substructuring: History, Review and Classification of Techniques. *AIAA Journal*, *46*(5), 1169–1181.

Krenk, S. (2009). *Non-linear modeling and analysis of solids and structures.* Cambridge, UK: Cambridge University Press.

Krüger, W. (2007). *Multibody Dynamics for the Coupling of Aeroelasticity and Flight Mechanics of Highly Flexible Structures.*

Lai, M. C., & Peskin, C. S. (2000). An Immersed Boundary Method with Formal Second-Order Accuracy and Reduced Numerical Viscosity. *Journal of Computational Physics*, *160*(2), 705–719.

Lauer, E., Hu, X. Y., Hickel, S., & Adams, N. A. (2012). Numerical modelling and investigation of symmetric and asymmetric cavitation bubble dynamics. *Computers & Fluids*, *69*, 1–19.

Lee, J., & You, D. (2013). An implicit ghost-cell immersed boundary method for simulations of moving body problems with control of spurious force oscillations. *Journal of Computational Physics*, *233*, 295–314.

Leishman, J. G. (2006). *Principles of helicopter aerodynamics.* Cambridge: Cambridge University Press.

Le Tallec, P., & Mouro, J. (2001). Fluid structure interaction with large structural displacements. *Computer Methods in Applied Mechanics and Engineering*, *190*(24), 3039–3067.

Li, G., Law, Y. Z., & Jaiman, R. K. (2019a, jan). A 3D variational multibody aeroelastic

formulation for bio-inspired flight dynamics in turbulent flow. In *AIAA Scitech 2019 Forum.*

Li, G., Law, Y. Z., & Jaiman, R. K. (2019b). A novel 3D variational aeroelastic framework for flexible multibody dynamics: Application to bat-like flapping dynamics. *Computers & Fluids*, *180*, 96–116.

Li, Y., Castro, A. M., Martin, J. E., Sinokrot, T., Prescott, W., & Carrica, P. M. (2017). Coupled computational fluid dynamics/multibody dynamics method for wind turbine aero-servo-elastic simulation including drivetrain dynamics. *Renewable Energy*, *101*, 1037–1051.

Likins, P. (1967). Modal method for analysis of free rotations of spacecraft. *AIAA Journal*, *5*, 1304–1308.

Lilium. (n.d.). *Lilium the jet.* https://lilium.com/the-jet. (Accessed: 2020-12-08)

Liu, H., & Wang, X. (2019). Aeroservoelastic design of piezo-composite wings for gust load alleviation. *Journal of Fluids and Structures*, *88*, 83–99.

Liu, J., Jaiman, R. K., & Gurugubelli, P. S. (2014). A stable second-order scheme for fluid-structure interaction with strong added-mass effects. *Journal of Computational Physics*, *270*, 687–710.

Luo, H., Dai, H., Sousa, P. J. S. A. Ferreira de, & Yin, B. (2012). On the numerical oscillation of the direct-forcing immersed-boundary method for moving boundaries. *Computers & Fluids*, *56*, 61–76.

MacNeal, R. H. (1971). A hybrid method of component mode synthesis. *Computers & Structures*, *1*(4), 581–601.

Maiti, S., Roy, J., Mallik, A. K., & Bhattacharjee, J. K. (2016). Nonlinear dynamics of a rotating double pendulum. *Physics Letters A*, *380*(3), 408–412.

Majumdar, S., Iaccarino, G., & Durbin, P. (2002). RANS solvers with adaptive structured boundary non-conforming grids. *Center for Turbulence Research Annual Research Briefs*, 353–366.

Malik, M. R., & Bushnell, D. M. (2012). *Role of Computational Fluid Dynamics and Wind Tunnels in Aeronautics R and D* (Tech. Rep. No. 20120016316). Langley Research Center.

Matthies, H. G., & Steindorf, J. (2003). Partitioned strong coupling algorithms for fluid-structure interaction. *Computers & Structures*, *81*(8), 805–812.

Mcalister, K., Pucci, S., Mccroskey, W., & Carr, L. (1982a). *An Experimental Study of Dynamic Stall on Advanced Airfoil Sections. Volume 1. Summary of the Experiment.* (NASA Technical Memorandum No. 84245). National Aeronautics and Space Administration Moffett Field CA AMES Research Center.

Mcalister, K., Pucci, S., Mccroskey, W., & Carr, L. (1982b). *An Experimental Study of Dynamic Stall on Advanced Airfoil Sections. Volume 2. Pressure and Force Data.* (NASA Technical Memorandum No. 84245). National Aeronautics and Space Administration Moffett Field CA AMES Research Center.

Mcalister, K., Pucci, S., Mccroskey, W., & Carr, L. (1982c). *An Experimental Study of Dynamic Stall on Advanced Airfoil Sections. Volume 3. Hot-Wire and Hot-Film Measurements.* (NASA Technical Memorandum No. 84245). National Aeronautics and Space Administration Moffett Field CA AMES Research Center.

Minguzzi, E. (2015, Mar). Rayleigh's dissipation function at work. *European Journal of Physics*, *36*(3), 035014.

Mittal, R., Dong, H., Bozkurttas, M., Najjar, F., Vargas, A., & Loebbecke, A. (2008,

May). A versatile sharp interface immersed boundary method for incompressible flows with complex boundaries. *Journal of computational physics*, *227*, 4825–4852.

Mittal, R., & Iaccarino, G. (2005). Immersed boundary method. *Annual Review of Fluid Mechanics*, *37*(1), 239–261.

Mittal, R., Seshadri, V., & Udaykumar, H. S. (2004). Flutter, Tumble and Vortex Induced Autorotation. *Theoretical and Computational Fluid Dynamics*, *17*(3), 165–170.

Mo, H., Lien, F.-S., Zhang, F., & Cronin, D. S. (2018, October). An immersed boundary method for solving compressible flow with arbitrarily irregular and moving geometry. *Int J Numer Meth Fluids*, *88*(5), 239–263.

Mohd-Yusof, J. (1997). Combined Immersed Boundaries/B-Splines Methods for Simulations of Flows in Complex Geometries. In *Annual Research Brief* (pp. 317–327). Center for Turbulence Research.

Mohd-Yusof, J., Orlandi, P., & Haworth, D. (1998, January). LES in complex geometries using boundary body forces. *Proceedings of the Summer Program*.

Morton, S., Cummings, R., & Kholodar, D. (2007, November). High Resolution Turbulence Treatment of F/A-18 Tail Buffet. *Aerospace Engineering*, *44*.

Murray, A. J., Thornber, B., Flaig, M., & Vio, G. A. (2019, January). Highly Parallel, Multi-stage Mesh Motion using Radial Basis Functions for Fluid-Structure Interaction. In *Aiaa scitech 2019 forum.*

Métivier, V., Dumas, G., & Poirel, D. (2008). Simulations of self-excited pitch oscillations of a NACA 0012 airfoil in the transitional Reynolds number regime. *CSME Forum*, 5–8.

Métivier, V., Dumas, G., & Poitrel, D. (2009). Aeroelastic dynamics of a NACA 0012 airfoil at transitional Reynolds numbers. *AIAA J*, *4034*, 1–18.

Neto, M. A., Amaro, A., Roseiro, L., Cirne, J., & Leal, R. (2015). *Engineering Computation of Structures: The Finite Element Method.* Springer Interntional Publishing.

Newmark, N. M. (1959). *A Method of Computation for Structural Dynamics.* American Society of Civil Engineers.

Newmark Nathan, M. (1959, July). A Method of Computation for Structural Dynamics. *Journal of the Engineering Mechanics Division*, *85*(3), 67–94.

Nikishkov, G. P. (2004). *Introduction to the finite element method.* Lecture Notes, University of Aizu.

Noordt, W. van, Ganju, S., & Brehm, C. (2021, July). Immersed-Boundary Wall-Modeled Large-Eddy Simulation of High Mach Number Boundary Layer Flows. American Institute of Aeronautics and Astronautics.

Nowakowski, C., Fehr, J., Fischer, M., & Eberhard, P. (2012). Model Order Reduction in Elastic Multibody Systems using the Floating Frame of Reference Formulation. *IFAC Proceedings Volumes*, *45*(2), 40–48.

Obrecht, C., Kuznik, F., Tourancheau, B., & Roux, J.-J. (2013). Multi-GPU implementation of the lattice Boltzmann method. *Computers & Mathematics with Applications*, *65*(2), 252–261.

Örley, F., Pasquariello, V., Hickel, S., & Adams, N. A. (2015). Cut-element based immersed boundary method for moving geometries in compressible liquid flows with cavitation. *Journal of Computational Physics*, *283*, 1–22.

Palacios, R., Cesnik, C., & Reichenbach, E. (2007, January). Re-examined Structural Design Procedures for Very Flexible Aircraft. *International Forum of Aeroelasticity and Structural Dynamics*, *51*.

Park, K. C., Felippa, C. A., & Ohayon, R. (2001). Partitioned formulation of internal fluid-structure interaction problems by localized lagrange multipliers. *Computer Methods in Applied Mechanics and Engineering*, *190*(24), 2989–3007.

Pasquariello, V., Hammerl, G., Örley, F., Hickel, S., Danowski, C., Popp, A., et al. (2016). A cut-cell finite volume - finite element coupling approach for fluid-structure interaction in compressible flow. *J. Comput. Phys.*, *307*, 670-695.

Pember, R. B., Bell, J. B., Colella, P., Curtchfield, W. Y., & Welcome, M. L. (1995). An Adaptive Cartesian Grid Method for Unsteady Compressible Flow in Irregular Regions. *Journal of Computational Physics*, *120*(2), 278–304.

Peskin, C. S. (1973). Flow patterns around heart valves: a digital computer method for solving the equations of motion. *IEEE Transactions on Biomedical Engineering*, *BME-20*(4), 316–317.

Peskin, C. S. (1982). The Fluid Dynamics of Heart Valves: Experimental, Theoretical, and Computational Methods. *Annual Review of Fluid Mechanics*, *14*(1), 235–259.

Pinelli, A., Naqavi, I. Z., Piomelli, U., & Favier, J. (2010). Immersed-boundary methods for general finite-difference and finite-volume Navier-Stokes solvers. *Journal of Computational Physics*, *229*(24), 9073–9091.

Poirel, D., Harris, Y., & Benaissa, A. (2006, 07). *Aeroelastic Dynamics of a NACA 0012 Airfoil in the Transitional Reynolds Number Regime* (Vols. Volume 9: 6th FSI, AE and FIV and N Symposium).

Poirel, D., Harris, Y., & Benaissa, A. (2008). Self-sustained aeroelastic oscillations of a NACA0012 airfoil at low-to-moderate Reynolds numbers. *Journal of Fluids and Structures*, *24*(5), 700–719.

Rankin, C. C., & Brogan, F. A. (1986, May). An Element Independent Corotational Procedure for the Treatment of Large Rotations. *J. Pressure Vessel Technol*, *108*(2), 165–174.

Rayleigh, J. W. S. (1945). *The theory of sound.* (Vol. 2). New York: Dover. (Sec.)

Rendall, T. C. S., & Allen, C. (2009, January). Improved radial basis function fluid-structure coupling via efficient localized implementation. *International Journal for Numerical Methods in Engineering*, *78 (10)*, 1188–1208.

Rendall, T. C. S., & Allen, C. B. (2008). Unified fluid-structure interpolation and mesh motion using radial basis functions. *International Journal for Numerical Methods in Engineering*, *74*(10), 1519-1559.

Ribeiro, A. F. P., Casalino, D., & Fares, E. (2016). Lattice-Boltzmann Simulations of an Oscillating NACA0012 Airfoil in Dynamic Stall. In M. Braza, A. Bottaro, & M. Thompson (Eds.), *Advances in fluid-structure interaction* (pp. 179–192). Cham: Springer International Publishing.

Roma, A. M., Peskin, C. S., & Berger, M. J. (1999). An Adaptive Version of the Immersed Boundary Method. *Journal of Computational Physics*, *153*(2), 509–534.

Rong, B., Rui, X., Tao, L., & Wang, G. (2019). Theoretical modeling and numerical solution methods for flexible multibody system dynamics. *Nonlinear Dynamics : An International Journal of Nonlinear Dynamics and Chaos in Engineering Systems*, *98*(2), 1519-1553.

Roughen, K., Baker, M., Seber, G., & Taylor, T. (2006). A System for Aerothermodynamic, Servo, Thermal, Elastic, Propulsive Coupled Analysis (ASTEP). In *47th aiaa/asme/asce/ahs/asc structures, structural dynamics, and materials conference.*

Rubin, S. (1975, August). Improved Component-Mode Representation for Structural

Dynamic Analysis. *AIAA Journal*, *13*(8), 995–1006.

Sahin, M., & Mohseni, K. (2009). An arbitrary Lagrangian-Eulerian formulation for the numerical simulation of flow patterns generated by the hydromedusa Aequorea victoria. *Journal of Computational Physics*, *228*(12), 4588–4605.

Saiki, E., & Biringen, S. (1996). Numerical Simulation of a Cylinder in Uniform Flow: Application of a Virtual Boundary Method. *Journal of Computational Physics*, *123*(2), 450–465.

Sarkar, A., & Schlüter, J. (2013). Numerical investigation of the turbulent energy budget in the wake of freely oscillating elastically mounted cylinder at low reduced velocities. *Journal of Fluids and Structures*, *43*, 441 - 462.

Schuster, D., Liu, D., & Huttsell, L. (2003, 02). Computational Aeroelasticity: Success, Progress, Challenge. *Journal of Aircraft*, *40*.

Schuster, D. M. (2011). The Expanding Role of Applications in the Development and Validation of CFD at NASA. In (pp. 3–29). Berlin, Heidelberg : Springer Berlin Heidelberg.

Schwarz, J. B., Dowell, E. H., Thomas, J. P., Hall, K. C., Rausch, R. D., & Bartels, R. E. (2009, November). Improved Flutter Boundary Prediction for an Isolated Two-Degree-of-Freedom Airfoil. *Journal of Aircraft*, *46*(6), 2069–2076.

Sempere, J. (2009). *Yaw, pitch and roll.* Available from https://commons.wikimedia.org/wiki/File:Plane.svg (Accessed: 2020-16-03)

Serino, D. A., Banks, J. W., Henshaw, W. D., & Schwendeman, D. W. (2019). A stable added-mass partitioned (AMP) algorithm for elastic solids and incompressible flow. *Journal of Computational Physics*, *399*, 108923.

Shabana, A. A. (1996a). *An Absolute Nodal Coordinate Formulation for the Large Rotation and Deformation Analysis of Flexible Bodies.* Department of Mechanical and Industrial Engineering, University of Illinois at Chicago.

Shabana, A. A. (1996b, June). Finite Element Incremental Approach and Exact Rigid Body Inertia. *J. Mech. Des*, *118*(2), 171–178.

Shabana, A. A. (1997). Flexible Multibody Dynamics: Review of Past and Recent Developments. *Journal of Multibody System Dynamics*, 189–222.

Shabana, A. A. (2020). *Dynamics of Multibody Systems* (5th ed.). Cambridge University Press.

Shabana, A. A., & Schwertassek, R. (1998). Equivalence of the floating frame of reference approach and finite element formulations. *International Journal of Non-Linear Mechanics*, *33*(3), 417–432.

Sharifnia, M., & Akbarzadeh, A. (2017). A constrained assumed modes method for dynamics of a flexible planar serial robot with prismatic joints. *Multibody System Dynamics*, *40*(3), 261–285.

Shi, B., Yang, X., Jin, G., He, G., & Wang, S. (2019). Wall-modeling for large-eddy simulation of flows around an axisymmetric body using the diffuse-interface immersed boundary method. *Applied Mathematics and Mechanics*, *40*(3), 305–320.

Slotnick, J. P., Khodadoust, A., Alonso, J. J., Darmofal, D. L., Gropp, W., Lurie, E. A., et al. (2014). *CFD Vision 2030 Study: A Path to Revolutionary Computational Aerosciences* (NASA Contractor Report No. 20140003093). Langley Research Center.

Smagorinsky, J. (1963, January). General Circulation Experiments with the Primitive Equations. *Monthly Weather Review*, *91*(3), 99.

Soriano, H. L., & Filho, F. V. (1988). On the modal acceleration method in structural dynamics. Mode truncation and static correction. *Computers & Structures*, *29*(5), 777–782.

Sotiropoulos, F., & Yang, X. (2014). Immersed boundary methods for simulating fluid-structure interaction. *Progress in Aerospace Sciences*, *65*, 1–21.

Steeves, E., & Walton, W. C. (1969). *A new matrix theorem and its application for establishing independent coordinates for complex dynamical systems with constraints* (NASA Technical Report No. R-326).

Stengel, R. F. (2004). *Flight Dynamics*. Princeton University Press.

Subbaraj, K., & Dokainish, M. (1989). A survey of direct time-integration methods in computational structural dynamics—II. Implicit methods. *Computers & Structures*, *32*(6), 1387 - 1401.

Swaczyna, M. (2011). Several examples of nonholonomic mechanical systems. *Communications in Mathematics*, *19*(1), 27–56.

Tamaki, Y., & Kawai, S. (2021, Nov). Wall modeling for large-eddy simulation on non-body-conforming Cartesian grids. *Phys. Rev. Fluids*, *6*, 114603.

Tatsuno, M., & Bearman, P. W. (1990). A visual study of the flow around an oscillating circular cylinder at low Keulegan-Carpenter numbers and low Stokes numbers. *Journal of Fluid Mechanics*, *211*, 157-182.

Tewari, A. (2015). *Aeroservoelasticity: Modeling and Control* (1st ed.). Springer-Verlag New York.

Theis J. J, J. (2020). Robust modal damping control for active flutter suppression. *Journal of Guidance, Control, and Dynamics*, *43*(6), 1056–1068.

Thévenaz, P., Blu, T., & Unser, M. (2000, Jul). Interpolation revisited. *IEEE transactions on medical imaging*, *19*, 739-58.

Tseng, Y.-H., & Ferziger, J. H. (2003). A ghost-cell immersed boundary method for flow in complex geometry. *Journal of Computational Physics*, *192*(2), 593–623.

TU-Delft. (n.d.). *Flying-v*. https://www.tudelft.nl/en/ae/flying-v. (Accessed: 2021-01-25)

Turek, S., Hron, J., Mádlík, M., Razzaq, M., Wobker, H., & Acker, J. (2010, September). Numerical Simulation and Benchmarking of a Monolithic Multigrid Solver for Fluid-Structure Interaction Problems with Application to Hemodynamics. *Lecture Notes in Computational Science and Engineering*, *73*, 193–220.

Udaykumar, H., Shyy, W., & Rao, M. (1996, April). Elafint: A mixed Eulerian-Lagrangian method for fluid flows with complex and moving boundaries. *Int. J. Numer. Meth. Fluids*, *22*(8), 691–712.

Udaykumar, H. S., Mittal, R., Rampunggoon, P., & Khanna, A. (2001). A Sharp Interface Cartesian Grid Method for Simulating Flows with Complex Moving Boundaries. *Journal of Computational Physics*, *174*(1), 345–380.

Uhlmann, M. (2005). An immersed boundary method with direct forcing for the simulation of particulate flows. *Journal of Computational Physics*, *209*(2), 448–476.

Van Brummelen, H. (2009, March). Added Mass Effects of Compressible and Incompressible Flows in Fluid-Structure Interaction. *Journal of Applied Mechanics*, *76*, 021206.

Vanella, M., & Balaras, E. (2009, October). A moving-least-squares reconstruction for embedded-boundary formulations. *Journal of Computational Physics*, *228*(18), 6617-6628.

Van Ingen, J. L. (2008). *The eN method for transition prediction: Historical review of work at TU Delft.* AIAA.

Vierendeels, J., Dumont, K., & Verdonck, P. R. (2008). A partitioned strongly coupled fluid-structure interaction method to model heart valve dynamics. *Journal of Computational and Applied Mathematics*, *215*(2), 602–609.

Vreman, A. W. (2004). An eddy-viscosity subgrid-scale model for turbulent shear flow: Algebraic theory and applications. *Physics of Fluids*, *16*, 3670–3681.

Wang, J., & Li, Z. (2015). Implementation of HHT algorithm for numerical integration of multibody dynamics with holonomic constraints. *Nonlinear Dynamics*, *80*(1), 817–825.

Williams, D. (1945). *Dynamic loads in aeroplanes under given impulsive loads with particular reference to landing and gust loads on a large flying boat* (ARC Technical Report No. 551768504).

Wilson, E. (1968). *A Computer Program for the Dynamic Stress Analysis of underground Structures* (Tech. Rep.). U.S. Army Engineering Waterways Experiment Station.

Wilson, E., Yuan, M., & Dickens, J. M. (1982). Dynamic analysis by direct superposition of Ritz vectors. *Earthquake Engineering & Structural Dynamics*, *10*, 813-821.

Wohlmuth, B. (2000, January). A Mortar Finite Element Method Using Dual Spaces For The Lagrange Multiplier. *SIAM Journal on Numerical Analysis*, *38*.

Wood, J. N., Breuer, M., & De Nayer, G. (2020). Experimental investigations on the dynamic behavior of a 2-DOF airfoil in the transitional Re number regime based on digital-image correlation measurements. *Journal of Fluids and Structures*, *96*, 103052.

Wright, J. R., & Cooper, J. E. (2014). *Introduction to Aircraft Aeroelasticity and Loads.* (2nd ed. ed.). Hoboken: Wiley.

Xie, D., Jian, K., & Wen, W. (2017). An element-free Galerkin approach for rigid-flexible coupling dynamics in 2D state. *Applied Mathematics and Computation*, *310*, 149–168.

Yang, Y., Bashir, M., Michailides, C., Li, C., & Wang, J. (2020). Development and application of an aero-hydro-servo-elastic coupling framework for analysis of floating offshore wind turbines. *Renewable Energy*, *161*, 606–625.

Ye, T., Mittal, R., Udaykumar, H. S., & Shyy, W. (1999). An Accurate Cartesian Grid Method for Viscous Incompressible Flows with Complex Immersed Boundaries. *Journal of Computational Physics*, *156*(2), 209–240.

Yi, L. I. U., & Changchuan, X. I. E. (2018). Aeroservoelastic stability analysis for flexible aircraft based on a nonlinear coupled dynamic model. *Chinese Journal of Aeronautics*, *31*(12), 2185–2198.

Zhang, B., Ding, W., Cheng, J., & Zhang, J. (2016, February). Transonic flutter analysis of an AGARD 445.6 wing in the frequency domain using the Euler method. *Engineering Applications of Computational Fluid Mechanics*, *10*, 244–255.

Zhang, J., & Dalton, C. (1996). Interactions of vortex-induced vibrations of a circular cylinder and a steady approach flow at a Reynolds number of 13,000. *Computers & Fluids*, *25*(3), 283 - 294.

Zhang, P., & Huang, S. (2011). Review of aeroelasticity for wind turbine: Current status, research focus and future perspectives. *Frontiers in Energy*, *5*(4), 419–434.

Zhou, M., Zhang, B., Chen, T., Peng, C., & Fang, H. (2020). A three-field dual mortar method for elastic problems with nonconforming mesh. *Computer Methods in*

Applied Mechanics and Engineering, *362*, 112870.

Zuijlen, A. H. (2006). *Fluid-structure interaction simulations: Efficient higher order time integration of partitioned systems.* Unpublished doctoral dissertation, TU Delft; Aerospace Engineering.

Appendix A

Derivatives of Euler parameters

Euler angles are used in the definition of the intial condition and output files of the present code. The present code computes the Euler parameters and time derivatives of the Euler parmeters of the initial condition based on the user prescribed Euler angles. The derivation of the Euler parameters and their time derivatives requires the partial derivatives of the Euler parameters with respect to the Euler angles. The derivatives are presented in this appendix. The partial derivatives of the Euler parameter θ_0 are given by

$$\begin{aligned}
\frac{\partial \theta_0}{\partial \phi} &= -\frac{1}{2}\sin\phi/2\cos\theta/2\cos\psi/2 + \frac{1}{2}\cos\phi/2\sin\theta/2\sin\psi/2 \\
\frac{\partial \theta_0}{\partial \theta} &= -\frac{1}{2}\cos\phi/2\sin\theta/2\cos\psi/2 + \frac{1}{2}\sin\phi/2\cos\theta/2\sin\psi/2 \\
\frac{\partial \theta_0}{\partial \psi} &= -\frac{1}{2}\cos\phi/2\cos\theta/2\sin\psi/2 + \frac{1}{2}\sin\phi/2\sin\theta/2\cos\psi/2
\end{aligned} \tag{A.1}$$

$$
\begin{aligned}
\frac{\partial^2\theta_0}{\partial\phi\partial\phi} &= -\frac{1}{4}\cos\phi/2\cos\theta/2\cos\psi/2 - \frac{1}{4}\sin\phi/2\sin\theta/2\sin\psi/2 \\
\frac{\partial^2\theta_0}{\partial\theta\partial\phi} &= +\frac{1}{4}\sin\phi/2\sin\theta/2\cos\psi/2 + \frac{1}{4}\cos\phi/2\cos\theta/2\sin\psi/2 \\
\frac{\partial^2\theta_0}{\partial\psi\partial\phi} &= +\frac{1}{4}\sin\phi/2\cos\theta/2\sin\psi/2 + \frac{1}{4}\cos\phi/2\sin\theta/2\cos\psi/2 \\
\frac{\partial^2\theta_0}{\partial\phi\partial\theta} &= +\frac{1}{4}\sin\phi/2\sin\theta/2\cos\psi/2 + \frac{1}{4}\cos\phi/2\cos\theta/2\sin\psi/2 \\
\frac{\partial^2\theta_0}{\partial\theta\partial\theta} &= -\frac{1}{4}\cos\phi/2\cos\theta/2\cos\psi/2 - \frac{1}{4}\sin\phi/2\sin\theta/2\sin\psi/2 \\
\frac{\partial^2\theta_0}{\partial\psi\partial\theta} &= +\frac{1}{4}\cos\phi/2\sin\theta/2\sin\psi/2 + \frac{1}{4}\sin\phi/2\cos\theta/2\cos\psi/2 \\
\frac{\partial^2\theta_0}{\partial\phi\partial\psi} &= +\frac{1}{4}\sin\phi/2\cos\theta/2\sin\psi/2 + \frac{1}{4}\cos\phi/2\sin\theta/2\cos\psi/2 \\
\frac{\partial^2\theta_0}{\partial\theta\partial\psi} &= +\frac{1}{4}\cos\phi/2\sin\theta/2\sin\psi/2 + \frac{1}{4}\sin\phi/2\cos\theta/2\cos\psi/2 \\
\frac{\partial^2\theta_0}{\partial\psi\partial\psi} &= -\frac{1}{4}\cos\phi/2\cos\theta/2\cos\psi/2 - \frac{1}{4}\sin\phi/2\sin\theta/2\sin\psi/2
\end{aligned}
\tag{A.2}
$$

The partial derivatives of the Euler parameter θ_1 are given by

$$
\begin{aligned}
\frac{\partial\theta_1}{\partial\phi} &= +\frac{1}{2}\cos\phi/2\cos\theta/2\cos\psi/2 + \frac{1}{2}\sin\phi/2\sin\theta/2\sin\psi/2 \\
\frac{\partial\theta_1}{\partial\theta} &= -\frac{1}{2}\sin\phi/2\sin\theta/2\cos\psi/2 - \frac{1}{2}\cos\phi/2\cos\theta/2\sin\psi/2 \\
\frac{\partial\theta_1}{\partial\psi} &= -\frac{1}{2}\sin\phi/2\cos\theta/2\sin\psi/2 - \frac{1}{2}\cos\phi/2\sin\theta/2\cos\psi/2
\end{aligned}
\tag{A.3}
$$

$$
\begin{aligned}
\frac{\partial^2\theta_1}{\partial\phi\partial\phi} &= -\frac{1}{4}\sin\phi/2\cos\theta/2\cos\psi/2 + \frac{1}{4}\cos\phi/2\sin\theta/2\sin\psi/2 \\
\frac{\partial^2\theta_1}{\partial\theta\partial\phi} &= -\frac{1}{4}\cos\phi/2\sin\theta/2\cos\psi/2 + \frac{1}{4}\sin\phi/2\cos\theta/2\sin\psi/2 \\
\frac{\partial^2\theta_1}{\partial\psi\partial\phi} &= -\frac{1}{4}\cos\phi/2\cos\theta/2\sin\psi/2 + \frac{1}{4}\sin\phi/2\sin\theta/2\cos\psi/2 \\
\frac{\partial^2\theta_1}{\partial\phi\partial\theta} &= -\frac{1}{4}\cos\phi/2\sin\theta/2\cos\psi/2 + \frac{1}{4}\sin\phi/2\cos\theta/2\sin\psi/2 \\
\frac{\partial^2\theta_1}{\partial\theta\partial\theta} &= -\frac{1}{4}\sin\phi/2\cos\theta/2\cos\psi/2 + \frac{1}{4}\cos\phi/2\sin\theta/2\sin\psi/2 \\
\frac{\partial^2\theta_1}{\partial\psi\partial\theta} &= +\frac{1}{4}\sin\phi/2\sin\theta/2\sin\psi/2 - \frac{1}{4}\cos\phi/2\cos\theta/2\cos\psi/2 \\
\frac{\partial^2\theta_1}{\partial\phi\partial\psi} &= -\frac{1}{4}\cos\phi/2\cos\theta/2\sin\psi/2 + \frac{1}{4}\sin\phi/2\sin\theta/2\cos\psi/2 \\
\frac{\partial^2\theta_1}{\partial\theta\partial\psi} &= +\frac{1}{4}\sin\phi/2\sin\theta/2\sin\psi/2 - \frac{1}{4}\cos\phi/2\cos\theta/2\cos\psi/2 \\
\frac{\partial^2\theta_1}{\partial\psi\partial\psi} &= -\frac{1}{4}\sin\phi/2\cos\theta/2\cos\psi/2 + \frac{1}{4}\cos\phi/2\sin\theta/2\sin\psi/2
\end{aligned}
\tag{A.4}
$$

The partial derivatives of the Euler parameter θ_2 are given by

$$
\begin{aligned}
\frac{\partial\theta_2}{\partial\phi} &= -\frac{1}{2}\sin\phi/2\sin\theta/2\cos\psi/2 + \frac{1}{2}\cos\phi/2\cos\theta/2\sin\psi/2 \\
\frac{\partial\theta_2}{\partial\theta} &= +\frac{1}{2}\cos\phi/2\cos\theta/2\cos\psi/2 - \frac{1}{2}\sin\phi/2\sin\theta/2\sin\psi/2 \\
\frac{\partial\theta_2}{\partial\psi} &= -\frac{1}{2}\cos\phi/2\sin\theta/2\sin\psi/2 + \frac{1}{2}\sin\phi/2\cos\theta/2\cos\psi/2
\end{aligned}
\tag{A.5}
$$

$$
\begin{aligned}
\frac{\partial^2\theta_2}{\partial\phi\partial\phi} &= -\frac{1}{4}\cos\phi/2\sin\theta/2\cos\psi/2 - \frac{1}{4}\sin\phi/2\cos\theta/2\sin\psi/2 \\
\frac{\partial^2\theta_2}{\partial\theta\partial\phi} &= -\frac{1}{4}\sin\phi/2\cos\theta/2\cos\psi/2 - \frac{1}{4}\cos\phi/2\sin\theta/2\sin\psi/2 \\
\frac{\partial^2\theta_2}{\partial\psi\partial\phi} &= +\frac{1}{4}\sin\phi/2\sin\theta/2\sin\psi/2 + \frac{1}{4}\cos\phi/2\cos\theta/2\cos\psi/2 \\
\frac{\partial^2\theta_2}{\partial\phi\partial\theta} &= -\frac{1}{4}\sin\phi/2\cos\theta/2\cos\psi/2 - \frac{1}{4}\cos\phi/2\sin\theta/2\sin\psi/2 \\
\frac{\partial^2\theta_2}{\partial\theta\partial\theta} &= -\frac{1}{4}\cos\phi/2\sin\theta/2\cos\psi/2 - \frac{1}{4}\sin\phi/2\cos\theta/2\sin\psi/2 \\
\frac{\partial^2\theta_2}{\partial\psi\partial\theta} &= -\frac{1}{4}\cos\phi/2\cos\theta/2\sin\psi/2 - \frac{1}{4}\sin\phi/2\sin\theta/2\cos\psi/2 \\
\frac{\partial^2\theta_2}{\partial\phi\partial\psi} &= +\frac{1}{4}\sin\phi/2\sin\theta/2\sin\psi/2 + \frac{1}{4}\cos\phi/2\cos\theta/2\cos\psi/2 \\
\frac{\partial^2\theta_2}{\partial\theta\partial\psi} &= -\frac{1}{4}\cos\phi/2\cos\theta/2\sin\psi/2 - \frac{1}{4}\sin\phi/2\sin\theta/2\cos\psi/2 \\
\frac{\partial^2\theta_2}{\partial\psi\partial\psi} &= -\frac{1}{4}\cos\phi/2\sin\theta/2\cos\psi/2 - \frac{1}{4}\sin\phi/2\cos\theta/2\sin\psi/2
\end{aligned}
\tag{A.6}
$$

The partial derivatives of the Euler parameter θ_3 are given by

$$
\begin{aligned}
\frac{\partial\theta_3}{\partial\phi} &= -\frac{1}{2}\sin\phi/2\cos\theta/2\sin\psi/2 - \frac{1}{2}\cos\phi/2\sin\theta/2\cos\psi/2 \\
\frac{\partial\theta_3}{\partial\theta} &= -\frac{1}{2}\cos\phi/2\sin\theta/2\sin\psi/2 - \frac{1}{2}\sin\phi/2\cos\theta/2\cos\psi/2 \\
\frac{\partial\theta_3}{\partial\psi} &= +\frac{1}{2}\cos\phi/2\cos\theta/2\cos\psi/2 + \frac{1}{2}\sin\phi/2\sin\theta/2\sin\psi/2
\end{aligned}
\tag{A.7}
$$

$$
\begin{aligned}
\frac{\partial^2\theta_3}{\partial\phi\partial\phi} &= -\frac{1}{4}\cos\phi/2\cos\theta/2\sin\psi/2 + \frac{1}{4}\sin\phi/2\sin\theta/2\cos\psi/2 \\
\frac{\partial^2\theta_3}{\partial\theta\partial\phi} &= +\frac{1}{4}\sin\phi/2\sin\theta/2\sin\psi/2 - \frac{1}{4}\cos\phi/2\cos\theta/2\cos\psi/2 \\
\frac{\partial^2\theta_3}{\partial\psi\partial\phi} &= -\frac{1}{4}\sin\phi/2\cos\theta/2\cos\psi/2 + \frac{1}{4}\cos\phi/2\sin\theta/2\sin\psi/2 \\
\frac{\partial^2\theta_3}{\partial\phi\partial\theta} &= +\frac{1}{4}\sin\phi/2\sin\theta/2\sin\psi/2 - \frac{1}{4}\cos\phi/2\cos\theta/2\cos\psi/2 \\
\frac{\partial^2\theta_3}{\partial\theta\partial\theta} &= -\frac{1}{4}\cos\phi/2\cos\theta/2\sin\psi/2 + \frac{1}{4}\sin\phi/2\sin\theta/2\cos\psi/2 \\
\frac{\partial^2\theta_3}{\partial\psi\partial\theta} &= -\frac{1}{4}\cos\phi/2\sin\theta/2\cos\psi/2 + \frac{1}{4}\sin\phi/2\cos\theta/2\sin\psi/2 \\
\frac{\partial^2\theta_3}{\partial\phi\partial\psi} &= -\frac{1}{4}\sin\phi/2\cos\theta/2\cos\psi/2 + \frac{1}{4}\cos\phi/2\sin\theta/2\sin\psi/2 \\
\frac{\partial^2\theta_3}{\partial\theta\partial\psi} &= -\frac{1}{4}\cos\phi/2\sin\theta/2\cos\psi/2 + \frac{1}{4}\sin\phi/2\cos\theta/2\sin\psi/2 \\
\frac{\partial^2\theta_3}{\partial\psi\partial\psi} &= -\frac{1}{4}\cos\phi/2\cos\theta/2\sin\psi/2 + \frac{1}{4}\sin\phi/2\sin\theta/2\cos\psi/2
\end{aligned}
\tag{A.8}
$$